Andreas Gudahl Tufte

# Predicting motion of wave-propelled USVs using closed-form expressions

March 2024

Master's thesis
2024
Andreas Gudahl Tufte

**NTNU**
Norwegian University of Science and Technology
Faculty of Information Technology and Electrical Engineering
Department of Engineering Cybernetics

NTNU
Norwegian University of Science and Technology

NTNU
Norwegian University of
Science and Technology

# Predicting motion of wave-propelled USVs using closed-form expressions

Andreas Gudahl Tufte

Guidance, Navigation and Control of Vehicles
Submission date: March 2024
Supervisor: Tor Arne Johansen
Co-supervisor: Morten Breivik
Andrew Ross

Norwegian University of Science and Technology
Department of Engineering Cybernetics

# Abstract

This work presents closed-form expressions for a new model architecture for wave-propelled uncrewed surface vehicles (USVs) for the analysis and support of a physical speed model. A simple expression for the wave-foil propulsion forces inspired by rudder theory is presented. Viscous damping effects from the foils are incorporated directly in the wave-induced seakeeping motions of the vehicle by an efficient monohull geometry. Moreover, the maneuvering motion is also found through a set of design parameters of the vehicle. In total, the joint unified motion of the maneuvering and seakeeping models provides an excitation of the foil model, driving the motion of the hydrofoils through the water. The equations of motion for the foils is found by modeling the angles relative to an inertial frame of reference, and correcting inertia forces provided by the interacting motion with the overall USV.

The hydrodynamic principles for the common use of correcting spring-loaded foils on such vehicles are modeled by considering factors such as high angles of attack, three-dimensional effects and unsteady effects. Semi-empirical equations are proposed to describe quasi-steady lift and drag curves, along with assumptions regarding stability and model applicability. The forces on the foils are considered through a simple wing model, where the forces are evaluated by considering the kinematics involved and the relative motion through irregular sea, which was expressed by a superposition of linear wave potentials.

Fluid memory effects in wave-induced motion on the efficient monohull geometry is found by least squares optimization of the impulse response of the matrix of retardation to support closed-form expression suited for simulation purposes. Additionally, unsteady thin foil theory, which is unfitted for simulation purposes in its analytical form, was incorporated by a velocity-dependent reduced order state-space representation with good agreement of the frequency-domain analytical response.

A case study involving the AutoNaut vehicle demonstrates the feasibility of the model in different wave, wind, and sea current environmental conditions, paving the way for further research and adaptation of the framework proposed.

The simulation in this work suggest that three different spring settings available in this particular case study are most efficient for different sea states. The soft springs were efficient in wave-frequencies below $\omega < 1.4$ [$s^{-1}$], the medium stiffness was efficient around $\omega = 1.8$ [$s^{-1}$] and the stiff spring was efficient for $\omega > 2.2$ [$s^{-1}$].

Future work includes the development of a general simulation model and incorporating validation methods for the maneuvering- and foil models.

# Sammendrag

*This abstract is written in Norwegian as per the requirements for the master's thesis.*

Arbeidet presenterer en ny modellarkitektur med lukkede uttrykk for bølgedrevne ubemannede overflatefartøy (USVer) for analyse og forskning av en fysisk hastighetsmodell. Det ble foreslått et enkelt uttrykk for fremdriften fra bølgekreftene gjennom foilene som var inspirert av rorteori. Viskøse dempningseffekter fra foilene er direkte inkorporet i de bølge-induserte bevegelsene til fartøyet ved hjelp av et effektiv monoskrog. Videre ble manøvreringsbevegelsen også funnet gjennom en sett med designparametere for fartøyet. De samlede bevegelsene av manøvrerings- og bølgebevegelsene gir en eksitasjon av dynamikken til foilene gjennom vannet. Bevegelsesligningene for foilene er funnet ved å modellere vinklene i forhold til en inertial referanseramme, korrigert av inertialkrefter gitt ved samspillet av den overordnede bevegelsen til fartøyet. Hydrodynamiske effekter ved bruk av korrigerende fjærlasteded foiler på slike fartøy er modellert ved å ta i betraktning faktorer som høye angrepsvinkler, tredimensjonale effekter og ustabile effekter. Semi-empiriske ligninger er foreslått for å beskrive kvasi-stasjonære løfte- og dragkurver, hvor stabilitet og modellens anvendelighet er tatt med i betraktning. Kreftene på foilene ble funnet fra en enkel foreslått vingemodell, hvor kinematikken fra fartøybevegelsen og den relative hastigheten fra sjøen er tatt med. Sjøens matematiske modell består av en superposisjon av lineære bølgepotensialer. Minneeffekter fra vannet i den bølgeinduserte bevegelse på den effektive monoskroggeometrien var funnet ved minste kvadraters metode av impulsresponsen til en matrise for å finne lukkede uttrykk som passer seg for simuleringsformål. I tillegg ble ikke-stasjonær foilteori, som dessverre ikke egner seg for simuleringsformål i sin analytiske form, approksimert ved en enkel hastighetsavhengig tilstandsromsrepresentasjon som ga god overensstemmelse med den analytiske responsen i frekvensdomenet. Et case-studie av AutoNaut-fartøyet viste at modellen egner seg for simularing under ulike forhold på sjøen, med både bølger, vind og strøm. Videre forskning og tilpasning av det foreslåtte rammeverket er mulig. Simuleringsmodellen utviklet i dette arbeidet antyder at tre forskjellige fjærinnstillinger på case-studiet er optimale for ulike sjøtilstander. De myke fjærene fungerte best for bølgefrekvenser under $\omega < 1.4$ [$s^{-1}$], middels stive fjærer var best egnet rundt $\omega = 1.8$ [$s^{-1}$] og den stive fjæren var mest effektiv for $\omega > 2.2$ [$s^{-1}$].

Videre arbeid inkluderer utviklingen av en generell simuleringsmodell, samt å foreslå gode valideringsmetoder for manøvreringsmodellen og modellen for foildynamikken.

# Preface

This report is submitted in partial fulfilment for the requirements for the degree of Master of Science in the field of Cybernetics and Robotics at the Department of Engineering Cybernetics, Norwegian University of Science and Technology (NTNU), in Trondheim. It corresponds to a full semester's work load. The thesis is supervised by Tor Arne Johansen, with co-supervisors Morten Breivik and Andrew Ross.

The original scope of this project was to find a dynamic speed model of wave-propelled uncrewed surface vehicles (USVs) for advanced control purposes. The thesis has evolved into a study of the general hydrodynamic and mathematical modelling of foil propulsion models where closed-form expressions are identified. The motion of wave-propelled USVs are found by merging this result with existing and recently emerged methods developed by the department.

I am grateful to my supervisor Tor Arne Johansen who has been orderly and helpful along the process. Additionally, I would like to thank Morten Breivik, Andrew Ross, Thor I. Fossen, Henning Øveraas and Alberto Dallolio for shared insight and contributions. Discussion with Kristoffer Gryte made me pursue this interesting topic.

Finally, I would like to express my sincere gratefulness for the opportunity I was given to work on this project and support from family and friends.

March 12th, 2024

# Contents

# Nomenclature

All angular measurements are expressed in radians, and the International System of Units (SI) [1] is employed unless explicitly stated otherwise. Additional nomenclature used in the report are defined as they appear.

$\alpha$ Ratio between wave encounter frequency to wave frequency

$\beta$ Encounter angle waves

$\beta_c$ Crab angle

$\beta_k$ Cardinal wave direction

$\beta_{V_c}$ Cardinal current direction

$\beta_{V_w}$ Cardinal wind direction

$\boldsymbol{\alpha}_i$ Parameter list for model $i$

$\boldsymbol{\tau}$ Body linear and angular forces

$\boldsymbol{\Theta}_{\text{nb}} = [\phi, \theta, \psi]^\top$ Euler angles: roll, pitch and yaw

$\chi$ Cardinal course angle

$\delta$ Rudder angle

$\delta_{\text{geo}}$ Geometric parameter for hull

$\Gamma, \gamma$ Circulation and vortex distribution

$\gamma_{\text{w}}$ Angle of attack wind

$\kappa$ Smith's correction factor

$\kappa$ Torsion spring stiffness

$\lambda$ Wavelength

$\Lambda_{\text{R}}, \Lambda_{\text{F}}$ Aspect ratio: rudder, wave foils

$\Lambda_{\text{T}}, \Lambda_{\text{L}}$ Vehicle aspect ratio: transversal and longitudinal

$\mathbf{B}$ Damping matrix

$\mathbf{C}(\boldsymbol{\nu})$ Coriolis and centripetal force matrix

$\mathbf{f}^b = [X, Y, Z]^\top$ Linear body forces

$\mathbf{G}$ Gravity and restoring matrix

$\mathbf{M}$ Mass matrix

$\mathbf{m}^b = [K, M, N]^\top$ Angular body moments

$\mathbf{Q}$ Generalized forces

$\mathbf{q}$ General coordinates for configuration

$\mathbf{R}_b^n$ Rotation matrix from $\{n\}$ to $\{b\}$

$\mathbf{v}_{\text{nb}}^b = [u, v, w]^\top$ Body linear velocities

$\mu, \nu$ Fluid viscosity, kinematic viscosity

$\mu_B$ Ratio viscous damping to critical damping

$\nabla, \Delta$ Displacement, Displacement mass

$\omega, \omega_{\text{e}}$ Wave frequency, Encounter wave frequency

$\Phi, \varphi$ Wave potential, complex wave potential

$\psi$ Cardinal heading angle

$\rho, \rho_{\text{a}}$ Sea and air density

$\Sigma_i$ Model $i$

$\text{GM}_{\text{L}}$ Longitudinal metacentric height

$\text{GM}_{\text{T}}$ Transverse metacentric height

$\zeta, \zeta_{\text{a}}$ Wave elevation, wave amplitude

$A_{\text{Fw}}, A_{\text{Lw}}$ Frontal and lateral projected vehicle area above free surface

$a_{\text{H}}$ Force factor rudder

$A_{\text{R}}, A_{\text{F}}$ Rudder area, hydrofoil area

$B$ Breadth

$b$ Sectional hydrodynamic damping

$c$ Chord length

$c_x, c_y, c_n$ Wind coefficients

$d$ Longitudinal distance between IMU and $\mathrm{CG}_x$

$g$ Acceleration due to gravity

$h$ Water depth

$H_a^b(s)$ Transfer function from $a$ to $b$

$k$ Linear spring coefficient

$k, k_\mathrm{e}$ Wave number (w.n.), encounter w.n.

$K_0, M_0, N_0$ Angular forcing functions

$L, L_\mathrm{oa}$ Length, Length over all

$L_\mathrm{pp}$ Length between perpendiculars

$P$ Pressure

$p, q, r$ Body angular velocities

$R_{ii}$ Radius of gyration in axis $i$

$s$ Laplace variable

$S, b$ Span, half-span for foil

$T$ Draft (or draught)

$t$ Time

$t_\mathrm{R}, t_\mathrm{F}$ Drag coefficient rudder and hydrofoil

$T_i$ Time period in DOF $i$

$u_\mathrm{c}, v_\mathrm{c}, w_\mathrm{c}$ Current velocities in body frame

$u_\mathrm{r}, v_\mathrm{r}, w_\mathrm{r}$ Relative velocities in body frame

$V_\mathrm{c}$ Current speed

$V_\mathrm{w}$ Wind speed

$X_0, Y_0, Z_0$ Linear forcing functions

$x_\mathrm{H}$ Interaction coefficient rudder

$x_\mathrm{R}$ Longitudinal rudder position coordinate

$x_\mathrm{p}, y_\mathrm{p}, z_\mathrm{p}$ Position of pivot point for foil

$\mathrm{C_{3D}}$ Three-dimensional correction coefficient

$\mathrm{C_a}$ Non-circulatory force coefficient

$\mathrm{C_B}$ Block coefficient

$\mathrm{C_D}$ Drag coefficient

$\mathrm{C_{geo}}$ Geometric integral constant

$\mathrm{C_{hull}}$ Geometric hull constant

$\mathrm{C_L}$ Lift coefficient

$\mathrm{C_N}$ Normal force coefficient

$\mathrm{C_{Th}}$ Theodorsen function

$\mathrm{C_{wp}}$ Waterplane area coefficient

CG Center of gravity (usage, e.g. $x_\mathrm{g}$)

CO Coordinate origin body

CP Center of pressure (usage, e.g. $x_\mathrm{c.p.}$)

# Chapter 1

# Introduction

## 1.1 Motivation

Despite the long history of wave-propelled boats since the 1890s and proposals dating back to 1858, their mainstream adoption has been limited. Today, the growing economic incentive to reduce fossil fuel usage, alongside environmental concerns like global warming, has led to renewed interest in utilizing renewable energy for ship propulsion. [2]

Wave energy offers an advantage over traditional sails for ship propulsion due to its typically lower variability, as waves propagate uniformly across oceans from distant storm sources. The primary method employed in wave-propelled boats involves the use of lift-surfaces called foils, which convert the relative motion between the foil and the water into propulsive thrust.

A promising area for the practical application of wave-propulsion is through foils mounted underneath the hull on uncrewed surface vehicles (USVs). When there are sufficient waves, the wave-induced motions of the hull, coupled with the interaction of the foils, propel the vehicle forward without any additional fuel. This will in principle allow the USV to operate with an unrestricted endurance – if not for regular maintenance – with many new and exciting applications, e.g. in marine robotics or remote oceanography monitoring without human interventions.

A drawback however, is that the forward speed rely on the environmental sea state, and is thus not actively controlled. Course over ground control is challenging when the drift forces exerted by the environment predominate the steering and propulsion forces generated by the waves. Guidance, navigation and control (GNC) systems implemented on wave-propelled USVs need to show a degree of robustness to allow autonomous operations across different environmental states. For steering control purposes, it is thus beneficial to predict future vehicle's states. Such predictions can be estimated from a physical speed model of the USV along present and forecast sea states, winds and ocean currents.

This work serves as a continuation on previous work on steering control for a specific wave-propelled USV at the Norwegian University of Science and Technology (NTNU), wherein

> *"... a speed model is key and would provide useful knowledge used for mission planning and course control purposes. The investigation of a speed model for this unique wave-propelled USV is left as a future work."* – Dallolio et al., 2022 [3]

### 1.1.1 Foils in the marine context

Hydrofoils are lift-generating surfaces – *foils* – operating below the free surface. Unlike aerial counterparts, marine vehicles are mainly using lift-generating surfaces for control purposes. Lifting surfaces, such as rudders, are used to create forces and moments for steering boats, while stabilizing fins dampen wave-induced motions. *Hydroplanes* are actively controlled lifting surfaces for adjusting the elevation of submarines. [4]

The two most common ways of adjusting lifting surfaces are through the use of trailing edge flaps to control the camber, or by adjusting the attack angle via incidence control [5]. The adjustment of the attack angle can be achieved by moving either or both the lifting part of the foil and the supporting strut. In the latter case, the actuators need to be even more powerful.

A hydrofoil boat is a boat where foils are used to lift the hull partly or fully above the waterline to reduce resistance, or drag of the hull, through water [6].

### 1.1.2 Wave-propulsion from foils

In this work, a special type of hydrofoils whose role is to create horizontal lift able to propel a marine vehicle forward is researched. Pitch and heave motion of a marine craft pushes and drags the foils through water, generating propulsive thrust for anOne of the earliest working concepts for a wave-propelled boat is illustrated in Fig. 1.1, where elastic metal plates were used as foils [7]. In that case, both the curvature and the attack angle of the foils were controlled passively by the stiffness in the metal plates, chosen by trial and error.

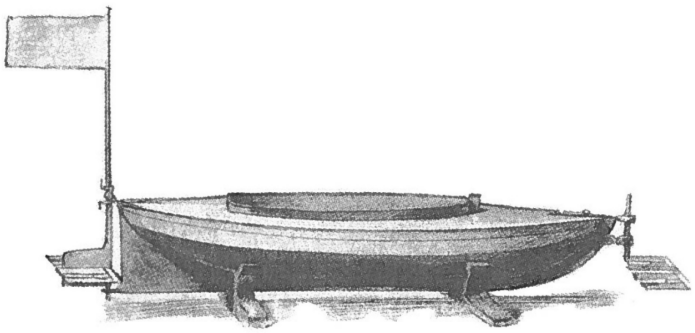

**Figure 1.1:** Drawing of the wave-propelled boat *Autonaut* from Pearson's Magazine, December 1898. Facsimile from Burnett [7].

A classification of longitudinal displacements of the foils is illustrated in Fig. 1.2. Foils used for wave-propulsion is usually placed at the bow or at the stern to extract combined pitching and heaving motion of the vehicle for forward thrust. The foil propulsion works much like a rectifier, converting energy in the vertical motion into forward thrust.

Bøckmann [2] investigated wave propulsion of ships through the use of auxiliary foils, and found that a ". . . spring-loaded foil with welltuned spring stiffness is preferable over a fixed foil". However, Bøckmann also found that "the drawback of a spring-loaded wavefoil . . . is that the spring stiffness needs to be tuned for the instantaneous wave condition."

An additional challenge arises when sea waves are absent, in which case wave-propelled USVs drift in the ocean current without sufficient forward thrust [8].

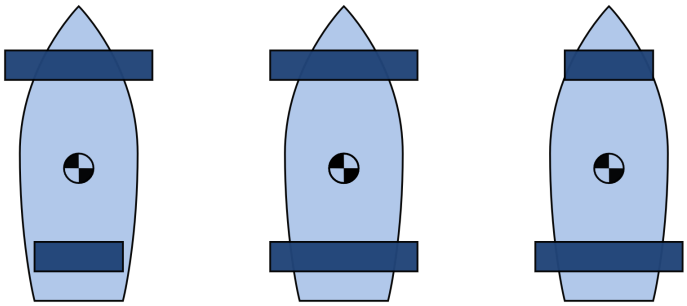

**(a)** Plane/classic **(b)** Tandem **(c)** Canard

**Figure 1.2:** Longitudinal displacement and relative sizes of foils corresponding to *plane/classic*, *tandem* and *canard* configuration. The illustration is a bottom view of vehicles. the blue rectangles represent lifting surfaces. Based on Ploe [5].

## 1.2 Previous work

Ship maneuvering in calm water has long been investigated, and a vast collection of existing maneuverability standards is found from the International Maritime Organization (IMO), for instance in resolutions [9] and [10]. The handbook of Fossen [4] delivers a great overview on marine craft modeling and control and is a great source of reference used throughout this work. According to Fossen, "The models in this book can be used for prediction, real-time simulation, decision-support systems, situational awareness as well as controller-observer-design." Rapid estimation of the motion of marine vehicles in 6 degrees of freedom (DOFs) can be found in Taimuri et al. [11] and references therein. Mathematical modeling of ships for control purposes may also be referred to Perez [12].

The literature on oscillating foils extend far beyond the realm of wave propulsion of ships [2]. The theoretical framework on foils as lifting surfaces has been studied for over a hundred years, with significant results from thin airfoil theory with experimental results in Jacobs et al. [13], and analytical results for unsteady circulatory forces on foils are given by Theodorsen [14]. A great reference to lift and drag with application on foils can be found in the corresponding books by Hoerner [15] and [6]. Updated literature on the fundamentals in airfoil theory can be found in the book by Anderson [16]. One of the limitations in the existing models is the assumption of small attack angles. The characteristics of foils through all attack angles has been de-prioritized. On wave-propelled USVs however, the speed is small and closed-form expressions for foil forces beyond small attack angles is necessary. Empiric formulae for sectional lift and drag curves based on physical models was proposed by Tufte [17].

Previous theoretical models typically neglects the effects of stall, which is reasonable only when the ship speed is high or for small wave amplitudes [2]. An early study of the extraction of

wave energy from wings oscillating in waves can be found in Wu [18]. Hydrodynamics of oscillating foils beneath the free surface can for instance be found in Filippas and Belibassakis [19]. An analytical model of the study of flapping hydrofoil for wave propulsion can be found in Lopes et al. [20]. One of the best references to wave-propulsion models with hydrofoils is the thesis from Bøckmann [2] and the master's thesis from Eitzen [21] investigated mathematical framework for wave-propulsion from foils.

Recently, Zghyer [22] investigated the role of ship simulators and maneuvering models in maritime operations: "Full autonomy holds great promise for enhancing safety and efficiency in the maritime industry. Control is the main challenge: Autonomous ships' main development challenge is merely a collision detection and avoidance problem." If wave-propulsion becomes more widespread, an additional dimension for ship autonomy is introduced.

Wave-propelled USVs are heavily affected by sea waves and knowledge of the wave encounter frequency can be used by the steering control algorithm for guidance and control purposes. Investigation of ship motion in waves can for instance be found in the book by Jensen [23] and is also treated in the hydrodynamics book by Newman [24]. Analytical estimation of ship motion in waves using closed-form expressions can be found in Jensen et al. [25] and successful estimation of the wave encounter frequency was developed and tested for a wave-propelled USV by Dallolio et al. [26].

Recently, linear and Gaussian regression has been applied to predict the speed of wave-propelled USVs, see Øveraas et al. [27]. This method is based on met-ocean forecast. A proposed control strategy for steering of wave-propelled USVs is reported in Dallolio et al. [8] by using gain-scheduled control.

It is hoped that a development for a physical speed model for wave-propelled USVs contribute to the research on such vehicles, paving the way for possible advanced control strategies, decision-support and a working simulation framework.

## 1.3 Research question

A simple overview of the dynamics of wave-proepelled USVs is presented in Sect. 1.3.1 and the research question is stated in Sect. 1.3.2.

### 1.3.1 Overview of dynamics

Denote $\mathbb{X}$ the *configuration space* of a given USV, and the states $\mathbf{x} \in \mathbb{X}$ the *coordinates* for the position and attitude of this vehicle including foils and their time-derivatives.

The workspace for the USV, at sea, contains stochastic disturbances from sea waves, ocean current and wind. Denote this *environmental configuration space* by $\mathcal{E}$ and by $\boldsymbol{\epsilon} \in \mathcal{E}$ the environmental configuration. The control problem for the USV is to steer the rudder angle $\delta$.

The general vehicle dynamics is a state-space dynamics driven by the current and previous states, affected by the environment and steered by rudder control $\delta_c$ by

$$\dot{\mathbf{x}}(t) = \mathbf{f}(\mathbf{x}(t), \boldsymbol{\epsilon}(t), \delta_c(t) \mid \mathbf{x}(\tau) \text{ for } \tau \leq t), \quad \mathbf{x} \in \mathbb{X}. \tag{1.1}$$

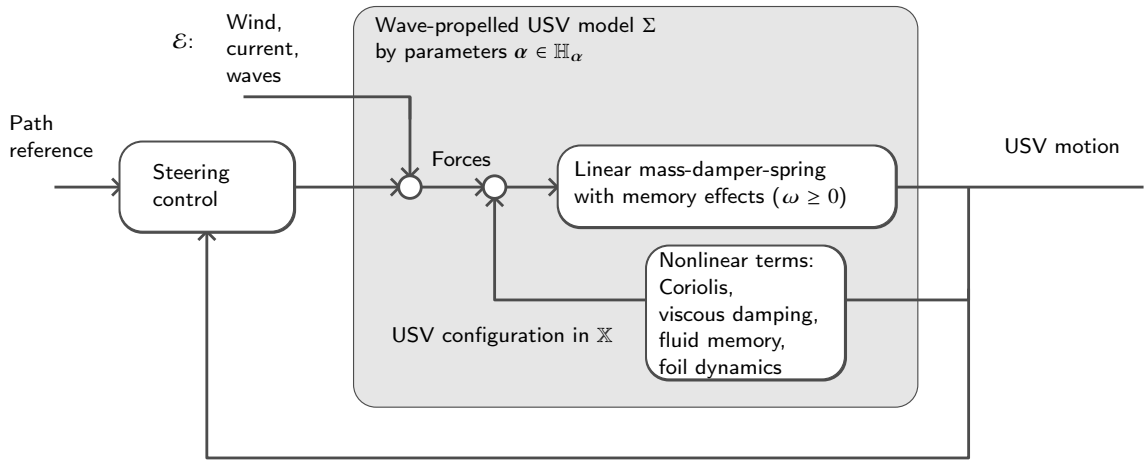


**Figure 1.3:** Overall wave-propelled USV model is denoted by $\Sigma$ and the model parameters are given by the vector $\boldsymbol{\alpha}$. The overall model is a frequency-dependent, and nonlinear forces are present. Theses will be described in this work, Coriolis, centripetal forces, viscous damping, fluid memory effects and unsteady effects in the foil dynamics. The simulation model can be simulated in closed-loop by active steering controller.

The overall system model, denoted by $\Sigma$ is illustrated in Fig. 1.3. The vehicle dynamics is a highly nonlinear system because of the various forces and effects present in such systems. The model may be parametrized by a parameter vector $\boldsymbol{\alpha}$ which is bounded to a set $\mathbb{H}_\alpha$.

### 1.3.2 Problem statement

The primary objective of this work is the derivation of a physical speed model for wave-propelled USVs. The model architecture is proposed with a fresh perspective from the discipline engineering cybernetics. The articulated problem statements are:

**Problem statement 1.** ***(Modeling)***
*Propose a model architecture for the general dynamics in Eq. (1.1) for wave-propelled USVs, preferably by using closed-form expressions.*

**Problem statement 2.** ***(Case study)***
*Perform a case study with the proposed method on the vehicle NTNU AutoNaut*[1].

**Remark 1.** *In addition to the above problem statements, a proper validation of the case study should be performed with available data sets.*

[1]A specific version of the wave-propelled USV AutoNaut from the company AutoNaut Ltd. [28], owned by NTNU.

## 1.4 Contributions

This research offers a fresh perspective on the limitations of applying conventional thin foil theory in the context of wave-propelled USV's unique operational conditions, emphasizing the need for auxiliary models.

In the developing stages of this work, various approaches was considered, among a frequency-domain description of the USV vehicle. Time-domain analysis is however necessary since drag forces on foils oscillates with twice the frequency of the vehicle. Furthermore, a time-domain model allow making spatial motion prediction from the simulation model. The additional advantage with this approach is that the vehicle motions can be found even when the vehicle is subjected to forces varying arbitrarily with time. On the contrary, wave-induced motions of marine vehicles are still considered in the frequency domain, and this approach is also taken here based on a monohull geometry describing wave-induced motions. Regarding foils, contributions have been made in the development for closed-form expressions of foil forces as well as identifying unsteady forces for a wide range of attack angles.

A summary of main contributions in this work include, but are not limited to:

- Proposed empiric lift and drag curves for foils beyond stall angle, including variation in center of pressure from the relative attack angle
- Identification of transient foil dynamics with added mass, damping and three-dimensional effects
- Proposed models for wing sections and span geometry
- The mutual wave-induced motion the vehicle and foils is designed in frequency-domain
- Identification of state-space representation of fluid-memory effects for efficient monohull geometry capturing wave-induced motions
- Proposed unified model architecture for wave-propelled USVs: The model is split into a 3-DOF maneuvering model affected mainly by currents and winds driven by a wave-propulsion system
- Performed a case study on NTNU AutoNaut by collection of physical measures and estimation of parameters $\alpha$ for the proposed unified model architecture
- Performed a successful simulation of NTNU AutoNaut, suggesting feasibility in the method

## 1.5 Outline

The outline of the report is:

- **Chapter 1: Introduction**: Motivation and challenges for the project, previous work and listing the main contributions of this work.
- **Chapter 2: Theory**: Contains all relevant theoretical models as well as derivations of contributions in the field of foil theory.
- **Chapter 3: Method to model wave-propelled USVs**: A unified maneuvering and seakeeping model is presented in which case the wave-propelled USV excites the foil dynamics through wave-induced motion. A general model $\Sigma$ with parameters $\boldsymbol{\alpha}$ and estimation methods to obtain the parameters is presented.
- **Chapter 4: Case study: NTNU AutoNaut**: The parameters for the AutoNaut vehicle is determined in order to proceed with a simulation environment.
- **Chapter 5: Simulation results and discussion**: Direct results and feasibility of the simulation of the case study is presented. Discussions for the model and a summary of main contributions from this work.
- **Chapter 6: Conclusion and future work**: The final conclusion and a list of possible continuations of this work.

# Chapter 2

# Theory

This chapter describes the necessary mathematical framework, hydrodynamic effects and non-linear theory for foils that must be taken into account in order to make a physical model for wave-propelled USVs. Notation, dynamics and kinematic preliminaries are presented in Sect. 2.1. This is followed by a treatment of the equations of motion in Sect. 2.2, which is written on a matrix-vector notation proposed by Fossen [4]. A brief mathematical foundation in fluid mechanics is found in Sect. 2.3, which is necessary to describe linear waves, understanding marine forces in Sect. 2.4 and understanding the theory developed for foils in Sect. 2.6. The last section presents a common model for rudders.

## 2.1 Notation and preliminaries

The notation used in this thesis complies with the convention from the Society of Naval Architects and Marine Engineers (SNAME) [29], see Tab. 2.1. Here, the coordinate system follows an Eulerian description of the vessel, where $[x^b, y^b, z^b]^\top$ is the body-frame $\{b\}$. The body frame and motion components are illustrated in Fig. 2.1. Reference frames are treated in Sect. 2.1.2.

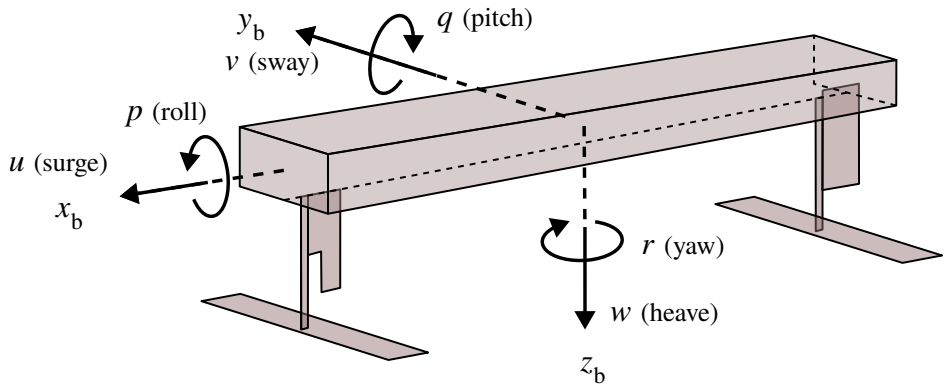


**Figure 2.1:** Motion components in 6 degrees of freedom on a marine craft. A wave-propulsion system is illustrated under the hull.

**Table 2.1:** Common notation for marine craft's. The notation complies with SNAME [29].

| | | forces $\boldsymbol{\tau}_{1-3}$ | linear velocity $\boldsymbol{\nu}_{1-3}$ | position $\boldsymbol{\eta}_{1-3}$ |
|---|---|---|---|---|
| Motion along $x^b$-axis: | surge | $X$ | $u$ | $x$ |
| Motion along $y^b$-axis: | sway | $Y$ | $v$ | $y$ |
| Motion along $z^b$-axis: | heave | $Z$ | $w$ | $z$ |
| | | moments $\boldsymbol{\tau}_{4-6}$ | angular velocity $\boldsymbol{\nu}_{4-6}$ | Euler angles $\boldsymbol{\eta}_{4-6}$ |
| Rotation about $x^b$-axis: | roll | $K$ | $p$ | $\phi$ |
| Rotation about $y^b$-axis: | pitch | $M$ | $q$ | $\theta$ |
| Rotation about $z^b$-axis: | yaw | $N$ | $r$ | $\psi$ |

### 2.1.1 Main particulars for wave-propelled USVs

A set of common particulars of a marine craft is briefly explained in this section and illustrated in Fig. 2.2 displaying the length $L$, breadth $B$ and draft $T$ of the vehicle as well as the foil span $S$ and chord length $c$, which will be treated in Sect. 2.6. The length of the vehicle is commonly measured by the length over all $L_{\text{oa}}$ and the length between perpendiculars $L_{\text{pp}}$ given in Fig. 2.3.

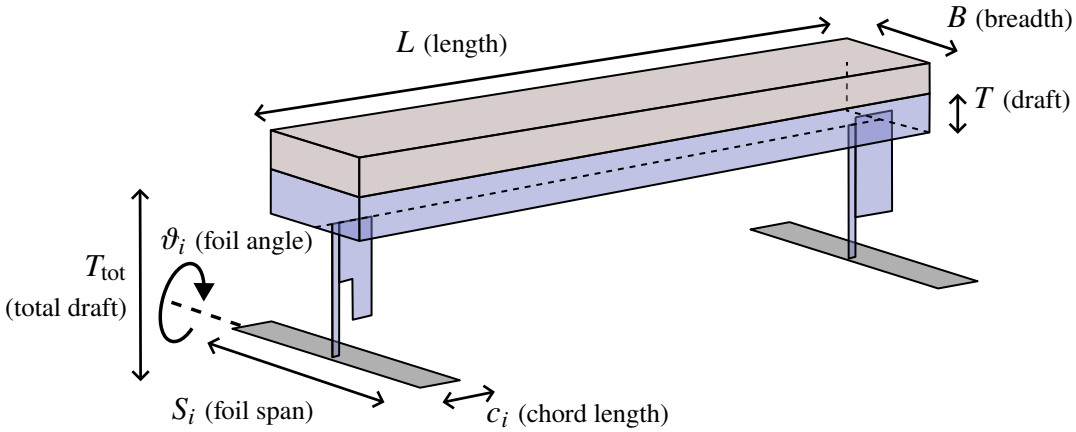


**Figure 2.2:** Main particulars of length $L$, breadth $B$ and draft $T$ illustrated for a wave-propelled USV where the submerged hull is blue. The total draft includes strut length and vertical contribution from the maximum deflection of the foil angle $\vartheta_i$ with chord length $c_i$ at the deepest reaching foil $i$. The total breadth depends on the maximum foil span $S_i$.

A description of the main particulars and parameters for a marine craft is [4]:

- **Length $L$:** The length of the vessel, often measured at the waterline, between perpendiculars $L_{\text{pp}}$ or as the overall length from forward tip to aft tip $L_{\text{oa}}$. For USVs, the length $L$ can be set as the overall length $L = L_{\text{oa}}$ and $L_{\text{pp}} < L$.

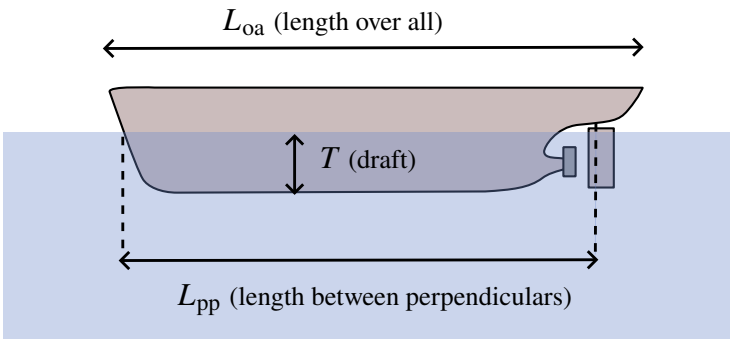


**Figure 2.3:** Common length measurement is length between perpendiculars $L_{pp}$ and length over all $L_{oa}$.

- **Breadth $B$:** The maximum width of the vessel, typically measured at the widest point. In this report, the breadth is limited to the hull of the craft without foils.
- **Draft $T$:** The vertical distance from the waterline to the lowest point of the vessel's hull. It represents how deep the vessel extends into the water.
- **Displaced volume $\nabla$:** The mass or weight of the vessel, expressed in kilograms for USVs. It includes the weight of the vessel's structure and cargo.
- **Waterplane area $A_{wp}$:** It represents the projection of the vessel's hull onto the plane of the water surface. The waterplane area is important to calculate the vessel's stability and might be used to calculate hydrodynamic coefficients and resistance as the vessel moves through the water.
- **Block coefficient $C_B$:** Dimensionless measure for the hull's underwater volume divided by the volume of a rectangular block with the same length, breadth and draft. For $C_B$ closer to 1, the vessel's hull closely resembles a rectangular block suggesting a fuller and more buoyant form. For $C_B$ around 0.5, the hull is more slender with less underwater volume relative to the block suggesting a more streamlined vessel with less resistance.
- **Waterplane area coefficient $C_{wp}$:** The waterplane area coefficient represents the proportion of a vessel's waterplane area to that of a rectangle with equivalent length and breadth. It helps to characterize the cross-sectional shape relative to its size.

Some useful relations is found from the list above:

**Remark 2.** *From the descriptions, the displaced volume is related to the block coefficient by*

$$\nabla \equiv LBTC_B, \tag{2.1}$$

*and the waterplane area can be related to the waterplane area coefficient by*

$$A_{wp} \equiv LBC_{wp}. \tag{2.2}$$

The dimensions of different wave-propelled USVs differ in size, and results across different vessels should only be directly compared after a proper similarity normalization. The next section describes the common normalization practice to compare results across different vessels.

### Prime normalization for marine craft

In order to relate results and discussions among different vessel types, non-dimensional units have been developed by SNAME in a system called *the prime normalization system* [29]. The system is the most commonly accepted non-dimensional analysis employed.

The system uses the ship's length $L$ as a basis for reference distance, and $t' = U/L$ as a basis time unit, which corresponds to the passage of time required for the vessel to travel a distance of it's length. Tab. 2.2 lists the conversion factors for the Prime normalization system.

**Table 2.2:** Conversion factors for the Prime normalization system. From SNAME [29] and Fossen [4].

| Magnitude | Conversion |
|---|---|
| Time | $t' = (U/L)t$ |
| Length | $x' = (1/L)x$ |
| Mass | $m' = (0.5\rho L^3)^{-1}m$ |
| Inertia | $I' = (0.5\rho L^5)^{-1}I$ |
| Area | $A' = (1/L^2)A$ |
| Force | $F' = (0.5\rho U^2 L^2)^{-1}F$ |
| Moment | $M' = (0.5\rho U^2 L^3)^{-1}M$ |
| Velocity | $v' = (1/U)v$ |
| Acceleration | $\dot{v}' = (L/U^2)\dot{v}$ |
| Angular velocity | $r' = (L/U)r$ |
| Angular acceleration | $\dot{r}' = (L^2/U^2)\dot{r}$ |

### Prime normalization for foils

A non-dimensional system for foils may by utilized in the same manner, and is listed in Tab. 2.3. The reduced frequency $\omega' = k_{\mathrm{F}}$ is introduced in unsteady foil theory, and non-dimensional forces are written with the coefficient $C_F$ for the force $F$. Here, a prime will however denote lift and lift coefficients per unit length of the span of the wing.

**Table 2.3:** Conversion factors for normalization system used on foils used in this work.

| Magnitude | Conversion |
|---|---|
| Time | $t' = (2U/c)t$ |
| Length | $x' = (1/c)x$ |
| Area | $A' = (1/c^2)A$ |
| Frequency | $\omega' \equiv k_{\mathrm{F}} = (c/2U)\omega$ |
| Force | $C_F = (0.5\rho U^2 c^2)^{-1}F$ |
| Force per unit span | $C'_F = (0.5\rho U^2 c^2 S)^{-1}F$ |

### 2.1.2 Reference frames and coordinates

In order to describe physical quantities and denote mathematical relations, a convenient notation for vectors, relativity and frame of reference follows. Fig. 2.4 displays the most commonly used reference frames: The North-East-Down frame and the body frame. A seakeeping frame is also illustrated, which will is concerned in the maneuvering model of the wave-propelled USV explained in Sect. 3.2. The material in this section is based on Fossen [4].

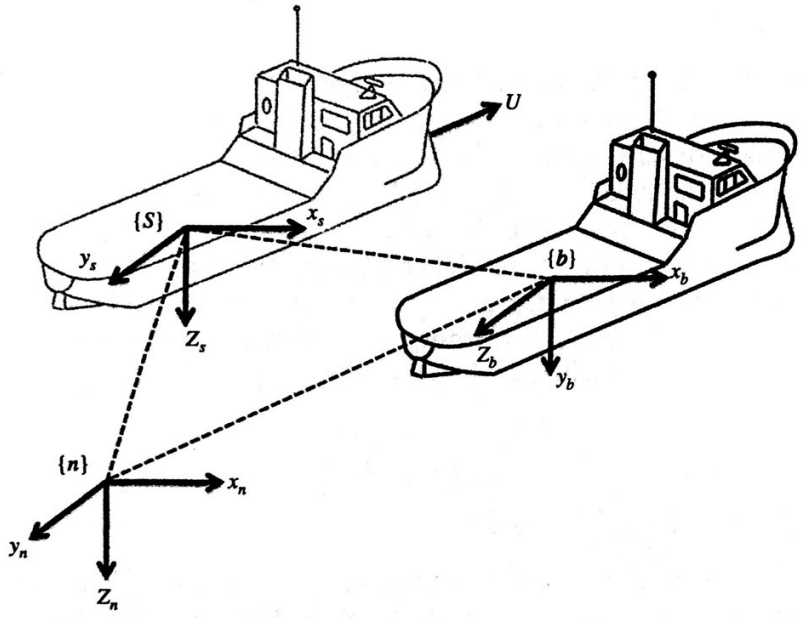


**Figure 2.4:** Commonly used reference frames for marine vehicles. The North-East-Down frame $\{n\}$ is inertial and the body frame $\{b\}$ follows the marine craft, oscillating with seakeeping motions perturbed from the mean seakeeping frame $\{s\}$. Adapted facsimile from Fossen [4].

#### North-East-Down frame

The North-East-Down reference frame is defined relative to a tangent plane on Earth's surface. Its $x^n$-axis point North, $y^n$-axis point East and $z^n$ axis point downwards (not necessarily radially down to center of Earth). The reference frame is denoted as $\{n\}$ and assumed inertial.

**Remark 3.** *The position and attitude of the wave-propelled USV is described relative to a local NED-frame.*

### Body frame

The body fixed reference frame is defined to follow the body of the marine craft at a chosen point of the craft with fixed axis following the craft's attitude. For marine craft the usual convention is that the $x^b$-axis point directly forwards, $y^b$-axis point starboard and $z^b$ completes the frame by pointing downwards from the craft's perspective. When the craft is rigid, any point on the craft will have the same coordinate in the body frame. The reference frame is denoted as $\{b\}$ and the origin of the frame is usually chosen at midships in the waterline or at the center of gravity.

### Vectors

A *coordinate free vector* is denoted $\vec{r}$, which has a magnitude $|\vec{r}|$ and a unit direction $\vec{r}/|\vec{r}|$. Such vectors, e.g. Newton's second law of motion, $\vec{F} = m\vec{a}$ (which is true in an inertial reference frame), can be acted upon with an operator ${}^b\hat{F}$ relative to the frame of reference $\{b\}$. Newton's law can then be stated as $\vec{F} = m\,{}^i\frac{\mathrm{d}}{\mathrm{d}t}\vec{v}$, where the time differentiation is taken with respect to an inertial reference frame $\{i\}$.

A *coordinate vector* on the other hand, is an Euclidean realization denoted as a boldface with superscript for the frame of reference. For the vector above, $\mathbf{r}^i \in \mathbb{R}^{3\times 1} = \mathbb{R}^3$.

Velocities and accelerations relative to a frame of reference are denoted with two letters in subscripts. The first one is the relative frame of reference, and the second one is the point of interest. One example is a rigid body (b) velocity relative to an inertial frame $\{n\}$, expressed in body frame $\{b\}$, $\mathbf{v}^b_{\mathrm{nb}}$. Another example is an angular velocity of a rigid body (b) relative to inertial frame $\{n\}$, expressed in the inertial frame, $\boldsymbol{\omega}^n_{\mathrm{nb}}$.

### Generalized coordinates

A marine vessel operates in three linear motion components and three rotational motion components described by a total of six degrees of freedom which was illustrated in Fig. 2.1. The longitudinal motion is denoted as *surge*, sideways motion is *sway* and vertical motion is *heave*.

The Euler angle convention with three successive rotations describes fully the attitude of the vessel. These rotations constitutes the *yaw* angle, or the heading of the vessel about a vertical axis, *roll* as the rotation about the longitudinal axis and *pitch* as the rotation about the transverse axis. The generalized position, velocity and force vectors according to SNAME [29] are

$$\boldsymbol{\eta} \triangleq [x^n, y^n, z^n, \phi, \theta, \psi]^\mathsf{T} \in \mathbb{R}^3 \times \mathbb{T}^3, \qquad \text{(position)} \tag{2.3a}$$

$$\boldsymbol{\nu} \triangleq [u, v, w, p, q, r]^\mathsf{T} \in \mathbb{R}^6, \qquad \text{(velocity)} \tag{2.3b}$$

$$\boldsymbol{\tau} \triangleq [X, Y, Z, K, M, N]^\mathsf{T} \in \mathbb{R}^6, \qquad \text{(forces)} \tag{2.3c}$$

where the North-East-Down position vector is

$$\mathbf{p} \triangleq [x^n, y^n, z^n]^\mathsf{T} \in \mathbb{R}^3, \tag{2.4}$$

and the Euler angles are represented by the vector

$$\boldsymbol{\Theta}_{\mathrm{nb}} \triangleq [\phi, \theta, \psi]^\mathsf{T} \in \mathbb{T}^3. \tag{2.5}$$

Here, the *Euclidean space* $\mathbb{R}^n$ is a vector of real values for $n$-dimensions, and the *hypertorus* $\mathbb{T}^m = \underbrace{\mathbb{S}^1 \times \cdots \times \mathbb{S}^1}_{m \text{ times}}$ denotes the cartesian product of angles wrapped in the interval $\mathbb{S}^1 = [0, 2\pi)$. Linear forces are denoted as $\mathbf{f}_{\text{b}}^b \triangleq [X, Y, Z]^\mathsf{T}$ given in the body-frame. Similarly, the moments are $\mathbf{m}_{\text{b}}^b \triangleq [K, M, N]^\mathsf{T}$, also in body frame. The linear body velocity is $\mathbf{v}_{\text{nb}}^b \triangleq [u, v, w]^\mathsf{T}$ and the angular velocity of the body is $\boldsymbol{\omega}_{\text{nb}}^b \triangleq [p, q, r]^\mathsf{T}$ [4].

### 2.1.3 Kinematics

Kinematics refer to the study of the motion of bodies and concerns the geometrical relations. The material in this section is based on Egeland and Gravdahl [30].

To clarify the kinematic relation for time differentiation, let $\vec{r} = [\vec{r}_{\text{ab}}]^i + [\vec{r}_{\text{bc}}]^b$ denote a physical vector from the inertial point "a" to a body-fixed point "c". The notations $[\cdot]^i$ and $[\cdot]^b$ denote that the vectors contained within the brackets are fixed to the frame in superscript. An inertial time differentiation of this vector is

$$ {}^i\frac{\mathrm{d}}{\mathrm{d}t}[\vec{r}] \equiv {}^i\frac{\mathrm{d}}{\mathrm{d}t}[\vec{r}_{\text{ab}}]^i + \underbrace{\vec{\omega}_{\text{ib}} \times [\vec{r}_{\text{bc}}]^b}_{\text{frame velocity}} + \underbrace{{}^b\frac{\mathrm{d}}{\mathrm{d}t}[\vec{r}_{\text{bc}}]^b}_{\text{frame derivative}}, \tag{2.6} $$

which constitutes the frame movement ${}^i\frac{\mathrm{d}}{\mathrm{d}t}[\vec{r}_{\text{ab}}]^i$, the frame rotational component $\vec{\omega}_{\text{ib}} \times [\vec{r}_{\text{bc}}]^b$ and the fixed frame differentiation ${}^b\frac{\mathrm{d}}{\mathrm{d}t}[\vec{r}_{\text{bc}}]^b$. Expressed in coordinate vectors, then the relation can be written as

$$ {}^i\frac{\mathrm{d}}{\mathrm{d}t}\mathbf{r}^b = \mathbf{v}_{\text{ib}}^b + \mathbf{S}(\boldsymbol{\omega}_{\text{ib}}^b)\mathbf{r}_{\text{bc}}^b + \mathbf{v}_{\text{bc}}^b, \tag{2.7} $$

where $\mathbf{S}(\mathbf{a})\mathbf{b} = \mathbf{a} \times \mathbf{b}$ represents the vector cross product as a the skew-symmetric operator

$$ \mathbf{S}(\mathbf{k}) \equiv -\mathbf{S}(\mathbf{k})^\mathsf{T} \triangleq \begin{pmatrix} 0 & -k_3 & k_2 \\ k_3 & 0 & -k_1 \\ -k_2 & k_1 & 0 \end{pmatrix}, \tag{2.8} $$

where $\mathbf{k} = [k_1, k_2, k_3]^\mathsf{T}$. To transform a vector in basis $\{b\}$ to $\{a\}$ without translation, the rotation matrix is introduced:

$$ \mathbf{r}^a = \mathbf{R}_b^a \mathbf{r}^b. \tag{2.9} $$

**Remark 4.** *In the general transformation case, when a vector is transformed from a basis to another with rotation and translation, this is referred to as a homogeneous transformation. The reader is referred to the book by Egeland and Gravdahl [30].*

The notation $\mathbf{R}_b^a \in \mathrm{SO}(3)$ implies that the matrix $\mathbf{R}_b^a$ is an active rotation from $\{a\}$ to $\{b\}$ in the *special orthogonal group* (of order 3):

$$\mathrm{SO}(n) = \{\mathbf{R} \mid \mathbf{R} \in \mathbb{R}^{n\times n},\ \mathbf{R} \in \mathrm{O}(n) \text{ is orthogonal},\ \det(\mathbf{R}) \equiv 1\}, \tag{2.10}$$

where the orthogonality is defined as

$$\mathrm{O}(n) = \{\mathbf{R} \mid \mathbf{R}\mathbf{R}^\mathsf{T} \equiv \mathbf{R}^\mathsf{T}\mathbf{R} = \mathbb{I}_{n\times n}\}. \tag{2.11}$$

**Remark 5.** *From the definition of the rotation matrices, Eq. 2.10, it follows* $\mathbf{R}_b^{a^\mathsf{T}} \equiv \mathbf{R}_b^{a^{-1}} \equiv \mathbf{R}_a^b$.

Simple active rotation matrices for rotations in $x$-, $y$- and $z$-axes are

$$\mathbf{R}_{z,\psi} \triangleq \begin{pmatrix} c(\psi) & -s(\psi) & 0 \\ s(\psi) & c(\psi) & 0 \\ 0 & 0 & 1 \end{pmatrix}, \quad \mathbf{R}_{y,\theta} \triangleq \begin{pmatrix} c(\theta) & 0 & s(\theta) \\ 0 & 1 & 0 \\ -s(\theta) & 0 & c(\theta) \end{pmatrix}, \quad \mathbf{R}_{x,\phi} \triangleq \begin{pmatrix} 1 & 0 & 0 \\ 0 & c(\phi) & -s(\phi) \\ 0 & s(\phi) & c(\phi) \end{pmatrix}, \tag{2.12}$$

where $s(\cdot) \equiv \sin(\cdot)$ and $c(\cdot) \equiv \cos(\cdot)$.

### 2.1.4 Dynamics

In the following thesis, *dynamics* refer to the study of forces and torques and how they relate to the motion at study. This term will be used indistinguishably from "kinetics," which is a common phrase in engineering studies that explains the same phenomena. The primary two methods used in the report are the Newtonian mechanics, relating the motion to the forces involved, and the Lagrangian mechanics, which is an energy consideration.

#### Newtonian dynamics

The linear dynamical equation is Newton's second law of motion which relates force $\mathbf{f}$, regardless of attack point on the body, to the time differentiation of the body's linear momentum $m\mathbf{v}$. For constant mass, the force $\mathbf{f}$ relates to the acceleration $\mathbf{a}$ of the center of mass as

$$\mathbf{f} = {}^i\frac{\mathrm{d}}{\mathrm{d}t}(m\mathbf{v}) = m\mathbf{a}. \tag{2.13}$$

Euler's equation of motion is an extension to Eq. (2.13) for arbitrary moments and rotations for rigid bodies. The moments $\mathbf{m}$ acting on a body is related to the time differentiation of the angular momentum $\mathbf{I}\boldsymbol{\omega}$, where $\mathbf{I}$ is the inertia dyadic representing the mass distribution, as

$$\mathbf{m} = {}^i\frac{\mathrm{d}}{\mathrm{d}t}(\mathbf{I}\boldsymbol{\omega}) = \mathbf{S}(\boldsymbol{\omega})\mathbf{I}\boldsymbol{\omega} + \mathbf{I}\dot{\boldsymbol{\omega}}. \tag{2.14}$$

### Lagrangian dynamics

The dynamics of a mechanical system can be derived from the principle of least action, see for instance the classic reference in Goldstein [31] or the control-oriented approach in Egeland and Gravdahl [30]. For systems described by generalized positions $\mathbf{q} = [\{q_k\}]^\mathsf{T}$, kinetic energy $T = T(\dot{\mathbf{q}})$ and potential energy $V = V(\mathbf{q})$, the Lagrangian dynamics is

$$\left(\frac{\partial L}{\partial \mathbf{q}}\right)^\mathsf{T} - {}^{i}\frac{\mathrm{d}}{\mathrm{d}t}\left(\frac{\partial L}{\partial \dot{\mathbf{q}}}\right)^\mathsf{T} = \mathbf{Q}, \tag{2.15}$$

where $L \triangleq T - V$ is the *Lagrangian* of the system and $\mathbf{Q}$ is the generalized forces acting on the system [31]. This form is useful when there are unknown constraints in our system. Depending on the forces $\mathbf{Q}$, Eq. (2.15) is conservative unless a *Rayleigh-dissipation* on the form

$$\mathcal{F} = \sum_n \frac{1}{n+1} \sum_k R_{kn} \dot{q}_k^{(n+1)}, \tag{2.16}$$

is included in the general force at right hand side with the dissipative force $\left(\frac{\partial \mathcal{F}}{\partial \dot{\mathbf{q}}}\right)^\mathsf{T}$. Here, $\dot{q}_k$ is the $k$-th component of the generalized velocities $\dot{\mathbf{q}}$, and $R_{kn}$ is the dissipation term. The number $n$ represents the dissipation to $n$-th order.

**Remark 6.** *Proportional friction is included with Rayleigh-dissipation in the coordinate $q_k$ by setting $n = 1$ such that the friction becomes $-R_{k1}\dot{q}_k$. Equations of motion from Lagrange's method from Eq. (2.15) is*

$$\left(\frac{\partial L}{\partial \mathbf{q}}\right)^\mathsf{T} - {}^{i}\frac{\mathrm{d}}{\mathrm{d}t}\left(\frac{\partial L}{\partial \dot{\mathbf{q}}}\right)^\mathsf{T} = \mathbf{Q} + \left(\frac{\partial \mathcal{F}}{\partial \dot{\mathbf{q}}}\right)^\mathsf{T}.$$

## 2.2 Marine craft equations of motion

In this section the equations of motions for marine craft, including wave-propelled USVs are derived with a matrix-vector notation inspired by the conventions used in robotics [30] [4].

### 2.2.1 Marine kinematics

The vessel is assumed to operate in a geographical area limited to a local tangent-plane with the North-East-Down (NED) reference frame convention. The NED frame $\{n\}$ can be considered inertial because the effects of Earth's rotation is negligible in consideration with the hydrodynamic forces experienced in $\{n\}$. This means that Coriolis and centripetal forces due to the movement of the NED frame from Earth's rotation are disregarded, and that Newton's laws of motion can be applied directly in $\{n\}$.

### Linear velocity transformation

The rotation matrix $\mathbf{R}_b^n$ from $\{n\}$ to $\{b\}$ expressed from Euler angles through the three simple rotations yaw $\psi$, pitch $\theta$ and roll $\phi$

$$\mathbf{R}_b^n(\Theta_{nb}) = \mathbf{R}_{z,\psi}\mathbf{R}_{y,\theta}\mathbf{R}_{x,\phi}, \tag{2.17}$$

where the simple rotations are defined in Eq. (2.12).

### Angular velocity transformation

The angular velocities $\boldsymbol{\omega}_{\text{nb}}^b$ changes with the attitude of the body such that a direct integration of $\boldsymbol{\omega}_{\text{nb}}^b$ do not have any physical interpretation as the Euler angles do [4]. The angular velocity of the body is related to the Euler angles $\boldsymbol{\Theta}_{\text{nb}}$ via the transformation matrix $\mathbf{T}(\boldsymbol{\Theta})$, implicitly found

$$\boldsymbol{\omega}_{\text{nb}}^b = \begin{pmatrix}\dot{\phi}\\0\\0\end{pmatrix} + \mathbf{R}_{x,\phi}^\top\begin{pmatrix}0\\\dot{\phi}\\0\end{pmatrix} + \mathbf{R}_{x,\phi}^\top\mathbf{R}_{y,\theta}^\top\begin{pmatrix}0\\0\\\dot{\psi}\end{pmatrix} = \begin{pmatrix}1 & 0 & -s(\theta)\\0 & c(\phi) & c(\theta)s(\phi)\\0 & -s(\phi) & c(\theta)c(\phi)y\end{pmatrix}\begin{pmatrix}\dot{\phi}\\\dot{\theta}\\\dot{\psi}\end{pmatrix} =: \mathbf{T}(\boldsymbol{\Theta}_{\text{nb}})^{-1}\dot{\boldsymbol{\Theta}}_{\text{nb}}, \tag{2.18}$$

where the transformation matrix $\mathbf{T}(\boldsymbol{\Theta})$ was identified with [4]

$$\mathbf{T}(\boldsymbol{\Theta}) \triangleq \begin{pmatrix}1 & s(\phi)t(\theta) & c(\phi)t(\theta)\\0 & c(\phi) & -s(\phi)\\0 & s(\phi)/c(\theta) & c(\phi)/c(\theta)\end{pmatrix}. \tag{2.19}$$

### Kinematic equation

Combining the linear and angular velocity transformation, the kinematic transformation from $\{n\}$ to $\{b\}$ is

$$\begin{pmatrix}\dot{\mathbf{p}}_{\text{nb}}^n\\\dot{\boldsymbol{\Theta}}_{\text{nb}}\end{pmatrix} = \begin{pmatrix}\mathbf{R}_b^n(\boldsymbol{\Theta}_{\text{nb}}) & \mathbf{0}_{3\times3}\\\mathbf{0}_{3\times3} & \mathbf{T}(\boldsymbol{\Theta}_{\text{nb}})\end{pmatrix}\begin{pmatrix}\dot{\mathbf{v}}_{\text{nb}}^b\\\dot{\boldsymbol{\omega}}_{\text{nb}}^b\end{pmatrix} =: \mathbf{J}_\Theta(\boldsymbol{\eta})\boldsymbol{\nu}^b, \tag{2.20}$$

where the kinematic transformation matrix $\mathbf{J}_\Theta(\boldsymbol{\eta})$ was identified in the equation above.

## 2.2.2 Equations of motion

### Equations of motion about center of gravity

Let the body frame be fixed in the center of gravity of a rigid body. Euler's equation of motion from Eq. (2.14) can be stated as

$$\mathbf{I}_g^b\dot{\boldsymbol{\omega}}_{\text{nb}}^b - \mathbf{S}(\mathbf{I}_g^b\boldsymbol{\omega}_{\text{nb}}^b)\boldsymbol{\omega}_{\text{nb}}^b = \mathbf{m}_g^b, \tag{2.21}$$

where $\mathbf{I}_{\text{g}}^b$ is the inertia dyadic, $\boldsymbol{\omega}_{\text{nb}}^b$ is the body angular velocity relative to NED expressed in body $\{b\}$ and $\mathbf{m}_{\text{g}}^b$ is the sum of external moments acting on the body. Newton's second law takes

the form

$$m\dot{\mathbf{v}}^b_{\mathrm{ng}} + m\mathbf{S}(\boldsymbol{\omega}^b_{\mathrm{nb}})\mathbf{v}^b_{\mathrm{ng}} = \mathbf{f}^b_{\mathrm{g}}, \tag{2.22}$$

where $m$ is the rigid body mass, $\mathbf{v}^b_{\mathrm{nb}}$ is the velocity of center of gravity relative to NED expressed in body $\{b\}$ and $\mathbf{f}^b_{\mathrm{g}}$ is the sum of external forces acting on the body.

Eqs. (2.21) and (2.22) can be combined into the generalized velocity $\boldsymbol{\nu}_{\mathrm{g}} = [{\mathbf{v}^b_{\mathrm{ng}}}^\top, {\boldsymbol{\omega}^b_{\mathrm{ng}}}^\top]^\top$ and forces $\boldsymbol{\tau}_{\mathrm{g}} = [{\mathbf{f}^b_{\mathrm{g}}}^\top, {\mathbf{m}^b_{\mathrm{g}}}^\top]^\top$ by

$$\begin{pmatrix} m\mathbb{I}_{3\times 3} & \mathbf{0} \\ \mathbf{0} & \mathbf{I}^b_{\mathrm{g}} \end{pmatrix} \dot{\boldsymbol{\nu}}_{\mathrm{g}} + \begin{pmatrix} m\mathbf{S}(\boldsymbol{\omega}^b_{\mathrm{nb}}) & \mathbf{0} \\ \mathbf{0} & -\mathbf{S}(\mathbf{I}^b_g\boldsymbol{\omega}^b_{\mathrm{nb}}) \end{pmatrix} \boldsymbol{\nu}_{\mathrm{g}} = \boldsymbol{\tau}_{\mathrm{g}}. \quad \text{(Newton-Euler dynamics)} \tag{2.23}$$

The above equation is true when the body frame $\{b\}$ is given in the center of gravity. The next section will provide the necessary formulae for expressing the equations of motion in a general body-fixed frame.

### Equations of motion in a body-fixed frame

It is desirable to choose the craft's body-frame in regards to various considerations, and in general the desired body-frame do not coincide with the craft's center of gravity. Thus, when the body frame do not coincide with the center of gravity, the generalized equations of motion is altered by a kinematic coordinate transformation.

Denote $\mathbf{r}^b_{\mathrm{bg}}$ as the position of the center of mass relative to the body frame. The coordinate transformation is performed on the velocity $\boldsymbol{\nu}$.

**Remark 7.** *Consider the similarity transformation* $\mathbf{z} = \mathbf{T}\mathbf{x}$ *on the system* $\dot{\mathbf{x}} = \mathbf{A}\mathbf{x}$*, where* $\mathbf{T}$ *is constant and a diffeomorphism. The new coordinate dynamic is* $\dot{\mathbf{z}} = \mathbf{T}\dot{\mathbf{x}} = \mathbf{T}\mathbf{A}\mathbf{x} = \mathbf{T}\mathbf{A}\mathbf{T}^{-1}\mathbf{z}$*. From this, it is concluded that the coordinate is changed by* $\mathbf{T}$ *and the matrix is changed by pre-multiplying with* $\mathbf{T}$ *and post-multiplying with* $\mathbf{T}^{-1}$*.*

For the velocity $\boldsymbol{\nu} = [\mathbf{v}^b_{\mathrm{nb}}; \boldsymbol{\omega}^b_{\mathrm{nb}}]$, the linear velocity is related to the new frame via Eq. 2.7 as

$$\mathbf{v}^b_{\mathrm{ng}} = \mathbf{v}^b_{\mathrm{nb}} + \mathbf{S}(\boldsymbol{\omega}^b_{\mathrm{ng}})\mathbf{r}^b_{\mathrm{bg}}, \tag{2.24}$$

or $\mathbf{v}^b_{\mathrm{nb}} = \mathbf{v}^b_{\mathrm{ng}} + \mathbf{S}(\mathbf{r}^b_{\mathrm{bg}})\boldsymbol{\omega}^b_{\mathrm{ng}}$ and the angular velocity is unchanged. Following the notation in Fossen [4], the similarity transformation from center of gravity to the new body frame is $\mathbf{H}(\mathbf{r}^b_{\mathrm{bg}})$:

$$\boldsymbol{\nu}^b_{\mathrm{ng}} = \mathbf{H}(\mathbf{r}^b_{\mathrm{bg}})\boldsymbol{\nu}^b_{\mathrm{nb}}, \qquad \mathbf{H}(\mathbf{r}^b_{\mathrm{bg}}) = \begin{pmatrix} \mathbb{I}_{3\times 3} & \mathbf{S}(\mathbf{r}^b_{\mathrm{bg}})^\top \\ \mathbf{0}_{3\times 3} & \mathbb{I}_{3\times 3} \end{pmatrix}. \tag{2.25}$$

Carrying out the calculations, the new equations of motion is

$$\mathbf{H}(\mathbf{r}_{\text{bg}}^{b})^{\top}\begin{pmatrix} m\mathbb{I}_{3\times 3} & \mathbf{0} \\ \mathbf{0} & \mathbf{I}_{\text{g}}^{b} \end{pmatrix}\mathbf{H}(\mathbf{r}_{\text{bg}}^{b})\dot{\boldsymbol{\nu}} + \mathbf{H}(\mathbf{r}_{\text{bg}}^{b})^{\top}\begin{pmatrix} m\mathbf{S}(\boldsymbol{\omega}_{\text{nb}}^{b}) & \mathbf{0} \\ \mathbf{0} & -\mathbf{S}(\mathbf{I}_{g}^{b}\boldsymbol{\omega}_{\text{nb}}^{b}) \end{pmatrix}\mathbf{H}(\mathbf{r}_{\text{bg}}^{b})\boldsymbol{\nu} = \mathbf{H}(\mathbf{r}_{\text{bg}}^{b})^{\top}\boldsymbol{\tau}_{\text{g}}. \tag{2.26}$$

**Remark 8.** *The above equation can be interpreted by intuition: The velocities $\boldsymbol{\nu}$ given in the origin of the body frame, needs to be transformed by $\mathbf{H}$ such that the velocities are expressed at the center of gravity, $\boldsymbol{\nu}_g = \mathbf{H}\boldsymbol{\nu}$. Then the Newton-Euler dynamics by Eq. 2.23 describes the dynamics, and the inverse transformation $\mathbf{H}^{\top}$ can be post-multiplied to return back to the coordinate frame $\{b\}$.*

The transformation of the body-fixed forces do not alter the linear force terms, $\mathbf{f}_{\text{b}}^{b} = \mathbf{f}_{\text{g}}^{b}$, but the moments are changed by $\mathbf{m}_{\text{b}}^{b} = \mathbf{S}(\mathbf{r}_{\text{bg}}^{b})\mathbf{f}_{\text{g}}^{b} + \mathbf{m}_{\text{g}}^{b}$.

### 2.2.3 Matrix-vector representation

The body dynamics is expressed in matrix-vector form according to Fossen [4] as

$$\mathbf{M}_{\text{RB}}\dot{\boldsymbol{\nu}} + \mathbf{C}_{\text{RB}}(\boldsymbol{\nu})\boldsymbol{\nu} = \boldsymbol{\tau}_{\text{RB}}, \tag{2.27}$$

where the inertia matrix $\mathbf{M}_{\text{RB}}$ and the Coriolis and centripetal matrix $\mathbf{C}_{\text{RB}}(\boldsymbol{\nu})$ are identified from Eq. (2.26) with

$$\mathbf{M}_{\text{RB}} \triangleq \begin{pmatrix} m\mathbb{I}_{3\times 3} & -m\mathbf{S}(\mathbf{r}_{\text{bg}}^{b}) \\ m\mathbf{S}(\mathbf{r}_{\text{bg}}^{b}) & \mathbf{I}_{\text{bg}}^{b} - m\mathbf{S}(\mathbf{r}_{\text{bg}}^{b})^{2} \end{pmatrix}, \tag{2.28}$$

and

$$\mathbf{C}_{\text{RB}}(\boldsymbol{\nu}) \triangleq \begin{pmatrix} m\mathbf{S}(\boldsymbol{\omega}_{\text{nb}}^{b}) & -m\mathbf{S}(\boldsymbol{\omega}_{\text{nb}}^{b})\mathbf{S}(\mathbf{r}_{\text{bg}}^{b}) \\ m\mathbf{S}(\mathbf{r}_{\text{bg}}^{b})\mathbf{S}(\boldsymbol{\omega}_{\text{nb}}^{b}) & -m\mathbf{S}(\mathbf{r}_{\text{bg}}^{b})\mathbf{S}(\boldsymbol{\omega}_{\text{nb}}^{b})\mathbf{S}(\mathbf{r}_{\text{bg}}^{b}) - \mathbf{S}(\mathbf{I}_{g}^{b}\boldsymbol{\omega}_{\text{nb}}^{b}) \end{pmatrix}. \tag{2.29}$$

The complete vehicle model is fully described by the kinematic and dynamic equations

$$\begin{aligned} \dot{\boldsymbol{\eta}} &= \mathbf{J}_{\Theta}(\boldsymbol{\eta})\boldsymbol{\nu}, \\ \mathbf{M}_{\text{RB}}\dot{\boldsymbol{\nu}} + \mathbf{C}_{\text{RB}}(\boldsymbol{\nu})\boldsymbol{\nu} &= \boldsymbol{\tau}_{\text{RB}}, \end{aligned} \tag{2.30}$$

where the transformation matrix $\mathbf{J}_{\Theta}(\boldsymbol{\eta})$ was found in Sect. 2.2.1.

Properties of the system inertia matrix $\mathbf{M}_{\text{RB}}$ and the Coriolis and centripetal matrix $\mathbf{C}_{\text{RB}}$ is well known in the literature on marine systems, and the interested reader is referred to Fossen in the chapter "Rigid-body Kinetics" [4].

**Remark 9.** *For marine equations of motion, the notation $X_{ij}$, for element $(i, j)$ in the matrix $\mathbf{X}$ indicates a coupled interaction from degree of freedom $j$ in direction $i$.*

## 2.3 Fluid mechanics

The dynamics of Eqs. (2.13), (2.14) and (2.15) are fundamental for the derivations of the marine craft equations of motion, and the kinematics in Sect. 2.1.3 is the geometrical interpretation of these motions. One needs to understand the underlying fluid mechanical forces and assumptions therein to provide mathematical description of the forces in the equations of motion. A great introduction in fluid mechanics can be found in the book "Fluid Mechanics" from White [32], and applications for hydrodynamics can be found in Lamb [33] and Newman [24]. Fig. 2.5 is included for the motivation for the following mathematics in fluid mechanics for a proper understanding for modeling of wave-propelled USVs.

**Figure 2.5:** The mathematics of sea waves and the interconnection with wave-propelled USVs can be derived from fluid mechanics. Image free of use under Creative Common license, from [34].

### 2.3.1 Non-dimensional numbers

In fluid mechanics and hydrodynamics, there exist countless non-dimensional numbers used to characterize flow patterns and different phenomena. The two most important numbers for the study of the motion of surface vehicles are *Reynold's number* and *Froude number*.

#### Reynold's number

According to White [32], Reynold's number is "... the most important parameter in fluid mechanics". The number is always influential, and can be neglected only in flow regions away from high-velocity gradients. It is defined according to

$$\mathrm{Re} \triangleq \frac{UL}{\nu}, \qquad \text{(Reynold's number)} \tag{2.31}$$

where $\nu = \mu/\rho$ is the kinematic viscosity, with further explanation in Definition 1.

**Definition 1.** ***(Reynolds number)***
*The relation between inertia forces and shear forces in a fluid, defined by a characteristic length L and a characteristic speed U by Eq.* (2.31).

**Remark 10.** *Reynolds number can be used to classify if a flow is turbulent or laminar. However, the range of the number will vary depending on the system under study since the characteristic length is chosen in accordance to a physical length at the system. The number is particularly useful when geometrical similarity is present between systems.*

### Froude number

The Froude number characterizes the dominant effect in the case of free-surface flows and is totally unimportant if there is no free surface [32]. In hydrodynamic design of ships, the Froude number is used to establish similarity between towing-tank tests and full-scale operation in regard to wave pattern and resistance [6]. It is defined according to

$$\mathrm{Fn} \triangleq \frac{U}{\sqrt{Lg}}, \qquad \text{(Froude number)} \tag{2.32}$$

with an explanation in Definition 2.

**Definition 2.** ***(Froude number)***
*The relation between inertia forces and gravitational forces in a fluid, defined by a characteristic length L and a characteristic speed U by Eq.* (2.32).

**Remark 11.** *The definition of Froude number given in Definition 2 is the one used throughout this report. In ship hydrodynamics this number is denoted by* Fn. *The reader should be aware that the number might also be defined according to* $\mathrm{Fr} = \mathrm{Fn}^2 = \frac{U^2}{gL}$ *which is the square of Eq.* (2.32)*, and the definition found in White [32].*

**Remark 12.** *A hydrodynamic classification of surface vessels from Froude number can be found at pp. 4 in Fossen [4]. Due to its low speeds, wave-propelled USVs are according to Definition 2 classified as "displacements vessels", where the restoring forces dominate relative to hydrodynamic forces.*

In this section, it is concluded that the non-dimensional numbers of Reynold's number and Froude number is useful to understand the motion of surface vehicles and flow patterns. The governing physics should be described by potential theory.

### 2.3.2 Potential theory

The following assumptions are fundamental for potential theory for liquids such as water. The first two assumptions relates to conservation principles:

**Assumption 1.** ***(Conservation of mass)***
*Conservation of mass must apply.*

**Assumption 2.** ***(Conservation of momentum)***
*Conservation of momentum must apply.*

In the handbook on lift [6], Hoerner states that "for all practical purposes, the density can be considered to be constant". This is referred to as the incompressibility condition, meaning that a given water amount has constant volume:

**Assumption 3.** ***(Incompressible)***
*The fluid can be considered incompressible, i.e. the density $\rho$ is constant.*

Lastly, the flow field is assumed conservative with the following assumption:

**Assumption 4.** ***(Irrotational)***
*The flow field is irrotational and continuous, i.e. the field is conservative.*

By conservation of mass in Assumption 1, incompressibility in Assumption 3 and applying the divergence theorem, the continuity equation always holds

$$\operatorname{div}(\mathbf{V}) = \boldsymbol{\nabla} \cdot \mathbf{V} = \frac{\partial u}{\partial x} + \frac{\partial v}{\partial y} + \frac{\partial w}{\partial z} = 0, \tag{2.33}$$

where $\mathbf{V} = [u, v, w]^\mathsf{T}$ is the fluid flow field. The flow field is presumed continuous throughout the domain. From Assumption 4, any line integral is path independent such that energy is not lost, only converted. This means that the conservative flow field can be described by the gradient

$$\mathbf{V} = \operatorname{grad}(\Phi) = \boldsymbol{\nabla}\Phi = \left[\frac{\partial \Phi}{\partial x}, \frac{\partial \Phi}{\partial y}, \frac{\partial \Phi}{\partial z}\right]^\mathsf{T}, \tag{2.34}$$

satisfying the irrotational assumption since the curl of a gradient is zero, $\boldsymbol{\nabla} \times \mathbf{V} = \boldsymbol{\nabla} \times (\boldsymbol{\nabla}\Phi) = 0$. The potential $\Phi$ is a scalar function in the domain of interest. Substituting Eq. (2.34) into Eq. (2.33), it follows that the potential must follow Laplace's equation

$$\boldsymbol{\nabla}^2 \Phi = 0. \tag{2.35}$$

From White [32], viscosity can be defined according to:

**Definition 3.** ***(Viscosity)***
*Viscosity is a quantitative measure of a fluid's resistance to flow. More specifically, viscosity determines the fluid strain rate as a result of an applied shear stress.*

In accordance with the momentum conservation from Assumption 2 and incorporating viscosity effects from Definition 3, the incompressible *Navier-Stokes* equations

$$\rho \frac{\mathrm{D}}{\mathrm{D}t}\mathbf{V} = \rho\mathbf{g} - \boldsymbol{\nabla} P + \mu \boldsymbol{\nabla}^2 \mathbf{V}, \qquad \text{(Navier-Stokes equation)} \tag{2.36}$$

where $\frac{\mathrm{D}}{\mathrm{D}t}$ represents the material derivative, $\mathbf{g}$ is the acceleration due to gravity, $P$ is the pressure and $\mu$ is the fluid viscosity, characterizes the fluid motion well [32]. The terms in Eq. (2.36) depend on the position in the domain analyzed.

By neglecting viscosity, Eq. (2.36) can be transformed to the unsteady Bernoulli's equation. Along a streamline, the energy density $e$ is constant

$$P + \rho \frac{\partial \Phi}{\partial t} - \rho g z^n + \frac{1}{2}\rho |\mathbf{V}|^2 = e, \qquad \text{(Bernoulli's equation)} \tag{2.37}$$

where the terms are evaluated on the streamline of the flow.

**Remark 13.** *A practical use-case for Bernoulli's equation, is to compare Eq.* (2.37) *at two separate points along a streamline in order to cancel the constant energy density e such that relation between e.g. velocity* $|\mathbf{V}|$ *and pressure P is found.*

When the motion of fluids is analyzed, it is common to find a solution for the velocity potential $\Phi$ in the domain of interest. This process is referred to as the *boundary value problem* (BVP) defined according to Definition 4, and is the method employed to describe sea waves in Sect. 2.3.3.

**Definition 4.** ***(Boundary value problem)***

*The boundary value problem in fluid mechanics relates to finding solutions for the velocity potential* $\Phi$ *satisfying Laplace's equation from Eq.* (2.35) *everywhere within the fluid, and various boundary conditions defined in the domain. These can for instance be kinematic conditions or dynamic conditions on surfaces or interfaces.*

**Remark 14.** *An example of a kinematic boundary condition is impermeability, meaning that the normal velocity of a fluid on a surface at rest is zero,* $\frac{\partial \Phi}{\partial n} = 0$.

### 2.3.3 Wave theory

In order to describe the effects of ocean waves on a floating body on the free surface, a mathematical description of the waves is necessary. The common way of describing ocean waves is by using potential theory from Sect. 2.3.2. When only linear terms are kept, this is referred to as linear wave theory, which is the core theory used in ocean and coastal engineering and naval architecture [35].

#### Linear regular waves

Let the mean free sea level be defined by $z^n = 0$, following the NED convention. A single regular wave component may be described by an amplitude $\zeta_{\mathrm{a},i}$, wave frequency $\omega_i$, cardinal direction

$\beta_{k,i}$ and a phase $\epsilon_i$. The sea elevation – the elevation from *irregular waves* – is the summation

$$\zeta(t) = \sum_i \zeta_{\mathrm{a},i} \sin(\omega_i t - \mathbf{k}_i^\top \mathbf{r} + \epsilon_i), \tag{2.38}$$

where $\mathbf{k}_i = [k_x, k_y, 0]^\top$ such that $\beta_{k,i} = \arctan(k_y, k_x)$. The dominating wave frequency encounters the surface vehicle with an angle $\beta$, illustrated in Fig. 2.6. The wave encounter angle is defined according to:

**Definition 5.** ***(Wave encounter angle)***
*The wave encounter angle $\beta$ is the angle from the bow to the direction of the wave $\beta_k$ positive along the $z^b$-axis of the vehicle, by the right hand screw convention.*

The figure also shows the wave number $\mathbf{k}$ and the wavelength $\lambda$ of a regular wave component.

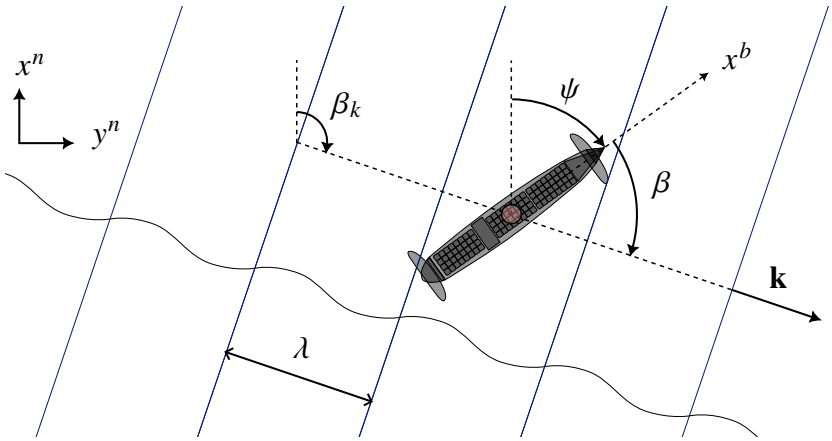


**Figure 2.6:** Regular waves encounter the USV by an angle $\beta = \beta_k - \psi$.

The undisturbed wave potential is usually expressed for a single wave component $\Phi_i$ such that the irregular wave potential is $\Phi = \sum_i \Phi_i$. The following assumptions need to be fulfilled for a single wave component:

**Assumption 5.** ***(Impermeability at sea bed)***
*The vertical velocity at the bottom of the sea is zero.*

**Assumption 6.** ***(Dynamic condition on the free surface)***
*Pressure is continuous over the free surface.*

**Assumption 7.** ***(Kinematic condition on the free surface)***
*Fluid particles at the surface stays at the surface.*

The material in this section is based on Krogstad and Arntsen [35]. Without loss of generality, the potential for a single undisturbed wave is found. The index $i$ is dropped for now. Let a regular wave traverse in direction $x^n$ with zero phase, such that the wave elevation is

$$\zeta(t) = \zeta_{\mathrm{a}} \sin(\omega t - k x^n). \tag{2.39}$$

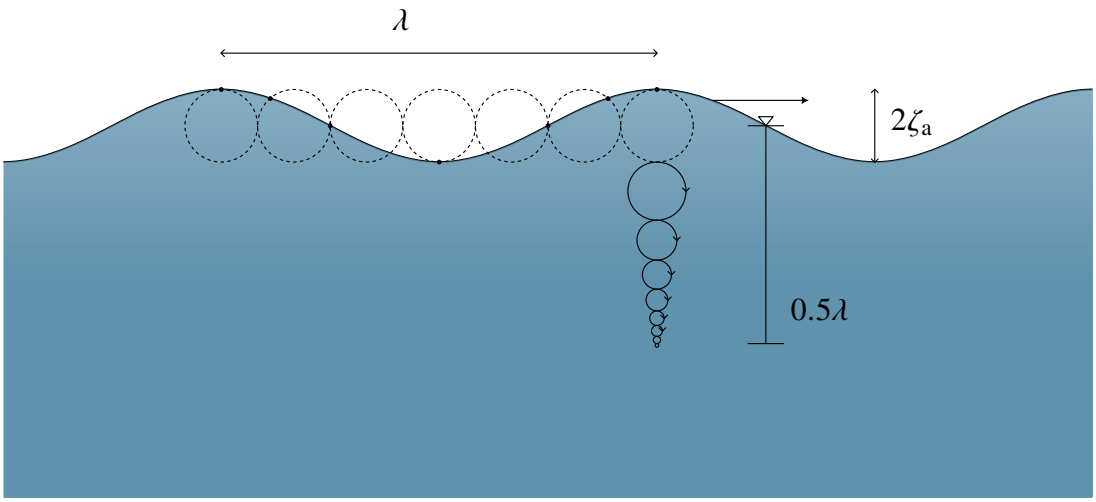


**Figure 2.7:** Regular waves. Fluid parcel motion follows near circular paths in deep water, until about half a wavelength in depth, which is the necessary depth when deep water assumption is valid.

From the above assumptions, the following boundary conditions, given in Remarks 15–17 for the potential $\Phi$. Recall that Laplace's equation for the potential is always held inside the fluid. Fig. 2.7 show the wavelength $\lambda$ and the wave amplitude $\zeta_a$.

**Remark 15.** *Assumption 5 suggests that the vertical velocity is zero at the sea bed at depth h,*

$$\frac{\partial \Phi}{\partial z^n} = 0. \qquad (at\ z^n = h) \tag{2.40}$$

**Remark 16.** *Assumption 6 suggest that the water pressure P at the surface is equal to the air pressure $P_a$. From the linear terms in Bernoulli's equation from Eq. (2.37) – meaning that the term $\frac{1}{2}|\mathbf{V}|^2$ is neglected – one arrives at the linear dynamic condition*

$$\frac{\partial \Phi}{\partial t} = g\zeta. \qquad (at\ z^n = 0) \tag{2.41}$$

**Remark 17.** *Assumption 7 suggest that the vertical velocity of the water will follow the vertical velocity of the surface elevation. By keeping linear terms, it can be shown that*

$$\frac{\partial \zeta}{\partial t} = \frac{\partial \Phi}{\partial z^n}. \qquad (at\ z^n = 0) \tag{2.42}$$

Combining the boundary conditions from Eqs. (2.41) and (2.42), the linear undisturbed wave potential satisfy

$$\frac{\partial^2 \Phi}{\partial t^2} + g\frac{\partial \Phi}{\partial z^n} = 0. \qquad (\text{at } z^n = 0) \qquad (\text{linear wave eq.}) \tag{2.43}$$

After the linear boundary conditions is stated, Laplace's equation can be solved analytically for the wave potential of undisturbed linear waves. According to Krogstand and Arntsen, written in terms of NED-coordinates, the wave potential is found as

$$\Phi_i = \frac{\zeta_{a,i} g}{\omega} \frac{\cosh(k_i[h - z^n])}{\cosh(k_i h)} \cos(\omega t - k_{x,i} x^n - k_{y,i} y^n + \epsilon_i), \tag{2.44}$$

where $_i$ is the phase.

**Remark 18.** *The wave potential in Eq. (2.44) can be simplified when the wave depth $h$ is large compared to the wavelength $\lambda$. According to [35], a deep water approximation is accurate when the depth is $h > 0.5\lambda$.*

### Deep water regular waves

For the deep water assumption, the velocity potential is approximately [35]

$$\Phi_i = \frac{\zeta_{a,i} g}{\omega_i} e^{-k_i z^n} \cos(\omega_i t - k_i \cos(\beta_{k,i}) x^n - k_i \sin(\beta_{k,i}) y^n + \epsilon_i), \tag{2.45}$$

and the dispersion relation is

$$\omega^2 = gk. \quad \text{(dispersion relation)} \tag{2.46}$$

**Remark 19.** *The velocity field from the wave potential $\Phi$ is found by the gradient such that*

$$\mathbf{V}_{\text{waves}} = \boldsymbol{\nabla}\Phi. \tag{2.47}$$

### Wave potential forces

The usual method for finding the hydrodynamic forces acting on a vehicle in waves, is based on the superposition of the diffraction forces due to the wave forces on a non-moving vehicle, and of the radiation forces due to the vehicle motion in an undisturbed sea [24].

The wave potential in Eq. (2.45) is the potential for an undisturbed wave. According to Jensen [23], the forces due to an undisturbed wave, the Froude-Krylov force, is an important method for finding wave forces.

**Definition 6.** ***(Froude-Krylov force)***
*The hydrodynamic forces introduced on a submerged body from the undisturbed waves as if the body was not present.*

**Remark 20.** *The Froude-Krylov forces can be found by integrating the unsteady pressure $P_d$ over the wetted surface $S$ of a submerged body*

$$\mathbf{F}_{\text{FK}} = \iint_S P_d \mathrm{d}\mathbf{A}, \tag{2.48}$$

*where the unsteady pressure field from the potential $\Phi$ is*

$$P_d = \frac{\partial \Phi}{\partial t}. \tag{2.49}$$

**Remark 21.** *The Froude-Krylov force is only a function of the ambient wave potential and easy to evaluate. The diffraction force is a function of the diffraction potential and requires the solution of a boundary value problem.*

A useful formulation in more advanced methods in hydrodynamics is to calculate forces from complex potentials. The complex wave potential from Eq. (2.45) is

$$\varphi = \frac{\zeta_a g}{\omega} e^{-kz^n} e^{i\omega t} e^{-ik\cos(\beta_k)x^n - ik\sin(\beta_k)y^n}. \tag{2.50}$$

### Wave spectra

The instantaneous wave elevation is Gaussian distributed with zero mean [4]. It is usual to assume that the wave process is stationary under short time considerations of about 20 minutes to 3 hours and the process is ergodic [36]. The wave frequencies present can be described by a wave spectrum $S(\omega)$. When a discrete wave spectrum is employed for simulation purposes and the distance between each wave component $\omega_i$ is $\Delta\omega$, the different wave amplitudes are

$$\zeta_{a,i} = \sqrt{2S(\omega_i)\Delta\omega}. \tag{2.51}$$

According to Fossen [4], different wave spectra is useful for different sea states. The Pierson-Moskowitz spectrum

$$S(\omega) = A\omega^{-5}\exp\left(-B\omega^{-4}\right), \tag{2.52}$$

where the parameters $A$ and $B$ are adjusted, is used as a basis for several spectral formulations. Common values for a one-parameter spectra is with [4]

$$A = 0.0081g^2, \qquad B = \frac{3.11}{H_s^2}.$$

For fully developed sea at large depth, the *modified Pierson-Moskowitz spectrum* is suggested. For non-developed sea, the *JONSWAP* or *Torsethaugen* spectra is recommended. The spectral density function for non-developed sea will be more peaked than those representing fully-developed sea. The Torsethaugen spectrum has the added benefit of describing a low frequency peak similar to the JONSWAP spectrum, and a high frequency peak representing newly developed sea. A detailed discussion and numerical values for the different spectra can be found in [4].

**Remark 22.** *For wave-propelled USVs operating in fjords, the wave spectrum contains higher wave frequencies than that of open seas. This suggest that the Torsethaugen spectrum is the correct wave spectrum to use.*

### Dominating forces on wave-propelled USV

When the forces due to waves are to be found on a wave-propelled USV, it may be beneficial to classify the type of forces on the vehicle, preferably also on the vehicle hull and the foils.

The classification helps in determining whether or not the undisturbed Froude-Krylov force from Sect. 2.3.3 applies, or if the present of the body structure diffracts the impinging waves significantly such that this method is inapplicable.

According to Pettersen [36], it is common to distinguish between small-scale constructions and large-scale constructions in naval architecture. The definitions are:

**Definition 7.** ***(Large-scale constructions)***
*From a hydrodynamic standpoint, a structure is regarded as a large-scale construction when the structure's ability to generate waves is important when calculating the hydrodynamic forces.*

**Definition 8.** ***(Small-scale constructions)***
*A structure is regarded as a small-scale construction when Definition 7 do not apply.*

An analytical distinction is found for the case of vertical cylinders standing in regular waves. For a regular wave with wave height $H = 2\zeta_a$ and wavelength $\lambda$, the following definitions from Pettersen [36] can be used:

**Definition 9.** ***Classification of cylinders standing in regular waves)***
*Given a vertical cylinder standing in regular waves. If the relationship between the wavelength and diameter is less than 5, a construction is classified as a large-scale constructions in Definition 7. Otherwise, it is classified as a small-scale construction according to Definition 8.*

**Definition 10.** ***(Classification of dominating forces on small-scale construction)***
*Let a vertical cylinder standing in regular waves be classified as a small-scale construction according to Definition 9. If the relationship between the wave height and diameter is less than $4\pi$, mass forces dominate. Otherwise, drag forces dominate.*

The following remark showcases an example on how different forces can be determined on the different parts of a wave-propelled USV:

**Remark 23.** *Definitions 9 and 10 are applicable for cylinders standing in regular waves. Let these classifications apply to a wave-propelled USV with length $L = 5.0$ [m] and the foils have chord width $c = 0.2$ [m]. The foils are supported by struts with diameter $d = 0.05$ [m]. According to the dispersion relation from Eq. (2.46), the wavelength is found through $\lambda = \frac{2\pi}{\omega^2} g$, since $k = 2\pi/\lambda$.*

*Let the wave frequency be $\omega = 2.5$ [$s^{-1}$] and the wave height $H = 1$ [m], such that the wavelength is $\lambda = 9.9$ [m]. According to Definition 9, the USV may be regarded as a large-scale construction (since $\lambda/L < 5$), while the foils and the supporting struts are small-scale constructions. Additionally, according to Definition 10, mass forces are dominating on the foils (since $H/c < 4\pi$), while drag forces is the dominating force on the struts (since $H/d > 4\pi$).*

## 2.4 Marine craft forces

The governing equations of motion for a marine craft was found in Sect. 2.2, and the nature of the interaction forces and moments $\boldsymbol{\tau}_{\text{RB}}$ between the craft and the surrounding environment from sea and air is explained briefly in this section before the subsequent sections determines values. The theory can be found in any standard textbook on hydrodynamics, for instance the handbook from Fossen 2021, chapters 4–6 [4]. Inspiration was also found in the master's thesis from Pinit, a thesis describing hydrodynamic modeling and simulation of ships explaining sea loads [37]. Additionally, not seen to this extent, a direct classification of forces[1] into first order and second order effects is included to enhance the understanding of marine craft behavior.

### 2.4.1 Classification of forces

Firstly, note that the forces (relating to both linear forces and moments) is time-varying and their origins can be separated, meaning that

$$\boldsymbol{\tau}_{\text{RB}} = \boldsymbol{\tau}_{\text{RB}}(t) = \sum_i \boldsymbol{\tau}_{\text{RB},i}(t). \tag{2.53}$$

Secondly, any observation of a marine craft facilitates the comprehension that some of the degrees of freedom oscillates around a mean position, e.g. in heave, roll and pitch, indicating that the forces can be categorized into a *first order* oscillatory forces and a *second order* drift forces accordingly

$$\boldsymbol{\tau}_{\text{RB}} = \boldsymbol{\tau}_1(\omega t) + \boldsymbol{\tau}_2(t), \tag{2.54}$$

where $(\omega t)$ indicates that the forces oscillates.

**Definition 11.** ***(First order forces and moments on marine craft)***
*The first order forces and moments $\boldsymbol{\tau}_1(t)$ corresponds to zero mean oscillatory forces such that $\langle \boldsymbol{\tau}_1 \rangle = 0$ when $\langle \cdot \rangle$ indicates a sufficient time average.*

**Definition 12.** ***(Second order forces and moments on marine craft)***
*The second order forces and moments $\boldsymbol{\tau}_2(t)$ corresponds to a mean drift force such that typically $\langle \boldsymbol{\tau}_2 \rangle \neq 0$ when $\langle \cdot \rangle$ indicates a time average.*

As a direct consequence of Definitions 11 and 12, the mean position of the craft, in concern for navigation purposes, can be determined solely by the second order forces acting on the marine craft.

### 2.4.2 Environmental forces

#### Sea waves

Sea waves induce a time-varying *excitation* force on the vehicle due to changes in water pressure around the hull. As a result, the vehicle initiates movement and oscillation, leading to a feedback

[1] The term forces refer to both linear forces as well as moments

reaction that disturbs the water momentum, called *radiation*. Together, these forces are called *hydrodynamic* forces.

This reaction comprises a conservative component, proportional to the vehicle's acceleration, and a non-conservative part proportional to the velocity. The former reflects the energy loss carried away from the hull, transforming into a source of radiated waves.

The effects of excitation and radiation forces can be considered separate due to linearity, where the overall effect when they act at the same time is found through superposition, and their interactions is a negligible factor.

The excitation force from the waves can be split into a *Froude-Krylov* force $\boldsymbol{\tau}_{\text{FK}}$, representing the effects of undisturbed waves on the vehicle, and the *diffraction* force $\boldsymbol{\tau}_{\text{diff}}$ due to the vehicle appearing as a solid obstacle conforming the incoming waves. In summary, the excitation force is represented by

$$\boldsymbol{\tau}_{\text{exc}} = \boldsymbol{\tau}_{\text{FK}} + \boldsymbol{\tau}_{\text{diff}}. \tag{2.55}$$

It turns out that the excitation force causes both a first order force and a second order force. The second order force is categorized as a mean *wave-drift force*.

The radiation force represents the energy propagated away from the vehicle to the sea when a forced oscillation of the craft in calm sea is performed. This reaction force is due to the adhesive acceleration of surrounding water causing an in-phase force called the *added mass* force, and an out-of-phase damping force caused by all previous velocity motion of the vehicle up to that point, referred to as *fluid memory effect*. Thus the instantaneous momentum change of the vehicle causes a future force contribution. Cummins 1962 [38], showed that the radiation force is represented by an added mass force and a damping force on the form

$$\boldsymbol{\tau}_{\text{rad}} = -\mathbf{M}_{\text{A}}\ddot{\boldsymbol{\eta}} - \boldsymbol{\mu}(t), \qquad \boldsymbol{\mu}(t)\text{: fluid memory effect depending on history of } \dot{\boldsymbol{\eta}}. \tag{2.56}$$

where $\mathbf{M}_{\text{A}}$ is the added inertia, which is defined later in Sect. 2.4.4.

### Restoring forces

The mean position of the vehicle in heave, pitch and roll is the result of interaction between the gravitational effect on the vehicle and the changing bouyant force from the static pressure field in the water around the hull. The action of other hydrodynamic forces causes the position of the vehicle to move, causing a slight shift in the center of bouyancy of the craft, which tends to oppose the perturbation of the position in heave, pitch and roll. The restoring force is $\boldsymbol{\tau}_{\text{res}}$.

### Viscous damping

Additional damping, called *viscous damping* is present due to skin friction and vortex shedding. *Skin friction* arises primarily due to water flowing along the hull-water boundary. The molecules at the interface adhere to the hull surface due to molecular forces, and those in the adjacent layers experience a drag force as they slide past each other. *Vortex shedding* on the other hand, is the alternating formation and shedding of vortexes when water flow past the hull.

### Sea currents

Sea currents are considered to be slowly changing, and the forces related to currents are incorporated into the marine craft dynamics in Eq. (2.30) by substituting the velocities appearing in the second line with relative velocities instead. Correspondingly,

$$\begin{aligned} \dot{\boldsymbol{\eta}} &= \mathbf{J}_\Theta(\boldsymbol{\eta})\boldsymbol{\nu}, \\ \mathbf{M}_{\mathrm{RB}}\dot{\boldsymbol{\nu}}_\mathrm{r} + \mathbf{C}_{\mathrm{RB}}(\boldsymbol{\nu}_\mathrm{r})\boldsymbol{\nu}_\mathrm{r} &= \boldsymbol{\tau}_{\mathrm{RB}}, \end{aligned} \tag{2.57}$$

where $\boldsymbol{\nu}_\mathrm{r} = \boldsymbol{\nu} - \boldsymbol{\nu}_\mathrm{c}$ incorporates the effect of sea currents in the equations of motion. The sea current has a speed $V_\mathrm{c}$ and cardinal direction $\beta_{V_\mathrm{c}}$ is illustrated in Fig. 2.8. The current angle of attack is $\gamma_\mathrm{c}$ and defined according to:

**Definition 13.** ***(Relative current angle of attack)***
*The angle $\gamma_w$ is the angle from the bow to the negative direction of the wind $\mathbf{V}_w$, counter-clockwise along $z^b$-axis.*

**Remark 24.** *This method is possible due to the choice of the Coriolis and centripetal matrix $\mathbf{C}(\boldsymbol{\nu})$ in this work. According to Fossen, several parametrization for this matrix exist, and Property 10.1 in Fossen addresses this issue [4].*

**Assumption 8.** *The ocean current velocity in the inertial frame is short-term constant and irrotational.*

**Remark 25.** *Assumption 8 is a reasonable simplification of the real-world situation and is a standard assumption in marine control theory [4].*

The current speed is $\mathbf{V}_\mathrm{c}^b = [u_\mathrm{c}, v_\mathrm{c}, 0]^\top$ in the body frame.

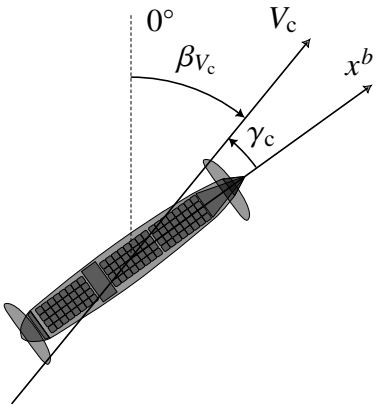


**Figure 2.8:** Current speed $V_\mathrm{c} = |\mathbf{V}_\mathrm{c}|$, current direction $\beta_{V_\mathrm{c}}$ and angle of attack $\gamma_\mathrm{c}$ relative to the bow.

### Wind

The ambient air exerts a force $\boldsymbol{\tau}_{\text{wind}}$ on the hull surface above the waterline, inducing a drag force aligned with the relative wind direction and a moment. The cardinal wind angle is $\beta_{V_w}$ and the relative wind angle $\gamma_w$ is defined in Fig. 2.9 and by:

**Definition 14.** ***(Relative wind angle of attack)***
*The angle $\gamma_w$ is the angle from the bow to the negative direction of the wind $\mathbf{V}_w$, counter-clockwise along $z^b$-axis.*

**Assumption 9.** *The air pressure above the free surface is constant and unchanging $P_a$.*

**Assumption 10.** *The mean wind velocity in the inertial frame is considered constant and irrotational for the instantaneous wind forces and moments.*

**Remark 26.** *Assumption 10 is a reasonable simplification for the mean wind forces and moments in the real-world situation when the wind velocity is slowly changing. Gusts and other wind effects are neglected in the model.*

**Remark 27.** *Notice that the attack angle for wind differs from the convention for attack angle for sea current given in Definition 13. Accordingly, $\gamma_w = \psi - \beta_{V_w} - \pi$.*

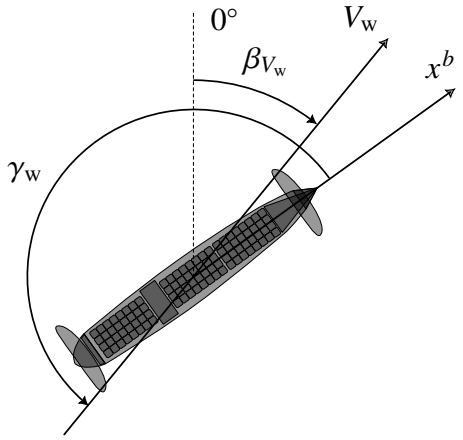


**Figure 2.9:** Wind speed $V_w = |\mathbf{V}_w|$, wind direction $\beta_{V_w}$ and angle of attack $\gamma_w$ relative to the bow.

### 2.4.3 Hydrostatic forces

87Hydrostatic forces, commonly known as restoring forces, act on a vessel due to the combined effects of gravity and buoyancy. Gravity exerts a constant force on the vessel as long as its mass remains constant, while buoyancy is proportionate to the weight of the fluid displaced by the vessel. The center of gravity (CG) is the point where the resultant gravity force acts on the body, and the center of buoyancy (CB) is where buoyant forces act on the vessel. The material in this section is based on Fossen [4].

#### Restoring forces

For a floating vessel the effects due to gravity and forces from buoyancy are

$$\vec{W} = m\vec{g}, \qquad \vec{B} = -\rho\vec{g}[\nabla + \delta\nabla(t)], \tag{2.58}$$

where $W = |\vec{W}|$ is the weight of the vessel and $B = |\vec{B}|$ is the bouyancy. In equilibrium when $\delta\nabla = 0$, the weight of the displaced volume $\nabla$ equals the weight of the vessel such that $W = B$. The gravity and bouyancy force expressed in $\{n\}$ are

$$\mathbf{f}_{\mathrm{g}}^{n} = \begin{pmatrix} 0 \\ 0 \\ mg \end{pmatrix}, \qquad \mathbf{f}_{\mathrm{b}}^{n} = \begin{pmatrix} 0 \\ 0 \\ -\rho g[\nabla + \delta\nabla(t)] \end{pmatrix}, \tag{2.59}$$

and the resultant restoring force is the sum $\mathbf{f}_{\mathrm{r}}^{n} = \mathbf{f}_{\mathrm{b}}^{n} + \mathbf{f}_{\mathrm{g}}^{n}$ which equals

$$\mathbf{f}_{\mathrm{r}}^{n} = \begin{pmatrix} 0 \\ 0 \\ -\rho g\delta\nabla(t) \end{pmatrix}. \tag{2.60}$$

The variation in the displaced volume, $\delta\nabla(t)$ varies with the vessel's motion and the free surface. For calm water and small pitch and roll motions, the time-varying part of the displaced volume is approximated by

$$\delta\nabla(z) = \int_{0}^{z^{n}} A_{\mathrm{wp}}(z')\mathrm{d}z', \tag{2.61}$$

where $A_{\mathrm{wp}}$ is the waterplane area of the vessel.

#### Restoring moments

For surface vessels, hydrostatic moments depend on the positions of the vessel's CG and CB, and the magnitude of the forces. The metacenter height is defined as the theoretical point where an imaginary vertical line through the CB intersects another imaginary vertical line through a new CB formed when the vessel is tilted in the water. This results in decomposed longitudinal metacentric height $\mathrm{GM_L}$ and a transverse metacentric height $\mathrm{GM_T}$. [4]

In equilibrium, CG lies vertically above CB, and the restoring moments depend on the horizontal displacement of CB relative to CG. The moment arm is

$$\mathbf{r}_{\mathrm{GM}}^{b} = \begin{pmatrix} -\mathrm{GM_L}\sin(\theta) \\ \mathrm{GM_T}\sin(\phi) \\ 0 \end{pmatrix}, \tag{2.62}$$

and the restoring moment about CG is the bouyancy force $\mathbf{f}_{\mathrm{b}}^{b}$. The restoring moment is thus $\mathbf{m}_{\mathrm{r}}^{b} = \mathbf{S}(\mathbf{r}_{\mathrm{GM}}^{b})\mathbf{f}_{\mathrm{b}}^{b}$ where the bouyancy force in body is $\mathbf{f}_{\mathrm{b}}^{b} = \mathbf{R}_{n}^{b}\mathbf{f}_{\mathrm{b}}^{n}$:

$$\mathbf{f}_{\mathrm{b}}^{b} = \mathbf{R}_{n}^{b}\mathbf{f}_{\mathrm{b}}^{n} = -\rho g \nabla \begin{pmatrix} -\sin(\theta) \\ \cos(\theta)\sin(\phi) \\ \cos(\theta)\cos(\phi) \end{pmatrix}. \tag{2.63}$$

Notice that no force due to the perturbation $\delta\nabla$ is included. This is a good approximation. The restoring moment becomes

$$\mathbf{m}_{\mathrm{r}}^{b} = \mathbf{S}(\mathbf{r}_{\mathrm{GM}}^{b})\mathbf{f}_{\mathrm{b}}^{b} = -\rho g \nabla \begin{pmatrix} \mathrm{GM_T} s(\phi)c(\theta)c(\phi) \\ \mathrm{GM_L} s(\theta)c(\theta)c(\phi) \\ -\mathrm{GM_L} c(\theta) + \mathrm{GM_T} s(\phi)s(\theta) \end{pmatrix}. \tag{2.64}$$

### Restoring forces

Combined, a gravitational vector capturing the restoring forces and moments for surface vessels is on the form $\mathbf{g}(\boldsymbol{\eta}) = -\boldsymbol{\tau}_{\mathrm{hs}}(\boldsymbol{\eta}) = -[\mathbf{f}_{\mathrm{r}}^{b\,\mathsf{T}}, \mathbf{m}_{\mathrm{r}}^{b\,\mathsf{T}}]^{\mathsf{T}}$:

$$\mathbf{g}(\boldsymbol{\eta}) = \rho g \begin{pmatrix} -\int_0^{z_n} A_{\mathrm{wp}}(z')\mathrm{d}z' s(\theta) \\ \int_0^{z_n} A_{\mathrm{wp}}(z')\mathrm{d}z' c(\theta)s(\phi) \\ -\int_0^{z_n} A_{\mathrm{wp}}(z')\mathrm{d}z' s(\theta) \\ \nabla \mathrm{GM_T} s(\phi)c(\theta)c(\phi) \\ \nabla \mathrm{GM_L} s(\theta)c(\theta)c(\phi) \\ -\nabla \mathrm{GM_L} c(\theta) + \nabla \mathrm{GM_T} s(\phi)s(\theta) \end{pmatrix}. \tag{2.65}$$

### 2.4.4 Hydrodynamic forces

When the vessel moves through the water, the surrounding water parcels is pushed due to impermeability causing frequency-dependent *oscillatory derivatives* [39]. From Bailey et al. [40], for the generalized force $F$ in

$$F \in \{X, Y, Z, K, M, N\},$$

and motion component $\alpha$

$$\alpha \in \{x, y, z, \phi, \theta, \psi, u, v, w, p, q, r, \dot{u}, \dot{v}, \dot{w}, \dot{p}, \dot{q}, \dot{r}\},$$

the frequency-dependent oscillatory derivative is written as

$$\tilde{F}_\alpha(\omega), \quad \text{(oscillatory derivative)} \tag{2.66}$$

which corresponds to the contribution of the generalized force $F$ due to a motion component $\alpha$ when the oscillation occurs at frequency $\omega$. The generalized force $F$ is approximated as the sum

$$F(\omega) = \sum_\alpha \tilde{F}_\alpha(\omega)\alpha. \tag{2.67}$$

One example is $\tilde{X}_{\dot{v}}(\omega)$ which corresponds to a force contribution in $x^b$-direction due to the sideways acceleration $\dot{v}$. For zero-frequency $\omega = 0$, the oscillatory derivative is defined as the *hydrodynamic derivative*:

$$F_\alpha \triangleq \tilde{F}_\alpha(0). \quad \text{(hydrodynamic derivative)} \tag{2.68}$$

From SNAME [29] this suggests that the hydrodynamic derivative is found from

$$F_\alpha \triangleq \frac{\partial F}{\partial \alpha}. \tag{2.69}$$

#### Added inertia forces

Hydrodynamic added mass is an additional mass that appears when a body moves through a fluid (like water). As the body accelerates or moves in the fluid, it causes the surrounding fluid to also move and be displaced. This displacement creates a resistance or inertia effect, similar to the way you might feel resistance if you have ever tried to run through snow.

**Remark 28.** *In a one-dimensional linear motion, Newton's second law would take on an extra virtual mass, the added mass $m_a$ in the equation*

$$\vec{F} = (m + m_a)\vec{a}.$$

The hydrodynamic derivatives representing the added mass takes the following form

$$\mathbf{M}_{\mathrm{A}} \triangleq -\begin{pmatrix} X_{\dot{u}} & X_{\dot{v}} & X_{\dot{w}} & X_{\dot{p}} & X_{\dot{q}} & X_{\dot{r}} \\ Y_{\dot{u}} & Y_{\dot{v}} & Y_{\dot{w}} & Y_{\dot{p}} & Y_{\dot{q}} & Y_{\dot{r}} \\ Z_{\dot{u}} & Z_{\dot{v}} & Z_{\dot{w}} & Z_{\dot{p}} & Z_{\dot{q}} & Z_{\dot{r}} \\ K_{\dot{u}} & K_{\dot{v}} & K_{\dot{w}} & K_{\dot{p}} & K_{\dot{q}} & K_{\dot{r}} \\ M_{\dot{u}} & M_{\dot{v}} & M_{\dot{w}} & M_{\dot{p}} & M_{\dot{q}} & M_{\dot{r}} \\ N_{\dot{u}} & N_{\dot{v}} & N_{\dot{w}} & N_{\dot{p}} & N_{\dot{q}} & N_{\dot{r}} \end{pmatrix}, \tag{2.70}$$

where the added mass force and moment is $\boldsymbol{\tau}_{\mathrm{A}} = -\mathbf{M}_{\mathrm{A}}\dot{\boldsymbol{\nu}}$. Note that the matrix is multiplied with $-1$ such that $M_{\mathrm{A}} > 0$ is positive definite.

**Remark 29.** *If experimental data is used to determine the added mass coefficients in Eq. 2.70, Fossen pp. 145 [4] states that the added inertia matrix can be symmetrized according to*

$$\mathbf{M}_A = \frac{1}{2}(\hat{\mathbf{M}}_A + \hat{\mathbf{M}}_A^{\mathsf{T}}),$$

*where* $\hat{\mathbf{M}}_A$ *contains the experimentally data.*

### Dissipative forces

Different damping terms contribute to both linear and quadratic damping. These effects are difficult to separate so the total hydrodynamic damping can be taken as the combination of linear damping $\mathbf{B}_p$ and quadratic (viscous) damping $\mathbf{B}_v(\boldsymbol{\nu})$ such that

$$\mathbf{B}(\boldsymbol{\nu}) = \mathbf{B}_p + \mathbf{B}_v(\boldsymbol{\nu}). \tag{2.71}$$

The linear damping is defined as

$$\mathbf{B}_p \triangleq -\begin{pmatrix} X_u & X_v & X_w & X_p & X_q & X_r \\ Y_u & Y_v & Y_w & Y_p & Y_q & Y_r \\ Z_u & Z_v & Z_w & Z_p & Z_q & Z_r \\ K_u & K_v & K_w & K_p & K_q & K_r \\ M_u & M_v & M_w & M_p & M_q & M_r \\ N_u & N_v & N_w & N_p & N_q & N_r \end{pmatrix}. \tag{2.72}$$

### Restoring matrix

Denote the matrix $G$ as

$$\mathbf{G} \triangleq -\begin{pmatrix} X_x & X_y & X_z & X_\phi & X_\theta & X_\psi \\ X_x & Y_y & Y_z & Y_\phi & Y_\theta & Y_\psi \\ Z_x & Z_y & Z_z & Z_\phi & Z_\theta & Z_\psi \\ K_x & K_y & K_z & K_\phi & K_\theta & K_\psi \\ M_x & M_y & M_z & M_\phi & M_\theta & M_\psi \\ N_x & N_y & N_z & N_\phi & N_\theta & N_\psi \end{pmatrix}, \tag{2.73}$$

which is the linear restoring force $\boldsymbol{\tau}_{\mathrm{hs}} = -\mathbf{G}\boldsymbol{\eta}$.

### Wave forces

The first order wave forces causing oscillatory motion may be described by a superposition over wave frequencies $\omega_n$ by the components $\boldsymbol{\tau}_{\text{wave1},n}$ of the following equation

$$\boldsymbol{\tau}_{\text{wave1}} = \sum_{n=1}^{\infty} \boldsymbol{\tau}_{\text{wave1},n} \cos(\omega_n t + \epsilon_n), \tag{2.74}$$

where $\epsilon_n$ is the phase angle. In this work, *forcing functions* $\boldsymbol{\tau}_0$, or force response amplitude operators (force RAOs) $\boldsymbol{\tau}_0$ from the wave amplitude $\zeta_{\text{a}}$ are used, for instance in Sect. 3.3:

$$\boldsymbol{\tau}_{\text{wave1}} = \sum_{n=1}^{\infty} \boldsymbol{\tau}_0 \zeta_{\text{a},n} \cos(\omega_n t + \epsilon_n). \tag{2.75}$$

### Wind forces

For a marine craft moving with forward speed, the 6-DOF wind forces and moments according to Fossen in the chapter "Environmental Forces and Moments" [4] are

$$\boldsymbol{\tau}_{\text{wind}} = \frac{1}{2}\rho_{\text{a}} V_{\text{rw}}^2 \begin{pmatrix} C_X(\gamma_{\text{rw}}) A_{\text{Fw}} \\ C_Y(\gamma_{\text{rw}}) A_{\text{Lw}} \\ C_Z(\gamma_{\text{rw}}) A_{\text{Fw}} \\ C_K(\gamma_{\text{rw}}) A_{\text{Lw}} H_{\text{Lw}} \\ C_M(\gamma_{\text{rw}}) A_{\text{Fw}} H_{\text{Fw}} \\ C_N(\gamma_{\text{rw}}) A_{\text{Lw}} L_{\text{oa}} \end{pmatrix}, \tag{2.76}$$

where $\rho_{\text{a}}$ is the air density, $V_{\text{rw}}$ is the relative wind speed and the parameters $A_{\text{Fw}}, H_{\text{Fw}}$ and $A_{\text{Lw}}, H_{\text{Lw}}$ is the frontal and lateral projected areas and heights above water.

**Remark 30.** *For longitudinal and lateral symmetrical vehicles, the wind coefficients in degrees of freedom* $\{1, 2, 6\}$ *can be approximated by [4]*

$$C_X(\gamma) \simeq -c_x \cos(\gamma), \qquad C_Y(\gamma) \simeq c_y \sin(\gamma), \qquad C_N(\gamma) \simeq c_n \sin(2\gamma). \tag{2.77}$$

### Wave-propulsion

According to Definition 11, oscillatory wave excitation forces on the marine craft do not serve any purpose for the maneuvering characteristics of the craft. However, by the addition of spring-loaded hydrofoils, the first order wave forces can be converted to directional second order forces, resulting in an overall green propulsion of the marine craft.

The treatment of an expression for the wave-propulsion force is given in Sect. 2.6.6 in which the theory of foils given in Sect. 2.6 should be read first.

### 2.4.5 Slender body theory

Slender body theory in fluid mechanics is a simplification technique applied to long and slender objects, like an aircraft wing or along a slender marine craft. The assumption is that the cross-sectional dimensions are small compared to the overall length. This allows to integrate any known sectional characteristic along the length of the object, approximating the overall effect but neglecting certain three-dimensional effects. Crude approximations from strip theory calculations can be found in Journée 1992 [41].

In strip theory, the marine craft is divided into a finite number of strips where each strip is considered two-dimensional under the slender body approximation. Hydrodynamic coefficients for the whole marine craft can thus be found by summarising the contributions from the lone strips. [42]

One might compare strip theory applied to slender bodies with slices of a bread where the length of the bread is much greater than the width. The overall characteristic of the bread can be approximated by summing up each slice of bread along the length. Here, the sectional characteristics is e.g. a function of the crisp of the bread.

An application of strip theory is found in MARINTEK's ShipX-VERES software, where strip theory is used to determine the coefficients [21].

Fossen, 2005 [39] states that traditional strip theory, developed by Salvesen et al. 1970 [43], is valid up to Froude number of about $\mathrm{Fn} < 0.25 - 0.3$, where the characteristic length is the length of the ship. From the definition of Froude number in Sect. 2.3.1, this suggest that for useful purposes of strip theory is applicable for marine craft speeds up to

$$U_{\max} = 0.3\sqrt{gL}. \tag{2.78}$$

In the article of Clarke et al. 1982 [44], slender body strip method is employed to find the hydrodynamic derivatives in sway and yaw. See Sects. 2.4.4 and 2.4.4 for these definitions. By using the horizontal added mass coefficient $C_{\mathrm{H}}$ for sections along the hull, the non-dimensionless hydrodynamic derivatives was found. This method assumes that the zero-frequency added mass coefficient at the non-dimensional position $x' = x/L$ from midships is known. An example of practical use of slender body theory from Clarke et al. [44] is the calculation

$$Y'_{\dot{v}} = -\pi \left(\frac{T}{L}\right)^2 \int_{\mathrm{Bow}}^{\mathrm{Stern}} C_{\mathrm{H}}(x')\, \mathrm{d}x'. \tag{2.79}$$

The method of slender body theory is advantageous when the dimensions of the marine craft is known in advance, in which case Eq. (2.79) and similar found in [44], with the definition of the prime normalization method in Sect. 2.1.1, can be used to find numerical or analytical expressions.

**Remark 31.** *In the general case for a commercially available wave-propelled USV, the vehicle's dimensions and shapes might not be known and empirical equations might be the correct method to use instead of slender body theory.*

## 2.5 Complete marine craft model

The complete vessel dynamics is described by the equation

$$\mathbf{M}_{\mathrm{RB}}\dot{\boldsymbol{\nu}} + \mathbf{C}_{\mathrm{RB}}(\boldsymbol{\nu})\boldsymbol{\nu} = \boldsymbol{\tau}_{\mathrm{RB}}, \tag{2.80}$$

which accounts for the vessel's inertia $\mathbf{M}_{\mathrm{RB}}$ and attitude dynamics from the Coriolis and centripetal matrix $\mathbf{C}_{\mathrm{RB}}$. The forces and moments applied to the vessel are all fluid mechanical forces of some sort:

$$\boldsymbol{\tau}_{\mathrm{RB}} = \boldsymbol{\tau}_{\mathrm{hs}} + \boldsymbol{\tau}_{\mathrm{hyd}} + \boldsymbol{\tau}_{\mathrm{wind}} + \boldsymbol{\tau}_{\mathrm{rudd}} + \boldsymbol{\tau}_{\mathrm{foil}} + \boldsymbol{\tau}_{\mathrm{wave}} + \boldsymbol{\tau}_{\mathrm{prop}}. \tag{2.81}$$

Where the rigid body forces $\boldsymbol{\tau}_{\mathrm{RB}}$ is given as the summation of hydrostatic forces $\boldsymbol{\tau}_{\mathrm{hs}}$, hydrodynamic forces $\boldsymbol{\tau}_{\mathrm{hyd}}$, wind forces $\boldsymbol{\tau}_{\mathrm{wind}}$, rudder forces $\boldsymbol{\tau}_{\mathrm{rudd}}$, foil-propulsion forces $\boldsymbol{\tau}_{\mathrm{foil}}$, wave forces $\boldsymbol{\tau}_{\mathrm{wave}}$ and propeller forces $\boldsymbol{\tau}_{\mathrm{prop}}$.

The forces applied to the vessel can be split into low frequency components and their perturbations, $\boldsymbol{\tau}_{\mathrm{RB}} = \boldsymbol{\tau}_{\mathrm{RB,\,LF}} + \delta\boldsymbol{\tau}_{\mathrm{RB}}$.

### 2.5.1 Maneuvering and seakeeping models

From Fossen 2005 [39] and Fossen 2021 [4], the following description distinguishing maneuvering -and seakeeping models is used in the model architecture:

In *maneuvering*, the vessel is assumed to be moving in restricted calm water without interference of waves. The dynamical model might be nonlinear, and usually derived for a ship moving at a nominal speed $U$. The theory for the dynamics thus utilizes a zero-frequency assumption from the effects of waves.

In *seakeeping* analysis however, the effects of waves are usually investigated at a given speed (including stationkeeping with $U = 0$) in irregular seaways or for a given heading for sinusoidal regular waves. The analysis is employed for adopting operability criteria in different sea-states. It also includes frequency-dependent terms describing the dynamics in the time-domain. These perturbations are zero-mean oscillations from an equilibrium state, defined by a ship moving with constant heading and speed.

**Remark 32.** *According to Fossen [4], the maneuvering motion of a craft is commonly modeled on a 3-DOF dynamic model for the horizontal-plane motion defined by the 2D-position in the North-East directions* $(x^n, y^n)$ *and cardinal heading* $\psi$*. A standard for ship motions in surge, sway and yaw is to use the zero-frequency added mass and damping coefficients, the motion derivatives [40].*

**Remark 33.** *The wave motion in seakeeping mainly affects the 3-DOF system in heave, roll and pitch [4]. As a consequence, first-order wave forces* $\boldsymbol{\tau}_{wave1}$ *are usually found in DOF* $\{3, 4, 5\}$.

Let the frequency-dependent forces and moments be denoted by subscript 1

$$\boldsymbol{\tau}_{\mathrm{RB1}} := \delta\boldsymbol{\tau}_{\mathrm{RB}} = \boldsymbol{\tau}_{\mathrm{hs}} + \boldsymbol{\tau}_{\mathrm{hyd}} + \delta\boldsymbol{\tau}_{\mathrm{foil}} + \boldsymbol{\tau}_{\mathrm{wave1}}, \tag{2.82}$$

and let the low-frequency (slow motion) forces and moments be denoted by subscript 2

$$\boldsymbol{\tau}_{\mathrm{RB2}} \triangleq \boldsymbol{\tau}_{\mathrm{RB,\,LF}} = \boldsymbol{\tau}_{\mathrm{hyd}}(0) + \boldsymbol{\tau}_{\mathrm{wind}} + \boldsymbol{\tau}_{\mathrm{rudd}} + \boldsymbol{\tau}_{\mathrm{foil}} + \boldsymbol{\tau}_{\mathrm{wave2}} + \boldsymbol{\tau}_{\mathrm{prop}}. \tag{2.83}$$

Hydrostatic forces is only a frequency dependent force and hence $\boldsymbol{\tau}_{\mathrm{hs1}} \equiv \boldsymbol{\tau}_{\mathrm{hs}}$, likewise for wind, rudder and propeller forces which are all slow motion forces.

The mean vessel dynamics can be written as

$$\mathbf{M}_{\mathrm{RB}}\dot{\boldsymbol{\nu}}_{\mathrm{LF}} + \mathbf{C}_{\mathrm{RB}}(\boldsymbol{\nu}_{\mathrm{LF}})\boldsymbol{\nu}_{\mathrm{LF}} = \boldsymbol{\tau}_{\mathrm{RB2}}, \tag{2.84}$$

and with sea current and hydrodynamic forces, the equations will take the form

$$[\mathbf{M}_{\mathrm{RB}} + \mathbf{M}_{\mathrm{A}}(0)]\dot{\boldsymbol{\nu}}_{\mathrm{r}} + [\mathbf{B}_{\mathrm{p}} + \mathbf{B}_{\mathrm{v}}(0)]\boldsymbol{\nu}_{\mathrm{r}} + \mathbf{C}(\boldsymbol{\nu}_{\mathrm{r}})\boldsymbol{\nu}_{\mathrm{r}} = \boldsymbol{\tau}_{\mathrm{wind}} + \boldsymbol{\tau}_{\mathrm{rudd}} + \boldsymbol{\tau}_{\mathrm{foil}} + \boldsymbol{\tau}_{\mathrm{wave2}} + \boldsymbol{\tau}_{\mathrm{prop}}, \tag{2.85}$$

or, written commonly as the maneuvering model

$$\mathbf{M}\dot{\boldsymbol{\nu}}_{\mathrm{r}} + \mathbf{B}\boldsymbol{\nu}_{\mathrm{r}} + \mathbf{C}(\boldsymbol{\nu}_{\mathrm{r}})\boldsymbol{\nu}_{\mathrm{r}} = \boldsymbol{\tau}_{\mathrm{RB,\,LF}}. \tag{2.86}$$

From an inertial seakeeping frame, Newton's law for the perturbed motion becomes

$$\mathbf{M}_{\mathrm{RB}}\ddot{\boldsymbol{\xi}} = \boldsymbol{\tau}_{\mathrm{hyd}} + \boldsymbol{\tau}_{\mathrm{hs}} + \boldsymbol{\tau}_{\mathrm{wave1}} + \delta\boldsymbol{\tau}_{\mathrm{foil}}. \tag{2.87}$$

When the hydrostatic and hydrodynamic coefficients are written out, the classical frequency-domain equations for a wave-propelled USVs are thus

$$\left[\mathbf{M}_{\mathrm{RB}} + \mathbf{M}_{\mathrm{A,\,USV}}(\omega)\right]\ddot{\boldsymbol{\xi}} + [\mathbf{B}_{\mathrm{p}} + \mathbf{B}_{\mathrm{v,\,USV}}(\omega)]\dot{\boldsymbol{\xi}} + \mathbf{C}\boldsymbol{\xi} = \boldsymbol{\tau}_{\mathrm{wave1}} + \delta\boldsymbol{\tau}_{\mathrm{foil}}, \tag{2.88}$$

the presence of the foils will alter the dynamical equations for the USVs, and they are assumed to add a viscous damping $\mathbf{B}_{\mathrm{v,\,foil}}(\omega)$ and frequency-dependent added mass $\mathbf{M}_{\mathrm{A,\,foil}}(\omega)$ on the form

$$\left[\mathbf{M} + \mathbf{M}_{\mathrm{A,\,USV}}(\omega) + \mathbf{M}_{\mathrm{A,\,foil}}(\omega)\right]\ddot{\boldsymbol{\xi}} + [\mathbf{B}_{\mathrm{p}} + \mathbf{B}_{\mathrm{v,\,USV}}(\omega) + \mathbf{B}_{\mathrm{v,\,foil}}(\omega)]\dot{\boldsymbol{\xi}} + \mathbf{C}\boldsymbol{\xi} = \boldsymbol{\tau}_{\mathrm{wave1}}. \tag{2.89}$$

**Remark 34.** *The presence of hydrofoils alter the equations of motion for the USV compared to the USV without foils. This impose a challenge for employing standardized response amplitude operators for wave-induced motions on such vehicles.*

Summarized, the 6 DOF maneuvering model for the USV is

$$\dot{\boldsymbol{\eta}} = \mathbf{R}_m^n(\psi)\boldsymbol{\nu}, \tag{2.90a}$$

$$\mathbf{M}\dot{\boldsymbol{\nu}}_{\mathrm{r}} + \mathbf{C}(\boldsymbol{\nu}_{\mathrm{r}})\boldsymbol{\nu}_{\mathrm{r}} + [\mathbf{B}_{\mathrm{p}} + \mathbf{B}_{\mathrm{v}}(\boldsymbol{\nu}_{\mathrm{r}})]\boldsymbol{\nu}_{\mathrm{r}} = \boldsymbol{\tau}_{\mathrm{wind}} + \boldsymbol{\tau}_{\mathrm{wave2}} + \boldsymbol{\tau}_{\mathrm{foil}} + \boldsymbol{\tau}_{\mathrm{rudd}}, \tag{2.90b}$$

and the 6 DOF seakeeping model for the USV is

$$[\mathbf{M}_{\mathrm{RB}} + \mathbf{M}_{\mathrm{A}}(\omega)]\ddot{\boldsymbol{\xi}} + [\mathbf{B}_{\mathrm{p}} + \mathbf{B}_{\mathrm{v}}(\omega)]\dot{\boldsymbol{\xi}} + \mathbf{C}\boldsymbol{\xi} = \boldsymbol{\tau}_{\mathrm{wave1}}. \tag{2.91}$$

### 2.5.2 Frequency-domain model

The classical frequency domain equations of motion for perturbations from the first order wave forces is [4]

$$[\mathbf{M} + \mathbf{M}_{\mathrm{A}}(\omega)]\,\ddot{\boldsymbol{\xi}} + \mathbf{B}(\omega)\dot{\boldsymbol{\xi}} + \mathbf{C}\boldsymbol{\xi} = \boldsymbol{\tau}_{\mathrm{wave1}}, \tag{2.92}$$

where it is recognized that the form is a mass-spring-damper system where linear restoring forces $\boldsymbol{\tau}_{\mathrm{hs}} = -\mathbf{C}\boldsymbol{\xi}$ are included in the model. The equation is only valid under linear theory and for harmonicacally forced oscillations under steady-state. [4]

According to Fossen [4], the representation of Eq. (2.92) is an abuse of notation since both frequency and time is present. A correct way of describing the frequency-motion is by the Fourier transformation of Eq. (2.92). Assuming zero initial conditions, then

$$\left[-\omega^2\left[\mathbf{M} + \mathbf{M}_{\mathrm{A}}(\omega)\right] - j\omega\mathbf{B}(\omega) + \mathbf{C}\right]\boldsymbol{\xi}(j\omega) = \boldsymbol{\tau}_{\mathrm{wave1}}(j\omega) \tag{2.93}$$

describes the dynamics with the transfer function $\mathbf{H}(j\omega)$ in $\boldsymbol{\xi}(j\omega) = \mathbf{H}(j\omega)\boldsymbol{\tau}_{\mathrm{wave1}}(j\omega)$ as

$$\mathbf{H}(j\omega) = \left[-\omega^2\left[\mathbf{M} + \mathbf{M}_{\mathrm{A}}(\omega)\right] - j\omega\mathbf{B}(\omega) + \mathbf{C}\right]^{-1}. \tag{2.94}$$

Here, the imaginary unit is $j$.

### 2.5.3 Time-domain model

The former representation of a frequency-domain model describes ship motion only under the influence of frequency-dependent coefficients. When the sea state is represented by a wave spectrum, a Fourier analysis finds the proper frequency-modes, but would lead to a large number of equations to capture the frequency components. For this reason, a time domain dynamic model is desirable, who encourage Cummins, 1962 [38] to publish a fundamental report on a linear time-domain model for ship motion.

#### Cummins' equations of motion

The original phrasing of Cummin stated:

*"But what happens when we don't have a well defined frequency? The mathematical model becomes almost meaningless. True, a Fourier analysis of the exciting force (or encountered wave) permits the model to be retained, but physical reality is almost lost in the infinity of equations required to represent the motion."* – Cummins, 1962

The crucial points of the work of Cummins was to

- have a time-domain model of ship motions in 6-DOF without frequency-dependent coefficients,
- separate and identify explicitly the factors governing the response, both for the transient and stationary scenario.

A derivation of Cummins' equations can be found in the original literature [38], which states that the radiation-induced hydrodynamic forces $\boldsymbol{\tau}_{\text{rad}} = \boldsymbol{\tau}_{\text{hyd}}$ in an ideal fluid can be written as

$$\boldsymbol{\tau}_{\text{hyd}} = -\mathbf{M}_{\text{A}}(\infty)\ddot{\boldsymbol{\xi}} - \mathbf{B}(\infty)\dot{\boldsymbol{\xi}} - \int_{-\infty}^{t} \mathbf{K}(t-\tau)\dot{\boldsymbol{\xi}}(\tau)\,\mathrm{d}\tau, \tag{2.95}$$

where the hydrodynamic added mass and the damping matrix is evaluated at infinite frequency, and the matrix $\mathbf{K}(t)$ is known as the *matrix of retardation*. The inertia of the fluid causes a certain delay to the change of the hull's motion, which is expressed by the fluid memory term in the convolution. Hence the integral incorporates the energy dissipation due to the radiated waves.

### Ogilvie's transformation

A transformation proposed by Ogilvie, 1964 [45] suggest that the matrix of retardation is given by either

$$\mathbf{K}(t) \equiv \frac{2}{\pi}\int_0^{\infty} [\mathbf{B}(\omega) - \mathbf{B}(\infty)]\cos(\omega t)\,\mathrm{d}\omega, \tag{2.96a}$$

or

$$\mathbf{K}(t) \equiv \frac{2}{\pi}\int_0^{\infty} \omega[\mathbf{M}_{\text{A}}(\omega) - \mathbf{M}_{\text{A}}(\infty)]\sin(\omega t)\,\mathrm{d}\omega. \tag{2.96b}$$

When dealing with a causal system, the limits in Eq. (2.95) can be changed [4], resulting in the linear time-domain model for Cummins' equation:

$$[\mathbf{M} + \mathbf{M}_{\text{A}}(\infty)]\ddot{\boldsymbol{\xi}} + \mathbf{B}(\infty)\dot{\boldsymbol{\xi}} + \int_0^{t} \mathbf{K}(t-\tau)\dot{\boldsymbol{\xi}}(\tau)\,\mathrm{d}\tau + \mathbf{C}\boldsymbol{\xi} = \boldsymbol{\tau}_{\text{wave1}}. \tag{2.97}$$

### State space representation of fluid memory effects

According to Perez and Fossen [46], the convolution integral representing the fluid memory effects is unsuited for simulation and analysis for control system design. Kristiansen and Egeland [47] developed a state-space approximation to the convolution term in Eq. 2.97, and further discussion for the time-domain realization for a vessel with frequency-dependent hydrodynamic coefficients is found in Kristiansen et al. [48]. The fluid memory effect is

$$\boldsymbol{\mu}(t) \triangleq \int_0^{t} \mathbf{K}(t-\tau)\dot{\boldsymbol{\xi}}(\tau)\,\mathrm{d}\tau \equiv (\mathbf{K} * \dot{\boldsymbol{\xi}})(t). \tag{2.98}$$

Since convolution in the time domain equals a multiplication in the frequency domain, the corresponding Laplace transformation

$$\boldsymbol{\mu}(s) = \mathbf{K}(s)\dot{\boldsymbol{\xi}}(s), \tag{2.99}$$

can be implemented by the following state space formulation:

$$\begin{aligned} \dot{\mathbf{x}} &= \mathbf{A}_{\mathrm{r}}\mathbf{x} + \mathbf{B}_{\mathrm{r}}\dot{\boldsymbol{\xi}}, \\ \boldsymbol{\mu} &= \mathbf{C}_{\mathrm{r}}\dot{\boldsymbol{\xi}}. \end{aligned} \tag{2.100}$$

This system approximates the convolution integral with transfer function $\mathbf{K}(s) = \mathbf{C}_{\mathrm{r}}(s\mathbb{I}-\mathbf{A}_{\mathrm{r}})^{-1}\mathbf{B}_{\mathrm{r}}$.

The matrices $(\mathbf{A}_{\mathrm{r}}, \mathbf{B}_{\mathrm{r}}, \mathbf{C}_{\mathrm{r}})$ can be identified by frequency-domain identification algorithm proposed by Perez and Fossen, explained further in [46]. The algorithm is a part of the Marine Systems Simulator (MSS) developed for MATLAB, available online [49].

### Cummins' equations for a single degree of freedom

An uncoupled dynamics in a single degree of freedom may be described by

$$m(\omega)\ddot{\xi} + b(\omega)\dot{\xi} + c\xi = \tau, \tag{2.101}$$

where the frequency-dependent mass is $m(\omega)$, damping $b(\omega)$, restoring element $c$ and the forcing function is $\tau$. Cummin's equation from Eq. (2.97) for the causal system in Eq. (2.101) is

$$m(\infty)\ddot{\xi} + b(\infty)\dot{\xi} + \underbrace{\int_0^t k(t-\tau)\dot{\xi}\,\mathrm{d}\tau}_{\mu(t)} + c\xi = \tau, \tag{2.102}$$

where the retardation function can be approximated by

$$k(t) = \frac{2}{\pi}\int_0^\infty [b(\omega) - b(\infty)]\cos(\omega t)\,\mathrm{d}\omega, \tag{2.103}$$

and the fluid memory effect is the convolution integral

$$\mu(t) = \int_0^t k(t-\tau)\dot{\xi}\,\mathrm{d}\tau \equiv (k * \dot{\xi})(t), \tag{2.104}$$

which is approximated by

$$\hat{k}(s) = \mu(s)/\dot{\xi}(s) = \mathbf{C}_{\mathrm{r}}(s\mathbb{I} - \mathbf{A}_{\mathrm{r}})^{-1}\mathbf{B}_{\mathrm{r}}, \tag{2.105}$$

where the matrices $\mathbf{A}_{\mathrm{r}}$, $\mathbf{B}_{\mathrm{r}}$ and $\mathbf{C}_{\mathrm{r}}$ is the state-space realization.

**Remark 35.** *Stability considerations for the time-domain system in Eq. (2.101) with the state-space realization for the fluid memory effects in Eq. (2.105) is found by an effective system with states* $[\dot{\xi}, \ddot{\xi}, \dot{\mathbf{x}}_r^\mathsf{T}]^\mathsf{T}$ *on the form*

$$\begin{pmatrix} \dot{\xi} \\ \ddot{\xi} \\ \dot{\mathbf{x}}_r \end{pmatrix} = \underbrace{\begin{pmatrix} 0 & 1 & \mathbf{0} \\ -\frac{c}{m} & 0 & -\frac{1}{m}\mathbf{C}_r \\ \mathbf{0} & \mathbf{B}_r & \mathbf{A}_r \end{pmatrix}}_{\mathbf{A}_{\mathrm{eff}}} \begin{pmatrix} \xi \\ \dot{\xi} \\ \mathbf{x}_r \end{pmatrix} + \begin{pmatrix} \frac{1}{m} \\ 0 \\ \mathbf{0} \end{pmatrix} \tau, \tag{2.106}$$

*where the effective system matrix* $\mathbf{A}_{\mathrm{eff}}$ *can be analyzed to interpret the stability properties.*

## 2.6 Foil theory

This section describes the necessary semi-empirical equations developed for the governing forces on foils due to the surrounding fluid velocity field. The foils are typically mounted on wave-propelled USVs, as illustrated in Fig. 2.10. Regarding position, the following assumptions are made:

**Assumption 11.** *The foils are mounted symmetrically on the midline of the USV with the wing span in port/starboard direction.*

**Assumption 12.** *The foils can rotate by an angle $\vartheta_i$ along $y^b$-direction at the pivot position.*

**Remark 36.** *From Assumption 11, the constant pivot position for the foils are* $\mathbf{r}^b_{p,i} = [x_{p,i}, 0, z_{p,i}]^\top$.

The dynamics of the foils will be given in Sect. 3.4, whereas the geometry of the foils and their forces are derived here.

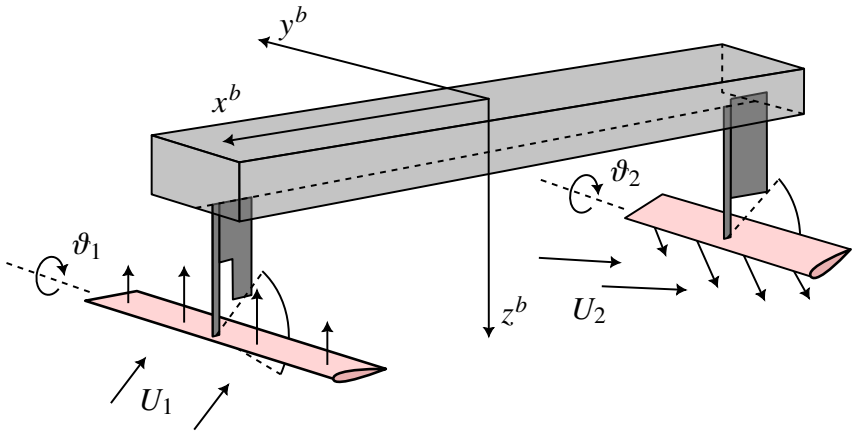


**Figure 2.10:** Typical foil (in red) placement on a wave-propelled USV. The forces on the foils depend on the relative velocity inflow $U$.

### 2.6.1 Geometry

The vast literature on foils is related to airfoils developed for the aircraft industry. Most of the literature can be adopted for hydrofoils as well, which is the equivalent description for foils that are submerged in water.

In order to proceed with the physical principles for the dynamics of the foils, the following assumptions about the geometry of the foils, as illustrated in Fig. 2.11, are made:

**Assumption 13.** *The foils are assumed to have zero dihedral angle. This means that the foils do not have a "V"-shape seen from the front.*

**Assumption 14.** *The foils are assumed to have no curvature.*

**Assumption 15.** *The foils are assumed to have constant cross-sectional shape.*

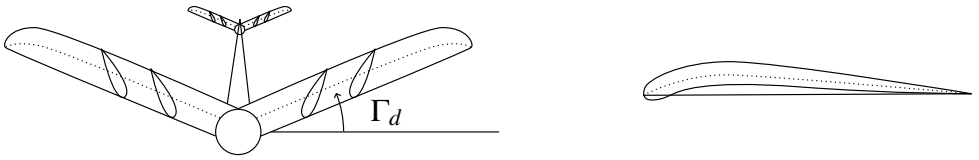


UAV front Wing section with camber

**Figure 2.11:** Dihedral angle $\Gamma_d$ shown to left for an uncrewed aerial vehicle (UAV) and camber line is shown dashed to right at a wing section, commonly called foil.

Furthermore, there is no general assumption on the geometry along the *span* of the wing, which is the wing seen from above. The span is denoted by $S = 2b$, where $b$ is the half span. If one knows the foil section and span, the foil shape is completely determined. A couple of remarks to the above assumptions are made before the span shape and section is described:

**Remark 37.** *Assumptions 13 and 14 can be considered valid for wave-propelled USVs since the foils operate symmetrically with both positive and negative attack angles during sinusoidal wave-induced motion.*

**Remark 38.** *A consequence of Assumption 14 is that the camber value is zero, and that the camber line equals the chord line.*

**Remark 39.** *Assumption 15 is also common in propeller theory [50]. As a consequence, the cross-sectional shape scales with the chord length. This is illustrated with the dashed line over the span of the wing in Fig. 2.11.*

### Span shape

The author did not find any standard equations relating to the shape of wings along the span. Therefore, the following equations can serve as an empiric description.

When the maximum chord width $c_{\max}$ appears at the midline, the span shape can be approximated by super-elliptic functions [2] characterized by the span $S$, the maximum chord width $c_{\max}$ and the endpoint $x_e \in [0, c_{\max}]$. The characteristics is illustrated in Fig. 2.12.
The suggested equations for leading edge (LE) and trailing edge (TE) was found to be

$$x_{\text{LE}}^{\text{TUFTE}} = x_e + (c_{\max} - x_e)\left[1 - \frac{y^{q_l}}{(S/2)^{q_l}}\right]^{1/q_l}, \tag{2.107a}$$

and

$$x_{\text{TE}}^{\text{TUFTE}} = x_e - x_e\left[1 - \frac{y^{q_t}}{(S/2)^{q_t}}\right]^{1/q_t}, \tag{2.107b}$$

where $q_l$ and $q_t$ are tuning parameters with higher values describing a more rectangular shape. The chord length over the span is the difference between Eqs. (2.107a) and (2.107b):

[2] Super elliptic meaning on the form $[(x - x_0)/a]^n + [(y - y_0))/b]^n = 1$, where $\min(a, b)$ is the semi-minor axis and $\max(a, b)$ is the semi-major axis

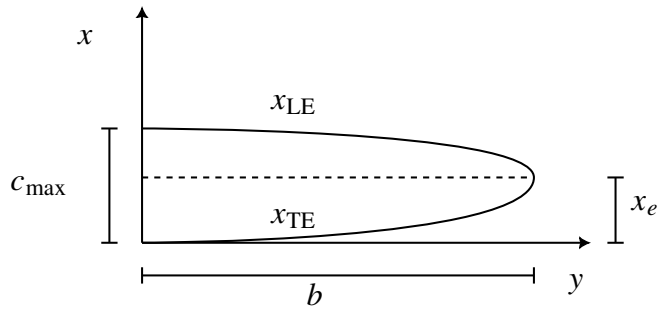


**Figure 2.12:** Simplified span shape characteristics over the half span $b = S/2$.

$$c(y) = x_{LE} - x_{TE} = (c_{max} - x_e)\left[1 - \frac{y^{q_l}}{(S/2)^{q_l}}\right]^{1/q_l} - x_e\left[1 - \frac{y^{q_t}}{(S/2)^{q_t}}\right]^{1/q_t}. \tag{2.108}$$

In this work, suggested values are $q_l, q_t \in [2.0, 3.0]$. However, these values have not been tested thoroughly, but should serve as a good approximation at an early stage.

**Remark 40.** *The suggested shape of Eqs. (2.107a) and (2.107b) can be used with slender body theory from Sect. 2.4.5 when the forces along the span is known.*

**Remark 41.** *The span shape discussed can further be simplified as a rectangular shape.*

### Standardized foil sections

According to Hoerner, several families of practical foil sections have been developed by systematic variation of their geometry to establish some order for foil sections [6]. To achieve an efficient control surface, which can generate sufficient lift with minimum drag, National Advisory Committee for Aeronautics (NACA) published a 4-digit series in 1933 [13]. The 4-digit NACA series was intended for practical design and construction of airplane wings.

For our case, only the symmetrically 4-digit NACA airfoils is of interest. The formula for such shapes of foil sections is on the form `NACA00xx`. The latter "xx" represents the thickness in percentage of $t_{\max}/c$. According to Jacobs et al. [13], the NACA sections are described by

$$\pm y'_{\text{NACA}}(t') = t' \cdot 5\,[0.2969x^{0.5} - 0.1260x - 0.3516x^2 + 0.2843x^3 - 0.1015x^4], \quad (2.109)$$

where prime denotes the normalized measure along the normalized chord length $c' = 1$, and the normalized thickness is $t' = t_{\max}/c$. Eq. (2.109) describes the thickness from leading edge to trailing edge.

**Remark 42.** *The expression in Eq.* (2.109) *introduces a nonzero trailing edge thickness of* $0.0105t$. *If one requires a zero trailing edge thickness, the last term in Eq.* (2.109) *can be switched to* $0.1036$. *This augmentation introduces an overall small change to the foil section.*

**Remark 43.** *By default, the NACA series has a maximum thickness appearing at* 30 % *along the chord length. Thus the NACA series do not properly describe all the variations one might encounter in the model design of wave-propelled USVs.*

Eq. (2.109) do not describe sections when the point of maximum thickness do not lie at exactly 30 %. In order to describe a wide range of foil sections, the following part proposes to characterize the foil section through a leading edge ellipse and a trailing edge constant slope.

### Proposed foil section

As found in the "Control" chapter in Hoerner 1985, [6], a straight and thin trailing edge improves the maximum lift of hydrofoil sections. This insight might lead to commercial development of hydrofoils generating higher thrusts for wave-propelled USVs by altering the foil section from the standardized NACA series, which was developed for airplane wing sections. One might expect that not all manufactures for wave-propelled USVs will give a detailed description of the foil section.

This motivates the development of a simple foil section where the location and maximum thickness is arbitrarily given. Additionally, with the description of the span shape in Sect. 2.6.1, such a simple model enables to calculate moments of inertia, and finding the governing forces on the foils employed.

From the literature on foil sections, a section consisting of a leading edge ellipse followed by a constant slope for the trailing edge is motivated to approximate a range of foil sections. This

corresponds to practice as about 5 % of the lift is lost when making the leading edge sharp [6].

Denote the chord length by $c$ and the point of maximum thickness $x_m$ with thickness $t$. One can approximate the leading edge as an ellipse with semi-major axis $x_m$ and semi-minor axis $0.5tc$. The trailing edge is approximated by a constant slope. Solving for this scenario by demanding a smooth parametric surface everywhere except at the trailing edge, the section

$$\pm y_{\text{TUFTE}} = \begin{cases} t \cdot 0.5c \left[1 - \frac{(x-x_m)^2}{x_m^2}\right]^{0.5}, & 0 \leq x \leq \frac{cx_m}{c-x_m}, \quad \text{(elliptic part)} \\ t \cdot \frac{0.5}{(1-2x_m/c)^{0.5}}[c-x], & \frac{cx_m}{c-x_m} < x \leq c, \quad \text{(constant slope)} \end{cases} \tag{2.110}$$

is proposed as an early design analysis. A comparison with the section from the author in Eq. (2.110), and NACA0012 from Eq. (2.109) is shown in Fig. 2.13. The proposed model is "thinner" than that of the NACA section, but the advantage is that the point of maximum thickness can be chosen freely.

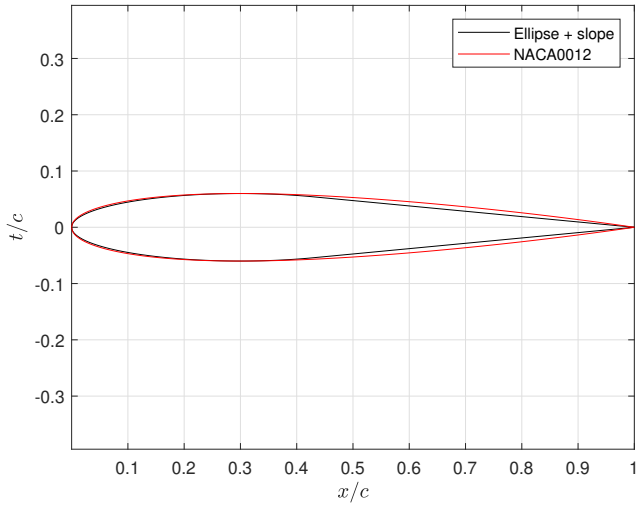


**Figure 2.13:** Proposed section compared to the NACA section. The maximum thickness is 12 % and appears at 30 % of the chord length from leading edge.

**Remark 44.** *Eq. (2.110) is analytical and smooth everywhere except at the trailing edge and has zero trailing edge thickness.*

**Remark 45.** *The leading edge radius is given by the semi-minor axis* $0.5tc$ *and semi-major axis* $x_m$ *as* $r = (0.5tc)^2/x_m$.

The non-dimensional version of Eq. (2.110) is found as:

$$\pm y'_{\text{TUFTE}}(t', x'_m) = \begin{cases} t' \cdot 0.5 \left[1 - \frac{(x-x'_m)^2}{x'^2_m}\right]^{0.5}, & 0 \leq x \leq \frac{x'_m}{1-x'_m}, \quad \text{(elliptic part)} \\ t' \cdot \frac{0.5}{(1-2x'_m)^{0.5}}[1-x], & \frac{x'_m}{1-x'_m} < x \leq 1, \quad \text{(constant slope)} \end{cases} \tag{2.111}$$

### 2.6.2 Foil characteristics

A flat plate inclined in steady flow has three forces: suction force $S$, lift force $L$ and drag force $D$, illustrated in Fig. 2.14. Under the assumption that the flow is attached, the leading edge suction force arise since the flow must accelerate around the plate creating a lower pressure at the leading edge. It can be shown that the component of the suction force $S$ parallel to the inflow is equal in magnitude to $D$, resulting in a free-stream cancellation of the drag force for a stationary flow in inviscid and incompressible fluid [51].

The continued analysis neglects the impact of the suction force $S$ and considers a flat plate with induced normal force. According to Steen [50], the normal force can be decomposed into a lift force and a drag force according to the following definitions:

**Definition 15.** ***(Lift)***
*Force component perpendicular to the mean fluid inflow.*

**Definition 16.** ***(Drag)***
*Force component parallel to the mean fluid inflow.*

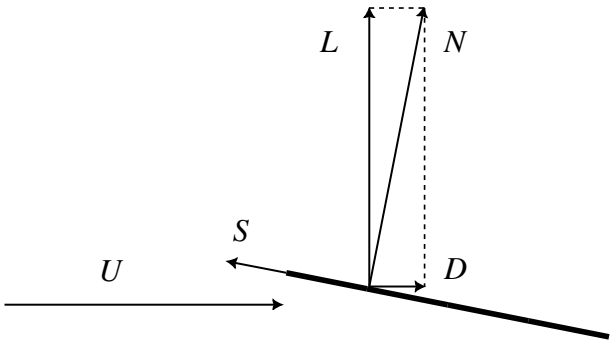


**Figure 2.14:** Lift $L$, drag $D$ and suction $S$ forces on a foil in steady flow.

The lift force $L$ and drag force $D$ on a foil can be expressed analytically via linear foil theory. The forces are found per unit span on an infinite wing, were the flow is assumed to be attached to the plate. The resulting forces on the foils are usually written in terms of the non-dimensional lift- and drag coefficients:

$$C'_L \triangleq \frac{L'}{\frac{1}{2}\rho U^2 c}, \tag{2.112a}$$

$$C'_D \triangleq \frac{D'}{\frac{1}{2}\rho U^2 c}, \tag{2.112b}$$

$$C'_N \triangleq \frac{N'}{\frac{1}{2}\rho U^2 c}. \tag{2.112c}$$

Here, $\rho$ is the density of water, $U$ is the relative inflow velocity and $c$ is the chord length. The prime denotes that the forces is per unit span.

### Linear foil theory

According to state-of-the-art results in linear foil theory, which e.g. can be found in Anderson 2001 [16], Fossen 2021 [4] or Steen 2014 [50], the lift coefficient for flat plates is found as

$$C'_L = 2\pi\alpha, \tag{2.113}$$

where $\alpha$ is the attack angle, defined according to Definition 17. For turbulent flow, model experiments suggest that the viscous drag $C_{Dv}$ depends on the thickness $t'$ as

$$C'_{Dv} = 2 \cdot (1 + 2t') \cdot C_F, \tag{2.114}$$

where $C_F$ is the International Towing Tank Conference (ITTC) friction line

$$C_F = \frac{0.075}{[\log(\mathrm{Re}) - 2]^2}, \tag{2.115}$$

where the Reynolds number from Eq. (2.31) is evaluated with chord length $c$ as characteristic length [50]. An alternative model for viscous drag on a foil profile is Migeotte's method [52] with

$$C'_{Dv} = 2 \cdot \left(1 + 2/3C'^2_{\mathrm{L}}\right) \cdot C_F. \qquad \text{(Migeotte's method)}$$

**Remark 46.** *For a nominal motion of a wave-propelled USV with speed $U \sim 1$ [m/s] and chord length $c = 0.2$ [m], then $C'_{Dv} = 0.018$ and $C'_{Di} = 0.127$ . Thus the induced drag dominates the viscous drag when the attack angle is not close to zero. Therefore, viscous drag is not a dominating force, and can be neglected in the dynamic model.*

The definition of the attack angle is based on Fossen [4], applied for the case of foils mounted on wave-propelled USVs:

**Definition 17.** ***(Angle of attack on propulsion foils for USVs)***
*The angle $\alpha$ from the relative fluid velocity vector to the chord line, in direction from the leading edge to the trailing edge of the foil, positive rotation into the paper in Fig. 2.14 by the right-hand screw convention.*

**Remark 47.** *From Definition 17, when the foils are attached to the USV by angle $\vartheta$ in the $y^b$-direction of the body (wing span in port/starboard direction), and the mean relative velocity fluid vector field at the foil is $\mathbf{U}^b = [u_\mathrm{r}, v_\mathrm{r}, w_\mathrm{r}]^\top$, the angle of attack is*

$$\alpha = \arctan(w_\mathrm{r}, u_\mathrm{r}) + \vartheta. \tag{2.116}$$

In order for the linear foil theory to be considered accurate, the following definition composed freely from Steen [50] is used:

**Definition 18.** ***(Prerequisite for linear foil theory)***
*Linear foil theory requires that camber, thickness and angle of attack is small compared to the chord length. A rule of thumb is that their respective lengths should not exceed 10 % of the chord lengths when measured normal to the chord line.*

**Remark 48.** *According to Definition 18, linear foil theory is applicable for attached flow around foils when the thickness $t' = t/c < 0.1$. Assumption 14, which assumes no curvature of the foils, already complies with the requirement in Definition 18.*

When foils are used for propulsion in the case of wave-propelled USVs, the prerequisite of linear foil theory in Definition 18 is not fulfilled since the attack angles are not guaranteed to be "small". For small attack angles, Eq. (2.113) can be considered valid. However, when the angle of attack increases, the flow around the foils separate, and the phenomena of *stall* occurs. This is treated in the next section. The interested reader can look into thickness effects on stall characteristics in Sarraf et al. [53].

### Characteristics above stall

The characteristics of foils operating at angles of attack above stall are of importance in analyzing wave-propelled USVs. For large attack angles, the boundary layer flow around a foil is separated, see Fig. 2.15, and the phenomena of stall occurs [50]. Stall can be defined according to:

**Definition 19.** ***(Stall)***
*The sudden reduction of lift by increasing angle of attack.*

Physically, upon increasing the angle of attack above the stall angle, the flow detaches, or separates, more or less suddenly from the suction side of the foil. This results in a sudden drop in lift until a combination of impact pressure on the pressure side, together with a scavenging effect in the wake, causes a slight increase in lift until about 45° of attack angle. Beyond the stall angle, the resultant force on the foil is essentially normal to the chord line. [6]

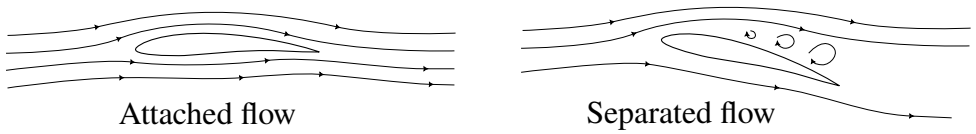


**Figure 2.15:** Attached flow below stall angle to the left and detached (separated) flow beyond stall angle to the right.

According to Anderson [16], two major consequences of the flow separating over a foil are:

1. A drastic loss of lift. This is called stall.
2. A major increase in drag. This is caused by pressure drag due to flow separation.

Most literature in the field explores the forces on foils only for small attack angles, giving lift and drag curves for angles below stall. As far as the author is concerned, there is no simple expressions for the forces present beyond the stall angle, in which case an interested reader is referred to dynamic stall conditions, for instance by Johnston 2004 [51] or Bøckmann 2014 [2].

In Hoerner's handbook on lift [6], only a single chapter of about one page is denoted to this phenomena throughout the book. It is treated briefly in the chapter "Airfoil characteristics above stall" at pp. 4-23. This is the only literature the author found to give semi-empirical

equations for lift and drag through 0°–180° degrees attack angle. Hoerner [6] describes this as "Correlation of Theory" which account for the loss of circulation (defined in Sect. 2.6.3) due to separation. Hoerner propose to use the coefficients

$$C'_{L,\text{HOERNER}} = (1.8 \text{ to } 2.0)\sin(\alpha)\cos(\alpha), \tag{2.117a}$$
$$C'_{D,\text{HOERNER}} = (1.8 \text{ to } 2.0)\sin(\alpha)^2, \tag{2.117b}$$
$$C'_{N,\text{HOERNER}} = (1.8 \text{ to } 2.0)\sin(\alpha). \tag{2.117c}$$

Additional information about drag on fully submerged foils is explained at length in chapters X and XI in the book "Fluid-Dynamic Drag" by Hoerner 1965 [15].

### 2.6.3 Circulatory forces

In determining semi-empirical equations for the governing forces on foils, a modification of linear foil theory is employed, which was shown by Tufte [17]. The material here is based on this approach since the original material is not intended for publication. The method here assumes that the flow around a flat plate is attached beyond the stall angle, before a correction of the equations are performed. The equations were developed without the knowledge of the semi-empirical relations given by Hoerner in Eq. (2.117).

The method is based on modeling a flat plate, a line similar to that in Fig. 2.14, in which a quote from Hoerner is appropriate:

"Foil sections, as used in wings or anything similar in flatness such as a plate for example, are not lines; in fact, only a mathematician can produce lift by means of a line." – Hoerner, 1985

#### Vortex distribution

In order to determine the forces on a foil, one may use Bernoulli's equations from Eq. (2.37) and place a vortex distribution along the chord length. Anderson discussed the use of vortex distributions as a method to analyze foils [16]:

"It was first espoused by Ludwig Prandtl and his colleagues at Göttingen, Germany, during the period 1912–1922. However, no general analytical solution for $\gamma = \gamma(s)$ exists for an airfoil of arbitrary shape and thickness. Rather, the strength of the vortex sheet must be found numerically, and the practical implementation (...) had to wait until the 1960s with the advent of large digital computers"

Excluding viscous forces, the resultant induced pressure force on a flat plate is normal to the face of the plate as shown in Fig. 2.16 with the normal force $N$ pointing in the direction from the pressure side to the suction side, acting in the center of pressure $x_{\text{c.p.}}$.

Evaluating Bernoulli's equation, as stated in Eq. (2.37), upstream in the free-stream flow with velocity $U$ and pressure $P_0$ and comparing to the foil surface, the pressure distributions are

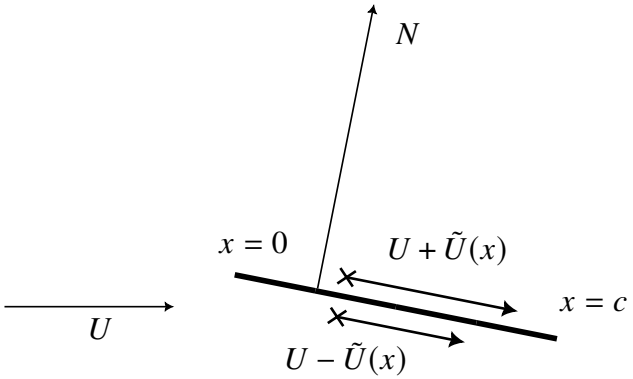


**Figure 2.16:** Perturbed velocity profile on the pressure side $U - \tilde{U}(x)$ and on the suction side $U + \tilde{U}(x)$.

$$P_{\text{pres.}}(x) = P_0 + \frac{1}{2}\rho[U^2 - (U - \tilde{U}(x))^2], \tag{2.118a}$$

$$P_{\text{suct.}}(x) = P_0 + \frac{1}{2}\rho[U^2 - (U + \tilde{U}(x))^2]. \tag{2.118b}$$

The normal force $N$ is found by integrating the pressure distribution over the chord length

$$N' = \int_0^c \Delta P(x)\,\mathrm{d}x = \rho U \int_0^c 2\tilde{U}(x)\,\mathrm{d}x := \rho U \int_0^c \gamma(x)\,\mathrm{d}x, \tag{2.119}$$

where $\Delta P(x) = P_{\text{pres.}}(x) - P_{\text{suct.}}(x) = (2.118a) - (2.118b)$ and $\gamma(x)$ is a vortex distribution.

The vortex $\gamma(x)$ is introduced in order to draw similarity to Kutta-Joukowski's theorem [32]. Firstly, the definition of circulation is given:

**Definition 20.** ***(Circulation)***
*In physics, circulation is the path integral of a vector field around a closed curve. For fluid mechanics, this vector field is the fluid velocity.*

Definition 20 is illustrated in Fig. 2.17 where the integration of an arbitrary velocity field is shown. Conversely, the inverse problem where the tangential velocity $V_\perp$ is found from a circulation source $\Gamma$ is shown to the right, analogous to Biot-Savart's law in electrodynamics,

$$V_\perp(r) = \frac{1}{2\pi r}\Gamma. \qquad \text{(Biot-Savart's law for velocity circulation)} \tag{2.120}$$

**Theorem 1.** ***(Kutta-Joukowski's theorem)***
*The two-dimensional lift on a submerged body is $L = \rho U\Gamma$, where $\rho$ is the fluid density, $U$ is the inflow velocity and $\Gamma$ is the fluid circulation around the body.*

**Remark 49.** *In Theorem 1, the circulation $\Gamma$ is related to the vortex distribution $\gamma(x)$ by $\Gamma = \int_0^c \gamma(x)\,\mathrm{d}x$.*

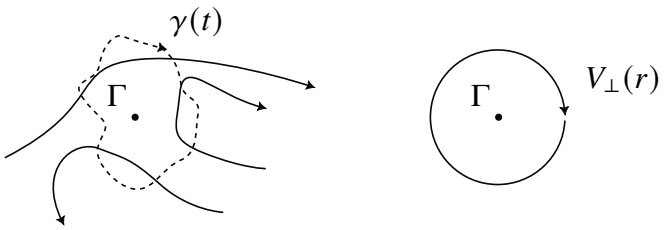


**Figure 2.17:** Circulation around an arbitrary closed curve $\gamma(t)$ in a velocity field to the left. To the right, the inverse problem of finding the tangential velocity $V_\perp$ at radius $r$.

**Remark 50.** *If the vortex distribution $\gamma(x)$ is known along the chord length, the induced lift and drag forces can be found with the components*

$$L' = \int_0^c \gamma(x)\,\mathrm{d}x\cos(\alpha), \qquad D' = \int_0^c \gamma(x)\,\mathrm{d}x\sin(\alpha). \tag{2.121}$$

For linear foil theory, it is customary to define the lift simply as the integral given by the normal force in Eq. (2.119), which is the method employed by Steen [50]. In order to find semi-empiric equations for the lift and drag force through 0°–180°, the definition for the normal force given here is used.

### Determining the vortex distribution

In order to determine the vortex distribution $\gamma(x)$ to find the forces acting on a flat plate, an impermeable condition and the infamous Kutta condition needs to be addressed.

The impermeability condition simply means that the solution of $\gamma(x)$ needs to be physically feasible, such that the surrounding water do not simply flow straight through the foil. The definition is:

**Definition 21.** ***(Impermeability condition)***
*There is no fluid flow through the foil surface.*

**Remark 51.** *A consequence of Definition 21 is that the normal velocity, which can be found from the integral of the continuous vortex distribution in Biot-Savart's law in Eq. (2.120), cancel the normal component $U\sin(\alpha)$ of the surrounding velocity field. The proper mathematical statement is that*

$$\frac{1}{2\pi}\int_0^c \frac{\gamma(\sigma)}{\sigma - x}\mathrm{d}\sigma = U\sin(\alpha). \tag{2.122}$$

When considering inviscid flow around an object, D'Alembert's principle states that the lift on the object is exactly zero [4]. In reality, viscous effects like skin friction and other specific boundary layer effects are present. In the study on the forces on a flat plate, the flow was assumed inviscid. This will in general result in infinite solutions for the vortex distribution $\gamma(x)$. However, the Kutta condition enforces a viscous effect in the flow pattern around flat plates by restricting the flow around sharp trailing objects [6]:

**Definition 22.** ***(Kutta condition)***
*There cannot be an infinite change of velocity at the trailing edge.*

A visualization of Kutta condition in for viscous flow around foils compared to ideal fluid flow is illustrated in Fig. 2.18.

**(a)** Zero-lift flow $\gamma(c) \to \infty$ **(b)** Kutta condition $\gamma(c) \equiv 0$

**Figure 2.18:** Kutta condition impose a viscous constraint on the circulation distribution such that $\gamma(c) \equiv 0$ for steady flow in **(b)**. The zero-lift flow **(a)** complies with D'Alembert's principle of zero lift for a submerged body moving in an ideal (inviscid) fluid. From Tufte [17].

**Remark 52.** *As a consequence of Definition 22, the flow at the trailing edge is tangential with the chord line and the circulation at this point is zero. This means that*

$$\gamma(x)\big|_{x=c} = 0. \tag{2.123}$$

From the impermeability condition given in Eq. (2.122) and Kutta condition in Eq. (2.123), Steen [50] states that the solution is

$$\gamma(x') = k \cdot \sqrt{\frac{1-x'}{x'}}, \tag{2.124}$$

where the constant is $k = 2\alpha U$ and $x'$ is the non-dimensional chord position $x/c$.

Tufte [17] showed that the proper circulation distribution for attached flow on flat plate is

$$\gamma(x) = 2\sin(\alpha) U \sqrt{\frac{c-x}{x}}, \tag{2.125}$$

by using the form of Eq. (2.124), which satisfies Definition 22, and solving for Definition 21.

### Uncorrected foil forces in attached flow

From Eq. (2.121) and Eq. (2.125), the uncorrected lift force is calculated as

$$L'_{\text{uncorr.}} = \rho U \int_0^c 2\sin(\alpha) U \sqrt{\frac{c-x}{x}}\, \mathrm{d}x \cdot \cos(\alpha),$$

and the uncorrected drag force for attached flow is

$$D'_{\text{uncorr.}} = \rho U \int_0^c 2\sin(\alpha) U \sqrt{\frac{c-x}{x}}\, \mathrm{d}x \cdot \sin(\alpha).$$

Since the integral $\int_0^1 \sqrt{\frac{1-x}{x}}\mathrm{d}x = \pi/2$, the uncorrected lift, drag and normal forces are

$$L'_{\text{uncorr.}} = \rho\pi U^2 c \sin(\alpha)\cos(\alpha), \tag{2.126a}$$
$$D'_{\text{uncorr.}} = \rho\pi U^2 c \sin(\alpha)^2, \tag{2.126b}$$
$$N'_{\text{uncorr.}} = \rho\pi U^2 c \sin(\alpha), \tag{2.126c}$$

with coefficients $C_{L,\text{uncorr.}} = 2\pi\sin(\alpha)\cos(\alpha) \simeq 2\pi\alpha$ and $C_{D,\text{uncorr.}} = 2\pi\sin(\alpha)^2 \simeq 2\pi\alpha^2$.

### Corrected foil forces

Tufte proposed to correct the magnitude of the foil forces in Eq. (2.126) according to the gains $\bar{C}_L = \frac{2.4}{\pi}$ and $\bar{C}_D = \frac{2}{\pi}$, based on experimental results for flat plates standing orthogonal to inflow. This results in the following force coefficients $C'_L = C_{'L,\text{uncorr.}\bar{C}_L}$

$$C'_{L,\text{TUFTE}} = 2.4\sin(\alpha)\cos(\alpha), \tag{2.127a}$$
$$C'_{D,\text{TUFTE}} = 2.0\sin(\alpha)^2, \tag{2.127b}$$
$$C'_{N,\text{TUFTE}} \simeq 2.0\sin(\alpha). \tag{2.127c}$$

This result was independently found to be almost identical to that of Hoerner given in Eq. (2.117), except that Hoerner properly corrected the drag coefficient with a lower drag than that of flat plates, which has $C_D = 2.0$ at orthogonal inflow [36]. The lift coefficient in Eq. (2.127) is more correct for small angles than Hoerner, but is less correct at greater angles.

**Remark 53.** *The forces in Eq. (2.127) shows an expected qualitative behavior with drag forces always opposing the inflow velocity, and the lift force is twice periodic in the attack angle through a complete revolution. Drag is zero at $\alpha = \{0, \pi\}$ and lift force is zero at $\alpha = \{0, \pi/2, \pi, 3\pi/2\}$.*

Stall considerations was not investigated in [17], but an empiric equation is proposed in the next section as a continuation on the work.

### Stall considerations

The equations for attached flow is accurate until the flow detaches from the suction side of the foil. Characteristics through 180 degrees is rare, but can for instance be found from Sheldahl 1981, Sandial National Laboratories, NACA [54]. The lift for `NACA0012` section, which was shown in Fig. 2.13, is given in Fig. 2.19.

A closer study of the lift coefficient in Fig. 2.19 suggest that the correction parameter $C_{Ln}(\alpha)$ for the uncorrected flat plate forces in Eq. (2.126) can be approximated by

1. $C_{Ln}(\alpha) \simeq 1$, during attached flow until middle of the stall transition,
2. $C_{Ln}(\alpha) \simeq 1 - C_{Ls}$ where $0 < C_{Ls} < 1$, during separated flow, beyond the stall transition.

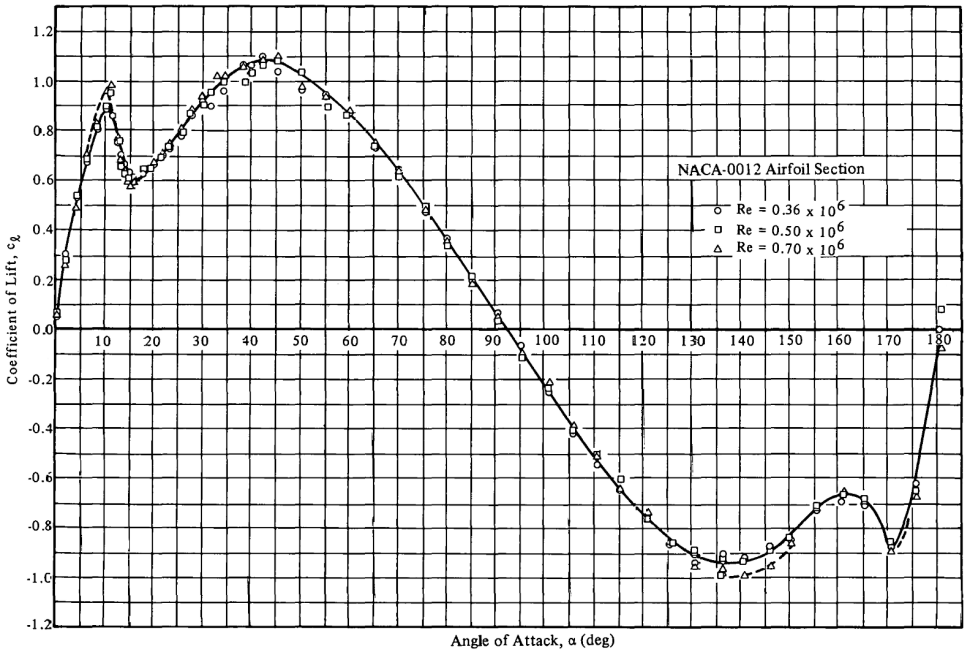


**Figure 2.19:** Lift coefficient for `NACA0012` through 0°–180° attack angles. Facsimile from [54].

A couple of remarks can be made:

**Remark 54.** *For suggestion 1, this corresponds to about 0°–13° and 167°–180° for the `NACA0012` section in Fig. 2.19.*

**Remark 55.** *For suggestion 2, this corresponds to about 13°–167° in Fig. 2.19, assuming symmetry through 0–180°. According to suggestion 2, (the amplitude determined by the peak at 45° in Fig. 2.19)*

**Remark 56.** *If one denote the middle of the stall transition for the angle $\alpha_s$, then Remark 54 and 55 can be summarised as*

$$C_{Ln}(\alpha) \simeq \begin{cases} 1, & 0 \leq \alpha < \alpha_s, \quad \textit{(attached flow)} \\ 1 - C_{Ls}, & \alpha_s \leq \alpha \leq \pi - \alpha_s, \quad \textit{(detached flow)} \\ 1, & \pi - \alpha_s < \alpha \leq \pi, \quad \textit{(attached flow)} \end{cases}$$

In order to smooth the stall transitions such that the lift force approximates the form in Fig. 2.19, a Sigmoid function can be introduced. Let a Sigmoid function with step from 0 to 1 at $x_0$ be denoted as

$$\sigma_k(x, x_0) \triangleq \frac{1}{1 + \exp(-\frac{10}{k}(x - x_0))}, \tag{2.128}$$

where $k$ approximates the width of the step as shown in Fig. 2.20.

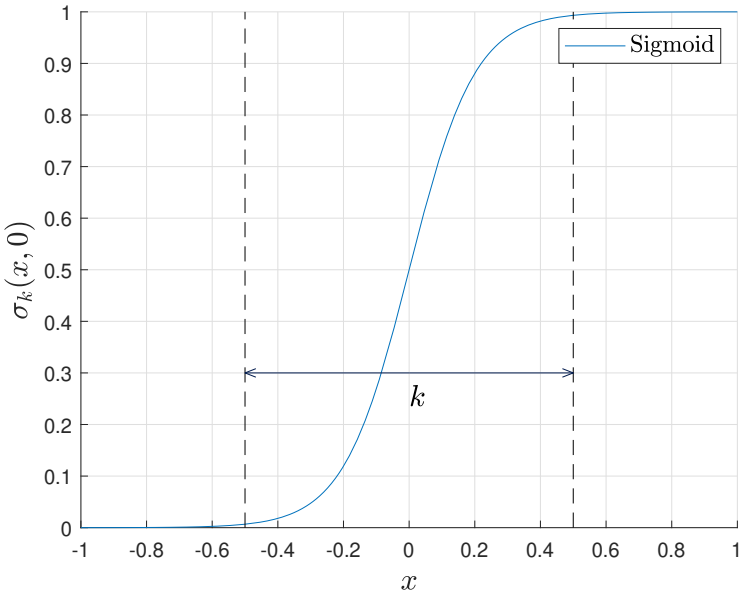


**Figure 2.20:** Sigmoid function as defined in Eq. (2.128). The width is approximately $k$, covering 1–99 % transient.

With the smoothing Sigmoid function in Eq. (2.128) and Remark 56, the corrected lift coefficient $C_{Ln}(\alpha)$ can be approximated with

$$C_{Ln}(\alpha) \triangleq [1 - C_{Ls}\sigma_{k_s}(|\alpha|, \alpha_s) + C_{Ls}\sigma_{k_s}(|\alpha|, \pi - \alpha_s)]. \tag{2.129}$$

Drag forces can be corrected as well by noting that when the flow detaches, the sudden decrease in lift force corresponds to a sudden increase in the drag force such that

$$C_{Dn}(\alpha) \triangleq C_{Ds}[1 + C_{Ls}\sigma_{k_s}(|\alpha|, \alpha_s) - C_{Ls}\sigma_{k_s}(|\alpha|, \pi - \alpha_s)], \tag{2.130}$$

where the coefficient $C_{Ds}$ approximates the effect of decreasing drag as a result of leading edge suction force $S$ and the overall amplitude of the drag force.

Assembling the governing forces on a foil with the approximations in this section, the corrected steady lift and drag forces can be written as

$$C'_{L,\text{corr.}} = 2\pi C_{Ln}(\alpha)\sin(\alpha)\cos(\alpha), \tag{2.131a}$$
$$C'_{D,\text{corr.}} = 2\pi C_{Dn}(\alpha)\sin(\alpha)^2, \tag{2.131b}$$
$$C'_{N,\text{corr.}} = 2\pi\sqrt{C_{Ln}(\alpha)^2 + C_{Dn}(\alpha)^2}\sin(\alpha), \tag{2.131c}$$

where the nonlinear corrections $C_{Ln}(\alpha)$ and $C_{Dn}(\alpha)$ are given by Eqs. (2.129) and (2.130).

An example of the correction for a given foil profile is shown in Fig. 2.21. Here, the program Xfoil, a software program developed by Massachusetts Institute of Technology, was

used to analyse a given foil section. The program uses panel method and a fully coupled viscous/inviscid interaction to evaluate drag, boundary layer transition, and separation on two-dimensional foils. The program can find lift and drag coefficients until slightly above the stall angle. [55]

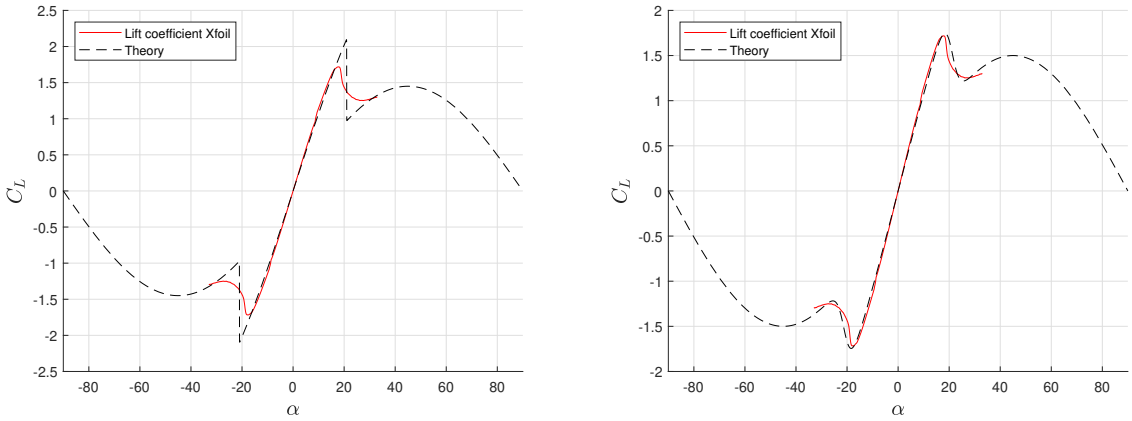


**(a)** Correction without smoothing function. **(b)** Correction with smoothing function.

**Figure 2.21:** Example of correction to the lift coefficient beyond stall angle. The thickness was set to 15% appearing at 20% of the chord line with the foil section determined by Eq. (2.110), and the Reynolds number was set to Re = $10^6$. The lift force was found with Xfoil.

### Center of pressure for attached flow

The center of pressure, or the *hydrodynamic center* on a submerged body, denoted by location $\vec{r}_{\text{c.p.}}$, can be defined according to the following definition:

**Definition 23.** ***(Center of pressure)***
*The center of pressure is the point where the combined pressure forces on a body is located, resulting in a single resultant force exerted through that point.*

The center of pressure on a submerged body can be calculated with the surface integral of the pressure force $\mathrm{d}\vec{F} = -P\mathrm{d}\vec{A}$, where $\mathrm{d}\vec{A}$ is the normal vector. The minus sign is needed since the convention is that the force is considered towards the surface of the body, while $\mathrm{d}\vec{A}$ points outward of the body. The location of the center of pressure is found by integrating

$$\vec{r}_{\text{c.p.}} = \frac{-\oiint_{\partial B} P\vec{r} \cdot \mathrm{d}\vec{A}}{-\oiint_{\partial B} P\, \mathrm{d}\vec{A}}, \tag{2.132}$$

where $\partial B$ denotes the body surface and the pressure $P$ is the local pressure at the surface $\partial B$. For a flat foil with chord length $c$, the center of pressure can be calculated with Eq. (2.132) as

$$x_{\text{c.p.}} = \frac{\int_0^c x\Delta P(x)\,\mathrm{d}x}{\int_0^c \Delta P(x)\,\mathrm{d}x} = \frac{\int_0^c x\gamma(x)\,\mathrm{d}x}{\int_0^c \gamma(x)\,\mathrm{d}x} = 0.25c. \quad \text{(exact)} \tag{2.133}$$

The calculations are not shown here, but by inserting the vortex distribution in Eq. (2.125), the center of pressure is shown to lie at exactly the quarter-chord position of the foil when the flow is attached and Kutta condition (Def. 22) applies.

A common assumption in modeling foils is that the center of pressure is constant at $x'_{\text{c.p.}} = 0.25$. This assumption is valid for modeling e.g. wings. However, this assumption has wrongfully been used in similar cases for wave-propulsion, for instance in an earlier report that models foil propulsion system [21]. Therefore, care is taken to ensure that the empiric model is sufficiently accurate with this model.

### Center of pressure for separated flow

The author did not find any general empiric equations for the center of pressure beyond the stall angle. For small attack angles typically less than 30 degrees, the experimental position for center of pressure for 78 foil shapes can be found in Jacobs et al. pp. 7–45 [13], for Reynolds number $\text{Re} = 3.2 \cdot 10^6$. These values lie at approximately the quarter-chord position for symmetrical foils for small attack angles, in accordance with linear foil theory. An example is shown for the `NACA0015` profile in Fig. 2.22.

In order to determine an empiric equation for the center of pressure, one can argue in the following manner. Denote $\Delta P'$ as the contributing part from the pressure $\Delta P$ determining the position $x'_{\text{c.p.}}$ in Eq. (2.133). The vortex distribution in Eq. (2.125) is accurate at attached flow around $\alpha = 0$, and the inverse (letting $x' \leftarrow 1 - x'$) around $\alpha = \pi$. When the flat plate is standing orthogonal to the inflow, at $\alpha = \pi/2$, the center of pressure should be $x'_{\text{c.p.}} = 0.5$ because of symmetry. The following should be correct from a physical insight:

$$\Delta P'_{\text{u}}: \quad \begin{cases} \Delta P'_{\text{u}}(x') \sim \sin(\alpha)\left(\frac{1-x'}{x'}\right)^{1/2}, & \alpha \simeq 0, \\ \Delta P'_{\text{u}}(x') \sim \text{symmetrical about } x' = 0.5, & \alpha \simeq \pi/2, \\ \Delta P'_{\text{u}}(x') \sim \sin(\alpha)\left(\frac{x'}{1-x'}\right)^{1/2}, & \alpha \simeq \pi. \end{cases} \tag{2.134}$$

From Eq. (2.134), one can argue that a certain monotonic function on the form

$$\sigma(x) = \begin{cases} -1, & x \ll 0, \\ 0, & x = 0, \\ 1, & x \gg 0, \end{cases} \tag{2.135}$$

can be used as a substitute for the exponent in Eq. (2.134) on the form

$$\Delta P'(x) \sim \left(\frac{c-x}{x}\right)^{-\frac{1}{2}\sigma(\text{ssa}(\alpha-\frac{\pi}{2}))}, \tag{2.136}$$

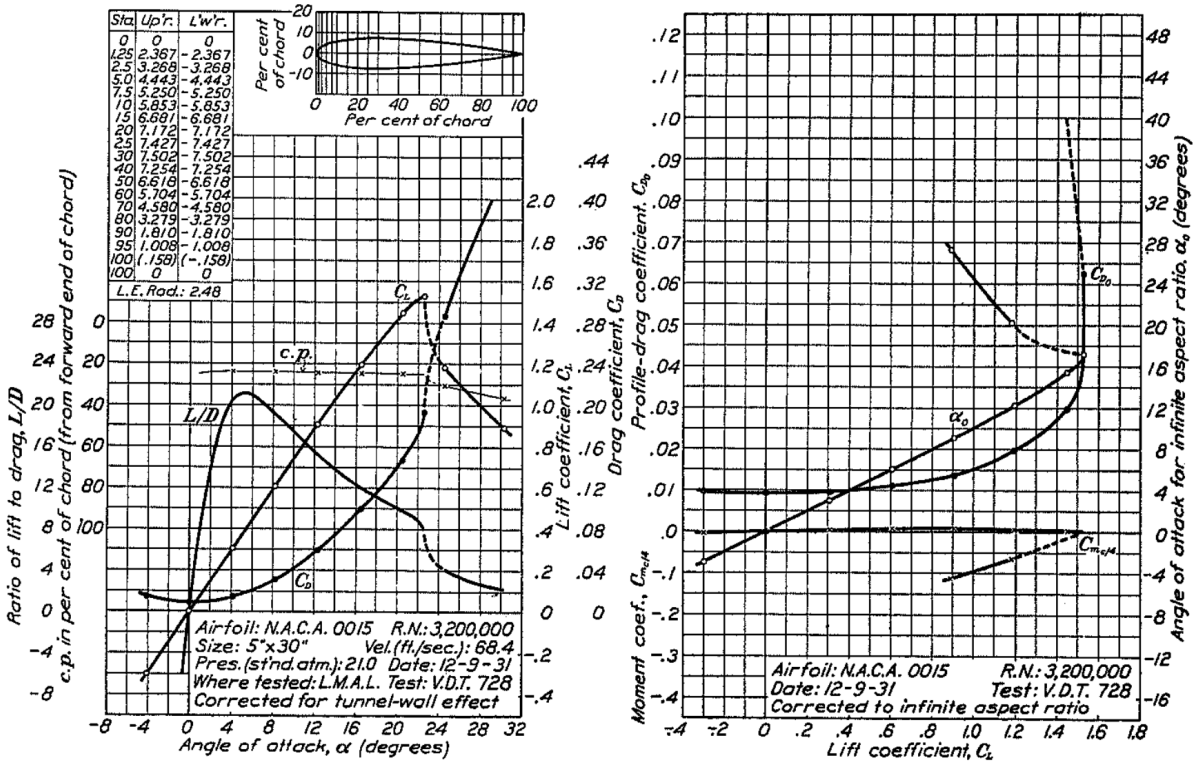


**Figure 2.22:** Experimental airfoil results with `NACA0015` profile showing a variation of the center of pressure with attack angle. Facsimile from NACA [13].

where $\text{ssa}(\cdot)$ is the smallest signed angle used for wrapping angles to the set $(-\pi, \pi]$ [4]. Expression for $\Delta P'$ in Eq. (2.136) do in fact satisfy Eq. (2.134), even when $\alpha = \pi/2$. Calculations show that when using $\Delta P'$ in Eq. (2.136), then

$$x_{\text{c.p.}} = \frac{\int_0^c x \Delta P'(x)\, \mathrm{d}x}{\int_0^c \Delta P'(x)\, \mathrm{d}x} \simeq c \left[ \frac{1}{2} + \frac{1}{4}\sigma(x) \right] \tag{2.137}$$

agrees within 1% accuracy of the numerical value when $\sigma(\cdot)$ is the monotonic function characterized by Eq. (2.135), not to be confused by the Sigmoid function in (2.128).

**Remark 57.** *Even though this approach is somewhat non-physical, the reasoning shows that the center of pressure is expected to start at around the quarter-chord, and move through the half-chord point when the attack angle is at 90 degrees.*

**Remark 58.** *If one can find a suitable approximation for $\sigma(x)$, then a closed-form expression is found for the center of pressure given by Eq. (2.137).*

Interestingly, an experimental test showcasing the center of pressure was indeed found in the literature. In the report by, Mirzaeisefat 2011, pp. 27 [56], the center of pressure was found for flat plates in uniform current. Here, the center of pressure was fitted into two linear segments

with a reasonable agreement with experiments and numerical simulation. The experiments were performed at Reynolds number $\mathrm{Re} = 1.17 \cdot 10^5$, and Mirzaeisefat found the relation

$$0.5 - x'_{\text{c.p.}} = \begin{cases} 0.1012\theta, & \theta \leq 55^\circ \\ 0.381\theta - 0.2745, & \theta > 55^\circ \end{cases}$$

where $\theta = \pi/2 - \alpha$. The above expression can be transferred to

$$x'_{\text{c.p.}} = \begin{cases} 0.1760 + 0.3810\alpha, & \alpha \leq 35^\circ \\ 0.3410 + 0.1012\alpha, & \alpha > 35^\circ \end{cases}. \qquad \text{(experimental fit)} \tag{2.138}$$

**Remark 59.** *There are numerical issues with Eq.* (2.138) *since the numerical approximations introduces discontinuous jumps at* $\alpha = 35^\circ$.

Inspired by the experimental and numerical results in [56], the following model for the center of pressure is proposed:

$$x'_{\text{c.p.}}{}^{\text{TUFTE}} = \begin{cases} \frac{1}{4}, & |\alpha| \leq 0.05\pi \\ \frac{1}{5} + \frac{1}{\pi}|\alpha|, & 0.05\pi < |\alpha| \leq 0.2\pi \\ \frac{1}{3} + \frac{1}{3\pi}|\alpha|, & 0.2\pi < |\alpha| \leq 0.8\pi \\ -\frac{1}{5} + \frac{1}{\pi}|\alpha|, & 0.8\pi < |\alpha| \end{cases}. \tag{2.139}$$

A comparison for the proposed model for center of pressure and the expermental one found in [56] is illustrated in Fig. 2.23. Some remarks follow.

**Remark 60.** *Eq.* (2.139) *is continuous, but not differentiable. A smoother empiric equation might increase the accuracy of the model.*

**Remark 61.** *Eq.* (2.139) *ensures that the center of pressure lies at the quarter-chord position for small attack angles and follows the experimental model in [56] for* $\alpha > 11^\circ$. *Additionally, the center of pressure is at* $x'_{c.p.} = 0.5$ *for* $\alpha = \pi/2$.

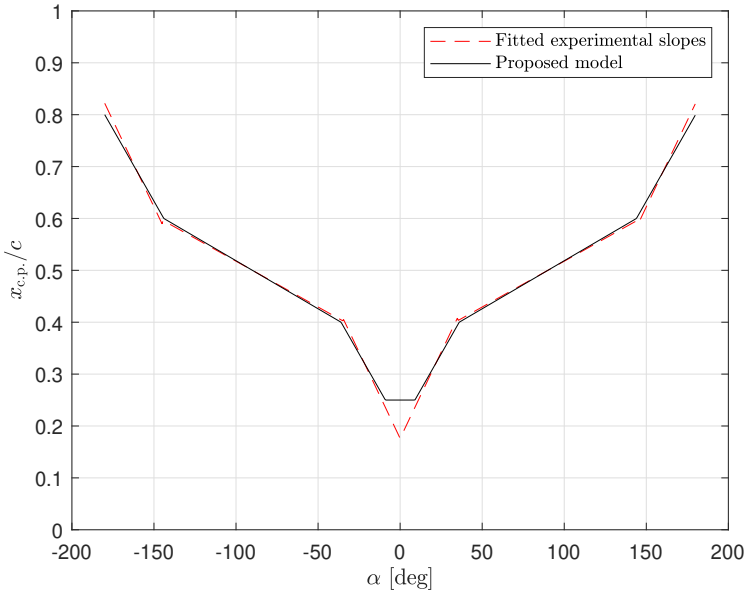


**Figure 2.23:** Approximation of the center of pressure from Eq. (2.139) for flat plate in Reynold number Re = $1.17 \cdot 10^5$. The fitted slope is obtained from [56].

### Three-dimensional corrections of circulatory forces

The lift and drag coefficients that was found in the last sections are correct for two-dimensional flow. Correcting for finite span on the foils involves accounting for the three-dimensional effects of the foil geometry, considering variations in lift and induced drag along the span. Empiric formulae exist in the literature, for instance in [6], [16], [50] and [57]. The three-dimensional effects are incorporated by defining the aspect ratio

$$\Lambda_{\mathrm{F}} \triangleq \frac{S}{c_m} = \frac{2b}{c_m} = \frac{S^2}{A_p}, \tag{2.140}$$

where $S = 2b$ is the span and $A_p$ is the projected area $A_p = Sc_m$, as defined in Sect. 2.6.1. Here, the mean chord length $c_m$ is used. The subscript "F" for foil is conveniently dropped for the rest of the section, $\Lambda = \Lambda_{\mathrm{F}}$.

The three-dimensional lift can be found from strip method by the slender body theory in Sect. 2.4.5. However, it is common to express the lift and drag forces according to

$$L = \frac{1}{2}\rho U^2 A_p C_L, \tag{2.141a}$$

$$D = \frac{1}{2}\rho U^2 A_p C_D, \tag{2.141b}$$

where it is understood that the lift and drag coefficients in this expression are the corresponding three-dimensional coefficients which are related to the two-dimensional one by

$$C_L = C_L'(\alpha) C_{3\mathrm{D}}(\Lambda), \qquad C_D = C_D'(\alpha) C_{3\mathrm{D}}(\Lambda).$$

Prandtl's lifting line theory predicts corrections to the forces in linear foil theory by assuming an elliptic circulation distribution along the span [50]. For this scenario, the lift is corrected according to

$$C_{3\mathrm{D}}^{\mathrm{Prandtl}}(\Lambda) = \frac{\Lambda}{\Lambda + 2}. \tag{2.142}$$

Prandtl's lifting line is valid for foils with elliptic span shape, which is the optimal shape to reduce drag. Anderson however, suggests that a modification to Prandtl's lifting line should be implemented to account for a finite wing with general planform with

$$C_{3\mathrm{D}}^{\mathrm{Anderson}}(\Lambda) = \frac{\Lambda}{\Lambda + 2(1+\tau)}, \tag{2.143}$$

where the induced factor for lift slope $\tau$ is introduced. Anderson reports the usual values for this value as $\tau \in [0.05, 0.25]$ [16]. For larger aspect ratios, Hoerner introduces a practical factor $\ddot{a}$ such that

$$C_{3\mathrm{D}}^{\mathrm{Hoerner}}(\Lambda) = \frac{\ddot{a}\Lambda}{\Lambda + 2\ddot{a}}, \tag{2.144}$$

where the factor should be on the order of $\ddot{a} = 0.9$ [6].

An experimental value on rudders was found by Fujii et al. [57]. Adopting to the framework in this report, the correction is readily

$$C_{3D}^{\text{Fujii}}(\Lambda) = \frac{6.13}{2\pi}\frac{\Lambda}{\Lambda + 2.25}. \tag{2.145}$$

Lastly, Du Cane [58] proposed to use the following correction, valid for $\Lambda > 3$

$$C_{3D}^{\text{Ducane}}(\Lambda) = \frac{\Lambda}{\Lambda + 2}\left(1 - \frac{2}{\Lambda^2}\right). \tag{2.146}$$

A few remarks for the three-dimensional corrections follow:

**Remark 62.** *The correction from Prandtl in Eq.* (2.142) *and from Anderson in Eq.* (2.143) *has the benefit that the when the span becomes infinite, $\Lambda \to \infty$, the values tend to the theoretical values since the correction approaches 1.*

**Remark 63.** *Both the correction from Hoerner in Eq.* (2.144) *and Anderson in Eq.* (2.143) *can be tuned by the parameters ä and $\tau$, respectively.*

**Remark 64.** *The correction from Du Cane given by Eq.* (2.146) *is only valid for aspect ratios above* 3 *and will hence not be considered.*

In the following, the asymptotic benefits and tuning option indicates that one should use Anderson's correction. In order to simplify the correction parameter used for modeling the forces on the foils for wave-propelled USVs, it was decided to combine the asymptotic behavior with the experimental denominator of Fujii such that the following correction was used:

$$C_{3D}^{\text{TUFTE}}(\Lambda) = \frac{\Lambda}{\Lambda + 2.25}. \quad \text{(three-dimensional correction)} \tag{2.147}$$

A comparison of the empiric correction methods is illustrated in Fig. 2.24. The benefit of using Eq. (2.147) is that it is in agreement with other empiric methods and do not need any additional tuning.

### 2.6.4 Non-circulatory forces

The non-circulatory force – the added mass force – is described in this section. This is the same force as described in Sect. 2.4.4 applied for the foils present in wave-propelled USVs. In the following, flat plates will be considered to approximate the forces on a real foil.

#### Added mass force

According to Pettersen [36], the added mass force on a flat plate due to linear acceleration is

$$A' = \frac{1}{4}\rho\pi c_m^2 \dot{U}_n, \tag{2.148}$$

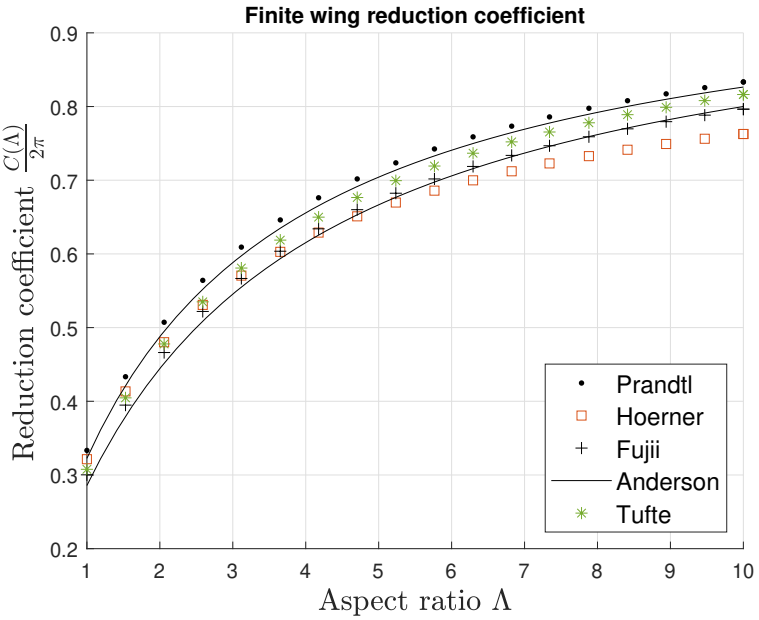


**Figure 2.24:** Comparison of three-dimensional reduction coefficients $C_{3D}(\Lambda)$. The expression for Anderson show suggested bounds, and the expression from Hoerner use $\ddot{a} = 0.9$.

where $\rho$ is the density of water, $c$ is the chord length and $\dot{U}_n$ is the relative acceleration normal to the plate. The force is per span, and acts through the center of the plate.

Expressions for the analytical correction for three-dimensional plates can be found in a dense mathematical report by Meyerhoff [59]. In the report, Meyerhoff calculated the added mass on 10 aspects ratios for flat plates, listed in Tab. 2.4. The added mass on a rectangular wing with width $c$ and span $S$, can be found by

$$A = A'SC_a(\Lambda). \tag{2.149}$$

**Remark 65.** *The reduction coefficients from Meyerhoff for the calculations of added mass needs to be interpolated in order to use it on arbitrary aspect ratios.*

The results of Meyerhoff is similar in nature to the three-dimension correction coefficients given in Sect. 2.6.3. In investigating the expression from Meyerhoff, a simple formula on the form $C_a(\Lambda) = \frac{\Lambda}{\Lambda+a}$ did unfortunately not represent the coefficients in Tab. 2.4 sufficiently. However, a simple least squares optimization for the expression

$$C_a(\Lambda) = \frac{\tilde{\Lambda}}{\tilde{\Lambda} + a}, \tag{2.150}$$

with $\tilde{\Lambda} = \Lambda - \Lambda_0$ was used with great results. When $C_a$ and $\Lambda$ are known from the listing in Tab. 2.4, the parameter $a = a(\Lambda_0)$ was calculated as

$$a(\Lambda_0) = \frac{\tilde{\Lambda} - \tilde{\Lambda}C_a}{C_a} = (\Lambda - \Lambda_0) \cdot \left(\frac{1}{C_a} - 1\right), \tag{2.151}$$

**Table 2.4:** Added mass reduction coefficient for flat plate with chord length $c$ and span $S$. Obtained from analytical values from Meyerhoff [59].

| Aspect ratio $\Lambda = S/c$ | Added mass coefficient $C_a(\Lambda)$ |
|---|---|
| 1.0 | 0.579 |
| 1.25 | 0.642 |
| 1.59 | 0.704 |
| 2.0 | 0.757 |
| 2.5 | 0.801 |
| 4.0 | 0.872 |
| 5.0 | 0.897 |
| 8.0 | 0.934 |
| 10.0 | 0.947 |
| $\infty$ | 1.000 |

which should be constant if Eq. (2.150) is valid. Therefore, the variance $\mathrm{Var}\,[a(\Lambda_0)]$ was minimized. A reasonable agreement was found for a small number of significant digits. The suggested interpolation is

$$C_{\mathrm{a}}^{\mathrm{TUFTE}}(\Lambda) = \frac{\Lambda - 0.26}{\Lambda + 0.29}, \tag{2.152}$$

when incorporating three-dimensional added mass forces for a plate with aspect ratio $\Lambda$. Fig. 2.25 shows the coefficients from Meyerhoff compared to the empiric relation in Eq. (2.152).

**Remark 66.** *The coefficient in Eq. (2.152) is zero for $\Lambda = 0.26$. In case $\Lambda$ approaches below 1, the added mass force can accordingly be found by switching the length and width of the plate.*

Denote the angle of attack for acceleration according to the following definition:

**Definition 24.** ***(Angle of attack for acceleration on propulsion foils for USVs)***
*The angle $\alpha_a$ from the relative fluid acceleration vector to the chord line, in direction from the sharp nominal trailing edge to the round leading edge of the foil, positive rotation into the paper in Fig. 2.14 by the right-hand screw convention.*

**Remark 67.** *From Definition 24, when the foils are attached to the USV by angle $\vartheta$ in the $y^b$-direction of the body (wing span in port/starboard direction) and the mean relative velocity fluid vector field at the foil is $\dot{\mathbf{U}}^b = [\dot{u}_{\mathrm{r}}, \dot{v}_{\mathrm{r}}, \dot{w}_{\mathrm{r}}]^\intercal$, the angle of attack for acceleration is*

$$\alpha_a = \arctan(\dot{w}_{\mathrm{r}}, \dot{u}_{\mathrm{r}}) + \vartheta. \tag{2.153}$$

For a foil mounted for propulsion on a wave-propelled USV, the non-circulatory force is

$$A = \frac{1}{4}\rho\pi c_m^2 S C_{\mathrm{a}}(\Lambda)\sqrt{\dot{u}_{\mathrm{r}}^2 + \dot{w}_{\mathrm{r}}^2}\,\sin(\alpha_{\mathrm{a}}), \tag{2.154}$$

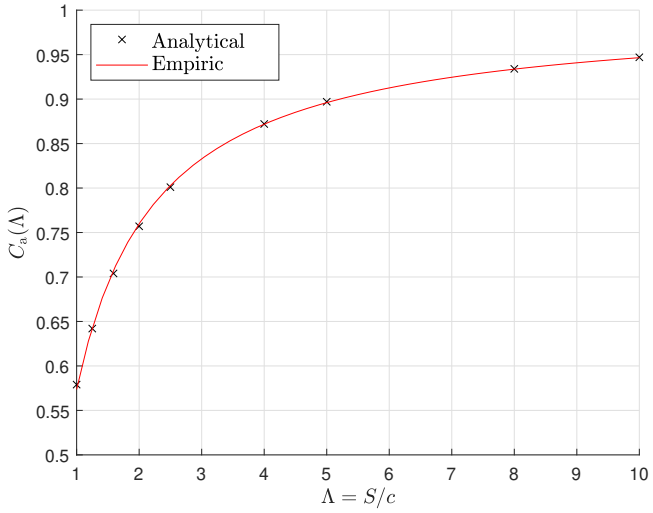


**Figure 2.25:** Reduction coefficient for added mass in flat plates with aspect ratio $\Lambda$. Cross marks the values found analytically by Meyerhoff [59], and the red line indicates the empiric interpolation proposed by Eq. (2.152).

where the force acts normal to the chord line at the midpoint, the correction parameter $C_a$ is given by Eq. (2.152) and the angle of attack for acceleration is given by Eq. (2.153).

### Added moment of inertia

The author found an analytical expression for the added moment of inertia for flat plates given in a table by Pettersen [36], where the source is from Hoarce Lamb [33]. In this analysis, only rotations in the direction of the span are considered. The added moment of inertia for rotation along the half point chord is

$$M'_{\ddot{\vartheta}_r} = \frac{1}{128}\rho\pi c_m^4 \ddot{\vartheta}_r. \tag{2.155}$$

**Remark 68.** *The added moment of inertia in Eq. (2.155) is evaluated at the half-chord point.*

The added moment of inertia for a given point at the chord line can be found by adding the moment of inertia of the rotation in Eq. (2.155) and the moment contribution from the linear added mass force from Eq. (2.148) as

$$\begin{aligned} M'_{\ddot{\vartheta}_r}(d) &= \frac{1}{128}\rho\pi c_m^4 \ddot{\vartheta}_r + d \cdot \frac{1}{4}\rho\pi c_m^2 \dot{U}_n \\ &= \frac{1}{128}\rho\pi c_m^4 \ddot{\vartheta}_r + \frac{1}{4}\rho\pi d^2 c_m^2 \ddot{\vartheta}_r, \end{aligned} \tag{2.156}$$

where $d$ is the distance from the half-chord position to the rotation axis.

**Remark 69.** *The resultant added moment of inertia given by Eq. (2.156) should be considered when finding the dynamics for the foils. However, it is probably sufficient to add the added force*

*in Eq.* (2.148) *as a separate force or moment in the dynamics and only consider the added moment of inertia contributed from Eq.* (2.155).

The added moment of inertia for the complete foil is approximated by the strip method from Sect. 2.4.5 by integrating the sectional added moment of inertia along the span $S$ such that

$$M_{\ddot{\vartheta}_\mathrm{r}} \simeq M'_{\ddot{\vartheta}_\mathrm{r}} S. \tag{2.157}$$

### Damping

No general expression was found for both linear and rotational damping of foils in the literature. Viscous damping, like drag forces, is already incorporated in the circulatory forces given in Sect. 2.6.3. When the rotational dynamics of the foils is derived later in Sect. 3.4, additional damping, which is not yet captured in the analysis, can be taken into account by adding a tuneable rotational damping as shown in this section.

Consider a general mass-spring-damper system on the form

$$m\ddot{x} + b\dot{x} + cx = F\sin(\omega t), \tag{2.158}$$

where $F\sin(\omega t)$ drives the dynamics. According to Fossen [4], the combined viscous and non-viscous damping $b$ is estimated according to relative damping ratio $\zeta$ as

$$\hat{b} = 2\zeta\sqrt{mc}. \tag{2.159}$$

Details about the relative damping ratio can be found in any standard textbook on differential equations.

**Remark 70.** *A practical use for the estimation of damping from Eq.* (2.159) *is only useful when both the mass m and the spring constant c is known and unchanging. In the general case for wave-propelled USVs, this method is not optimal as the springs of such USVs should be switched according to the sea state at the operational area.*

An alternative method for estimating the damping is through a damping period $T_\mathrm{foil}$. The damping can be estimated from the total foil inertia $M_\mathrm{foil} = J_\vartheta + M_{\ddot{\vartheta}_\mathrm{r}}$ according to

$$B_\mathrm{foil} = \frac{M_\mathrm{foil}}{T_\mathrm{foil}}, \tag{2.160}$$

where $T_\mathrm{foil}$ is the damping period to be tuned. Alternatively, by dimensional analysis, the damping moment can be added by the expression

$$B'_\vartheta = \frac{1}{128}\frac{\rho\pi c_m^4}{T_\vartheta}\dot{\vartheta}_\mathrm{r}, \tag{2.161}$$

where the proportional constant $\frac{1}{128}\pi$ is chosen from the added moment of inertia in Eq. (2.155). Here, the damping period is tuned relative to the added inertia from the water, not the foil inertia. The velocity derivative from Eq. (2.161) is $Q_{\dot{\vartheta}} = -\frac{1}{128}\frac{\rho\pi c_m^4}{T}$.

The total damping is found by integrating Eq. (2.161) along the span such that

$$B_{\vartheta} = B'_{\vartheta} S. \tag{2.162}$$

### 2.6.5 Unsteady forces

The circulatory forces derived in Sect. 2.6.3 applies to stationary flow around foils. When there is a step or change in the inflow velocity, there is a delay until the stationary forces is established. This realization lead to the development in classical unsteady foil theory. The Küssner effect looks at the step response in the inflow velocity. Otherwise, the equivalent results from Wagner function in time domain is related to the Theodorsen function in the frequency domain via a Laplace-transformation [2].

In this work, the similar procedure as Lopes et al. [20] was employed. They stated that:

"Recall that the Theodorsen function is only applicable for 2D foils, while the potential lift-drag relation is given for a 3D steady foil where time lag is not taken in consideration. Introducing the Theodorsen function in the drag definition is simply a result of the engineering approach combining 2D and 3D foil theory, and is not meaningful with regard to the phase. It is therefore simply assumed that the drag is in phase with the lift, as this will fulfill the lift-drag relation at all instants in time. Note that since the drag oscillates with double the frequency of the lift, the phrase "in phase with" has the meaning that the drag maxima are in phase with the lift extrema."

A motivation for the need for unsteady thin foil theory can be accompanied with Kelvin's theorem [16]:

**Theorem 2.** ***(Kelvin's circulation theorem)***

*In a barotropic, ideal fluid subject to conservative body forces, the circulation along a closed curve – tracing the same fluid elements – remains constant in time.*

**Remark 71.** *The statement in Theorem 2 is simply that the material derivative of circulation is*

$$\frac{\mathrm{D}\Gamma}{\mathrm{D}t} = 0.$$

According to the Theorem 2, one can follow the fluid particles sliding along the surface of the foil. Since the circulation for this amount of fluid is constant, the overall circulation for the foil experience an "inertia".

If the steady forces are used directly, this will be referred to as quasi-steady forces according to the definition:

**Definition 25.** ***(Quasi-steady forces)***

*When the stationary forces are applied directly without accounting for transient effects, the forces are referred to as quasi-steady forces.*

Theodorsen showed that unsteady circulatory forces on foils depend on the *reduced frequency*

$$k_{\mathrm{f}} \triangleq \frac{c_m}{2}\frac{\omega}{U}, \tag{2.163}$$

which is non-dimensional and amounts to the frequency of oscillation of the foil $\omega$ multiplied with half the chord length divided by the inflow velocity $U$ [14]. The unsteady forces are accounted for by multiplying the complex correction $C_{\mathrm{Th}}(k_{\mathrm{f}})$ – the *Theodorsen function* – into Eq. (2.141):

$$L = \frac{1}{2}\rho U^2 A_p C'_L(\alpha) C_{3\mathrm{D}}(\Lambda) C_{\mathrm{Th}}(k_{\mathrm{f}}), \tag{2.164a}$$

$$D = \frac{1}{2}\rho U^2 A_p C'_D(\alpha) C_{3\mathrm{D}}(\Lambda) C_{\mathrm{Th}}(k_{\mathrm{f}}). \tag{2.164b}$$

**Remark 72.** *In Eq. (2.164), it is understood that the complex correction $C_{\mathrm{Th}}(k_{\mathrm{f}})$ adds an attenuation gain and a phase to the forces. It will be shown that this gain is in the range of $[0.5, 1]$ and the phase is $[0, 15]$ deg.*

When unsteady forces are introduced, an effective angle of attack is experienced:

**Definition 26.** ***(Effective angle of attack on foils)***
*The effective angle of attack $\alpha_e$ is the angle of attack present in Eq. (2.164) as a consequence of the introduced phase from Theodorsen function.*

**Remark 73.** *From Definition 26 and inspired from [2], the effective angle of attack can be calculated as the real value of the attack angle multiplied by the Theodorsen function*

$$\alpha_e = Re\{\alpha C_{\mathrm{Th}}(k_{\mathrm{f}})\}. \tag{2.165}$$

Theodorsen function $C_{\mathrm{Th}}(k_{\mathrm{f}})$ is given by

$$C_{\mathrm{Th}}(k_{\mathrm{f}}) = \frac{H_1^{(2)}(k_{\mathrm{f}})}{H_1^{(2)}(k_{\mathrm{f}}) + jH_0^{(2)}(k_{\mathrm{f}})}, \tag{2.166}$$

where $H_\alpha^{(2)}(k_{\mathrm{f}})$ are Hankel functions, e.g. found in the mathematical handbook [60], that is

$$H_\alpha^{(2)}(x) = J_\alpha(x) - jY_\alpha(x), \tag{2.167}$$

where

$$J_\alpha(x) = \frac{1}{\pi}\int_0^\pi \cos(\alpha\theta - x\sin(\theta))\,\mathrm{d}\theta, \tag{2.168a}$$

$$Y_\alpha(x) = \frac{1}{\pi}\int_0^\pi \sin(x\sin(\theta) - \alpha\theta)\,\mathrm{d}\theta - \frac{1}{\pi}\int_0^\infty (\mathrm{e}^{\alpha\tau} + (-1)^\alpha \mathrm{e}^{-\alpha\tau})\,\mathrm{e}^{-x\sinh(\tau)}\,\mathrm{d}\tau. \tag{2.168b}$$

**Remark 74.** *The second integral in Eq. (2.168b) should be evaluated until infinity, but the integral was truncated to the upper bound $M_\infty = 10$ because of fast convergence properties.*

**Remark 75.** *The complex correction coefficient of Theodorsen function in Eq. (2.166) is not suited for simulation purposes or for developing a real-time model for wave-propelled USVs.*

Because of Remark 75, an approximation for the unsteady effects of the forces on the foils should be investigated. In [2], an analytical approximation which agreed to within 1 % was stated for the frequency domain. However, that transfer function approximation was not rational, thus causing an issue for practical implementation. This issue can be resolved by Padé-approximation, where the real transfer function can be approximated by an increasing degree of rational polynomials [61].

A rational transfer function for Theodorsen function was motivated by a method proposed in [21], where a rational transfer function approximation can be found by least-square fitting by built-in MATLAB [62] functionality with the function `invfreqs`. The degree of the numerator and the denominator can be specified, and the function finds the polynomial coefficients.

An approximated rational transfer function in reasonable agreement with Eq. (2.166) was found with the second order transfer function with the constraint $C_{\text{Th}}(0) = 1$ as

$$C_{\text{Th}}^{\text{2nd}}(s_\text{f}) = \frac{0.5\, s_\text{f}^2 + 0.549\, s_\text{f} + 0.095}{s_\text{f}^2 + 0.848\, s_\text{f} + 0.095}, \tag{2.169}$$

where the Laplace variable is $s_\text{f} = jk_\text{f}$. In terms of the frequency $\omega = 2Uk_\text{f}/c_m$, then

$$C_{\text{Th}}^{\text{2nd}}(s) = \frac{0.5\left(\frac{c_m}{2U}\right)^2 s^2 + 0.549\left(\frac{c_m}{2U}\right) s + 0.095}{\left(\frac{c_m}{2U}\right)^2 s^2 + 0.848\left(\frac{c_m}{2U}\right) s + 0.095} \tag{2.170}$$

describes a velocity-dependent transfer function. The effects of unsteady circulatory forces on a foil can thus be approximated with

$$C_{\text{Th}}(s) \simeq \frac{0.250\left(\frac{U}{c_m}\right) s + 0.190\left(\frac{U}{c_m}\right)^2}{s^2 + 1.696\left(\frac{U}{c_m}\right) s + 0.380\left(\frac{U}{c_m}\right)^2} + 0.500. \tag{2.171}$$

A Bode plot comparison of the analytical Theodorsen function and the approximation from Eq. (2.169) is illustrated in Fig. 2.26. The approximation approximates the magnitude well, but adds additional phase at $k_\text{f} = 0.2$. A better overall frequency-domain approximation can be found when the constraint $C_{\text{Th}}(0) = 1$ is relaxed or higher order polynomials are used. The constraint is kept in order to make sure that the steady forces has unity gain.

**Remark 76.** *When the frequency tends to infinity, Theodorsen's gain correction tends to exactly half. Physically, this predicts that any instantaneous inflow on the foils will cause an immediate non-zero effect.*

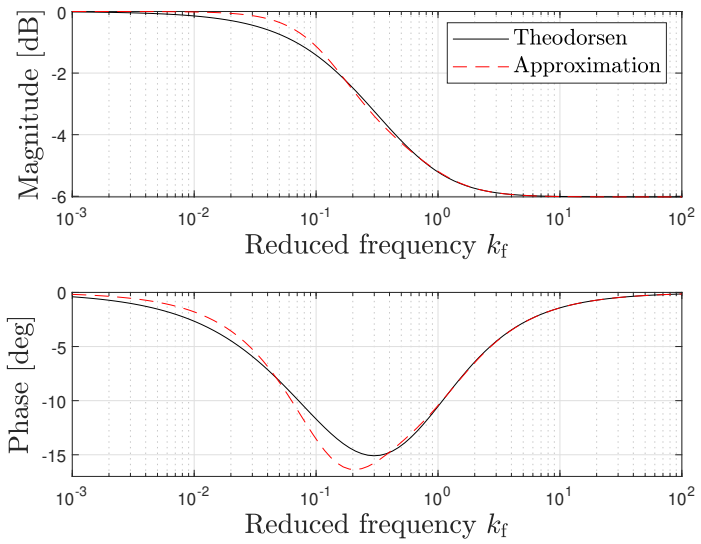


**Figure 2.26:** Bode plot of Theodorsen function and the approximation given by Eq. (2.169). The plot shows the magnitude and phase of the transfer function from quasi-steady circulatory forces to the unsteady circulatory forces on a thin foil expressed at the non-dimensional frequency $k_f$.

**Remark 77.** *By studying the step response of Eq.* (2.171)*, the simple expression*

$$C_{\text{Th}}(s) \simeq \frac{0.636U/c_m}{s + 0.636U/c_m} \qquad \textit{(low frequency approximation)} \tag{2.172}$$

*was found to approximate the step response by minimizing the error between Eq.* (2.171) *and Eq.* (2.172)*, illustrated in Fig. 2.27. By this simplification, this suggest that the effect of unsteady flow is approximated by the time constant $T_f = 1.57c_m/U$, or the non-dimensional time constant $T'_f = 3.14$. Physically, this means that the faster the relative inflow $U$ acts on the foils, the faster the steady forces are reached.*

By the gross simplification found in Remark 77, one can infer that the effective circulatory forces and the effective angle of attack on the foils will approximately follow a decaying exponential with the non-dimensional time constant $T'_f \simeq 3.14$.

### Practical realization of Theodorsen function

For a time domain implementation, the approximation of Theodorsen function from Eq. (2.171) can be implemented by the method in Appendix A.1 by Eq. (A.4) on the form

$$\begin{aligned} \dot{\mathbf{x}} &= \mathbf{A}(t)\mathbf{x} + \mathbf{B}(t)u, \\ y &= \mathbf{C}(t)\mathbf{x} + Du, \end{aligned} \tag{2.173}$$

where the transfer function is $C_{\text{Th}}(s) = \mathbf{C}[s\mathbb{I} - \mathbf{A}]^{-1} + D$ with matrices

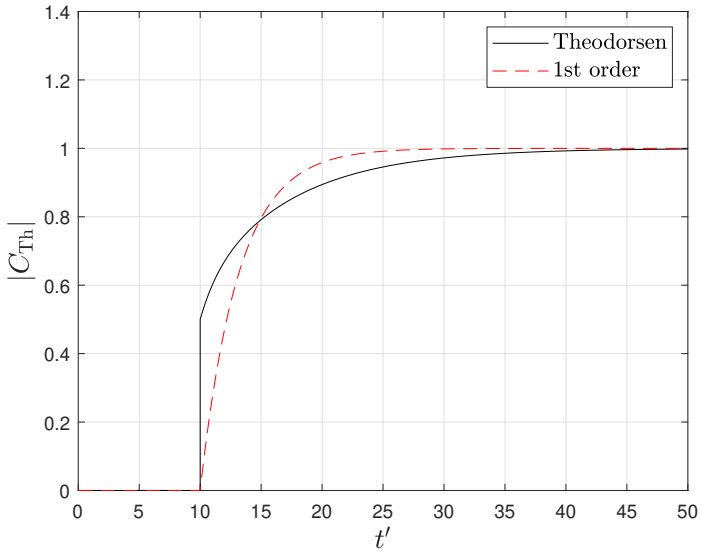


**Figure 2.27:** Magnitude of the step response of unsteady circulatory forces due to Theodorsen's function at the non-dimensional time $t' = (2U/c)t$. The first order step response lags behind Theodorsen's function until about $t' = 5$.

$$\mathbf{A}(U) = \begin{pmatrix} -1.696\left(\frac{U}{c_m}\right) & -0.380\left(\frac{U}{c_m}\right)^2 \\ 1 & 0 \end{pmatrix}, \quad \mathbf{B} = \begin{pmatrix} 1 \\ 0 \end{pmatrix}, \quad \mathbf{C}(U) = \begin{pmatrix} 0.250\left(\frac{U}{c_m}\right) \\ 0.190\left(\frac{U}{c_m}\right)^2 \end{pmatrix}^\top, \quad D = 0.5. \tag{2.174}$$

**Remark 78.** *The system matrix $\mathbf{A}(U)$ is Hurwitz, or stable, for any given $U = U_0 > 0$ since the real part of the eigenvalues are non-positive. However, the filter cannot be proven to be bounded since the matrix depend on the environment, and hence is time-variant.*

### 2.6.6 Wave-propulsion force

The foils considered follow Assumptions 11, 12, 13, 14 and 15. The hydrodynamic forces on the foils are the non-circulatory forces in Sect. 2.6.4, given by the added mass force $A$ in Eq. (2.154) and the circulatory forces, given by the normal force $N$ from Sect. 2.6.5. These forces act normal to the chord line of the foils such that only their magnitude is written.

Denote $A_i$ and $N_i$ as the hydrodynamic forces on foil $i$. The force contributions from a single foil will be shown first. From Newton's law of motion in Eq. (2.13), the forces acting on a foil are

$$\vec{N}_i + \vec{A}_i + \vec{G}_i + \vec{B}_i + \vec{F}_{c,i} = m\ddot{\vec{r}}_{\text{foil},i}, \tag{2.175}$$

where $\vec{r}_{\text{foil}}$ is the position of the center of mass for the foil, $\vec{N}$ is the circulatory normal force, $\vec{A}$ is the added mass force, $\vec{G}$ is gravitational force, $\vec{B}$ is buoyancy force and $\vec{F}_c$ is the constraint force acting from the vehicle to the foil. The propulsion forces from the foils are of interest in the forward direction of the USV. The forward-component of Eq. (2.175) when the vehicle pitches with angle $\theta$, is

$$(N_i + A_i)\sin(\theta + \vartheta_i) + X_{\text{c}} = m\ddot{x}_{\text{foil},i} \simeq 0, \tag{2.176}$$

where the acceleration is negligible at approximately constant forward speed. From Newton's third law of motion, the foil acts on the vehicle with the quasi-steady constraint force $-X_{c,i}$

$$-X_{c,i} = X_{\text{foil},i} = (N_i + A_i)\sin(\theta + \vartheta_i).$$

Inspired by the literature in rudder theory, the foil propulsion force in surge, sway and yaw is

$$\boldsymbol{\tau}_{\text{foil},i} = \begin{pmatrix} (N_i + A_i)(1 - t_{\text{F},i})\sin(\theta + \vartheta_i) \\ 0 \\ 0 \end{pmatrix}, \tag{2.177}$$

where the parameter $t_{\text{F}}$ is introduced as a resistance factor incorporating added resistance due to deflection in the foil angle. In rudder theory, this resistance factor is in the order of $t_{\text{F}} = 0.2$.

#### Total foil propulsion force

The total propulsion force from all of the foils present on the wave-propelled USV can be found by summing the contributions from each foil in Eq. (2.177) such that

$$\boldsymbol{\tau}_{\text{foil}} = \sum_{i=1}^{\#\text{foils}} \begin{pmatrix} (N_i + A_i)(1 - t_{\text{F},i})\sin(\theta + \vartheta_i) \\ 0 \\ 0 \end{pmatrix}. \tag{2.178}$$

**Remark 79.** *If a foil wing is separated such that the each half-span is free to rotate, the foil can be modeled as a single wing since this configuration mainly affects the roll damping.*

## 2.7 Rudder theory

Rudders are vertical control surfaces that produces a steering moment on a marine craft, usually placed at the stern of the vehicle as illustrated in Fig. 2.28. This enables the control of the vehicle's course through water. Experimental values can be found in Fujii et al. [57] and empiric formulae in Kijima et al. [63]. An overview of common models is presented in the chapter "Control Forces and Moments" in the marine craft handbook of Fossen [4]. The article from Liu et al. [64] discuss the impact of the rudder profile on maneuvering characteristics. In the following, the rudder profile is not considered.

In the case of wave-propelled USVs, the rudder is the main control input to steer the vehicle, since the foils mounted underneath or by the side of the hull is passively controlled by springs.

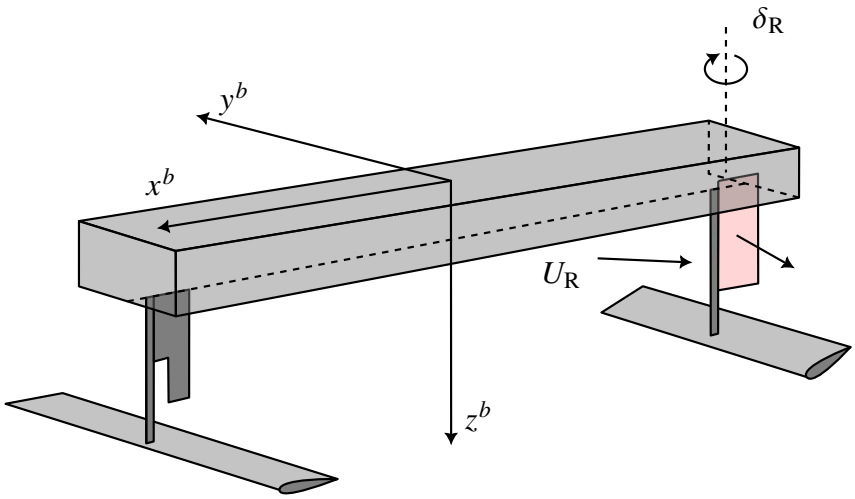


**Figure 2.28:** Typical rudder position and the rudder control angle $\delta_R$.

The rudder is a foil under the assumptions in thin foil theory, see Sect. 2.6. It will experience both circulatory and non-circulatory forces with the rudder inflow velocity $U_R$. However, it is common to only regard the quasi-steady normal force, commonly expressed as

$$F_{NR} = \frac{1}{2}\rho U_R^2 A_R C_N(\Lambda_R)\sin(\alpha_R), \tag{2.179}$$

where $A_R$ is the area of the rudder, the coefficient $C_N(\Lambda_R)$ is the force slope incorporating three-dimensional effects, $\Lambda_R$ is the rudder aspect ratio and $\alpha_R$ is the effective rudder angle [4]. The rudder coefficient $C_N$ equals

$$C_N(\Lambda) = 2\pi \cdot C_{3D}^{\text{Fujii}}(\Lambda) = \frac{6.13\Lambda}{\Lambda + 2.25}. \tag{2.180}$$

The convention is that the rudder angle $\delta$ is defined according to:

**Definition 27.** ***(Rudder angle)***
*A positive rudder angle $\delta$ results in a positive turning rate.*

**Remark 80.** *Per Definition 27, the actual rudder angle $\delta_R$, illustrated in Fig. 2.28, is $\delta_R \equiv -\delta$.*

The following definition for the effective rudder angle can be made:

**Definition 28.** ***(Effective rudder angle)***
*The angle $\alpha_R$ from the rudder velocity inflow $U_R$ to the rudder chord line, in direction from the trailing edge to the leading edge of the rudder, positive rotation about $z^b$-direction, by the right-hand screw convention.*

Assumptions about the rudder inflow is made:

**Assumption 16.** *The rudder inflow is assumed equal to the relative velocity.*

**Remark 81.** *From Remark 80, Definition 28 and Assumption 16, when the rudder is attached with rudder angle $\delta$ and the mean relative rudder inflow is $\mathbf{U}^b = [u_r, v_r, w_r]^\mathsf{T}$, the effective rudder angle is*

$$\alpha_R = \delta - \arctan(v_r, u_r) = -\delta_R - \arctan(v_r, u_r). \tag{2.181}$$

The rudder force and moments in surge, sway and yaw present on a wave-propelled USV can be expressed by

$$\boldsymbol{\tau}_{\text{rudder}} = \begin{pmatrix} F_{NR}(1 - t_R)\sin(\delta_R) \\ F_{NR}(1 + a_H)\cos(\delta_R) \\ F_{NR}\sin(\alpha_R)(x_R + a_H x_H)\cos(\delta_R) \end{pmatrix}, \tag{2.182}$$

where $t_R$ represents a coefficient for additional drag, $x_R$ is the longitudinal coordinate of the rudder, $a_H$ is a rudder force increase factor and $x_H$ is the longitudinal coordinate of the additional force [4]. According to Kijima et al. [63], the coefficient for additional drag can be approximated according to the method proposed by Matsumoto and Suemitsu [65] with

$$t_R = 0.45 - 0.28 C_B, \tag{2.183}$$

where $C_B$ is the USV block coefficient and the non-dimensional interaction force coefficients $a_H$ and $x'_H$ is determined according to Fig. 2.29. A rough estimate was found by the author as

$$a_H^{\text{TUFTE}} \simeq -0.7 + 1.8 C_B, \quad C_B \in [0.5, 0.8], \quad x'_H{}^{\text{TUFTE}} \simeq -5.9 + 7.0 C_B, \quad C_B \in [0.6, 0.8]. \tag{2.184}$$

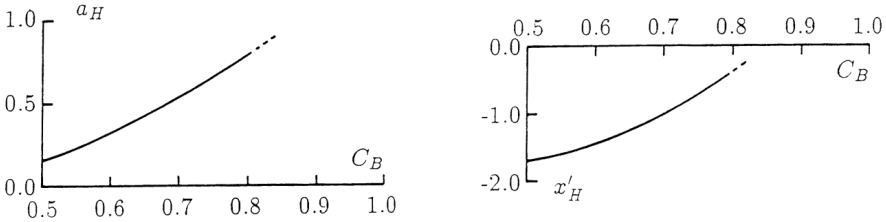


**Figure 2.29:** Interaction force coefficients $a_H$ and $x_H$ where $x'_H = x_H / L_{pp}$. Facsimile from Kijima et al. [63]

# Chapter 3

# Method to model wave-propelled USVs

This chapter describes the developed and proposed method of describing the motion of wave-propelled USVs based on the background theory presented in Chapter 2. The work is based on describing the mean position with a maneuvering model at low frequency ($\omega = 0$) and a seakeeping model for wave-induced motions ($\omega = \omega_e$). A unified time-domain architecture is presented in Sect. 3.1, where the foils are excited by the wave-induced motions. The architecture is presented to comply with more advanced control methods for later investigations.

Fig. 3.1 illustrates the wave-propelled USV AutoNaut on a field trip in Trondheim Fjord. This USV is a case study explored in Chapter 4. The next sections will however describe the general model which should be applicable for a wide range of wave-propelled USVs.

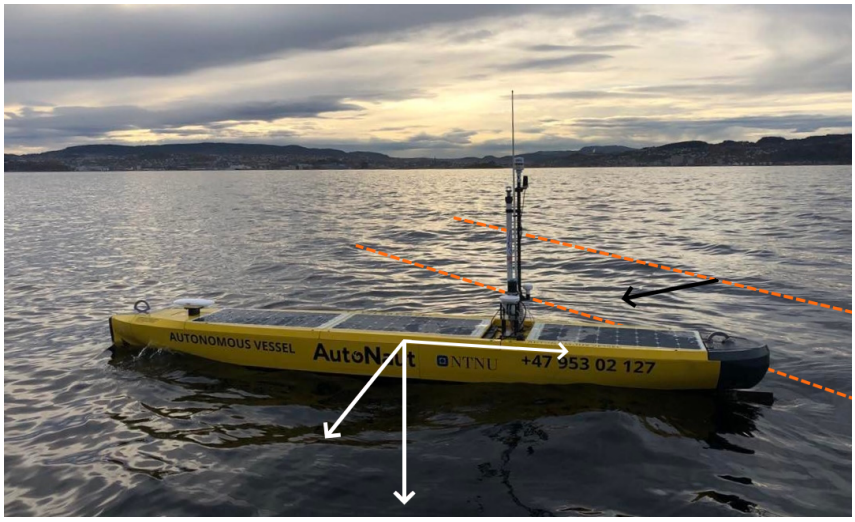


**Figure 3.1:** Example of a wave-propelled USV in near calm sea. The body frame (denoted by white arrows) follows the wave-induced motion of the USV – the seakeeping motion – where the mean position is given by the maneuvering model. The dominating forces by the sea waves can be approximated by a single wave-component (dashed orange lines) with a wave-direction (black arrow).

An overall tuned model of a wave-propelled USV may be expressed by the model $\Sigma$ by a parameter vector $\boldsymbol{\alpha}$, illustrated in Fig. 3.2. The model is a frequency-dependent linear mass-damper-spring system with nonlinear forces which is the function

$$\Sigma(\boldsymbol{\alpha})\big|_{\boldsymbol{\alpha}=\boldsymbol{\alpha}^*} : \mathbb{X} \to \mathbb{X} \left\{ \text{motion of wave-propelled USV given an environmental state } \mathcal{E}. \right. \tag{3.1}$$

Here, the set $\mathbb{X}$ denotes the set of state-space configuration of the wave-propelled USV, including both general positions and velocities of the vehicle body and foils. For sufficient performance, the parameters $\boldsymbol{\alpha}$ is optimized to $\boldsymbol{\alpha}^* \in \mathbb{H}_\alpha$ according to a scalar objective function

$$\boldsymbol{\alpha}^* = \arg\min_{\boldsymbol{\alpha}\in\mathbb{H}_\alpha} f(\boldsymbol{\alpha}), \qquad \text{(optimization problem)} \tag{3.2}$$

where the parameters are assumed bounded in the predetermined set $\mathbb{H}_{\boldsymbol{\alpha}}$. This is the *validation* part of the model. The next section shows how the model given by Eq. (3.1) and Fig. 3.2 can be separated into three separate sub-parts using a unified architecture.

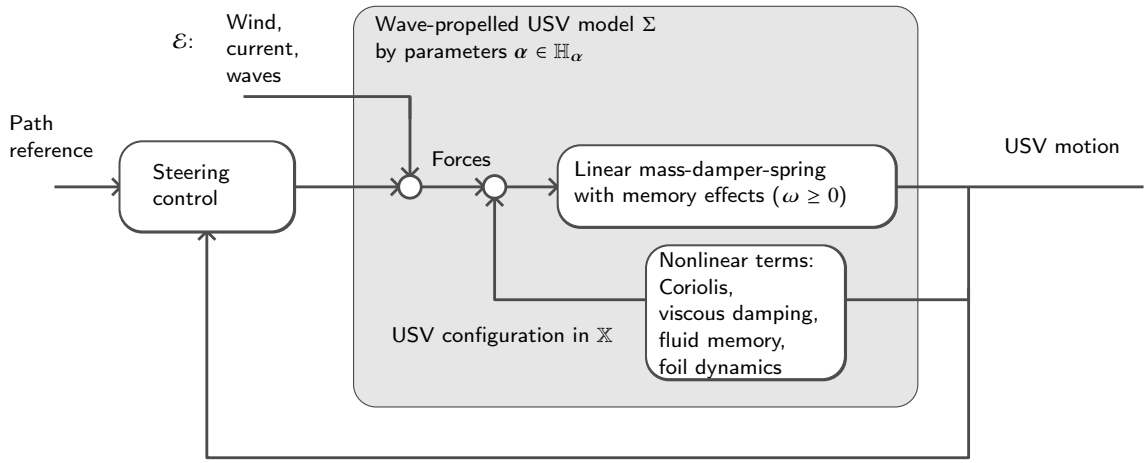


**Figure 3.2:** Overall wave-propelled USV model is denoted by $\Sigma$ and the model parameters is given by the vector $\boldsymbol{\alpha}$. The model is a frequency-dependent linear mass-damper-spring system with nonlinear forces including Coriolis, viscous damping, fluid memory effects and unsteady effects in the foil dynamics. The environmental state is given by the set $\mathcal{E}$, which includes wind, current and waves. The model can furthermore be simulated by a steering controller in order for the USV to follow a desired path.

## 3.1 Overview of model

The proposed model is a unified state-space model in which the maneuvering part and seakeeping part is decoupled from what might be interpreted in Fig. 3.2. The decoupled system is given in Fig. 3.3, which propose to use a superposition of a maneuvering model $\Sigma_1$ and a seakeeping model $\Sigma_2$. In addition, the foil propulsion system $\Sigma_3$ is excited by the joint USV seakeeping motion. The unified model (enclosed by dashed lines in Fig. 3.3) is inspired by the unified state-space model presented by Fossen [39]. The different sub-parts of the model will be described shortly in the next sections. Before the parts are elaborated, a couple of remarks follow.

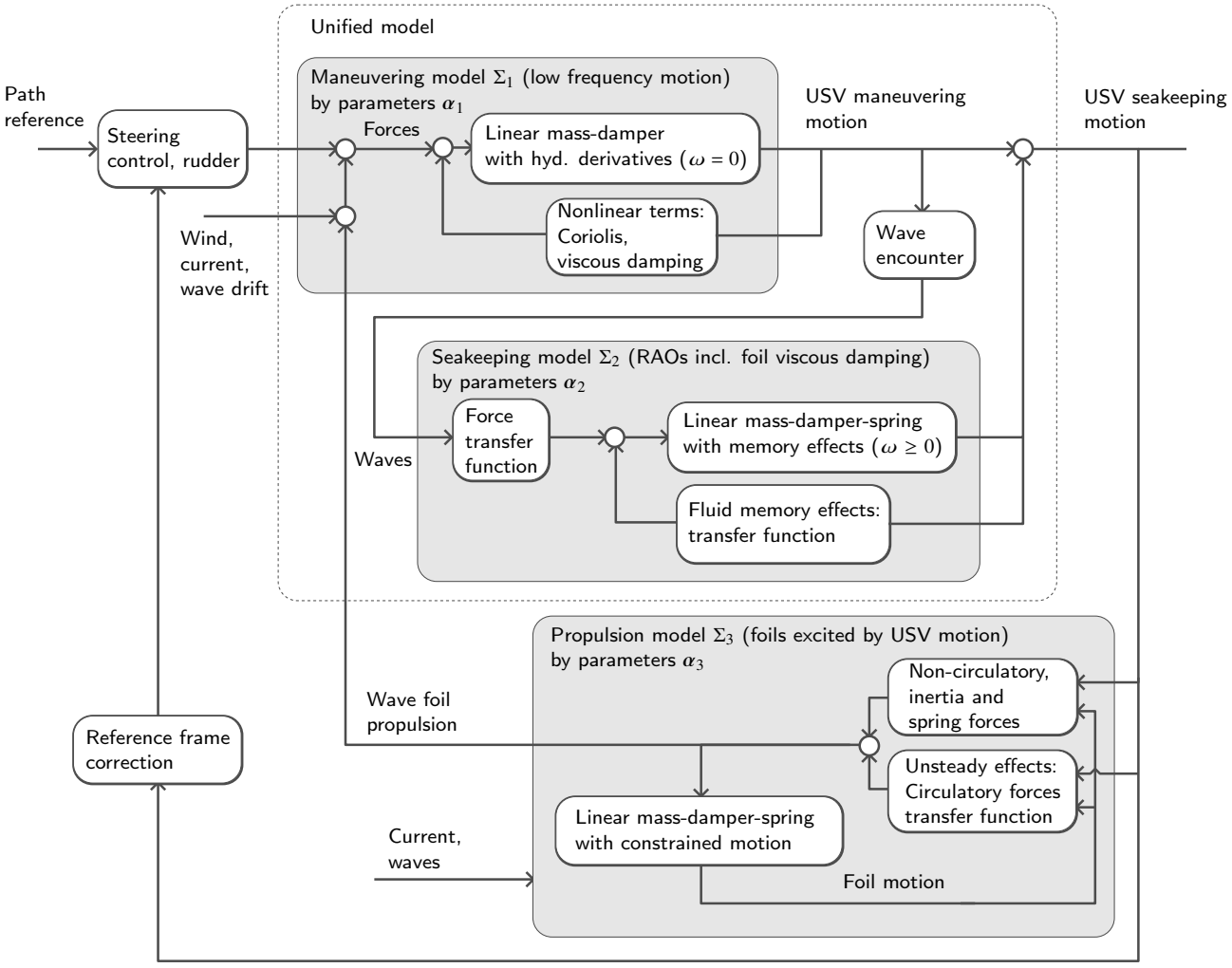


**Figure 3.3:** Proposed linear superposition of maneuvering model and wave frequency model with foil propulsion. Architecture inspired by Fossen [39].

**Remark 82.** *Physical system is conveniently described by an energy-flow description. However, the proposed method illustrated in Fig. 3.3 has an architecture based on the signal-flow formulation. The signal flows in the direction of the arrow, such that the description has unilateral interconnections. Definitions of flow systems can be found in Egeland and Gravdahl [30].*

**Remark 83.** *In a simplified form, the proposed model can be described by a cascade architecture of block-models* $\Sigma_1$–$\Sigma_3$*, see Fig. 3.4.*

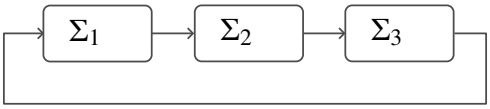


**Figure 3.4:** By the proposed model architecture, wave-propelled USVs may be described by a cascade system as a simplification from Fig. 3.3. A maneuvering model $\Sigma_1$ determines the encountered wave direction $\beta$ and wave encounter frequency $\omega_e$, which drives the wave-induced motion in model $\Sigma_2$ (including viscous foil damping). The joint motion of $\Sigma_1$ and $\Sigma_2$ excites the motion of foils in model $\Sigma_3$, which causes a wave-propelled thrust fed back to the maneuvering model $\Sigma_1$.

The benefits of the developed model architecture is that

1. the governing equations is written with closed-form semi-empiric expressions,
2. non-dimensional expressions is identified to describe a general wave-propelled USV,
3. the equations can be simulated in time-domain supporting further time-domain analysis,
4. the computational cost is reduced in the models by finding and utilizing optimal transfer functions based on non-dimensional expressions.

## 3.2 Maneuvering model in surge, sway and yaw

The maneuvering model is a mass-damper system driven by the Coriolis and centripetal forces and viscous damping shown in Fig. 3.3. The vehicle maneuvering model is denoted as $\Sigma_1$ and the vector $\boldsymbol{\alpha}_1$ the parameters in this model.

The mean position of the wave-propelled USV can solely be described by the slow motion dynamics with hydrodynamic derivatives given in Sects. 2.5.1 and 2.4.4 at motion components

$$\boldsymbol{\nu}_{\text{slow motion}} \simeq [u, v, 0, 0, 0, r]^\top. \tag{3.3}$$

Here, the forces acting on the degrees of freedom $\{1, 2, 6\}$ is second-order forces identified in Sect. 2.4.1. A great analogy for this model is a box sliding on top of a flat surface as illustrated in Fig. 3.5. The box is only able to move with a forward speed $u$, sideways speed $v$ and a yaw rate $r$.

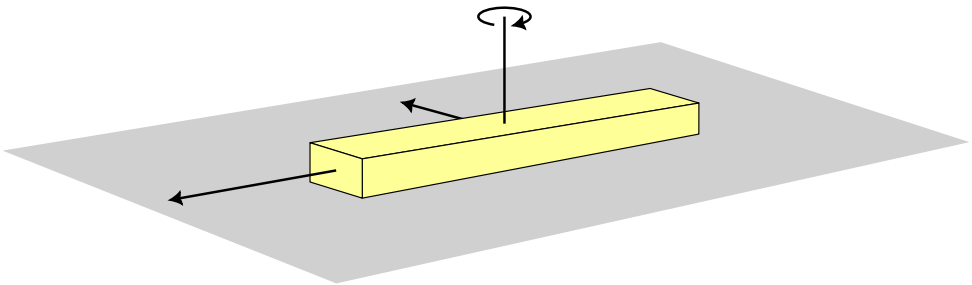

**Figure 3.5:** Maneuvering model as a "box-on-a-table" analogy. The vehicle may slide along a manifold (with friction) given by a flat surface with 3 degrees of freedom for motion given by the arrows. The frame attached to this body is the *seakeeping* frame since the actual vehicle body oscillates around this frame.

From the equations of motion given in Sect. 2.2.3 and inspired by Fossen [4], a 3 DOF dynamical model for the horizontal-plane motion is expressed. Let the position and cardinal heading in this context be denoted by the vector $\boldsymbol{\eta} \triangleq [x^n, y^n, \psi]^\top$ such that the model $\Sigma_1$ is

$$\begin{aligned} \dot{\boldsymbol{\eta}} &= \mathbf{R}_s^n(\psi)\boldsymbol{\nu}, \\ \mathbf{M}\dot{\boldsymbol{\nu}}_{\text{r}} + \mathbf{C}(\boldsymbol{\nu}_{\text{r}})\boldsymbol{\nu}_{\text{r}} + [\mathbf{B}_p + \mathbf{B}_v(\boldsymbol{\nu}_{\text{r}})]\boldsymbol{\nu}_{\text{r}} &= \boldsymbol{\tau}_{\text{wind}} + \boldsymbol{\tau}_{\text{wave2}} + \boldsymbol{\tau}_{\text{foil}} + \boldsymbol{\tau}_{\text{rudd}}. \end{aligned} \tag{3.4}$$

Here, $\boldsymbol{\nu} = \boldsymbol{\nu}_{\text{r}} + \boldsymbol{\nu}_{\text{c}} \triangleq [u, v, r]^\top$ is the body velocity, $\boldsymbol{\nu}_{\text{c}} = [u_c, v_c, 0]^\top$ is the sea current, $\boldsymbol{\nu}_{\text{r}}$ is the relative motion through the water, $\mathbf{M}$ is the mass matrix including zero-frequency hydrodynamic added mass $\mathbf{M}_{\text{A}}(0)$, $\mathbf{C}$ is the Coriolis and centripetal matrix for relative velocities, $\mathbf{B}_p$ is the linear damping matrix, $\mathbf{B}_v$ is viscous damping matrix and $\boldsymbol{\tau}(t) \triangleq [X_2(t), Y_2(t), N_2(t)]^\top$ denotes second-order body forces and moments in degrees of freedom $\{1, 2, 6\}$ caused by wind, waves, foil propulsion system and steering control from rudder, respectively. The rotation matrix is an

active rotation from NED to the seakeeping frame $\{s\}$ following the rotation $\mathbf{R}_z$ in Sect. 2.2.1 as

$$\mathbf{R}_s^n(\psi) = \begin{pmatrix} \cos(\psi) & -\sin(\psi) & 0 \\ \sin(\psi) & \cos(\psi) & 0 \\ 0 & 0 & 1 \end{pmatrix}. \tag{3.5}$$

### Maneuvering model matrices

It is common to decouple the surge dynamics from the sway-yaw system since the surge motion has no effect on the transverse motion of the vehicle under linear theory [44]. The mass matrix including added mass terms written in terms of Bailey et al. [40] and SNAME notation [29], see Sect. 2.4.4, is according to Fossen [4]

$$\mathbf{M} \triangleq \begin{pmatrix} M_{11} & 0 & 0 \\ 0 & M_{22} & M_{26} \\ 0 & M_{62} & M_{66} \end{pmatrix} = \begin{pmatrix} m - X_{\dot{u}} & 0 & 0 \\ 0 & m - Y_{\dot{v}} & mx_{\mathrm{g}} - Y_{\dot{r}} \\ 0 & mx_{\mathrm{g}} - N_{\dot{v}} & J_z - N_{\dot{r}} \end{pmatrix}. \tag{3.6}$$

The linear damping matrix is

$$\mathbf{B}_p \triangleq \begin{pmatrix} B_{11p} & 0 & 0 \\ 0 & B_{22p} & B_{26p} \\ 0 & B_{62p} & B_{66p} \end{pmatrix} = -\begin{pmatrix} X_u & 0 & 0 \\ 0 & Y_v & Y_r \\ 0 & N_v & N_r \end{pmatrix}, \tag{3.7}$$

and the viscous damping is for simplicity taken as a diagonal matrix as

$$\mathbf{B}_v(\boldsymbol{\nu}_{\mathrm{r}}) \triangleq \begin{pmatrix} B_{11v}|u_r| & 0 & 0 \\ 0 & B_{22v}|v_r| & 0 \\ 0 & 0 & B_{66v}|r| \end{pmatrix} = -\begin{pmatrix} X_{|u|u}|u_r| & 0 & 0 \\ 0 & Y_{|v|v}|v_r| & 0 \\ 0 & 0 & N_{|r|r}|r| \end{pmatrix}. \tag{3.8}$$

The Coriolis and centripetal matrix is calculated is

$$\mathbf{C}(\boldsymbol{\nu}_{\mathrm{r}}) \triangleq \begin{pmatrix} 0 & -mr & -mx_g r + Y_{\dot{v}} v_{\mathrm{r}} + Y_{\dot{r}} r \\ mr & 0 & -X_{\dot{u}} u_{\mathrm{r}} \\ mx_g r - Y_{\dot{v}} v_{\mathrm{r}} - Y_{\dot{r}} r & X_{\dot{u}} u_{\mathrm{r}} & 0 \end{pmatrix}. \tag{3.9}$$

In the matrices, $m$ is the vehicle mass, $J_z$ is the moment of inertia in yaw and $x_g$ is the longitudinal position of the center of gravity.

**Remark 84.** *According to Fossen [4]: "It is recommended to use different damping models depending on the regime of control system. In many cases, it is important to include both linear and quadratic damping, since only quadratic damping will cause oscillatory behavior at low speed. The main reason is that linear damping is needed for exponential convergence to zero. For marine craft operating in waves, linear damping will always be present due to potential damping and linear skin friction."*

*Quadratic damping with an exponential blend from linear term can be added on the form*

$$B \sim 0.5u \cdot \mathrm{e}^{-0.5u^2} + 0.05|u|u, \quad \textit{(Blending function for damping)} \tag{3.10}$$

*where $u$ is the velocity.*

### Maneuvering forces and moments

The forces and moments considered in the maneuvering model is the forces and moments identified in Sect. 2.4.2 for degrees of freedom $\{1, 2, 6\}$. The wind force model is described by Eq. (2.76) and the simplification from Remark 30 is utilized to express the wind model

$$\boldsymbol{\tau}_{\text{wind}} \triangleq \begin{pmatrix} X_{\text{wind}} \\ Y_{\text{wind}} \\ N_{\text{wind}} \end{pmatrix} = \frac{1}{2}\rho_{\text{a}}(u_{\text{rw}}^2 + v_{\text{rw}}^2) \begin{pmatrix} -c_x \cos(\gamma_{\text{rw}}) A_{\text{F}_\text{w}} \\ c_y \sin(\gamma_{\text{rw}}) A_{\text{L}_\text{w}} \\ c_n \sin(\gamma_{\text{rw}}) A_{\text{L}_\text{w}} L_{\text{oa}} \end{pmatrix}, \quad \text{(wind forces)} \tag{3.11}$$

where the tuning parameters are the wind coefficients $c_x, c_y, c_n$ and the relative wind speed is $V_{\text{rw}} = \sqrt{u_{\text{rw}}^2 + v_{\text{rw}}^2}$.

The steering forces and moments from the rudder was given in Sect. 2.7. The vector is

$$\boldsymbol{\tau}_{\text{rudd}} \triangleq \begin{pmatrix} X_{\text{rudd}} \\ Y_{\text{rudd}} \\ N_{\text{rudd}} \end{pmatrix} = F_{\text{NR}}(\alpha_{\text{R}}) \begin{pmatrix} -(1 - t_{\text{R}}) \sin(\delta_{\text{R}}) \\ -(1 + a_{\text{H}}) \cos(\delta_{\text{R}}) \\ -\sin(\alpha_{\text{R}})(x_{\text{R}} + a_{\text{HR}} x_{\text{HR}}) \cos(\delta_{\text{R}}) \end{pmatrix}, \quad \text{(steering model)} \tag{3.12}$$

where the rudder normal force $F_{\text{NR}}(\alpha_{\text{R}})$ was given by Eq. (2.179), the added resistance is $t_{\text{R}}$ and the interaction force parameters are $x_{\text{HR}}$ and $a_{\text{HR}}$.

The foil propulsion force is an input from model $\Sigma_3$ shown in Fig. 3.3. The force is only considered in the forward direction, and the developed and proposed model of the foils was derived in Sect. 2.6.6 as

$$\boldsymbol{\tau}_{\text{foil}} \triangleq \begin{pmatrix} X_{\text{foil}} \\ Y_{\text{foil}} \\ N_{\text{foil}} \end{pmatrix} = \sum_{i=1}^{\#\text{foils}} \begin{pmatrix} (F_{\text{NF},i} + A_{\text{F},i})(1 - t_{\text{F},i}) \sin(\theta + \vartheta_i) \\ 0 \\ 0 \end{pmatrix}, \quad \text{(foil propulsion)} \tag{3.13}$$

where the foil normal force $F_{\text{NF}}$ is found from the normal force coefficient in Eq. (2.131) applied to the unsteady lift and drag forces in Eq. (2.164), the added mass force is described by Eq. (2.154), the resistance parameter $t_{\text{F},i}$ should be tuned for each foil number $i$, pitch $\theta$ is described in the wave-induced model $\Sigma_2$ and the foil angle $\vartheta_i$ is found through the model $\Sigma_3$.

For simplicity, the second-order wave forces is set directly to zero

$$\boldsymbol{\tau}_{\text{wave2}} \triangleq \begin{pmatrix} X_{\text{wave2}} \\ Y_{\text{wave2}} \\ N_{\text{wave2}} \end{pmatrix} = \begin{pmatrix} 0 \\ 0 \\ 0 \end{pmatrix}, \quad \text{(wave drift forces)} \tag{3.14}$$

which is a constant estimate for the slow drift wave forces.

**Remark 85.** *If one would like to add second-order wave-drift forces into the simulation to test advanced steering control algorithms, a stable Gauss-Markov process can be implemented to obtain a zero-mean random walk process*

$$\dot{\boldsymbol{\tau}}_{wave2} = -\lambda_{wave2} \boldsymbol{\tau}_{wave2} + \mathbf{w}_{wave2}, \tag{3.15a}$$

$$\tag{3.15b}$$

*where* $\boldsymbol{w}_{wave2} \in \mathbb{R}^3$ *is a zero-mean Gaussian white noise process and* $\lambda_{wave2} > 0$.

### 3.2.1 Parameters in the maneuvering model

Some of the parameters in the maneuvering model $\Sigma_1$ can be measured on the wave-propelled USV, while other parameters cannot be measured directly. The nontrivial parameters needed to describe the maneuvering model might be to naively estimate all the hydrodynamic codes

$$\underbrace{\{X_{\dot{u}}, Y_{\dot{v}}, N_{\dot{r}}, Y_{\dot{r}}, N_{\dot{v}}\}}_{\text{added mass derivatives}}, \underbrace{\{X_u, Y_v, N_r, Y_r, N_v\}}_{\text{linear damping derivatives}}, \underbrace{\{X_{|u|u}, Y_{|v|v}, N_{|r|r}\}}_{\text{viscous damping}},$$

together with the force parameters

$$\underbrace{\{c_x, c_y, c_n\}}_{\text{wind coefficients}}, \underbrace{\{t_{\mathrm{R}}, x_{\mathrm{HR}}, a_{\mathrm{HR}}\}}_{\text{steering parameters}}, \underbrace{\{t_{\mathrm{F},i}\}}_{\text{propulsion parameter}}.$$

This leads to a high number of parameters needed to "tune" the model. A better alternative is to estimate the force parameters directly and formulate an optimization problem for the hydrodynamic derivatives implicitly, using empiric formulae found in the literature. The force parameters can be estimated by:

- Added resistance parameter for rudder, $t_{\mathrm{R}}$ is estimated by the empiric method by Matsumoto and Suemitsu [65] recited in Eq. (2.183).
- Interaction force parameters $x_{\mathrm{HR}}$ and $a_{\mathrm{HR}}$ is estimated by the graphical method by Kijima et al. [63] by Fig. 2.29 or from this author's proposed empirical formulae by Eq. (2.184).
- Wind coefficient parameters is estimated in a range suggested by Fossen, pp. 265 [4] as

  $$c_x \in [0.50, 0.90], \quad c_y \in [0.70, 0.95], \quad c_n \in [0.05, 0.20]. \tag{3.16}$$

  It should be noted that these parameters has been estimated on a case-study on a 5 meter long version of the wave-propelled USV AutoNaut by using the lower limit in Eq. (3.16) [3]. There was no explanation given for this choice. However, this might be reasonable since wave-propelled USVs are small in size, often encompassed as a streamlined body. The following values might thus serve as a rough estimate for the wind coefficients

  $$c_x \simeq 0.50, \quad c_y \simeq 0.70, \quad c_n \simeq 0.05. \tag{3.17}$$

- Added resistance parameter for the foils, $t_{\mathrm{F},i}$ is estimated in the range similar to that found in the rudder literature [57] such that

  $$t_{\mathrm{F}} \in [0.1, 0.3],$$

  which is equivalent to a direct 10–30 % energy loss from the horizontal force components from the foils into propulsive thrust of the vehicle body.

### Estimating hydrodynamic codes from empiric formulae

The hydrodynamic codes can be estimated by the method proposed by Clarke et al. [44] which used a data-driven method to estimate empiric formulae for the lateral hydrodynamic codes of a ship's maneuvering model. Here, the Prime normalization system, which was defined in Sect. 2.1.1, is employed.

The added mass matrix for the 3 DOF maneuvering model expressed with hydrodynamic derivatives written with Prime normalization according to Tab. 2.2 is

$$\mathbf{M}_{\mathrm{A}} = -\begin{pmatrix} X_{\dot{u}} & 0 & 0 \\ 0 & Y_{\dot{v}} & Y_{\dot{r}} \\ 0 & N_{\dot{v}} & N_{\dot{r}} \end{pmatrix} = -\begin{pmatrix} \frac{1}{2}\rho L^3 X'_{\dot{u}} & 0 & 0 \\ 0 & \frac{1}{2}\rho L^3 Y'_{\dot{v}} & \frac{1}{2}\rho L^4 Y'_{\dot{r}} \\ 0 & \frac{1}{2}\rho L^4 N'_{\dot{v}} & \frac{1}{2}\rho L^5 N'_{\dot{r}} \end{pmatrix}, \tag{3.18}$$

and the damping matrix is, for a forward speed $u$, readily

$$\mathbf{B}_p = -\begin{pmatrix} X_u & 0 & 0 \\ 0 & Y_v & Y_r \\ 0 & N_v & N_r \end{pmatrix} = -\begin{pmatrix} \frac{1}{2}\rho L^2 u X'_u & 0 & 0 \\ 0 & \frac{1}{2}\rho L^2 u Y'_v & \frac{1}{2}\rho L^3 u Y'_r \\ 0 & \frac{1}{2}\rho L^3 u N'_v & \frac{1}{2}\rho L^4 u N'_r \end{pmatrix}. \tag{3.19}$$

The hydrodynamic codes for the lateral maneuvering dynamics found in [44] is recited in Tab. 3.2 together with crude strip theory approximations from Journée 1992 [41]. If one knows the actual block coefficient $C_{\mathrm{B}}$, the hydrodynamic codes can be estimated by a set of main particulars $\{L_{\mathrm{d}}, B_{\mathrm{d}}, T_{\mathrm{d}}\} \in \{[0, 2L], [0, 2B], [0, 2T]\} \subset \mathbb{H}_{\alpha,1,1}$ such that

$$\{Y_{\dot{v}}, N_{\dot{r}}, Y_{\dot{r}}, N_{\dot{v}}, Y_v, N_r, Y_r, N_v\}^* = \text{empiric formulae from } \{L_{\mathrm{d}}, B_{\mathrm{d}}, T_{\mathrm{d}}\} \text{ in Tab. 3.2}, \tag{3.20a}$$

$$\{L_{\mathrm{d}}, B_{\mathrm{d}}, T_{\mathrm{d}}\} = \arg \min_{\{L_{\mathrm{d}}, B_{\mathrm{d}}, T_{\mathrm{d}}\} \in \mathbb{H}_{\alpha_{1,1}}} f_{1,1}(\{L_{\mathrm{d}}, B_{\mathrm{d}}, T_{\mathrm{d}}\}). \tag{3.20b}$$

Here, the objective function $f_{1,1}(\{L_{\mathrm{d}}, B_{\mathrm{d}}, T_{\mathrm{d}}\})$ should be a measure of how well the simulation model $\Sigma_1$ fits with experimentally obtained data, for instance by a "tow-and-release"-test.

**Table 3.1:** Lower and upper bounds for the fitting parameters $\boldsymbol{\alpha}_1$ corresponding to the set $\mathbb{H}_{\alpha,1}$ for the maneuvering model $\Sigma_1$.

| Element | Parameter | | Bounds | |
|---|---|---|---|---|
| $\boldsymbol{\alpha}_1[1]$ | $L_{\mathrm{d}}$ | length of maneuvering design model | $[0, 2L]$ | |
| $\boldsymbol{\alpha}_1[2]$ | $B_{\mathrm{d}}$ | breadth of maneuvering design model | $[0, 2B]$ | |
| $\boldsymbol{\alpha}_1[3]$ | $T_{\mathrm{d}}$ | draft of maneuvering design model | $[0, 2T]$ | |
| $\boldsymbol{\alpha}_1[4]$ | $T_1$ | surge period | $[0, 50]$ | [s] |
| $\boldsymbol{\alpha}_1[5]$ | $T_2$ | sway period | $[0, 10]$ | [s] |
| $\boldsymbol{\alpha}_1[6]$ | $T_6$ | yaw period | $[0, 10]$ | [s] |

**Remark 86.** *The eight hydrodynamic derivatives above can be found by only adjusting three design parameters* $\{L_d, B_d, T_d\}$.

**Remark 87.** *One disadvantage with the method proposed above is that a forward operating speed u is needed. The linear derivatives can instead be estimated by time periods* $B_{ii} = M_{ii}/T_i$.

**Table 3.2:** Empirical formulae for acceleration and velocity derivatives in the maneuvering model. From Clarke et al. [44].

| Prime derivative | Crude strip theory | Data-driven optimization |
|---|---|---|
| $-Y'_{\dot{v}}/\pi\left(\frac{T}{L}\right)^2$ | 1 | $1+0.16C_{\mathrm{B}}\frac{B}{T}-5.1\left(\frac{B}{L}\right)^2$ |
| $-Y'_{\dot{r}}/\pi\left(\frac{T}{L}\right)^2$ | 0 | $0.67\frac{B}{L}-0.0033\left(\frac{B}{T}\right)^2$ |
| $-N'_{\dot{v}}/\pi\left(\frac{T}{L}\right)^2$ | 0 | $1.1\frac{B}{L}-0.41\frac{B}{T}$ |
| $-N'_{\dot{r}}/\pi\left(\frac{T}{L}\right)^2$ | $\frac{1}{12}$ | $\frac{1}{12}+0.017C_{\mathrm{B}}\frac{B}{T}-0.33\frac{B}{L}$ |
| $-Y'_{v}/\pi\left(\frac{T}{L}\right)^2$ | 1 | $1+0.40C_{\mathrm{B}}\frac{B}{T}$ |
| $-Y'_{r}/\pi\left(\frac{T}{L}\right)^2$ | $-\frac{1}{2}$ | $-0.5+2.2\frac{B}{L}-0.080\frac{B}{T}$ |
| $-N'_{v}/\pi\left(\frac{T}{L}\right)^2$ | $\frac{1}{2}$ | $0.5+2.4\frac{T}{L}$ |
| $-N'_{r}/\pi\left(\frac{T}{L}\right)^2$ | $\frac{1}{4}$ | $0.25+0.039\frac{B}{T}-0.56\frac{B}{L}$ |

In the case that a forward operating speed is unknown or perhaps zero for a wave-propelled USV, the linear damping can be estimated by the linear time periods $T_i$ for $i = \{1, 2, 6\}$ for the diagonal elements. Comparing with the damping matrix with Prime normalization in Eq. (3.19), the diagonal as well as off-diagonal elements in the linear damping matrix $\mathbf{B}_{\mathrm{p}}$ is proposed to be estimated by

$$\mathbf{B}_p = -\begin{pmatrix} X_u & 0 & 0 \\ 0 & Y_v & Y_r \\ 0 & N_v & N_r \end{pmatrix} = \begin{pmatrix} M_{11}/T_1 & 0 & 0 \\ 0 & M_{22}/T_2 & L\cdot(M_{22}/T_2)(Y'_r/Y'_v) \\ 0 & L\cdot(M_{22}/T_2)(N'_v/Y'_v) & M_{66}/T_6 \end{pmatrix}. \tag{3.21}$$

Here, $M_{ii}$ is the diagonal mass elements from Eq. (3.6), $T_i$ is the linear time period and the prime normalized ratios $(N'_v/Y'_v)$ and $(Y'_r/Y'_v)$ is found from Tab. 3.2.

With the above estimation of linear dampingAn approximation for the surge added mass was found in Brix 1993 [66] on the form

$$X_{\dot{u}} = \frac{m}{\pi\sqrt{\frac{L^3}{\nabla}}-14}, \tag{3.22}$$

where care should be considered when using this approximation on small USVs.

### Tuning parameters

The maneuvering model can be described by the parameter vector

$$\boldsymbol{\alpha}_1 \triangleq \{L_{\mathrm{d}}, B_{\mathrm{d}}, T_{\mathrm{d}}, T_1, T_2, T_6\},$$

and the optimization problem

$$\boldsymbol{\alpha}_1^* = \arg \min_{\boldsymbol{\alpha}_1 \in \mathbb{H}_{\alpha,1}} f(\boldsymbol{\alpha}_1). \tag{3.23}$$

**Remark 88.** *It is left as a future work to determine an appropriate objective function for Eq.* (3.23).

### 3.2.2 Wave encounter frequency

When the vehicles moves, the relative encounter speed between the surface waves and the vehicle should be considered in order to proceed with seakeeping models. The appropriate method is to utilize the wave encounter frequency $\omega_e$ found by a proper Doppler-shift calculated from the speed of the vehicle $U = \sqrt{u^2 + v^2}$ and the encounter angle $\beta$ as

$$\omega_e = |\omega - kU\cos(\beta)| = \left|\omega - \frac{\omega^2}{g}\sqrt{u^2 + v^2}\cos(\beta)\right|, \qquad \text{(wave encounter frequency)} \tag{3.24}$$

where the deep water relationship is utilized from Sect. 2.3.3. The absolute value is needed in the general case if the speed of the vehicle exceeds the phase velocity of the waves [4].

The wave encounter frequency can also be defined by the non-dimensional number $\alpha$ with

$$\alpha: \quad \omega_e \equiv \alpha\omega, \tag{3.25}$$

which will be used in the response amplitude operators in Sect. 3.3. The following remark relates the parameter $\alpha$ to the Froude number, wave number $k$ and the wave encounter angle $\beta$:

**Remark 89.** *Given the Froude number $Fn = U/\sqrt{gL}$ defined in Eq.* (2.32) *and the Doppler shift in Eq.* (3.24)*, the parameter $\alpha$, as defined in Eq.* (3.25)*, is found to be*

$$\alpha \triangleq \left|1 - Fn\sqrt{kL}\cos(\beta)\right|. \tag{3.26}$$

## 3.3 Wave induced motion in heave, pitch and roll

Wave-induced perturbations, commonly denoted by $\boldsymbol{\xi}$ in the seakeeping coordinates $\{s\}$, is often modeled as a linear mass-damper-spring system with frequency-dependent terms which was shown in Sect. 2.5.1 [4]. In Fig. 3.3 the wave-induced model is denoted as $\Sigma_2$. The model is driven by wave elevation at the encounter frequency $\omega_e$ found from the Doppler shift calculated from Eq. (3.24), which is found by the mean USV motion from model $\Sigma_1$ given by Eq. (3.4). The degrees of freedom for the wave-induced perturbations considered in this work is heave, roll and pitch motion

$$\delta\boldsymbol{\nu}_{\text{wave frequency motion}} \simeq [0, 0, w, p, q, 0]^\top. \tag{3.27}$$

The overall USV motion can be found by adding the slow motion components from Eq. (3.3) and the wave frequency components from Eq. (3.27). A physical analogy for the wave-induced motions is illustrated in Fig. 3.6.

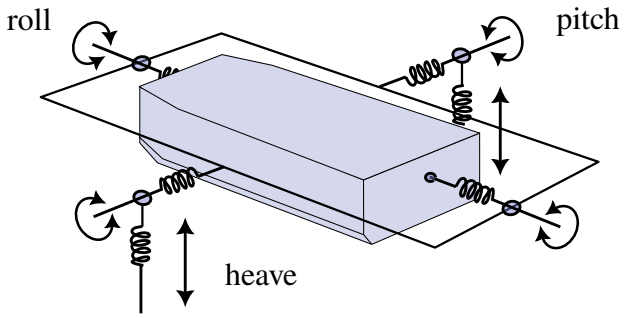


**Figure 3.6:** Wave-induced motion can be interpreted as a linear spring-damper-system in the degrees of freedom heave, roll and pitch. Here, the motion is illustrated with a rigid frame with both linear and torsion springs. The motions can be interpreted somewhat decoupled.

Denote in this context the 3 DOF coordinates in heave, roll and pitch as $\boldsymbol{\xi} \triangleq [z^n, \phi, \theta]^\top$. The wave-induced motion for a general wave-propelled USV will be shown in this section to be described by the model

$$\begin{aligned} \mathbf{M}_{\text{rao}}(\infty)\ddot{\boldsymbol{\xi}} + \mathbf{B}_{\text{rao}}(\infty)\dot{\boldsymbol{\xi}} + \boldsymbol{\mu}_r + \mathbf{C}_{\text{rao}}\boldsymbol{\xi} &= \boldsymbol{\tau}_{\text{wave1}}, \\ \dot{\mathbf{x}} &= \mathbf{A}_r\mathbf{x}_r + \mathbf{B}_r\dot{\boldsymbol{\xi}}, \\ \boldsymbol{\mu}_r &= \mathbf{C}_r\mathbf{x}_r, \end{aligned} \tag{3.28}$$

which incorporates a state-space approximation for the fluid memory effects $\boldsymbol{\mu}_r$ as described in Sect. 2.5.3. Here, the mass matrix including added mass is $\mathbf{M}_{\text{rao}}(\omega)$, the linear and viscous damping matrix is $\mathbf{B}_{\text{rao}}(\omega)$ and the linear restoring matrix is $\mathbf{C}_{\text{rao}}$. Since this theory is linear, there is no Coriolis and centripetal matrix. The matrices $\mathbf{A}_r$, $\mathbf{B}_r$, $\mathbf{C}_r$ represents a state-space approximation of the fluid memory effects. The equations of motion for Eq. (3.28) in the frequency domain is

$$\mathbf{M}_{\text{rao}}\ddot{\boldsymbol{\xi}} + \mathbf{B}_{\text{rao}}(\omega)\dot{\boldsymbol{\xi}} + \mathbf{C}_{\text{rao}}\boldsymbol{\xi} = \boldsymbol{\tau}_{\text{wave1}}. \tag{3.29}$$

The response amplitude operator from wave elevation to wave-induced motion in heave, roll and pitch for a wave-propelled USV is hard or perhaps impossible to predict analytically in the general case. This is due to the presence of foils causing added mass and viscous damping. Also, if numerical methods is used, foils need to be added if the response amplitude operators (RAOs) is to be found by a numerical program, e.g. WAMIT.

### Semi-empirical RAOs from monohull geometry

In this work approximations for the seakeeping model is found via monohull geometries according to the method proposed by Jensen et al. [25]. Furthermore, the data-driven method proposed by Mounet et al. [67] is used to determine the parameters for the monohull geometries based on operational data in . A sketch of the simplified geometries is illustrated in Fig. 3.7 and the main particulars for the simplified geometry is denoted with a tilde notation, e.g. $\tilde{L}, \tilde{B}, \tilde{T}$. The models should provide sufficient engineering accuracy to simulate the wave-induced motions for a wave-propelled USV. In the following, the tilde notation is dropped until

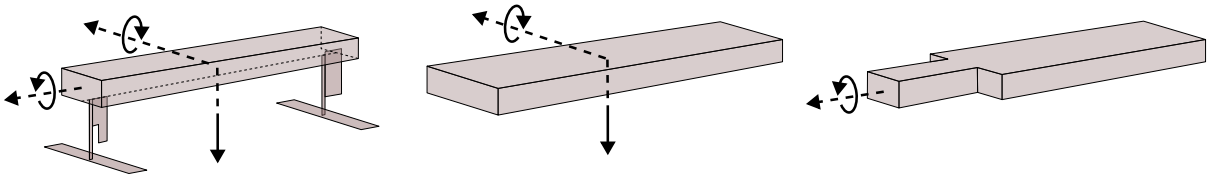

(a) Wave-propelled USV, actual geometry

(b) Heave and pitch, simple monohull geometry

(b) Roll model, altered monohull geometry

**Figure 3.7:** Simplified monohull geometries used to describe seakeeping motions. Heave and pitch dynamics is captured by the model of a rectangular box, whereas roll motion is described by a slightly more complex shape. Monohull geometries inspired by Jensen et al. [25].

According to Jensen [23], heave and pitch motion is coupled and driven by the amplitude of the encountered wave elevation $\zeta_{\text{a}}\cos(\omega_{\text{e}}t)$. Here, the wave encounter frequency $\omega_{\text{e}}$ is calculated from the Doppler shift in Eq. (3.24). The coupled motion is, according to Jensen, in a regular wave encounter frequency $\omega_{\text{e}}$, wave number $k$, wave amplitude $\zeta_{\text{a}}$ and wave direction $\beta$

$$M_{33}\ddot{z}^n + B_{33}(\omega_{\text{e}})\dot{z}^n + C_{33}z^n + B_{35}\dot{\theta} + C_{35}\theta = Z_0(k,\beta)\zeta_{\text{a}}\cos(\omega_{\text{e}}t) - Z_{\dot{w}}(\omega_{\text{e}})\dot{w}, \tag{3.30a}$$

$$M_{55}\ddot{\theta} + B_{55}(\omega_{\text{e}})\dot{\theta} + C_{55}\theta + B_{53}\dot{z}^n + C_{53}z^n = M_0(k,\beta)\zeta_{\text{a}}\sin(\omega_{\text{e}}t) - M_{\dot{q}}(\omega_{\text{e}})\dot{q}. \tag{3.30b}$$

Here, $M_{ii}$ is the mass elements, $B_{ij}$ is the damping in DOF $i$ caused by motion in DOF $j$ and $Z_0 = Z_0(k,\beta)$ and $M_0 = M_0(k,\beta)$ is the forcing functions found in the block "Force transfer function" in Fig. 3.3 which is driven by wave elevations $\zeta_{\text{a}}\cos(\omega_{\text{e}}t)$ and $\zeta_{\text{a}}\sin(\omega_{\text{e}}t)$ respectively.

The roll motion is decoupled from the other motions and from the altered monohull geometry in Fig. 3.7 on the form

$$M_{44}\ddot{\phi} + B_{44}(\omega_e)\dot{\phi} + C_{44}\phi = K_0(k,\beta)\zeta_a \cos(\omega_e + \epsilon_\phi), \tag{3.31}$$

where $K_0 = K_0(k,\beta)$ is the forcing function from wave elevation with the phase $\epsilon_\phi$.

The frequency response in heave and pitch can be derived analytically on a homogeneously loaded box-shaped vessel by using strip theory methods discussed in Sect. 2.4.5. According to Jensen et al. [25], one can decouple Eqs. (3.30a) and (3.30b) to simplify the analysis. By enforcing these motions as a separate harmonic oscillator with common relative damping ratio and natural frequency, Jensen et. al showed how heave and pitch can be expressed by neglecting coupling terms and assuming a constant sectional added mass equal to the displaced water. Written in terms of coordinates defined in Sect. 2.1.2, the dynamics of heave and pitch are

$$2\frac{kT}{\omega^2}\ddot{z}^n + \frac{A(\omega_e)^2}{kB\alpha^3\omega}\dot{z}^n + z^n = \frac{Z_0(k,\beta)}{C_{33}}\zeta_a \cos(\omega_e t), \tag{3.32a}$$

$$2\frac{kT}{\omega^2}\ddot{\theta} + \frac{A(\omega_e)^2}{kB\alpha^3\omega}\dot{\theta} + \theta = \frac{M_0(k,\beta)}{C_{55}}\zeta_a \sin(\omega_e t). \tag{3.32b}$$

Here, the wave number is $k$, the ratio between wave encounter frequency and the wave frequency is defined by the parameter $\alpha$ from Eq. (3.25) and the sectional hydrodynamic damping is modelled by the ratio of incoming and diffracted waves through the following approximation

$$A \triangleq 2\sin\left(\frac{1}{2}kB\alpha^2\right)\exp\left(-kT\alpha^2\right), \tag{3.33}$$

where $B$ is the breadth of the monohull box and $T$ is the draft of the box.

The sectional hydrodynamic damping for the box monohull geometry given in Fig. 3.7 is according to Yamamoto et al. [68] and Jensen [23], rewritten to the notation in this report,

$$b(\omega) = \frac{\rho g^2}{\omega^3}\left[2\sin\left(\frac{\omega^2}{2g}B\right)\exp\left(-\frac{\omega^2}{g}T\right)\right]^2, \tag{3.34}$$

where the total damping for pitch and heave is related to the sectional damping in Eq. (3.34) by a geometrical constant found by the strip method such that $B_{33}(\omega) = C_{\text{geo},3}b(\omega)$ and $B_{55}(\omega) = C_{\text{geo},5}b(\omega)$ by integrating the sectional damping along the hull.

**Remark 90.** *The sectional damping from Yamamoto et al. [68] given in Eq. (3.34) is related to the expression used in Jensen et al. [25] in Eq. (3.33) by the relation*

$$b(\omega) = \frac{\rho g^2}{\omega^3}A(\omega)^2. \tag{3.35}$$

**Remark 91.** *The RAOs in heave and pitch can be found by applying the Laplace transform. Denote $\bar{\xi}_i$ as either pitch or heave amplitude and $F_i$ the proportional gain. Let $RAO_i(s)$ denote the response amplitude operator between $\zeta_a$ and $\bar{\xi}_i$. From Eq. (3.32) the RAOs are*

$$RAO_i(s) = \frac{\bar{\xi}_i}{\zeta_a}(s) = \frac{F_i}{2\frac{kT}{\omega^2}s^2 + \frac{A^2}{kB\alpha^3\omega}s + 1}, \quad \text{for } i = 3,5 \tag{3.36}$$

*where $\omega$ is the wave frequency and the Laplace variable should be evaluated at the wave encounter frequency $\omega_e$. The frequency response at the encounter frequency, $s = j\omega_e$, is thus*

$$RAO_i(\omega_e) = \frac{F_i}{1 - 2kT\alpha^2 + j\frac{A^2}{kB\alpha^2}}, \quad for\ i = 3, 5, \tag{3.37}$$

$$|RAO_i(\omega_e)| = \frac{F_i}{\sqrt{(1 - 2kT\alpha^2)^2 + \left(\frac{A^2}{kB\alpha^2}\right)^2}}, \quad for\ i = 3, 5. \tag{3.38}$$

**Heave motion**

The terms in heave equation of motion has been identified from Eq. (3.32a), freely written to comply with the notation in this report as

$$M_{33}\ddot{z}^n + B_{33}(\omega_e)\dot{z}^n + C_{33}z^n = Z_0\zeta_a \cos(\omega_e t), \tag{3.39}$$

where the elements was identified as

$$M_{33} = 2\nabla\rho, \tag{3.40a}$$

$$B_{33}(\omega_e) = Lb(\omega_e) = L\frac{\rho g}{k\omega_e}\frac{A(\omega_e)^2}{\alpha^2}, \tag{3.40b}$$

$$C_{33} = \rho g LB. \tag{3.40c}$$

Here, the displaced volume is $\nabla = LBT$ since the block coefficient for the simplified box geometry is $C_B \equiv 1$ and it is recognized that $C_{geo,3} = L$. The forcing function was identified from Jensen et al. [25] on the form

$$Z_0 = C_{33}\,\mathrm{sinc}\,(\sigma)\,\kappa f, \tag{3.41}$$

where $\mathrm{sinc}(\sigma) \equiv \sin(\sigma)/(\sigma)$ is the sinc function with $\mathrm{sinc}(0) = 1$. Here, $\sigma \triangleq \frac{1}{2}k_e L$ is inspired from the notation in Fossen [4], $\kappa \triangleq e^{-k_e T}$ is Smith's correction factor and $k_e \triangleq |k\cos(\beta)|$ is the effective wave number. Also, the function

$$f = \sqrt{(1 - kT)^2 + \left(\frac{A^2}{kB\alpha^3}\right)^2}. \tag{3.42}$$

According to Jensen [23], "... the Smith correction factor arises because the dynamic pressure decays exponentially with respect to the vertical distance from the free surface contrary to the linear increase of the hydrostatic pressure." This can be inferred from the linear wave potential developed in Sect. 2.3.3.

**Remark 92.** *According to the simplified forcing function in Eq. (3.41), the force transfer function from wave elevation to heave motion is zero when $\sin(\sigma) = \sin(\frac{1}{2}k_e L) = 0$, or equivalently when the argument is $\frac{1}{2}k_e L = \frac{L}{\lambda_e}\pi = \pi n$ where $n$ is a whole number. As a result, the forcing function is zero whenever the box tuning length $L$ is a multiplum of the effective wave length $\lambda_e$.*

### Pitch motion

The terms in pitch equation of motion has been identified from Eq. (3.32b), freely written to comply with the notation in this report as

$$M_{55}\ddot{\theta} + B_{55}(\omega_e)\dot{\theta} + C_{55}\theta = M_0\zeta_a \sin(\omega_e t), \tag{3.43}$$

where the elements was identified according to

$$M_{55} = 2\rho\nabla T \mathrm{GM_L}, \tag{3.44a}$$

$$B_{55}(\omega_e) = LT\mathrm{GM_L}b(\omega_e) = LT\mathrm{GM_L}\frac{\rho g}{k\omega_e}\frac{A^2}{\alpha^2}, \tag{3.44b}$$

$$C_{55} = \rho g \nabla \mathrm{GM_L}. \tag{3.44c}$$

Here, the longitudinal metacentric height $\mathrm{GM_L} = \frac{1}{12}\frac{L^2}{T}$ for a box shaped vessel has been used by assuming that the center of buoyancy and center of mass coincide [4]. The forcing function has been rewritten to

$$M_0(k,\beta) = C_{55}\frac{6}{L\sigma}\left[\mathrm{sinc}(\sigma) - \cos(\sigma)\right]\kappa f, \tag{3.45}$$

with $\sigma$, $\kappa$ and $f$ defined earlier. At $\sigma = 0$, the expression approach $\sim \sin(\sigma) = 0$ by the use of L'Hôpital's rule. A slightly simpler, equivalent version of the formula has also been found:

$$M_0(k,\beta) = \frac{C_{33}}{k_e}\left[\mathrm{sinc}(\sigma) - \cos(\sigma)\right]\kappa f. \tag{3.46}$$

### Roll motion

The roll motion of the vehicle is significantly influenced by the hydrofoil structure beneath the hull, enhancing stability and mitigating the risk of overturning [67]. The following derivation for an approximated model of the roll motion of wave-propelled USVs is taken from Jensen et al. [25] for the forcing function in roll, $K_0$. The physics is based on strip theory on the altered monohull geometry illustrated in Fig. 3.8 and the dynamics is written to comply with the notation given in this report. A simplification on the roll forcing function is presented from Fossen [4]. The transversal metacentric height $\mathrm{GM_T}$ is estimated by empiric methods from the International Maritime Organization (IMO) [10] and [9].

The vehicle is assumed to consist of two prismatic beams with fore and aft breadths $B_f$ and $B_a$. The draft $T$ is the same and the cross sectional areas are $A_f$ and $A_a$. From the model, the main features in the roll motion is captured by a slight increase in complexity for the shape of the monohull vehicle. The geometric parameter $\delta$ represents the ratio of the aft beam length to the total vehicle length $L$. This parameter cannot be greater than the waterplane area coefficient $C_{wp}$. The waterplane area coefficient enables to directly calculate the cross-sectional areas with

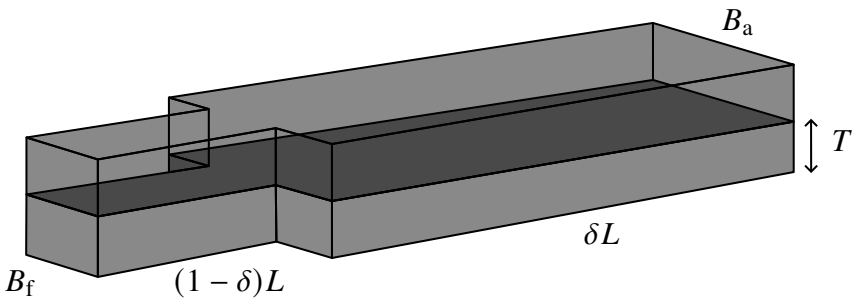


**Figure 3.8:** Altered vehicle geometry used to derive roll motion. The fore and aft breadths are denoted $B_f$ and $B_a$ and is partitioned by the parameter $\delta \in [0, 1]$.

the block coefficient $C_B$. The geometrical relations are

$$B_a = B, \qquad B_f = \gamma B, \tag{3.47a}$$

$$A_a = \frac{C_B}{C_{wp}} BT, \qquad A_f = \gamma A_a, \tag{3.47b}$$

where $\gamma \triangleq \frac{C_{wp}-\delta}{1-\delta}$ fully covers the mathematical expressions necessary to descirbe the monohull geometry in figure 3.8.

Neglecting coupling terms from other transverse motion, the equation of motion for roll was found from [25], [4], [9] and [10] to be

$$M_{44}\ddot{\phi} + B_{44}(\omega_e)\dot{\phi} + C_{44}\phi = K_0\zeta_a \cos(\omega_e t), \tag{3.48}$$

where the mass moment of inertia including added mass is estimated by the natural period $T_4$ by

$$M_{44} = \left(\frac{T_4}{2\pi}\right)^2 C_{44}, \tag{3.49}$$

and the restoring coefficient is

$$C_{44} = \rho g \nabla \mathrm{GM_T}. \tag{3.50}$$

The natural time period can be approximated by a geometric constant depending on the main particulars $L, B, T$ and the transversal metacentric height $\mathrm{GM_T}$ from the empiric method proposed by IMO in resolution A.685(17) [10]. The natural period in roll is estimated by

$$T_4 = \frac{2BC_{hull}}{\sqrt{\mathrm{GM_T}}}, \tag{3.51}$$

where the geometric constant $C_{hull}$ was proposed in IMO resolution A.562(14) [9] to be

$$\begin{aligned} C_{hull} &= 0.373 + 0.023B/T - 0.00043L, \\ &\simeq 0.373 + 0.023B/T. \end{aligned} \tag{3.52}$$

**Remark 93.** *For this project, the approximated geometric hull coefficient in Eq. (3.52) is used (second line) since the contribution from the length L is negligible for small USVs.*

The inviscid sectional damping are estimated through empirical calculations given in [25] as functions of $B_a$, $B_f$, $A_a$, $A_f$ and $T$. The sectional damping is

$$b_{44p}(\omega_e, \Lambda_T) = \rho A B^2 \sqrt{\frac{2g}{B}} a(\Lambda_T) e^{b(\Lambda_T)\omega_e^{-1.3}} \omega_e^{d(\Lambda_T)}, \tag{3.53}$$

where $\Lambda_T \triangleq B/T$ in this report is defined as the transversal aspect ratio of the vehicle and the cross-sectional area of the submerged part is $A$. According to Jensen et al. [25], the three functions $a$, $b$, $d$ satisfy to a linear approximation

$$1 \leq \Lambda_T \leq 3: \quad \begin{cases} a(\Lambda_T) = -3.94\Lambda_T + 13.69, \\ b(\Lambda_T) = -2.12\Lambda_T - 1.89, \\ d(\Lambda_T) = 1.16\Lambda_T - 7.97, \end{cases} \quad \text{(rectangular shaped)} \tag{3.54a}$$

$$3 \leq \Lambda_T \leq 6: \quad \begin{cases} a(\Lambda_T) = 0.256\Lambda_T - 0.286, \\ b(\Lambda_T) = -0.110\Lambda_T - 2.55, \\ d(\Lambda_T) = 0.033\Lambda_T - 1.419, \end{cases} \quad \text{(wider vehicles)} \tag{3.54b}$$

The inviscid hydrodynamic damping is the strip integration $B_{44p} = \int_L b_{44p}\, dx$ which equals

$$B_{44p}(\omega_e) = L[\delta b_{44p,a}(\omega_e) + (1-\delta) b_{44p,f}(\omega_e)]. \tag{3.55}$$

The total roll damping $B_{44}(\omega_e) = B_{44p}(\omega_e) + B_{44v}(\omega_e)$ is approximated as the sum of the inviscid damping $B_{44p}$ from Eq. (3.55) and a portion of the critical damping

$$B_{44}^c \triangleq \frac{C_{44} T_4}{\pi}, \tag{3.56}$$

such that viscous damping in roll motion is

$$B_{44v} = \mu_B B_{44}^c, \qquad 0 < \mu_B < 1, \tag{3.57}$$

and the total damping in roll is

$$B_{44}(\omega) = B_{44p}(\omega_e) + B_{44v}. \tag{3.58}$$

The excitation moment $K_0$ was found in Jensen et al. [25] by use of the Haskind relation expressed in terms of the sectional hydrodynamic damping $b_{44p}$ from (3.53). A derivation following Jensen et al. is given in Appendix B.2 for the stationary case of the vehicle. The excitation moment is given by Eq. (B.18) where the forward speed effect is approximately included in the expression by substituting the frequency $\omega$ with wave encounter frequency $\omega_e$. This expression is rather long, and according to Fossen [4], the damping may instead be estimated by the relative damping ratio $\zeta_4$ as

$$B_{44} = 2\zeta_4 \left(\frac{T_4}{2\pi}\right) C_{44}, \tag{3.59}$$

with the relative damping factor $\zeta_4$ and an estimate for the excitation moment $K_0$ is

$$K_0 = \sqrt{\frac{\rho g^2}{\omega_e} B_{44}} \sin(\beta). \tag{3.60}$$

In this report, the damping from Jensen et al. [25] given by Eqs. (3.55) and (3.57) is employed and the approximated forcing function from Eq. (3.60) is used.

**Remark 94.** *Another possible method to model the roll physics can be found in Matsui [69]. Otherwise, roll damping may also be modeled according to the theory by Ikeda et al. [70].*

### Wave-induced motion matrices

The model $\Sigma_2$ is the identified linear-mass-damper-spring model

$$\Sigma_2 : \quad \mathbf{M}_{\text{rao}}\ddot{\boldsymbol{\xi}} + \mathbf{B}_{\text{rao}}(\omega_e)\dot{\boldsymbol{\xi}} + \mathbf{C}_{\text{rao}}\boldsymbol{\xi} = \boldsymbol{\tau}_{\text{wave1}}, \tag{3.61}$$

where the force RAO is $\boldsymbol{\tau}_{\text{wave1}}(k,\beta) \triangleq [Z_0(k,\beta), K_0(k,\beta), M_0(k,\beta)]^\mathsf{T}$ found in Eqs. (3.41), (3.60) and (3.45). The mass matrix including added mass or moment of inertia is

$$\mathbf{M}_{\text{rao}} \triangleq \begin{pmatrix} M_{33} & 0 & 0 \\ 0 & M_{44} & 0 \\ 0 & 0 & M_{55} \end{pmatrix} = \begin{pmatrix} m - Z_{\dot{w}} & 0 & 0 \\ 0 & J_x - K_{\dot{p}} & 0 \\ 0 & 0 & J_y - M_{\dot{q}} \end{pmatrix}, \tag{3.62}$$

where the elements $M_{ii}$ for $i = 3,4,5$ for the effective model is found through Eqs. (3.40a), (3.49) and (3.44a). The frequency-dependent damping matrix for the derivative in roll and oscillatory derivatives in heave and pitch is

$$\mathbf{B}_{\text{rao}}(\omega) \triangleq \begin{pmatrix} B_{33}(\omega) & 0 & 0 \\ 0 & B_{44} & 0 \\ 0 & 0 & B_{55}(\omega) \end{pmatrix} = -\begin{pmatrix} \tilde{Z}_w(\omega) & 0 & 0 \\ 0 & K_p & 0 \\ 0 & 0 & \tilde{M}_q(\omega) \end{pmatrix}. \tag{3.63}$$

The elements $B_{ii}$ for $i = 3,4,5$ for the effective model is found in Eqs. (3.40b), (3.58) and (3.44b) respectively. The restoring matrix $\mathbf{C}_{\text{rao}}$ is

$$\mathbf{C}_{\text{rao}} \triangleq \begin{pmatrix} C_{33} & 0 & 0 \\ 0 & C_{44} & 0 \\ 0 & 0 & C_{55} \end{pmatrix} = -\begin{pmatrix} Z_z & 0 & 0 \\ 0 & K_\phi & 0 \\ 0 & 0 & M_\theta \end{pmatrix}, \tag{3.64}$$

where the elements $C_{ii}$ for $i = 3,4,5$ for the effective model is found in Eqs. (3.40c), (3.50) and (3.44c).

### 3.3.1 Parameters in the wave-induced motion model

The hydrodynamic codes of the physical USV model, is estimated by the semi-empirical method in Sect. 3.3 which was inspired by Jensen et al. [25] and Fossen [4]. The oscillatory derivatives present in the wave-induced motion model $\Sigma_2$ is

$$\underbrace{\{\tilde{Z}_{\dot{w}}, \tilde{K}_{\dot{p}}, \tilde{M}_{\dot{q}}\}}_{\text{added mass derivatives}} \ , \ \underbrace{\{\tilde{Z}_{w}, \tilde{K}_{p}, \tilde{M}_{q}\}}_{\text{damping derivatives}} , \ \underbrace{\{\tilde{Z}_{z}, \tilde{K}_{\phi}, \tilde{M}_{\theta}\}}_{\text{restoring coefficients}} ,$$

and the terms in the force response amplitude operators are

$$\underbrace{\{Z_0, K_0, M_0\}}_{\text{force RAOs}},$$

which was all found for the effective monohull geometry in Sect. 3.3 by the main particulars and characteristics $\tilde{L}, \tilde{B}, \tilde{T}$, $\tilde{\text{GM}}_\text{T}$, $\tilde{C}_\text{wp}$, $\delta_\text{geo}$ and $\mu_B$. Denote the effective model parameters by asterisk notation $(\cdot)^*$. In the following, an estimate for the vehicle oscillatory derivatives is found from the effective model by the following assumption and remark.

**Assumption 17.** *The restoring forces are presumed unchanged by the presence of hydrofoils.*

**Remark 95.** *According to Assumption 17, a conversion factor from the effective model which incorporates the foil propulsion structure to the physical model is obtained through the gain $(C/\tilde{C})$ where $C$ is the restoring force in the physical model and $\tilde{C}$ is the restoring force in the effective model.*

#### Oscillatory derivatives in heave

According to Assumption 17 and the following Remark 95, the conversion gain for the dynamical equation in heave is $Z_z/Z_z^* = A_\text{wp}/A_\text{wp}^* = C_\text{wp}BL/(\tilde{B}\tilde{L})$. An estimate for the oscillatory derivatives in heave is recognized as

$$\begin{aligned} -\tilde{Z}_{\dot{w}}(\omega) &= -Z_{\dot{w}} = 2\rho C_\text{wp} BL\tilde{T} - m, \\ -\tilde{Z}_{w}(\omega) &= \left(\frac{B}{\tilde{B}} C_\text{wp}\right) Lb(\omega), \\ -\tilde{Z}_{z}(\omega) &= -Z_z = \rho g C_\text{wp} BL, \end{aligned} \tag{3.65}$$

and the non-dimensional variants can be found through the conversion in Sect 2.1.1.

#### Oscillatory derivatives in roll

Applying the same logic for roll, an estimate for the oscillatory derivatives in roll is found through the gain $K_\phi/K_\phi^* = \nabla \text{GM}_\text{T}/\tilde{\nabla}\tilde{\text{GM}}_\text{T}$ such that

$$
\begin{aligned}
-\tilde{K}_{\dot{p}}(\omega) &= -K_{\dot{p}} = \left(\frac{T_4}{2\pi}\right)^2 \rho g \nabla \mathrm{GM_T} - J_x, \\
-\tilde{K}_{p}(\omega) &= -K_{p} = 2\zeta_4 \left(\frac{T_4}{2\pi}\right) \rho g \nabla \mathrm{GM_T}, \\
-\tilde{K}_{\phi}(\omega) &= -K_{\phi} = \rho g \nabla \mathrm{GM_T}.
\end{aligned}
\tag{3.66}
$$

### Oscillatory derivatives in pitch

The conversion gain for pitch is $K_\theta / K_\theta^* = \nabla \mathrm{GM_L} / \tilde{\nabla} \tilde{\mathrm{GM}}_\mathrm{L}$ such that

$$
\begin{aligned}
-\tilde{M}_{\dot{q}}(\omega) &= -M_{\dot{q}} = 2\rho \nabla \mathrm{GM_L} \tilde{T} - J_y, \\
-\tilde{M}_{q}(\omega) &= \left(\frac{B}{\tilde{B}} C_\mathrm{B}\right) \cdot T \mathrm{GM_L} L b(\omega), \\
-\tilde{M}_{\theta}(\omega) &= -M_{\theta} = \rho g \nabla \mathrm{GM_L}.
\end{aligned}
\tag{3.67}
$$

Here, the objective function $f_{1,1}(\{L_\mathrm{d}, B_\mathrm{d}, T_\mathrm{d}\})$ should be a measure of how well the simulation model $\Sigma_1$ fits with experimentally obtained data, for instance by a "tow-and-release"-test, for instance by the method in [50].

### Tuning parameters

Let the tuning parameters for the wave-induced model $\Sigma_2$ be denoted by

$$
\boldsymbol{\alpha}_2 \triangleq \{\tilde{L}, \tilde{B}, \tilde{T}, \tilde{\mathrm{GM}}_\mathrm{T}, \tilde{C}_\mathrm{wp}, \delta_\mathrm{geo}, \mu_B\}. \tag{3.68}
$$

The tuning parameters can be optimized according to the method proposed in Mounet et al. [67]. Denote a set of optimized variables by $\boldsymbol{\alpha}_2^*$ such that

$$
\boldsymbol{\alpha}_2^* = \arg \min_{\boldsymbol{\alpha}_2 \in \mathbb{H}_{\alpha,2}} f_2(\boldsymbol{\alpha}_2), \tag{3.69}
$$

where the parameter set $\mathbb{H}_{\alpha,2}$ is given in Tab. 3.5 and the objective function $f_2 : \mathbb{R}^8 \to \mathbb{R}$ is

$$
f_2(\boldsymbol{\alpha}_2) = \sum_{R=z,\phi,\theta} \int_0^\infty \frac{[\tilde{S}_{RR}(\omega; \boldsymbol{\alpha}_2) - S_{RR}(\omega)]^2}{m_{0,R}^2} \, \mathrm{d}\omega, \tag{3.70}
$$

which serves to minimize the discrepancy between the measured response spectra, denoted by $S_{RR}(\omega_\mathrm{e})$ obtained from in-situ operational measurements and the theoretical response spectra estimates $\tilde{S}_{RR}(\omega_\mathrm{e})$ from the model $\Sigma_2$. The objective function is normalized by the variance of the measured response by the factor $m_{0,R} = \int_0^\infty S_{RR}(\omega_\mathrm{e}) \, \mathrm{d}\omega_\mathrm{e}$. More detail on the optimization method is referred to the article [67].

**Table 3.3:** Lower and upper bounds for the fitting parameters $\boldsymbol{\alpha}_2$ corresponding to the set $\mathbb{H}_{\alpha,2}$ for the wave-induced model $\Sigma_2$. From Mounet et al. [67].

| Element | Parameter | | Bounds |
|---|---|---|---|
| $\boldsymbol{\alpha}_2[1]$ | $\tilde{L}$ | effective length | $[0, 2L]$ |
| $\boldsymbol{\alpha}_2[2]$ | $\tilde{B}$ | effective breadth | $[0, 2B]$ |
| $\boldsymbol{\alpha}_2[3]$ | $\tilde{T}$ | effective draft | $[0, 2T]$ |
| $\boldsymbol{\alpha}_2[4]$ | $\tilde{\mathrm{GM}}_\mathrm{T}$ | eff. transversal metacentric height | $[0, 2B]$ |
| $\boldsymbol{\alpha}_2[5]$ | $\tilde{C}_\mathrm{wp}$ | eff. waterplane area coefficient | $[0, 1]$ |
| $\boldsymbol{\alpha}_2[6]$ | $\delta_\mathrm{geo}$ | ratio of aft beam length to overall length | $[0, 1]$ |
| $\boldsymbol{\alpha}_2[7]$ | $\mu_B$ | ratio viscous damping to critical damping | $[0, 1]$ |

### 3.3.2 Identification of fluid-memory effects

The wave-induced motion model in Eq. (3.61) is frequency-dependent hence a proper time-domain implementation model is found through the method by incorporating fluid memory effects according to Cummin's equation in Eq. (2.97). Since the dynamics is uncoupled in heave, roll and pitch, the identified method in Sect. 2.5.3 is employed.

#### Retardation function in time-domain

This section shows the derivation for the simplest transfer function approximation for the fluid memory effects on the simplified monohull geometry used as an effective model for wave-propelled USVs. The frequency-domain identification of the function of retardation is performed on a proper transfer function applicable for heave and pitch motions, inspired by . Recall the sectional hydrodynamic damping from Newman [24] in Eq. (B.14)

$$b(\omega; B, T) = \frac{\rho g^2}{\omega^3}\left[2\sin\left(\frac{\omega^2}{2g}B\right)\exp\left(-\frac{\omega^2}{g}T\right)\right]^2, \quad \text{(sectional damping used in heave and pitch)} \tag{3.71}$$

where the total damping in heave and pitch is related to this expression by a geometrical constant. Introducing the dimensionless frequency $\omega' = \omega\sqrt{\frac{B}{2g}}$, then Eq. (3.71) reduces to

$$b'(\omega'; \Lambda_T) = \frac{b\left(\omega'\sqrt{2g/B}\right)}{\rho B\sqrt{2Bg}} = \frac{1}{\omega'^3}\sin\left(\omega'^2\right)^2\exp\left(-\frac{\omega'^2}{\Lambda_T}\right). \tag{3.72}$$

The retardation function is identified from a numerical integration by Eq. (2.103) with the damping from Eq. (3.72). A change of variables, $\omega = \omega'\sqrt{\frac{2g}{B}}$ such that $\mathrm{d}\omega/\mathrm{d}\omega' = \sqrt{\frac{2g}{B}}$, yields

$$k(t; \Lambda_T) = \frac{2}{\pi}\int_0^\infty \rho B\sqrt{2Bg}\, b'(\omega'; \Lambda_T)\cos\left(\omega' t\sqrt{2g/B}\right)\sqrt{\frac{2g}{B}}\,\mathrm{d}\omega', \tag{3.73}$$

where the dimensionless time $t' = t\sqrt{\frac{2g}{B}}$ enables to find the non-dimensional retardation function

$$k'(t'; \Lambda_T) = \frac{k(t)}{2\rho Bg} = \frac{2}{\pi}\int_0^\infty b'(\omega'; \Lambda_T)\cos(\omega' t')\,\mathrm{d}\omega'. \tag{3.74}$$

#### Closed-form approximating of the retardation function

In this work, a closed form expression is found for the fluid memory effects inspired by the identified properties in the identification method of fluid memory effects by Perez and Fossen [39]. Denote $k(s)$ the approximated proper transfer function for the retardation function. According to [39], the transfer function satisfy *prior* information which enables to refine the search for the appropriate model and its parameters. Tab. 3.4 summarizes the properties on the

**Table 3.4:** Properties of the retardation function. Adapted from Perez and Fossen [39], rewritten to an uncoupled single degree of freedom. Here, $\hat{k}(j\omega) = \hat{k}(s)\big|_{s=j\omega}$ denotes frequency-domain and $\hat{k}(t)$ denotes time-domain.

| Property | Implication on parametric model $\hat{k}(s) = q(s)/p(s)$ |
|---|---|
| $\lim_{\omega\to 0} \hat{k}(j\omega) = 0$ | There are zeros at $s = 0$, i.e. $q(0) = 0$. |
| $\lim_{\omega\to\infty} \hat{k}(j\omega) = 0$ | Strictly proper, i.e. $\deg(p(s)) > \deg(q(s))$. |
| $\lim_{t\to 0^+} \hat{k}(t) \neq 0$ | Relative degree 1, i.e. $\deg(p(s)) - \deg(q(s)) = 1$. |
| $\lim_{t\to\infty} \hat{k}(t) = 0$ | Bounded-input-bounded-output stable. |
| The mapping $\dot{\xi} \to \mu$ is passive. | $\hat{k}(j\omega)$ is positive real. |

retardation function and its implications on the parametric model $\hat{k}(s) = q(s)/p(s)$, where $q, p$ are polynomial in $s$.

According to the properties in Tab. 3.4, the simplest rational transfer function candidate to approximate the non-dimensional retardation function in Eq. (3.73) is

$$\hat{k}'(s') = \frac{q'_0 s'}{s'^2 + p'_1 s' + p'_0}, \tag{3.75}$$

where the small number of parameters are $q'_0$, $p'_1$ and $p'_0$. The parameters in this work was found through a least squares optimization in the time domain by the analytical solution. From the derivation given in Appendix B.3, the inverse Laplace transformation of Eq. (3.75) is

$$\hat{k}'(t') = q'_0 \mathrm{e}^{-\frac{p'_1}{2}t'} \cos\left(\left[p'_0 - \left(\frac{p'_1}{2}\right)^2\right]^{\frac{1}{2}} t'\right) - \frac{q'_0 p'_1}{2\left[p'_0 - \left(\frac{p'_1}{2}\right)^2\right]^{\frac{1}{2}}} \mathrm{e}^{-\frac{p'_1}{2}t'} \sin\left(\left[p'_0 - \left(\frac{p'_1}{2}\right)^2\right]^{\frac{1}{2}} t'\right). \tag{3.76}$$

### Least squares optimization

Denote the set of parameters adjusting $\hat{k}'$ as $\boldsymbol{\theta} \triangleq \{q'_0, p'_0, p'_1\}$. A least squares objective is to find optimal values $\boldsymbol{\theta}^*$ in order to minimize the squared discrepancy between Eq. (3.74) and Eq. (3.76) for a given transversal aspect ratio $\Lambda_\mathrm{T} = B/T$. The least squares optimization

$$\boldsymbol{\theta}^* = \arg\min_{\boldsymbol{\theta}} \int_0^\infty w(t') \cdot |k'(t') - \hat{k}'(t')|^2 \, \mathrm{d}t', \tag{3.77}$$

was employed by an approximate finite sum with weights $w_i$

$$\boldsymbol{\theta}^* = \arg\min_{\boldsymbol{\theta}} \sum_{i=1}^{N} \frac{1}{2} w_i \epsilon_i^2, \tag{3.78}$$

where $\epsilon_i \triangleq k'(t'[i]) - \hat{k}'(t'[i])$ is the time-domain discretization of the discrepancy by the index $i$. In this context the interval $t'[1] = 0$ to $t'[N] = 20$ was chosen. Denoting $\boldsymbol{\epsilon} = [\epsilon_1, \ldots, \epsilon_N]^\mathsf{T}$ and the weights $\mathbf{W} = \mathrm{diag}([w_1, \ldots, w_N]^\mathsf{T})$, a gradient descent algorithm for

$$\boldsymbol{\theta}^* = \arg\min_{\boldsymbol{\theta}} \frac{1}{2}\boldsymbol{\epsilon}^\mathsf{T}\mathbf{W}\boldsymbol{\epsilon}, \quad \text{(given } \Lambda_\mathrm{T}\text{)} \tag{3.79}$$

with the descent gain $\mu_{\boldsymbol{\theta}} = 0.3$ by

$$\boldsymbol{\theta}^*_{k+1} \leftarrow \boldsymbol{\theta}^*_k - \mu_{\boldsymbol{\theta}} \nabla_{\boldsymbol{\theta}} \left( \tfrac{1}{2}\boldsymbol{\epsilon}^\mathsf{T}\mathbf{W}\boldsymbol{\epsilon} \right) \Big|_{\boldsymbol{\theta}=\boldsymbol{\theta}^*_k},$$

gave excellent convergence for $\boldsymbol{\theta}^*$ for a small number of iterations $k$. The optimal values for a wide range of transversal aspect ratios $\Lambda_\mathrm{T}$ are reported in Tab. C.3 in Appendix **??**. Figs. 3.10 and 3.11 shows the numerical integration of the retardation function from Eq. (3.74) with the approximated retardation function identified. A comparison to a typical retardation function is shown in Fig. 3.12.

Closed form expression for the parameters in the retardation function was found empirically by a least-squares fit. The estimates is proposed to follow the functions

$$\begin{aligned} q'_0(\Lambda_\mathrm{T}) &\simeq 0.5696 \cdot \frac{\Lambda_\mathrm{T} - 0.018}{\Lambda_\mathrm{T} + 1.035}, \\ p'_0(\Lambda_\mathrm{T}) &\simeq 0.5917 \cdot \frac{\Lambda_\mathrm{T} - 0.245}{\Lambda_\mathrm{T} + 0.612}, \\ p'_1(\Lambda_\mathrm{T}) &\simeq 0.7376 \cdot \frac{\Lambda_\mathrm{T} + 0.394}{\Lambda_\mathrm{T} + 0.642}, \end{aligned} \tag{3.80}$$

which is illustrated in Fig. 3.9. The figure shows that the empiric values agrees well the optimal parameters for a wide range of values $\Lambda_\mathrm{T}$.

**Remark 96.** *For simplicity, the first parameter estimate in Eq. (3.80) can be set as*

$$q'_0(\Lambda_T) \simeq 0.5696 \cdot \frac{\Lambda_T}{\Lambda_T + 1.035}. \tag{3.81}$$

The conversion from the non-dimensional parameters in Eq. (3.80) to the parameters $q_0$, $p_1$ and $p_0$ was found to be

$$q_0 = 2\rho g\sqrt{2Bg}\, C_\mathrm{geo}\, q'_0(\Lambda_\mathrm{T}), \tag{3.82a}$$

$$p_1 = \sqrt{\frac{2g}{B}}\, p'_1(\Lambda_\mathrm{T}), \tag{3.82b}$$

$$p_0 = \frac{2g}{B}\, p'_0(\Lambda_\mathrm{T}). \tag{3.82c}$$

The retardation function for heave and pitch can be interpreted by

$$\hat{k}(s) = \frac{2\rho B g\sqrt{\frac{2g}{B}}\, q'_0 s}{s^2 + \sqrt{\frac{2g}{B}}\, p'_1 s + \frac{2g}{B} p'_0} C_\mathrm{geo}, \quad \text{with} \quad C_\mathrm{geo} = \begin{cases} L, & \text{(heave)} \\ LT\mathrm{GM_L}, & \text{(pitch)} \end{cases} \tag{3.83}$$

where the geometric constant $C_{\text{geo}}$ differ between the pitch motion and heave motion.

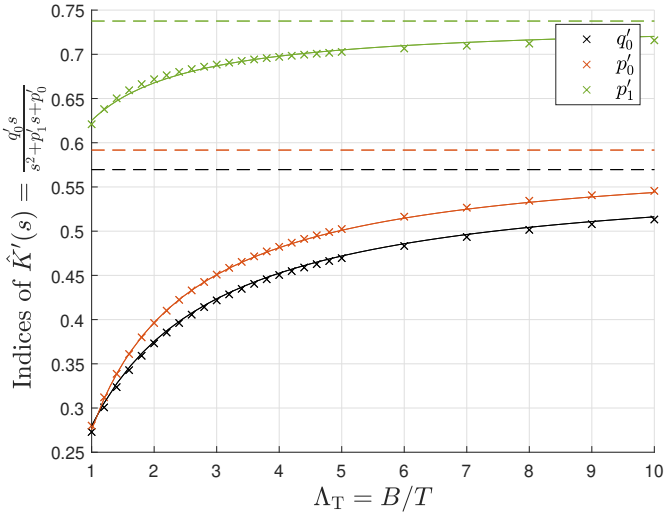


**Figure 3.9:** Indices of $\hat{k}'(s)$ and their optimized values marked with cross. Dashed line represents the asymptotic value for infinite $B/T$-ratio, and the solid line represents the empiric relations by Eq. (3.80).

### Fluid memory effects in time-domain

According to Sect. 2.5.3, the fluid memory effects for a single degree of freedom given by the dynamics in Eq. (2.101) can be approximated by the time domain dynamics

$$\begin{aligned} m(\infty)\ddot{\xi} + \mu + c\xi &= \tau, \\ \dot{\mathbf{x}}_{\text{r}} &= \mathbf{A}_{\text{r}}\mathbf{x}_{\text{r}} + \mathbf{B}_{\text{r}}\dot{\xi}, \\ \mu &= \mathbf{C}_{\text{r}}\mathbf{x}_{\text{r}}. \end{aligned} \tag{3.84}$$

The transfer function $\hat{k}'(s) = q(s)/p(s) = \mathbf{C}_{\text{r}}[s\mathbb{I} - \mathbf{A}_{\text{r}}]^{-1}\mathbf{B}_{\text{r}}$.

The seakeeping motion for the wave-propelled USV may be described by the fluid memory effect in heave and pitch described in this section, while roll motion is considered without fluid memory effects. The time-domain dynamics for the simplified monohull geometry is thus

$$\begin{aligned} \mathbf{M}_{\text{rao}}(\infty)\ddot{\boldsymbol{\xi}} + \mathbf{B}_{\text{rao}}(\infty)\dot{\boldsymbol{\xi}} + \boldsymbol{\mu}_{\text{r}} + \mathbf{C}_{\text{rao}}\boldsymbol{\xi} &= \boldsymbol{\tau}_{\text{wave1}}, \\ \dot{\mathbf{x}} &= \mathbf{A}_{\text{r}}\mathbf{x}_{\text{r}} + \mathbf{B}_{\text{r}}\delta\boldsymbol{\nu}_{\text{r}}, \\ \boldsymbol{\mu}_{\text{r}} &= \mathbf{C}_{\text{r}}\mathbf{x}_{\text{r}}, \end{aligned} \tag{3.85}$$

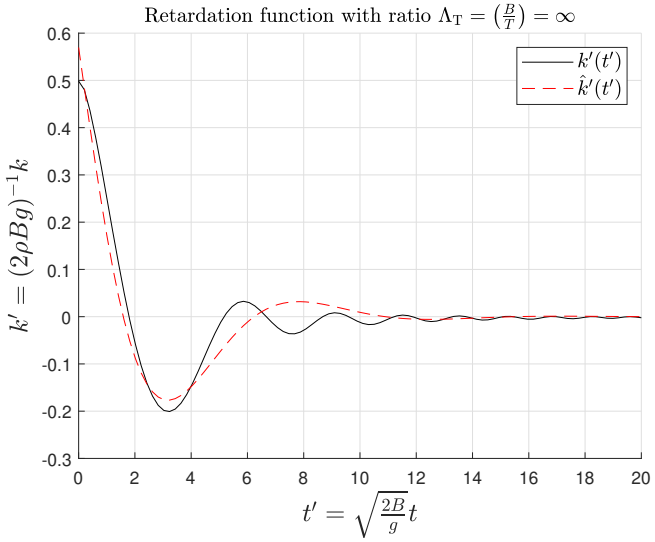


**Figure 3.10:** Retardation function at infinite ratio.

where the matrices for fluid memory effects for heave, roll and pitch is

$$\begin{aligned}\dot{\mathbf{x}}_r &= \underbrace{\begin{pmatrix}\mathbf{A}_{r33} & \mathbf{0} & \mathbf{0}\\ \mathbf{0} & \mathbf{A}_{r44} & \mathbf{0}\\ \mathbf{0} & \mathbf{0} & \mathbf{A}_{r55}\end{pmatrix}}_{\mathbf{A}_r}\mathbf{x}_r + \underbrace{\begin{pmatrix}\mathbf{B}_{r33} & \mathbf{0} & \mathbf{0}\\ \mathbf{0} & \mathbf{B}_{r44} & \mathbf{0}\\ \mathbf{0} & \mathbf{0} & \mathbf{B}_{r55}\end{pmatrix}}_{\mathbf{B}_r}\dot{\boldsymbol{\xi}},\\ \boldsymbol{\mu}_r &= \underbrace{\begin{pmatrix}\mathbf{C}_{r33} & \mathbf{C}_{r44} & \mathbf{C}_{r55}\end{pmatrix}}_{\mathbf{C}_r}\mathbf{x}_r,\end{aligned} \tag{3.86}$$

and $\mathbf{x}_r = [\mathbf{x}_{r33}^\mathsf{T}, \mathbf{x}_{r44}^\mathsf{T}, \mathbf{x}_{r55}^\mathsf{T}]^\mathsf{T}$. The sub-matrices were identified as

$$\mathbf{A}_{r33} = \mathbf{A}_{r55} = \begin{pmatrix}-\sqrt{\frac{2g}{B}}p_1'(\Lambda_T) & -\frac{2g}{B}p_0'(\Lambda_T)\\ 1 & 0\end{pmatrix}, \quad \mathbf{A}_{r44} = \mathbf{0}, \tag{3.87}$$

$$\mathbf{B}_{r33} = \mathbf{B}_{r55} = \begin{pmatrix}1\\ 0\end{pmatrix}, \quad \mathbf{B}_{r44} = \mathbf{0}, \tag{3.88}$$

$$\mathbf{C}_{r33} = \mathbf{C}_{r55} = \begin{pmatrix}2\rho g\sqrt{2Bg}C_{geo}q_0'(\Lambda_T) & 0\end{pmatrix}, \quad \mathbf{C}_{r44} = \mathbf{0}. \tag{3.89}$$

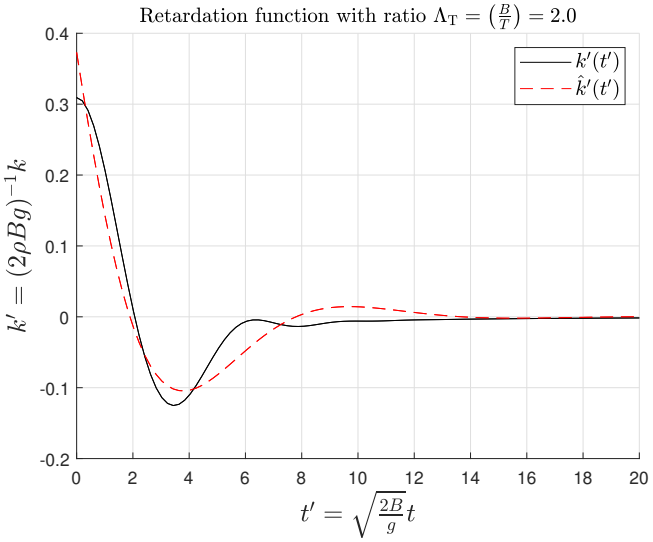


**Figure 3.11:** Retardation function at ratio $B/T = 2.0$.

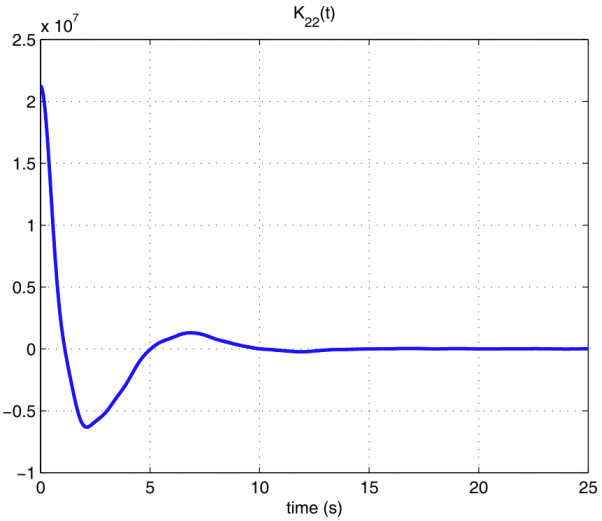


**Figure 3.12:** Typical impulse response function $K_{22}(t)$ in sway. Note the resemblance to the normalized heave and pitch approximation $\hat{k}'(t')$ in Fig. 3.10 and Fig. 3.11. Facsimile from Fossen [39].

## 3.4 Hydrofoil excitation model for wave-propulsion

In this section the individual foil dynamics for each foil is derived for use in the wave propulsion model $\Sigma_3$ in the proposed model architecture in Fig. 3.3. The foil motion is driven by the joint USV motion of the maneuvering position from model $\Sigma_1$ given in Sect. 3.2 and the wave-induced motion from model $\Sigma_2$ given in Sect. 3.3, and the wave propulsion force $\boldsymbol{\tau}_{\text{prop}}$ serves as an input for the maneuvering model $\Sigma_1$. Fig. 3.13, which is the same figure used in Sect. 2.6 shows that the movement of the vehicle drags the foils through the water.

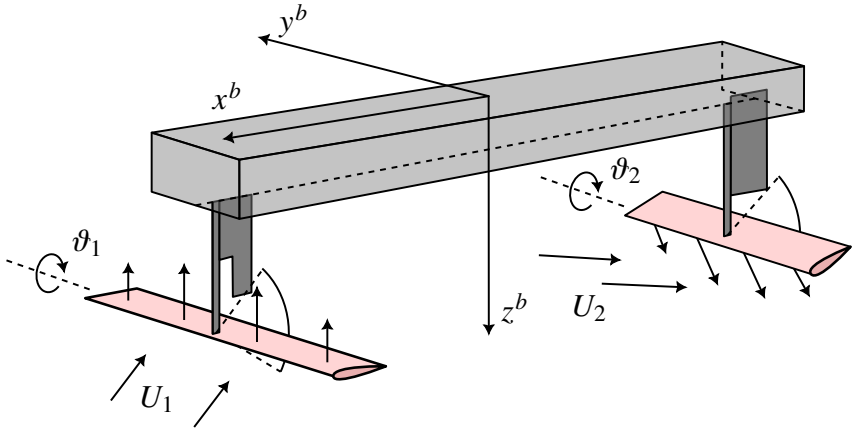


**Figure 3.13:** The foils on the USV (in red) are driven by the joint motion of the maneuvering and seakeeping motion affecting the local relative velocity inflow $U$.

The geometry of the individual foils are assumed to comply with Assumptions 11 and 12 given in Sect. 2.6 relating to the position of the foils on the midline of the USV and rotation along the $y^b$-axis of the vehicle. From Remark 36, the pivot position of foil $i$ in body is

$$\mathbf{r}^b_{p,i} = \begin{pmatrix} x_{p,i} \\ 0 \\ z_{p,i} \end{pmatrix}. \tag{3.90}$$

**Remark 97.** *The foils pivot point should not be confused with a ship's pivot point, definition given in pp. 192 in Fossen [4].*

In order to derive the dynamics for the foils, the following assumptions and remarks describes necessary simplifications. This section shows that the foil model $\Sigma_3$ can be written as

$$\begin{aligned} \Sigma_3: \quad \mathbf{M}_\vartheta \ddot{\boldsymbol{\vartheta}}_{\text{n}} + \mathbf{B}_\vartheta \dot{\boldsymbol{\vartheta}}_{\text{n}} + \mathbf{C}_\vartheta(\boldsymbol{\vartheta})\boldsymbol{\vartheta}_{\text{n}} &= \mathbf{C}_\vartheta(\boldsymbol{\vartheta})\mathbf{L}_\vartheta \boldsymbol{\xi} + \mathbf{Q}_{\text{non circ}} + \tilde{\mathbf{Q}}_{\text{circ}} + \mathbf{Q}_{\text{inertia}}, \\ \dot{\mathbf{x}}_{\text{circ}} &= \mathbf{A}(\boldsymbol{\nu}_{\text{r}})\mathbf{x}_{\text{circ}} + \mathbf{B}\mathbf{Q}_{\text{circ}}, \\ \tilde{\mathbf{Q}}_{\text{circ}} &= \mathbf{C}(\boldsymbol{\nu}_{\text{r}})\mathbf{x}_{\text{circ}} + \mathbf{D}\mathbf{Q}_{\text{circ}}, \end{aligned} \tag{3.91}$$

where the system is identified as a mass-damper-system driven by the wave-induced motion $\boldsymbol{\xi}$ from the USV with inertia correction $\mathbf{Q}_{\text{inertia}}$ and driven by the added force moment $\mathbf{Q}_{\text{non circ}}$ and filtered circulatory forces $\tilde{Q}_{\text{circ}}$. The dimensions is of order $\mathbb{R}^m$, where $m$ is the number of foils in the wave-propulsion model.

### Model assumptions for foil dynamics

In this part assumptions about the foils are made to simplify the derivaton of equations of motion:

**Assumption 18.** *The foils are neutrally buoyant.*

**Remark 98.** *Assumption 18 is common in underwater modeling of marine robots where the effects of gravity and buoyancy cancels. However, the assumption can be relaxed as explained in the next section by incorporating these forces. On the other hand, if the assumption is not accurate, a change of variables $\tilde{\vartheta} = \vartheta - \vartheta_0$, where $\vartheta_0$ is the equilibrium point for the foil angle due to the foils not being neutrally buoyant, approximately fullfils Assumption 18 anyway.*

**Assumption 19.** *The USV heading is slowly varying, meaning that $\dot{\psi} = r \simeq 0$.*

**Remark 99.** *From Assumption 19, any Coriolis or centripetal forces due to change in heading is ignored. This is a good approximation for wave-propelled USVs because of low vehicle speed $U = \sqrt{u^2 + v^2}$. During guidance operations, this will result in a slowly varying heading, e.g. when the USV is following a straight line. Thus the contribution from $\psi(t)$ is a negligible part of the dynamics for the foils. For any instance, the heading can be considered constant, $\psi = \text{const}$.*

**Remark 100.** *During stationkeeping in waves where the wave-foil technology generates propulsion, the USV needs to keep circling in order to keep its position. Thus Assumption 19 might be less accurate in those scenarios.*

**Assumption 20.** *The foils are symmetrical and placed on the midline of the USV and the effects of roll $\phi$ is negligible to the foil dynamics.*

**Remark 101.** *When the vehicle rolls, dominant hydrodynamic forces is port-starboard anti-symmetric, introducing a viscous damping moment for the USV vehicle, but do not alter the foil angles to a considerable degree. Additionally, roll motion contributes to a spanwise relative velocity field over the foils which is ignored in the analysis.*

**Remark 102.** *Contrary to Remark 101, only the hydrodynamic forces caused by relative velocities orthogonal to the foil span is included in the analysis of the foil dynamics. This means that only surge, heave and pitch motion of the USV vehicle is of interest for the motion of the foils.*

The dynamics for a single foil is derived in the next section, before the complete foil model $\Sigma_3$ is assembled with parameter vector $\boldsymbol{\alpha}_3$.

### Unconstrained foil dynamics without inertia correction

This sections shows the derivation of the governing dynamics for a single foil driven by the forces identified in Sect. 2.6 with Assumptions 18–20. The variables in this derivation is written without a subscript since it is understood that a subscript is needed to differentiate between the different foils. Ignoring the effects of rolling $\delta\dot{\phi} \simeq \delta\phi \simeq 0$ and assuming slowly-varying heading $\delta\dot{\psi} \simeq 0$, then Euler's equation of motion by Eq. (2.14) for the foils reduces to Newton's Second Law for rotation. Since this law is applicable in the inertial reference frame, then define the foil angles relative to NED as

$$\vartheta_n \triangleq \theta + \vartheta, \tag{3.92}$$

where $\theta$ is the USV pitch angle and $\vartheta$ is the foil angle measured relative to the USV. The foil angles given in Eq. (3.92) is the equivalence of measuring the hydrofoils relative to the horizontal. Fig. 3.14 shows the sectional characteristics for a foil driven by the motion of the USV. Newton's second law for rotation – the torque acting on an object is equal to the product of the moment of inertia and the angular acceleration – is applied on the pivot point

$$J\ddot{\vartheta}_n = \sum_i Q_{\text{pivot point},i}, \tag{3.93}$$

where $J$ is the moment of inertia of the foil at the pivot point along $y^b$-axis and $Q_{\text{pivot point},i}$ is a moment contribution acting on the foil. The following remarks describe the benefit and a drawback of employing Eq. (3.93):

**Remark 103.** *The benefits of describing the dynamics of the foil around the pivot point is that constraint forces between the USV and the foil is neglected in the analysis since the moment arm for the constraint forces is zero since the constraint forces must act through the pivot point. As a result, the contribution from constraint forces on the right hand side of Eq.* (3.93) *is exactly zero.*

**Remark 104.** *Applying the rotational dynamics in Eq.* (3.93) *directly is only valid as long as the pivot point do not undergo acceleration since the dynamical equation is only valid for inertial reference frames. A correction to the dynamics may be found by adding inertia forces, which is identified for instance by Euler-Lagrange method by Eq.* (2.15) *in Sect. 2.1.4.*

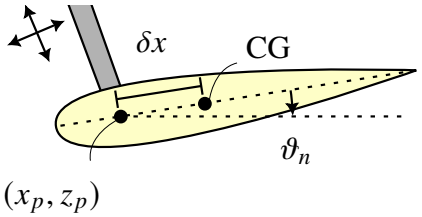


**Figure 3.14:** Foil coordinates $(x_p, z_p)$ with angle $\vartheta_n$. The coordinates is such that $x$-axis point to left and $z$-axis point downwards.

The dominating forces acting on the foil was found as:

- Non-circulatory moment corresponding to the added moment of inertia $-Q_{\ddot{\vartheta}}\ddot{\vartheta}_\text{r}$ in the relative acceleration $\ddot{\vartheta}_r$ approximated by the flat plate moment from Lamb [33] given by Eq. (2.155) evaluated at the mid-chord position.
- Added mass force $A$ according to Pettersen [36] by Eqs. (2.154) with the three-dimensional analytical correction by Meyerhoff [59] by the proposed empiric Eq. (2.152).
- Hydrodynamic damping $-Q_{\dot{\vartheta}}\dot{\vartheta}_\text{r}$ due to relative rotation $\dot{\vartheta}_\text{r}$ in the water.

- Spring forces by the passive incidence-control from the USV to the foil angle $\vartheta$, given by Hook's law $-C\vartheta$.
- Quasi-steady circulatory lift and drag forces found by the force coefficients in Eq. (2.131). approximated by the normal force $N$ with the three-dimensional correction inspired by Prandtl's lifting line [50], empiric correction from Anderson [16] and experimental results from Fujii and Tuda [57] by Eq. (2.147). The unsteady circulatory forces are filtered according to Theodorsen's function [14] approximated by the state-space representation in Eq. (2.169). The circulatory forces act at the center of pressure inspired by the analytical derivation from the vortex distribution and experimental and numerical results in Mirzaeisefat [56] by the proposed empiric Eq. (2.139).
- Damping forces $D$ due to relative linear velocity of the foil through the water.
- Buoyancy force $B$ acts in the static center of pressure of the foil.
- Gravitational effect $G$ acts in the mass center of the foil.

Neglecting friction between the strut and the foil, the dynamics for a single foil according to Eq. (3.93) was found as

$$
\begin{aligned}
J_{\text{p.p.}}\ddot{\vartheta}_n = &- Q_{\ddot{\vartheta}}\ddot{\vartheta}_{\text{r}} && \text{(added moment of inertia)} \\
&- Q_{\dot{\vartheta}}\dot{\vartheta}_{\text{r}} && \text{(relative rotational damping)} \\
&- Q_{\vartheta}(\vartheta)\vartheta && \text{(spring)} \\
&+ N(x_{\text{c.p.}} - x_{\text{p}}) && \text{(normal force)} \\
&+ A\sin(\alpha_a)(0.5c_m - x_{\text{p}}) && \text{(added mass force)} \\
&+ D\sin(\alpha_v)(0.5c_m - x_{\text{p}}) && \text{(damping force)} \\
&+ B\cos(\vartheta_n)(x_{\text{c.b.}} - x_{\text{p}}) && \text{(buoyancy)} \\
&- G\cos(\vartheta_n)(x_{\text{c.g.}} - x_{\text{p}}), && \text{(gravity)} \\
&(+ \text{ inertia force correction})
\end{aligned}
\tag{3.94}
$$

where the lengths are defined in Fig. 3.14 and the forces are defined in the list above and explained in parenthesis. The moment of inertia of the foil evaluated in the pivot point is $J_{\text{p.p.}}$.

An additional assumption about the mass density of the foils are also made:

**Assumption 21.** *The foils have homogeneous mass density.*

**Remark 105.** *From Assumption 18, buoyancy force and gravity effect included in Eq. (3.94) cancels completely for foils with homogeneous mass density, as assumed in Assumption 21. This reduces the complexity in the wave propulsion model* $\Sigma_2$.

Furthermore, the relative rotation rate $\dot{\vartheta}_{\text{r}}$ and acceleration $\ddot{\vartheta}_{\text{r}}$ through the water is needed in the dynamics. The following assumption is necessary to express the dynamics of the foils as a mass-damper-spring system:

**Assumption 22.** *Since the fluid is irrotational, see Sect. 2.3, the relative rotations of the foils through the water may be sufficiently approximated by*

$$\dot{\vartheta}_r \simeq \dot{\vartheta}_n, \qquad \ddot{\vartheta}_r \simeq \ddot{\vartheta}_n. \tag{3.95}$$

With the simplifications given in Assumptions 21 and 22, the foil dynamics reduces to

$$(J_{\text{p.p.}} + Q_{\ddot{\vartheta}})\ddot{\vartheta}_n + Q_{\dot{\vartheta}}\dot{\vartheta}_n + C(\vartheta)\vartheta = F_{\text{NF}}(x_{\text{c.p.}} - x_{\text{p}}) + A(0.5c_m - x_{\text{p}}), \tag{3.96}$$

which, by adding $C(\vartheta)\theta$ on both sides, a mass-damper-spring system is identified

$$M_\vartheta\ddot{\vartheta}_n + B_\vartheta\dot{\vartheta}_n + C_\vartheta\vartheta_n = C(\vartheta)\theta + F_{\text{NF}}(x_{\text{c.p.}} - x_{\text{p}}) + A(0.5c_m - x_{\text{p}}), \tag{3.97}$$

where the moments on right hand side relate to position $Q_x$, velocity $Q_{\dot{x}}$ and acceleration $Q_{\ddot{x}}$ as

$$Q_x \triangleq C\theta, \qquad Q_{\dot{x}} \triangleq F_{\text{NF}}(x_{\text{c.p.}} - x_{\text{p}}), \qquad Q_{\ddot{x}} \triangleq A(0.5c_m - x_{\text{p}}). \tag{3.98a}$$

The unconstrained foil dynamics for a single foil mounted on a wave-propelled USV with passive spring incidence control $C_\vartheta(\vartheta)\vartheta$ without inertia corrections are

$$M_\vartheta\ddot{\vartheta}_n + B_\vartheta\dot{\vartheta}_n + C_\vartheta\vartheta_n = Q_x + \tilde{Q}_{\dot{x}} + Q_{\ddot{x}}. \tag{3.99}$$

### Foil dynamics with inertia forces

The inertia forces was found through Euler-Lagrange's method in Appendix B.1, where the inertia forces was recognized in Eq. (B.12), which includes the inertial acceleration of the pivot point by Eq. (3.90)

$$Q_{\text{inertia}} = -\delta x m\ddot{z}_p\cos(\vartheta_n) - \delta x m\ddot{x}_p\sin(\vartheta_n), \tag{3.100}$$

where $m$ in this context is the mass of the foil and $\delta x > 0$ is the distance from the pivot point to the center of mass in the foil illustrated in Fig. 3.14. The equations of motion for a single foil is the combination of Eq. (3.99)

$$M_\vartheta\ddot{\vartheta}_n + B_\vartheta\dot{\vartheta}_n + C_\vartheta\vartheta_n = Q_x + \tilde{Q}_{\dot{x}} + Q_{\ddot{x}} + Q_{\text{inertia}}. \tag{3.101}$$

### Foil dynamics with constrained motion

In most wave-propelled USVs the foil angles $\vartheta_i$ will be constrained to the maximum and minimum deflections $\vartheta_{\max}$ and $\vartheta_{\min}$, respectively. The constraints are given by the physical attachment of the foils on the USV.

**Wave propulsion model**

Assume that the wave-propelled USV has $N$ foils. Denote the vector of foil angles as

$$\boldsymbol{\vartheta}_n \triangleq [\vartheta_{n,1}, \ \ldots \ , \vartheta_{n,N}]^\intercal \subset \mathbb{T}^N, \tag{3.102}$$

and by $\dot{\boldsymbol{\vartheta}}_n \in \mathbb{R}^N$ and $\ddot{\boldsymbol{\vartheta}}_n \in \mathbb{R}^N$ the time differentiation's of Eq. (3.102). The model $\Sigma_3$ is

$$\begin{aligned} \Sigma_3 : \quad \mathbf{M}_\vartheta \ddot{\boldsymbol{\vartheta}}_\mathrm{n} + \mathbf{B}_\vartheta \dot{\boldsymbol{\vartheta}}_\mathrm{n} + \mathbf{C}_\vartheta(\boldsymbol{\vartheta})\boldsymbol{\vartheta}_\mathrm{n} &= \mathbf{C}_\vartheta(\boldsymbol{\vartheta})\mathbf{L}_\vartheta \boldsymbol{\xi} + \mathbf{Q}_{\text{non circ}} + \tilde{\mathbf{Q}}_\text{circ} + \mathbf{Q}_\text{inertia}, \\ \dot{\mathbf{x}}_\text{circ} &= \mathbf{A}(\boldsymbol{\nu}_\mathrm{r})\mathbf{x}_\text{circ} + \mathbf{B}\mathbf{Q}_\text{circ}, \\ \tilde{\mathbf{Q}}_\text{circ} &= \mathbf{C}(\boldsymbol{\nu}_\mathrm{r})\mathbf{x}_\text{circ} + \mathbf{D}\mathbf{Q}_\text{circ}, \end{aligned} \tag{3.103}$$

where $\mathbf{L}_\vartheta$ is a constant selection matrix such that $\mathbf{C}_\vartheta(\boldsymbol{\vartheta})\mathbf{L}_\vartheta\boldsymbol{\xi} = \theta \mathbb{I}_{n\times 1}$. And the matrices $\mathbf{A}$, $\mathbf{B}$, $\mathbf{C}$ and $\mathbf{D}$ is chosen from the state-space representation of unsteady circulatory forces.

### 3.4.1 Parameters in the foil excitation model

The parameters $\boldsymbol{\alpha}_3$ for the wave propulsion model $\Sigma_3$ are

$$\underbrace{\{S, c_m, t', x'_m\}}_{\text{foil geometry}}, \underbrace{\{\alpha_s, k_s, C_{Ls}, C_{Ds}\}}_{\text{lift and drag curves}}, \underbrace{\{x'_\mathrm{p}, \delta x'\}}_{\text{foil lengths}} \tag{3.104}$$

**Table 3.5:** Lower and upper bounds for the fitting parameters $\boldsymbol{\alpha}_3$ corresponding to the set $\mathbb{H}_{\alpha,3}$ for the wave-propulsion model $\Sigma_3$.

| Element | Parameter | | Bounds |
|---|---|---|---|
| $\boldsymbol{\alpha}_3[1]$ | $S$ | span | $[0, \infty)$ |
| $\boldsymbol{\alpha}_3[2]$ | $c_m$ | chord length | $[0, \infty)$ |
| $\boldsymbol{\alpha}_3[3]$ | $t'$ | chord thickness | $[0, 1]$ |
| $\boldsymbol{\alpha}_3[4]$ | $x'_m$ | point of maximum thickness | $[0, 1]$ |
| $\boldsymbol{\alpha}_3[5]$ | $\alpha_s$ | effective stall angle | $[0, \pi/4]$ |
| $\boldsymbol{\alpha}_3[6]$ | $k_s$ | stall transition length | $[0, \pi/2]$ |
| $\boldsymbol{\alpha}_3[7]$ | $C_{Ls}$ | detached lift coefficient | $[0, 1]$ |
| $\boldsymbol{\alpha}_3[8]$ | $C_{Ds}$ | detached drag coefficient | $[0, 1]$ |
| $\boldsymbol{\alpha}_3[9]$ | $x'_\mathrm{p}$ | pivot point length | $[0, 1]$ |
| $\boldsymbol{\alpha}_3[10]$ | $\delta x'$ | length to center of mass | $[0, 1]$ |

**Foil geometry**

The foil geometry is determined by parameters span $S$, chord length $c_m$, thickness $t'$ and position of thickness $x'_m$, maximum chord length $c_\text{max}$,

$$\underbrace{\{S, c_m, t', x'_m\}}_{\text{foil geometry}}.$$

If the cross-sectional shape of the foils is not provided by the manufactures of the wave-propelled USV in study, a four-digit NACA-series, given by Eq. (2.109) can be chosen by measuring the cross-sectional thickness $t'$ of the foil. Alternatively, the proposed sectional shape by Eq. (2.110) can be chosen by measuring the thickness $t'$ and the position of maximum thickness $x'_m$. The sectional area is used to estimate lift and drag curves and to determine the foil's moment of inertia.

A spanwise chord distribution is needed to determine an effective rectangular wing for the foils and determine the position of this wing by positioning the wing according to the pivot point. In this work, the effective wing by span $S$ and mean chord length $c_m$ is found by assuming that the actual foil area $Sc_m = A_F$.

The position of the pivot point is found by assuming that the circulatory forces for small attack angles – which acts through the quarter-chord position – coincides between the actual wing geometry and the effective rectangular wing geometry. This is illustrated in Fig. 3.15 where the mean position of the quarter-chord positions coincide.

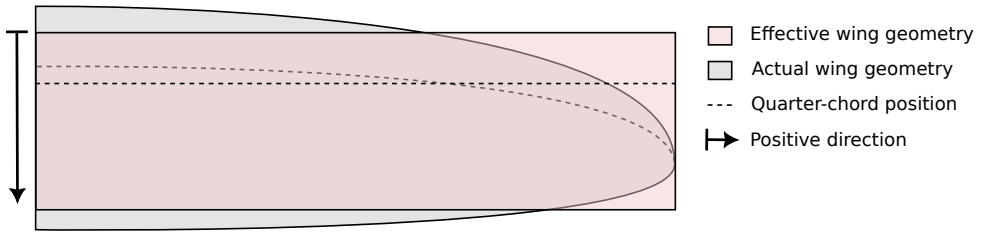


**Figure 3.15:** The foils are modeled according to an effective wing geometry by the span $S$ and mean chord length $c_m$. The mean quarter-chord positions along the span coincide.

### Lift and drag curves

Lift and drag curves for the foils through 180 degrees can be parameterized by the effective stall angle $\alpha_s$, the transition length $k_s$, detached lift coefficient $C_{Ls}$ and detached drag coefficient $C_{Ds}$ given in Sect. 2.6.3,

$$\underbrace{\{\alpha_s, k_s, C_{Ls}, C_{Ds}\}}_{\text{lift and drag curves}}.$$

The curves for a foil through 180 degrees may be found in a few sections by the experimental results in Sheldahl [54]. In the general case, one may choose to use numerical programs when the foil section geometry is determined. In this work the free software Xfoil [55] is suggested to determine the parameters for closed-form empiric expressions for lift and drag that was determined in Sect. 2.6.3. Denote the numerical lift and drag coefficients by $C_{L,\text{num}}$ and $C_{D,\text{num}}$. The parameters listed above can be determined, in order, by:

1. $C_{Ls}$ is determined by the amplitude of $C_{L,\text{num}}$ at $\alpha = 45°$ which should be equal to the lift coefficient $C_L$ in Eq. (2.131) with the nonlinear correction $C_{Ln}$ by Eq. (2.129). At $\alpha = 45°$ the lift coefficient is $(1 - C_{Ls})\pi = C_{L,\text{num}}(45°)$ which is solved for

$$C_{Ls} = 1 - \frac{C_{L,\text{num}}(45°)}{\pi}. \tag{3.105}$$

2. $C_{Ds}$ is determined by the parameter $C_{Ls}$ by the numerical drag coefficient at $\alpha = 90°$. From the drag coefficient $C_D$ in Eq. (2.131) with the nonlinear correction $C_{Dn}$ by Eq. (2.130), the amplitude at $\alpha = 90°$ is $2\pi C_{Ds}(1 + C_{Ls}) = C_{D,\text{num}}(90°)$ which is solved for

$$C_{Ds} = \frac{C_{D,\text{num}}(90°)}{2\pi C_{Ds}}. \tag{3.106}$$

   If numerical values for $C_{D,\text{num}}(90°)$ is not available, it can be estimated by the range 1.8–2.0 according to Hoerner [6].

3. $\alpha_s$ can be set as the midpoint angle between the local lift maximum $\alpha_{\max}$ at the stall angle and the following local minimum $\alpha_{\min}$. This can be illustrated by referring to Fig. 2.19 by the local maximum at about $\alpha_{\max}10°$ and the following local minimum at about $\alpha_{\min} = 15°$. An estimate for the effective stall angle is

$$\alpha_s \simeq \frac{\alpha_{\max} + \alpha_{\min}}{2}. \tag{3.107}$$

4. $k_s$ should be chosen on the order slightly larger than the stall transition length

$$k_s > |\alpha_{\min} - \alpha_{\max}|. \tag{3.108}$$

**Remark 106.** *For numerical stability in the simulation model, the parameter $k_s$ may safely be increased in order to reduce the oscillatory effects of fluttering phenomena of the foil motion by smoothing out the lift curve.*

### 3.4.2 Simulation of foil dynamics via a hybrid automata

The foils are subject to physical constraints by the connection to the struts and the foils must then be modeled as a hybrid automata. A state diagram for this hybrid model is illustrated in Fig. 3.16 with the definitions given below.

Let the state $q$ denote the case when $\vartheta < |\vartheta_{\max}|$ which the dynamics of a single foil from Eq. (3.99) with the correction given by Eq. (3.100) is

$$q: \quad M_\vartheta \ddot{\vartheta}_n + B_\vartheta \dot{\vartheta}_n + C_\vartheta \vartheta_n = C_\vartheta \theta + Q_x + \tilde{Q}_{\dot{x}} + Q_{\ddot{x}} + Q_{\text{inertia}}, \tag{3.109}$$

and the states $q_{\min}$ and $q_{\max}$ represents the dynamics at the maximum deflection $|\vartheta| = \vartheta_{\max}$ by

$$q_{\max} \text{ or } q_{\min}: \quad M_\vartheta \ddot{\vartheta}_n + B_\vartheta \dot{\vartheta}_n + C_\vartheta \vartheta_n = C_\vartheta \theta + Q_x + \tilde{Q}_{\dot{x}} + Q_{\ddot{x}} + Q_{\text{inertia}} + Q_c, \tag{3.110}$$

with the addition that $\ddot{\vartheta}_n = \ddot{\theta}$, $\dot{\vartheta}_n = \dot{\theta}$ and $\vartheta_n = \theta + \vartheta^{\max}$:

$$M_\vartheta \ddot{\theta} + B_\vartheta \dot{\theta} + C_\vartheta \vartheta^{\max} = Q_x + \tilde{Q}_{\dot{x}} + Q_{\ddot{x}} + Q_{\text{inertia}} + Q_c \tag{3.111}$$

Let $Q_c \triangleq C_\vartheta \vartheta^{\max} - M_x - Q_{\dot{x}} - Q_{\ddot{x}} + M_\vartheta \ddot{\theta} + B_\vartheta \dot{\theta}$ be the constraint moment. The set of guard conditions $\mathcal{G}$ and reset maps $\mathcal{R}$ describing the state diagram in Fig. 3.16 are:

- $\mathcal{G}(q_0, q_{\max}) : \vartheta_n - \theta > \vartheta_{\max}$ $\quad \mathcal{R}(q_0, q_{\max}) : \vartheta_n^+ = \theta - \vartheta_{\max},\ \dot{\vartheta}_n^+ = \dot{\theta},\ \ddot{\vartheta}_n^+ = \ddot{\theta}$
- $\mathcal{G}(q_0, q_{\min}) : \vartheta_n - \theta < \vartheta_{\min}$ $\quad \mathcal{R}(q_0, q_{\min}) : \vartheta_n^+ = \theta - \vartheta_{\min},\ \dot{\vartheta}_n^+ = \dot{\theta},\ \ddot{\vartheta}_n^+ = \ddot{\theta}$
- $\mathcal{G}(q_{\max}, q_0) : Q_c > 0$ $\quad \mathcal{R}(q_{\max}, q_0) : \vartheta_n^+ = \vartheta_n^-,\ \dot{\vartheta}_n^+ = \dot{\vartheta}_n^-,\ \ddot{\vartheta}_n^+ = \ddot{\vartheta}_n^-$
- $\mathcal{G}(q_{\min}, q_0) : Q_c < 0$ $\quad \mathcal{R}(q_{\min}, q_0) : \vartheta_n^+ = \vartheta_n^-,\ \dot{\vartheta}_n^+ = \dot{\vartheta}_n^-,\ \ddot{\vartheta}_n^+ = \ddot{\vartheta}_n^-$

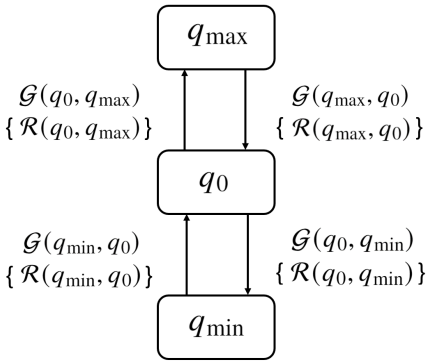


**Figure 3.16:** The foil state diagram used to describe the dynamics of a single foil. The foil is free to rotate in the state $q_0$. When the foil angle is at the maximum deflection angle, either by $q_{\max}$ or $q_{\min}$, the velocity and acceleration of the foil angle follows that of the pitch of the vehicle.

# Chapter 4

# Case study: NTNU AutoNaut

The AutoNaut is a wave-propelled USV developed and made commercially available by the British company AutoNaut Limited [71]. A case study is performed on a unique version of this vehicle – *NTNU AutoNaut* illustrated in Fig. 4.1 – owned by the Department of Engineering Cybernetics, NTNU. Steering is provided by a conventional rudder at the stern, and the vehicle is equipped with a submerged passive propulsion system. The wave-propulsion system consists of a hydrofoil placed at the bow and a pair of hydrofoils at the stern of the vehicle, both of which are passive-incidence controlled by correcting springs. A publicly available onboard navigation, communication and payload control system developed by NTNU is found online [28].

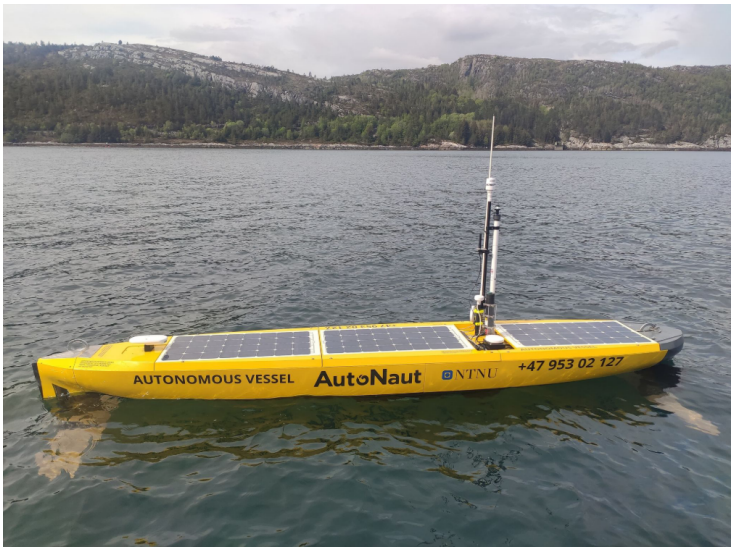


**Figure 4.1:** AutoNaut vehicle from the Department of Engineering Cybernetics, NTNU, on field operations. From Mounet et al. [67].

**Propulsion system**

The submerged hydrofoils transform wave-induced heaving and pitching motions into propulsive thrust with some minor effects of roll as well. According to AutoNaut Limited [71], the hull is designed to exploit waves that impinge on it from the side as well as on the bow and stern for additional propulsion.

Calm sea conditions pose the only real issue for wave propulsion, so an auxiliary thrust for the NTNU AutoNaut USV is an optional electric propulsion pod. The pod consists of a brush-less electric motor and a propeller in a waterproof housing, and the propulsion pod attaches to the stern strut that enables the vehicle to drive at up to 3 knots for short periods.

## 4.1 Physical dimensions

A technical illustration of the NTNU AutoNaut vehicle is shown in Fig. 4.2 with main particulars, a few of the coordinates for the pivot points for the foils and the physical limitation for the foils are shown. The model is not to scale.

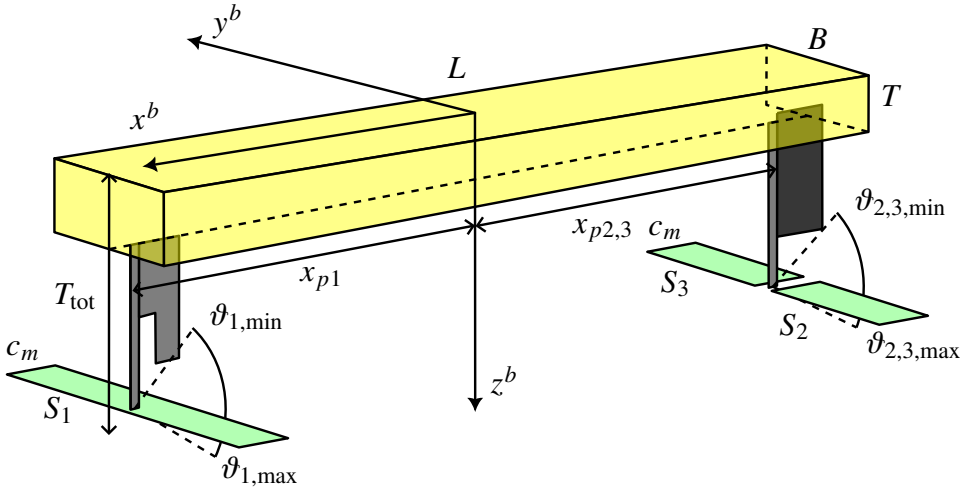


**Figure 4.2:** Technical drawing of NTNU AutoNaut. The length is taken as the overall length $L \equiv L_{\text{oa}} = 5.0$ [m], the breadth is $B = 0.8$ [m] and the length between perpendiculars is $L_{\text{pp}} = |x_{\text{p1}}| + |x_{\text{p2,3}}| = 4.7$ [m]. The draft is $T = 0.3$ [m] and the total draft is $T_{\text{tot}} = 0.8$ [m].

### 4.1.1 Main particulars

The main particulars for the AutoNaut vehicle is reported in Tab. 4.1.

**Table 4.1:** Main particulars for the 5 [m] version of the wave-propelled USV AutoNaut. Based on reported values from [3], [67] and [28].

| Main particulars and vehicle parameters | | | |
|---|---|---|---|
| Length, $L$ or $L_{oa}$ | 5.0 | [m] | |
| Length between perpendiculars, $L_{pp}$ | 4.6 | [m] | |
| Breadth at amidships, $B$ | 0.8 | [m] | |
| Draft, $T$ | 0.3 | [m] | |
| Total draft (with struts and foils), $T_{tot}$ | 0.8 | [m] | |
| Displacement mass, $\Delta$ | 250 | [kg] | |
| Block coefficient, $C_B$ | 0.505 | [-] | |
| Waterplane area coefficient, $C_{wp}$ | 0.8 | [-] | (estimated) |
| Transverse metacentric height, $GM_T$ | 0.113 | [m] | |
| Radius of gyration, $R_{66}$ | 0.25 $L_{pp}$ | [m] | |
| CG longitudinal displacement, $x_g$ | 0 | [m] | (estimated) |

### 4.1.2 Maneuvering model

The maneuvering model for this unique wave-propelled USV has been investigated by Dallolio et al. [3]. Inspired by their choice of maneuvering matrices, the reported values used in this report for model $\Sigma_1$ are given in Tab. 4.7.

**Table 4.2:** Parameters $\alpha_1^*$ used for the maneuvering model $\Sigma_1$.

| Element | Parameter | | Value | | |
|---|---|---|---|---|---|
| $\alpha_1^*[1]$ | $L_d^*$ | length of maneuvering design model | 4.6 | [m] | (5.0) |
| $\alpha_1^*[2]$ | $B_d^*$ | breadth of maneuvering design model | 0.8 | [m] | (0.8) |
| $\alpha_1^*[3]$ | $T_d^*$ | draft of maneuvering design model | 0.15 | [m] | (0.3) |
| $\alpha_1^*[4]$ | $T_1^*$ | surge period | 2.0 | [s] | |
| $\alpha_1^*[5]$ | $T_2^*$ | sway period | 4.0 | [s] | |
| $\alpha_1^*[6]$ | $T_6^*$ | yaw period | 3.0 | [s] | |

The inertia matrix was found by the design parameters given by Tab. 4.7, the empiric relations by Clarke et al. [44] reported in Tab. 3.2 and the method for estimating the added mass in surge by Eq. (3.22) from Brix [66]. In surge the total draft was used instead of the design draft. The water density was set to $\rho = 1025$ [kg/m$^3$]. An estimate for the added inertia matrix $\mathbf{M}_A$ and

the total inertia matrix $\mathbf{M}$ was found as

$$\hat{\mathbf{M}}_{\mathrm{A}} = \begin{pmatrix} 21.9\ [\mathrm{kg}] & 0 & 0 \\ 0 & 212.7\ [\mathrm{kg}] & 17.4\ [\mathrm{kg\ m}] \\ 0 & -0.0015\ [\mathrm{kg\ m}] & 252.9\ [\mathrm{kg\ m^2}] \end{pmatrix}, \tag{4.1}$$

where the matrix was symmetrized by the method $\mathbf{M}_{\mathrm{A}} = \frac{1}{2}(\hat{\mathbf{M}}_{\mathrm{A}} + \hat{\mathbf{M}}_{\mathrm{A}}^{\mathsf{T}})$ stated in Remark 29 such that the total inertia matrix was found (with $J_z = mR_{66}^2 + mx_g^2 = 330.6\ [\mathrm{kg\ m^2}]$),

$$\mathbf{M} = \begin{pmatrix} 271.9\ [\mathrm{kg}] & 0 & 0 \\ 0 & 462.7\ [\mathrm{kg}] & 8.7\ [\mathrm{kg\ m}] \\ 0 & 8.7\ [\mathrm{kg}] & 583.6\ [\mathrm{kg\ m^2}] \end{pmatrix}. \tag{4.2}$$

In Dallolio et al. [3], the off-diagonal elements were neglected and they used the values

$$\mathbf{M} = \begin{pmatrix} 277.7\ [\mathrm{kg}] & 0 & 0 \\ 0 & 462.9\ [\mathrm{kg}] & 0 \\ 0 & 0 & 593.4\ [\mathrm{kg\ m^2}] \end{pmatrix}.$$

From the periods $T_1^*$, $T_2^*$ and $T_6^*$, the damping matrix was estimated by Eq. (3.21)

$$\mathbf{B}_p = \begin{pmatrix} 136.0\ [\mathrm{kg/s}] & 0 & 0 \\ 0 & 115.6\ [\mathrm{kg/s}] & 0 \\ 0 & 0 & 194.5\ [\mathrm{m\ kg/s}] \end{pmatrix}, \tag{4.3}$$

which in [3] the following damping was used

$$\mathbf{B}_p = \begin{pmatrix} 138.85\ [\mathrm{kg/s}] & 0 & 0 \\ 0 & 115.73\ [\mathrm{kg/s}] & 0 \\ 0 & 0 & 197.8\ [\mathrm{m\ kg/s}] \end{pmatrix}.$$

**Remark 107.** *According to conversations with Øveraas [72], the reported values in the damping matrix in [3] might be off by a factor of 10, as the surge damping coefficient might be as little as $B_{p11} = 10$ [kg/s].*

The Coriolis and centripetal matrix $\mathbf{C}$ is calculated from Eq. (3.9), which is recomputed during simulations is not.

In the simulation model, additional viscous damping $\mathbf{B}_v$ is required for increased stability in the maneuvering model. Viscous damping in surge and sway was used:

$$\mathbf{B}_v(\boldsymbol{\nu}_{\mathrm{r}}) = \begin{pmatrix} 347.13|u_{\mathrm{r}}| & 0 & 0 \\ 0 & 289.33|v_{\mathrm{r}}| & 0 \\ 0 & 0 & 0 \end{pmatrix}. \tag{4.4}$$

### Current model

A constant ocean current with cardinal direction $\beta_{V_c}$ and magnitude $V_c$ is used in the simulation – a 2D irrotational model – such that the relative velocity $\boldsymbol{\nu}_r = \boldsymbol{\nu} - \boldsymbol{\nu}_c$ is calculated by the currents given in the body frame with

$$\boldsymbol{\nu}_c = \mathbf{R}_z(\beta_{V_c} - \psi)^\top \boldsymbol{\nu}_c^n = [u_c, v_c, 0]^\top. \tag{4.5}$$

**Table 4.3:** Ocean current simulation settings.

| Ocean current | | |
|---|---|---|
| Ocean current cardinal direction, $\beta_{V_c}$ | $[0°, 360°)$ | [deg] |
| Ocean current magnitude, $V_c$ | $[0, 1]$ | [m/s] |
| Ocean current constant in Gauss-Markov process, $T_c$ | 0 | [s] |

### Steering model parameters

The parameters in the steering model were identified in Dallolio et al. [3]. Reported values in accordance with the notation and methods in Sect. 2.7 are listed in Tab. 4.4. The rudder force vector $\tau_{\text{rudder}}$ is calculated by Eq. (2.182).

**Table 4.4:** NTNU AutoNaut steering model parameters. Obtained from Dallolio et al. [3].

| Steering parameters | | |
|---|---|---|
| Rudder area, $A_R$ | 0.11 | [$m^2$] |
| Aspect ratio, $\Lambda_R$ | 1.68 | [-] |
| Longitudinal rudder position coordinate, $x_R$ | -2.3 | [m] |
| Rudder coefficient, $C_{NR}$ | 1.56 | [-] |
| Drag coefficient, $t_R$ | 0.3 | [-] |
| Force factor, $a_{HR}$ | 0.2 | [-] |
| Interaction coefficient, $x_{HR}$ | -1.8 | [-] |

### Steering machine dynamics

A simplified representation of the steering machine dynamics is suggested by Van Amerongen [73] for simulation purposes, in which the maximum rudder angle $\delta_{\max}$, and rudder rate $\dot{\delta}_{\max}$ are specified according to Fig. 4.3. The rudder angle on the AutoNaut vehicle is limited to $\delta \in [-45°, 45°]$ [3], and the rudder rate limit was set to $\delta_{\max} = 5°$ [$s^{-1}$]. According to Fossen [4], for most commercial ships, the rudder rate limiter is $\dot{\delta}_{\max} \geq 2.3°$ [$s^{-1}$].

A simple transfer function from commanded rudder control to rudder was simulated by

$$\delta(s) = \frac{1}{1 + T_\delta s}\delta_c(s), \tag{4.6}$$

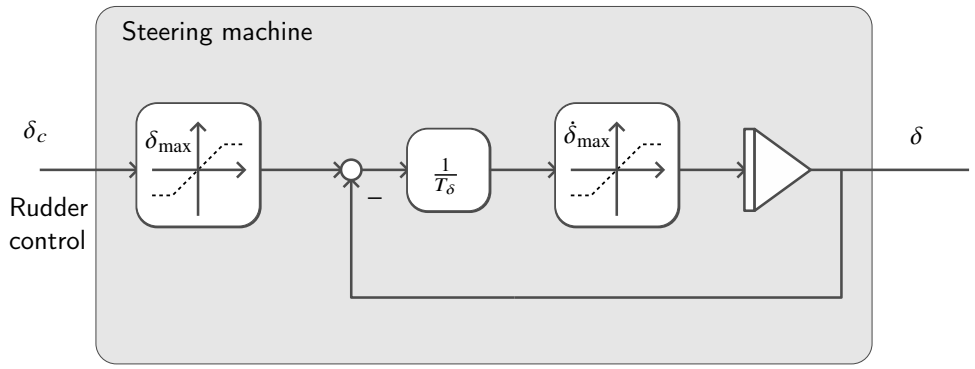


**Figure 4.3:** Diagram of simplified rudder control loop. Based on Van Amerongen [73] and Fossen [4] with the time constant $T_\delta$.

where the rudder time constant was set to $T_\delta = 0.2$ [s] in the simulation model with the constraints shown in Fig. 4.3.

### Wind model

The parameters in the wind model was identified in Dallolio et al. [3]. Reported values in accordance with the notation in Sect. 3.2 are listed in Tab. 4.5. The wind force vector $\tau_{\text{wind}}$ is calculated by Eq. (3.11) for air density $\rho_a = 1.25$ [kg/m$^3$]. In the simulation, a constant wind direction $\beta_{V_w}$ and magnitude $V_w$ are used without gust.

**Table 4.5:** NTNU AutoNaut wind model parameters. From Dallolio et al. [3].

| Wind parameters | | |
|---|---|---|
| Wind coefficient $x$-direction, $c_x$ | 0.50 | [-] |
| Wind coefficient $y$-direction, $c_y$ | 0.70 | [-] |
| Wind coefficient $z$-moment, $c_n$ | 0.05 | [-] |
| Frontal projected area, $A_{\text{Fw}}$ | 0.195 | [m$^2$] |
| Lateral projected area, $A_{\text{Lw}}$ | 1.5 | [m$^2$] |
| Length over all, $L_{\text{oa}}$ | 5.0 | [m] |

**Table 4.6:** Wind simulation settings.

| Wind | | |
|---|---|---|
| Wind cardinal direction, $\beta_{V_w}$ | $[0°, 360°)$ | [deg] |
| Wind magnitude, $V_w$ | $[0, 10]$ | [m/s] |
| Wind constant in Gust process, $T_w$ | 0 | [s] |

### 4.1.3 Wave-induced motion parameters

Wave-induced motion was investigated by Mounet et al. [67] for the frequency-domain response of the specific AutoNaut vehicle in study with medium spring stiffness. They found the weight-averaged tuning parameters reported in Tab. 4.7 by data points obtained by the field trials shown in Fig. 4.4.

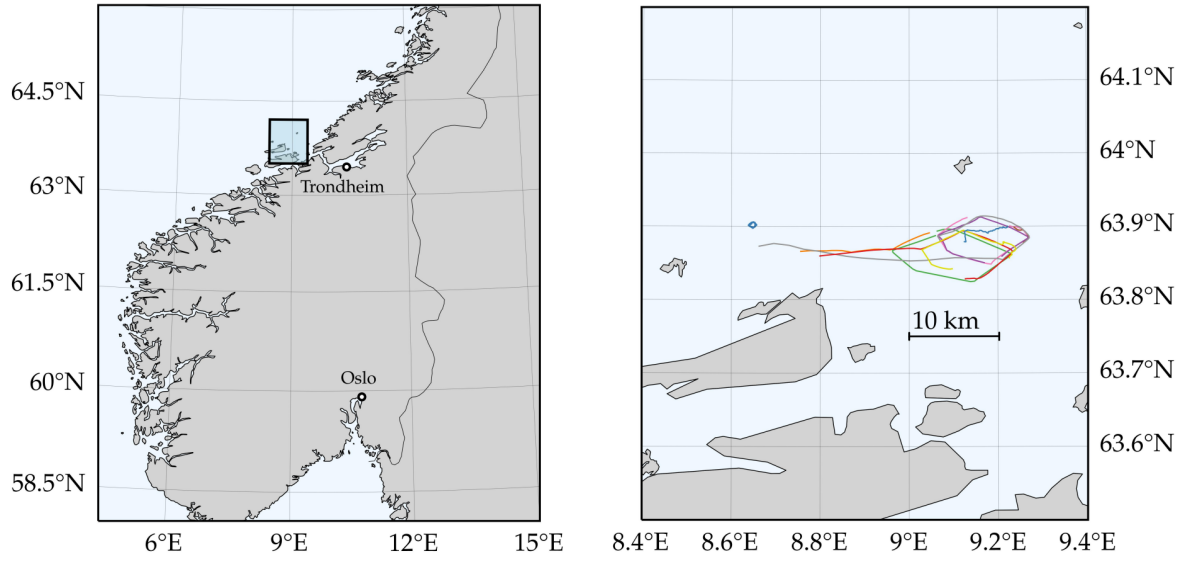


**(a)** Area of study: Frohavet. **(b)** Frohavet.

**Figure 4.4:** AutoNaut field operations from March/April 2022. Facsimile from Mounet et al. [67]

We see that the effective model of the AutoNaut vehicle is represented by main dimensions that are slightly longer and wider than the actual dimensions, and the draft is about the same.

#### Fluid memory effects

The transversal aspect ratio of the effective model is $\tilde{\Lambda}_{\mathrm{T}}^{*} = \tilde{B}^{*}/\tilde{T}^{*} = 4.31$. From the empiric equations for the fluid memory effects parameters in Eq. (3.80), the parameters for the non-dimensional transfer function for fluid memory effects in heave and pitch motion are

$$q_0' = 0.459, \quad p_0' = 0.489, \quad p_1' = 0.701,$$

and the geometric constant $C_{\mathrm{geo},3} = \tilde{L}^{*}$ for heave makes

$$q_0 = 27952, \quad p_0 = 7.76, \quad p_1 = 2.79, \qquad \text{(parameters for heave)} \tag{4.7}$$

and the geometric constant $C_{\mathrm{geo},5} = LT\mathrm{GM}_{\mathrm{L}}$ for pitch makes

$$q_0 = 87986, \quad p_0 = 7.76, \quad p_1 = 2.79, \qquad \text{(parameters for pitch)} \tag{4.8}$$

for the approximation $\mathrm{GM}_{\mathrm{L}} = \frac{1}{12}\tilde{L}^{*2}/\tilde{T}^{*}$.

**Table 4.7:** Parameters $\boldsymbol{\alpha}_2^*$ used for the maneuvering model $\Sigma_2$. Weight-averaged tuning parameters from in-situ measurements of the NTNU AutoNaut vehicle from the operations shown in Fig. 4.4. Optimal values obtained from Mounet et al. [67].

| Element | Parameter | | Value | | |
|---|---|---|---|---|---|
| $\boldsymbol{\alpha}_2^*[1]$ | $\tilde{L}^*$ | effective length | 6.146 | [m] | ( 5.0 ) |
| $\boldsymbol{\alpha}_2^*[2]$ | $\tilde{B}^*$ | effective breadth | 1.236 | [m] | ( 0.8 ) |
| $\boldsymbol{\alpha}_2^*[3]$ | $\tilde{T}^*$ | effective draft | 0.287 | [m] | ( 0.3 ) |
| $\boldsymbol{\alpha}_2^*[4]$ | $\tilde{\mathrm{GM}}_{\mathrm{T}}^*$ | eff. transversal metacentric height | 0.845 | [m] | |
| $\boldsymbol{\alpha}_2^*[5]$ | $\tilde{C}_{\mathrm{wp}}^*$ | eff. waterplane area coefficient | 0.683 | [-] | |
| $\boldsymbol{\alpha}_2^*[6]$ | $\delta_{\mathrm{geo}}^*$ | ratio of aft beam length to overall length | 0.149 | [-] | |
| $\boldsymbol{\alpha}_2^*[7]$ | $\mu_B^*$ | ratio viscous damping to critical damping | 0.110 | [-] | |
| | $d^*$ | longitudinal distance from IMU to CG | 1.705 | [m] | |

**Table 4.8:** Fluid memory effects parameters for the effective monohull geometry for motions in pitch and heave.

| Fluid memory effects | | |
|---|---|---|
| Parameter $q_0$ | 27952 / 87986 | pitch / heave |
| Parameter $p_0$ | 7.76 | |
| Parameter $p_1$ | 2.79 | |

The matrices for the wave-induced motion was found with the parameters $\boldsymbol{\alpha}_2$. The inertia matrix with added inertia $\mathbf{M}_{\mathrm{rao}}$ was from Eq. (3.62), the damping matrix $\mathbf{B}_{\mathrm{rao}}(\omega_{\mathrm{e}})$ was found from Eq. (3.63) and the restoring matrix $\mathbf{C}_{\mathrm{rao}}$ was found from Eq.(3.64). In practical simulations, the longitudinal metacentric height $\mathrm{GM_L}$ was not used, and the matrices was scaled accordingly. The damping matrix was evaluated at the encounter frequency $\omega_{\mathrm{e}}$ when simulated for a single wave frequency, whereas the fluid memory filter should be added for a general simulation model capable of simulating the vehicle response in irregular sea.

### 4.1.4 Wave-propulsion model

The wave-propulsion model $\Sigma_3$ was determined by measuring the position of the foils, approximating their geometry in order to assess the hydrodynamics forces involved, and by identifying the variable spring stiffness on the USV.

#### Positions and deflection angles

According to AutoNaut Ltd. [28], the total draft of this wave-propelled USV is about 0.8 [m]. This depth should include the total length of the struts and the maximum depth of the foils when the angles $\vartheta_i$ for $i = 1, 2, 3$ are turned at maximum. The vertical length of the struts was however measured below the hull line, marked by the line between the black and yellow paint on the physical vehicle from Fig. 4.1, to about 0.6 [m]. With the maximum deflection of the foils, this indicates a total draft of about 0.7 [m]. This length was however estimated as a measure from the design draft length of $T_\mathrm{d} = 0.15$ [m]. In correspondence with Johansen [74], strut lengths of 0.7 [m] – corresponding to vertical coordinate in the pivot positions – was employed in the simulation model. The positions of pivot points for the foil at the bow and the pair of foils at the stern, given in the body frame, are

$$\mathbf{r}^b_{\mathrm{p},1} = \begin{pmatrix} 2.4\ [\mathrm{m}] \\ 0\ [\mathrm{m}] \\ 0.7\ [\mathrm{m}] \end{pmatrix}, \quad \text{(foil mounted at bow)}, \tag{4.9a}$$

$$\mathbf{r}^b_{\mathrm{p},2} = \begin{pmatrix} -2.3\ [\mathrm{m}] \\ -0.3\ [\mathrm{m}] \\ 0.7\ [\mathrm{m}] \end{pmatrix}, \quad \mathbf{r}^b_{\mathrm{p},3} = \begin{pmatrix} -2.3\ [\mathrm{m}] \\ 0.3\ [\mathrm{m}] \\ 0.7\ [\mathrm{m}] \end{pmatrix}. \quad \text{(pair of foils at the stern)} \tag{4.9b}$$

The lateral coordinate for the pair of foils at the stern is included for evaluation of the local fluid velocity field for finding the forces on the foils. The longitudinal positions were found by setting the distance $x^b_\mathrm{p}[1] - x^b_\mathrm{p}[2] = L_\mathrm{pp} = 4.7$ [m].

The physical limits in the deflection angles for the foils were measured by analyzing the images given in Figs. 4.5 and 4.6, where the limits was determined by $\pm 50°$ and $\pm 45°$ respectively,

$$\boldsymbol{\vartheta} = \begin{pmatrix} \vartheta_1 \\ \vartheta_2 \\ \vartheta_3 \end{pmatrix}, \quad \boldsymbol{\vartheta} \leq \boldsymbol{\vartheta}_\mathrm{max} = \begin{pmatrix} 50° \\ 45° \\ 45° \end{pmatrix}. \tag{4.10}$$

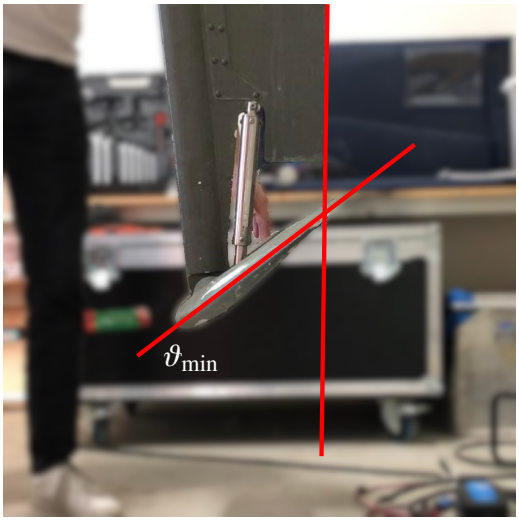


**(a)** Measured angle $\vartheta_{\text{min}} = -51° \pm 1°$.

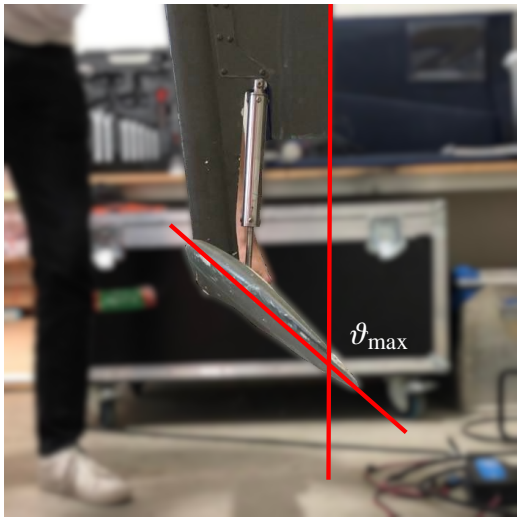


**(b)** Measured angle $\vartheta_{\text{max}} = 49° \pm 1°$.

**Figure 4.5:** The foil at the bow is limited to $\vartheta_1 \in [-50°, 50°]$. The angles are defined relative to the vehicle's axis $x^b$. In the images, it was measured relative to the vertical line of $z^b$ and converted. Adapted from Tufte [17].

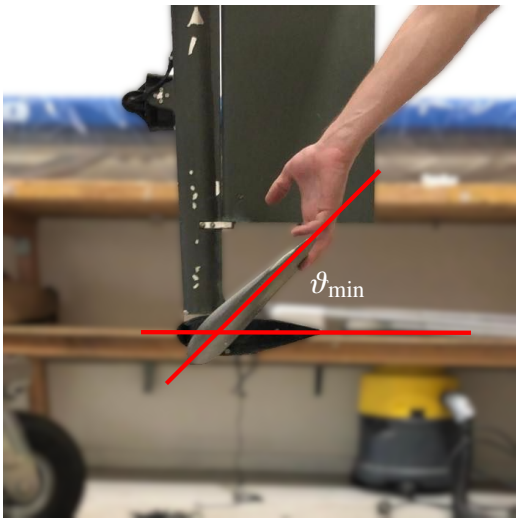


**(a)** Measured angle $\vartheta_{\text{min}} = -46° \pm 1°$.

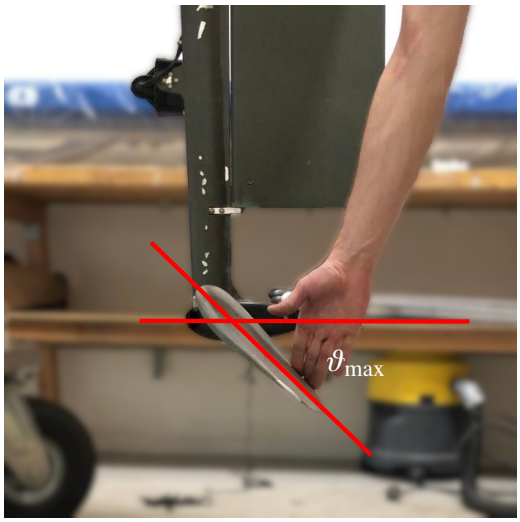


**(b)** Measured angle $\vartheta_{\text{max}} = 44° \pm 1°$.

**Figure 4.6:** The pair of foils at the stern is limited to $\vartheta_{2,3} \in [-45°, 45°]$. The angles were measured relative to the vehicle's axis $x^b$. Adapted from Tufte [17].

**Table 4.9:** Parameters $\boldsymbol{\alpha}_3^*$ used in the maneuvering model $\Sigma_3$.

| Element | Parameter | | Value | |
|---|---|---|---|---|
| $\boldsymbol{\alpha}_3^*[1]$ | $S^*$ | span | 1.3 | [m] |
| $\boldsymbol{\alpha}_3^*[2]$ | $c_m^*$ | mean chord length | 0.192 | [m] |
| $\boldsymbol{\alpha}_3^*[3]$ | $t'^*$ | chord thickness | 0.15 | |
| $\boldsymbol{\alpha}_3^*[4]$ | $x_m'^*$ | point of maximum thickness | 0.20 | |
| $\boldsymbol{\alpha}_3^*[5]$ | $\alpha_s^*$ | effective stall angle | 12° | |
| $\boldsymbol{\alpha}_3^*[6]$ | $k_s^*$ | stall transition length | 10° | |
| $\boldsymbol{\alpha}_3^*[7]$ | $C_{Ls}^*$ | detached lift coefficient | 0.653 | |
| $\boldsymbol{\alpha}_3^*[8]$ | $C_{Ds}^*$ | detached drag coefficient | 0.286 | |
| $\boldsymbol{\alpha}_3^*[9]$ | $x_{\mathrm{p}}'^*$ | pivot point length from LE | 0.209 | |
| $\boldsymbol{\alpha}_3^*[10]$ | $\delta x'^*$ | center of mass length from LE | 0.370 | |
| $\boldsymbol{\alpha}_3^*[11]$ | $T_\vartheta^*$ | damping period | 0.05 | [s] |

### Span of the foils

The chord distribution along the span was found by sketching the contour of the foils on a sheet of paper, included in Appendix **??**. Data points from this measurement are available in Tab. D.1. From the contour, the identified span of the foils were identical for the foil mounted at the bow and for the total span of the pair of foils mounted at the stern with $S = 1.3$ [m]. The maximum chord length was measured directly as $c_{\max} = 0.23$ [m].

The projected area of the foils were estimated by the contours given in Fig. D.1, with

$$A_{\mathrm{F}\,1} = 0.248\ [\mathrm{m}^2], \quad A_{\mathrm{F}\,2,3} = 0.127\ [\mathrm{m}^2], \tag{4.11}$$

from which the foil area $A_{\mathrm{F}} = 0.250$ [m$^2$] was decided to be used for the foil at the bow and for the combined area of the pair of foils at the stern. The mean chord length was found from the area to be $c_m = 0.192$ [m].

A non-dimensional parametrization of Eqs. (2.107a) and (2.107b) was found with the curvature parameters $q_l = 2.0$ and $q_t = 3.0$. The tip of the wing from trailing edge was measured at the distance $x'_e = 0.075$, where the prime notation in this context denotes per half span. The chord length was found to follow

$$x'_{\mathrm{LE}} = 0.075 + 0.275\left(1.0 - y^2\right)^{1/2}, \tag{4.12a}$$

$$x'_{\mathrm{TE}} = 0.075 - 0.075\left(1.0 - y^3\right)^{1/3}, \tag{4.12b}$$

and a comparison of the hand sketch and the model by Eq. (4.12) is illustrated in Fig. 4.7.

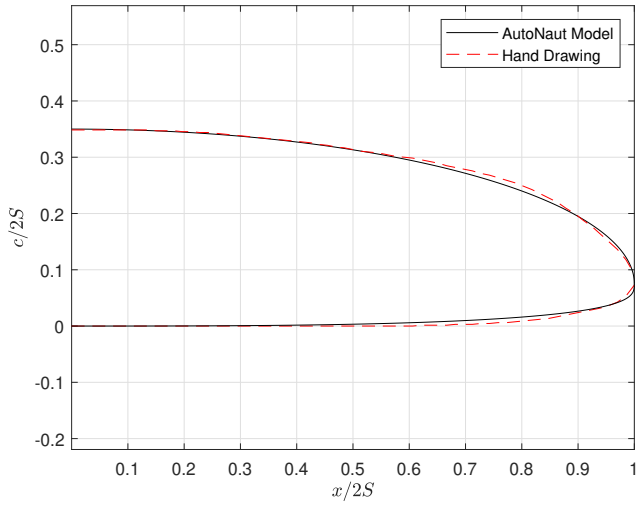


**Figure 4.7:** Comparison of the projected foil shape to the identified model. The simple super-elliptic curvature found in Eq. (4.12) approximated the shape to a reasonable degree according to the hand sketch, which was found by the tabular values in Tab. D.1.

### Sectional characteristics

The sectional shape of the foils is shown in Fig. 4.9 and were assumed identical for all of the foils. The thickness was measured to $t' = 0.15$ meaning that linear foil theory developed in Sect. 2.6 indeed is applicable according to Def. 18 on NTNU AutoNaut. The shape however was not a standardized NACA section, so the proposed method given in Sect. 2.6.1 was employed where the position of maximum thickness was measured as $x'_m = 0.20$.

From the section given by Eq. (2.111) and the assumption of homogeneous mass density from Assumption 21, the center of mass was inspired by the calculation by Tufte [17] and found to be

$$x'_{\mathrm{g}} = \frac{2}{a'_{\mathrm{F}}} \int_0^1 x' \cdot y'_{\mathrm{TUFTE}}(0.15, 0.20)\, \mathrm{d}x' = 0.37, \tag{4.13}$$

where $a'_{\mathrm{F}} = 0.0854$ is the cross sectional area.

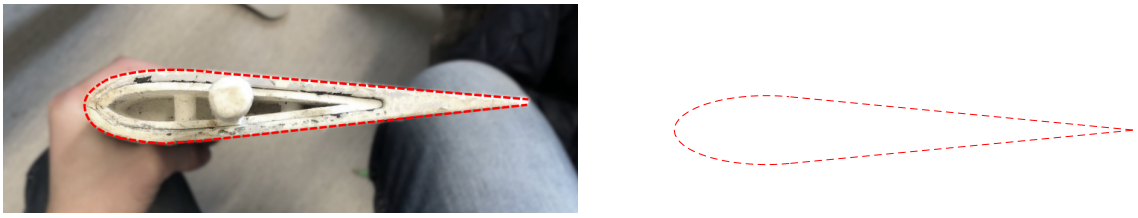

**(a)** Physical section. Adapted from Tufte [17]. **(b)** Foil profile with $t' = 0.15$ and $x'_m = 0.20$.

**Figure 4.8:** Comparison of the physical foil section on NTNU AutoNaut to the left, and identified section by Eq. (2.111) to the right. The physical section contains a nonzero trailing edge.

### Spring stiffness

The foil at the bow is attached by a linear spring, which can be seen in Fig. 4.5. For NTNU AutoNaut, the available spring settings are listed in Tab. 4.10. The spring is assumed ideal by Hooke's law and acts with the force $-k\delta l$, where $k$ [N/m] is the spring stiffness and $\delta l$ [m] is the perturbation distance representing a compression or stretch of the spring from equilibrium. The spring was measured to be attached at the distance $x_s = 60$ [mm] from the pivot point. The linearized spring moment around $\vartheta = 0$ is

$$-\kappa\vartheta = \underbrace{x_s}_{\text{arm}} \cdot \underbrace{(-kx_s\vartheta)}_{\text{moment}}, \quad \Longrightarrow \quad \kappa_{\text{lin.}} = kx_s^2.$$

The pair of foils mounted at the stern is passively controlled by a pair of closed wound torsion springs, shown in Fig. 4.11.

The spring constant for the pair of springs at the stern was constant. The stiffness was estimated by use of Castigliano's method to find the deflection in radians in the body of a torsion spring from an externally applied moment according to Timoshenko [75], see Appendix B.5. The spring parameters are listed in Tab. 4.11 and found by Eq. (B.33) with

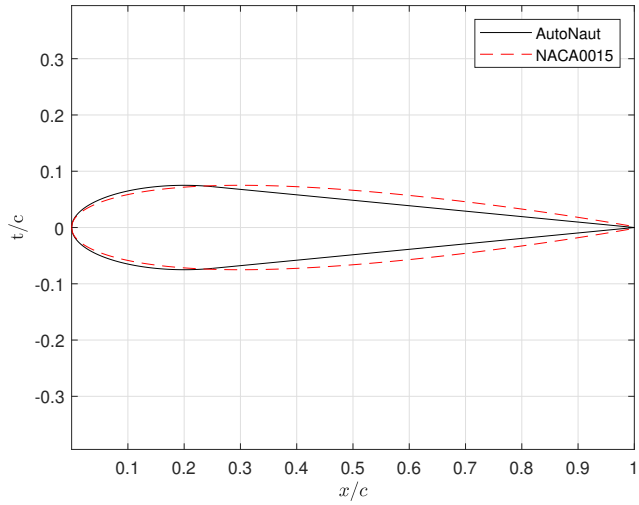


**Figure 4.9:** Comparison of foil sections from the identified empiric model in Eq. (2.110) of NTNU AutoNaut, compared to standardized NACA0015 section given by Eq. (2.109). The foil thickness is $t' = t/c = 0.15$ occurring at $x'_m = 0.20$. The actual section is slimmer with a straight trailing edge.

**Table 4.10:** Spring settings for the foil at the bow on NTNU AutoNaut.

| Spring setting | | | Lin. torsion stiffness | |
|---|---|---|---|---|
| Soft spring stiffness, $k_{\text{soft}}$ ($\kappa_{\text{f,soft}}$) | 1.226 | [N/mm] | 4.41 | [Nm/rad] |
| Medium stiff spring stiffness, $k_{\text{med.}}$ | 2.20 | [N/mm] | 7.92 | [Nm/rad] |
| Stiff spring stiffness, $k_{\text{stiff}}$ | 5.40 | [N/mm] | 19.4 | [Nm/rad] |

$$\kappa_{\text{a}} = \frac{Ed^4}{64DN_{\text{a}}},$$

with the result of $\kappa_{\text{a}} = 5.25$ [Nm/rad].

### Foil inertia

A sectional foil piece of length 0.44 [m] from NTNU AutoNaut was measured with mass of 1.240 [kg]. With the assumption of homogeneous mass density of the wings from Assumption 21, an estimate of the total mass of the foil at the bow and the pair of foils at the stern is about 3.5 [kg].

[1]The actual value was not measured. The approximate values was found from tables on steel characteristics. A value of 200 GPa was employed in the simulation.

[2]The actual value was not measured. The values was approximated from studying Fig. 4.11b

[3]When the pair of foils at the stern is considered as a single foil, the equivalent spring stiffness is doubled

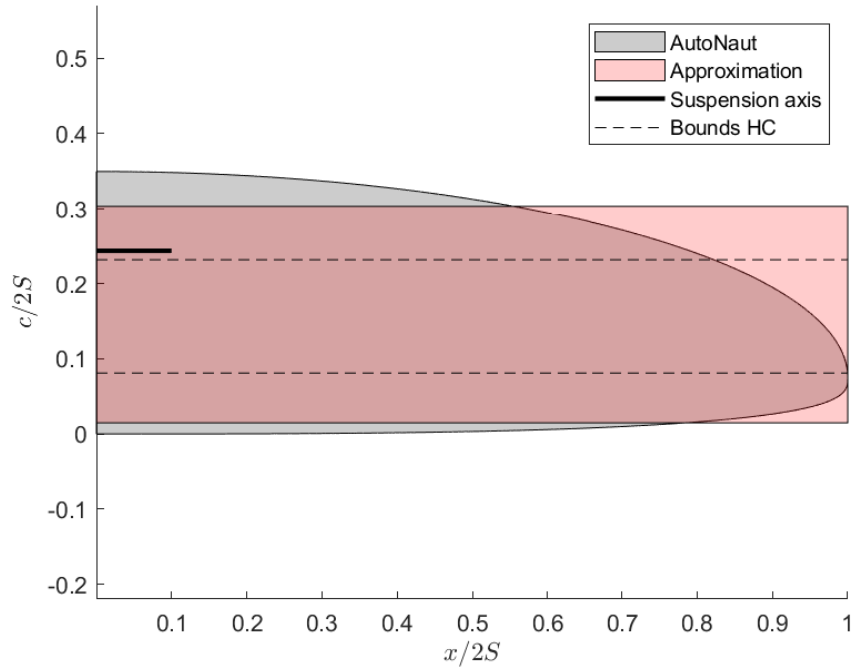


**Figure 4.10:** The wing approximation used for NTNU AutoNaut in which the rectangular shape was found by weighting the quarter-chord chord length from leading edge (top edge). The pivot point is denoted by suspension axis and the bounds for hydrodynamic center (HC), in dashed lines, represents the possible positions for the center of pressure.

**Remark 108.** *Calculations from the assumption of the wing being neutrally buoyant in Assumption 18 indicates a foil mass of about* $m_F = S\rho a'_F c_m^2 = 4.19$ *[kg] where* $\rho$ *is the sea density. Note that this calculation is based on the rectangular approximation, which overestimates the volume since the rectangular section was determined through the projected wing area without consideration of the volume. The assumption may however be considered valid for the foil dynamics since the rough estimation only indicates about 15 % discrepancy.*

From Remark 108 the actual foil density might be slightly buoyant with $\rho_{\mathrm{F}} = 900$ [kg/m$^3$]. Since the foil moment of inertia scales with the square of the chord length, the slightly lower mass density of $\rho_{\mathrm{F}} = 500$ [kg/m$^3$] calculated on the rectangular foil resulted in the moment of inertia

$$J_{\mathrm{F}} = 0.109 \text{ [kg m}^2\text{]}. \tag{4.14}$$

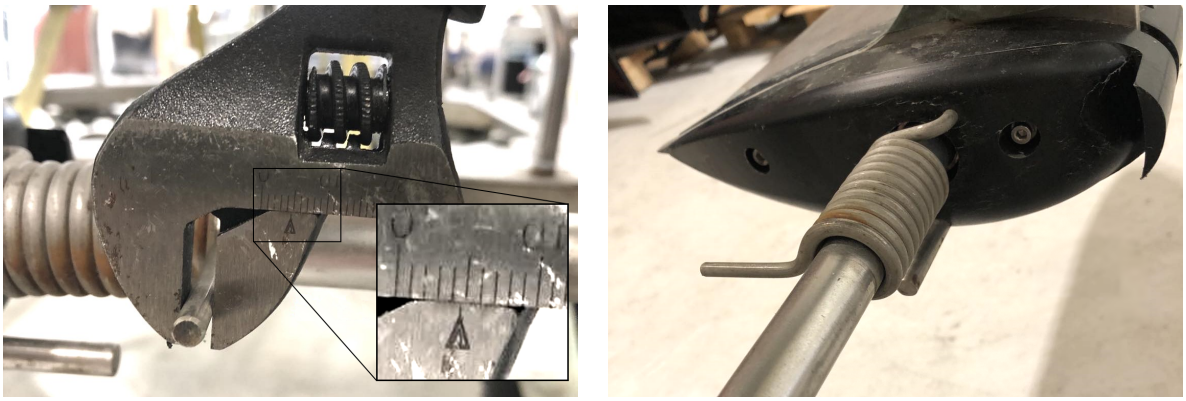

**(a)** Spring wire diameter was measured to 4.7 [mm]. **(b)** Number of active turns is $N_a = 10.3$.

**Figure 4.11:** Pair of closed-wound torsion springs attached at the stern. The spring wire diameter is shown to the left and the number of active turns is shown to the right.

**Table 4.11:** Parameters for the pair of closed wound torsion springs at the stern on NTNU AutoNaut.

| Spring parameter | | | |
|---|---|---|---|
| Number of active turns, $N_a$ | 10.3 | [-] | |
| Young's modulus, $E$ | 180–210 | [GPa] | (assumed[1]) |
| Spring wire diameter, $d$ | 4.7 | [mm] | |
| Mean coil diameter, $D$ | $6d \pm 1d$ | [mm] | (estimated[2]). |
| Spring stiffness, $\kappa_a$ | 4.1–6.6 | [Nm/rad] | (uncertainty) |
| Spring stiffness in simulation, $\kappa_a^*$ | 5.25 | [Nm/rad] | |
| Effective spring stiffness, $\kappa_a$ | 10.5 | [Nm/rad] | (eff. foil[3]) |

### List of geometrical parameters

In this work, the foil parameters listed in Tab. 4.12 has been identified by measuring the foils.

**Table 4.12:** NTNU AutoNaut geometric dimensions of the hydrofoil.

| Hydrofoil parameters | Value | Unit | |
|---|---|---|---|
| Foil span, $S$ | 1.30 | [m] | |
| Foil area, $A_{\mathrm{F}}$ | 0.250 | [$\mathrm{m}^2$] | |
| Mean chord length, $c_m$ | 0.192 | [m] | |
| Maximum chord length, $c_{\max}$ | 0.228 | [m] | |
| Tip distance from TE, $x_e$ | 0.05 | [m] | |
| Aspect ratio, $\Lambda_{\mathrm{F}}$ | 6.77 | [-] | |
| Pivot point from LE, $x'_p$ | 0.209 | [-] | |
| Center of mass from LE, $x'_{\mathrm{g}}$ | 0.37 | [-] | |
| Foil maximum thickness, $t'$ | 0.15 | [-] | |
| Position of maximum thickness from LE, $x'_m$ | 0.20 | [-] | |
| Mass, $m_{\mathrm{F}}$ | 3.5 | [kg] | (estimated[4]) |
| Moment of inertia, $J_{\mathrm{F}}$ | 0.109 | [kg $\mathrm{m}^2$] | (estimated[5]) |
| Curvature parameter LE, $q_l$ | 2.0 | [-] | |
| Curvature parameter TE, $q_t$ | 3.0 | [-] | |

### Lift and drag curves

The program Xfoil with the identified section given by Eq. (2.111) with thickness $t' = 0.15$ and its position $x'_m = 0.20$ were used to estimate numerically the lift curve. Lift, drag and normal coefficients from Eq. 2.131 are plotted in Fig. 4.12. The effective stall angle $\alpha_s = 12°$ and the transition length $L_s$ was set to 10°. The detached lift coefficient was found as $C_{Ls} = 0.653$ and the drag coefficient was determined according to the method in Sect. 3.4.1 by the drag coefficient amplitude 1.8 such that $C_{Ds} = 0.286$.

For practical reasons to avoid fluttering phenomena on the foil dynamics, the transition length was increased five-fold to $L_s = 50°$. The lift, drag and normal coefficients used in the simulation was therefor used with the curves in Fig. 4.13.

### Kinematic considerations

The relative fluid velocities to evaluate the forces on the foils was found with the USV linear motion $\mathbf{v}^b_{\mathrm{nb}}$ with the added kinematic relation from Eq. (2.6) with the position of the pivot points by $\mathbf{r}^b_{\mathrm{p}}$, from the velocity of the waves $\mathbf{v}^n_{\mathrm{waves}} = \boldsymbol{\nabla}\Phi^n$ from Eq. (2.47) where $\Phi^n$ is the wave

[4]The total mass of the foil is estimated by a sectional piece, and the total mass was hence not measured.

[5]a mass density of $\rho = 500$ [kg/$\mathrm{m}^3$] allowed calculation of moment of inertia from the sectional shape and mean chord length along the span

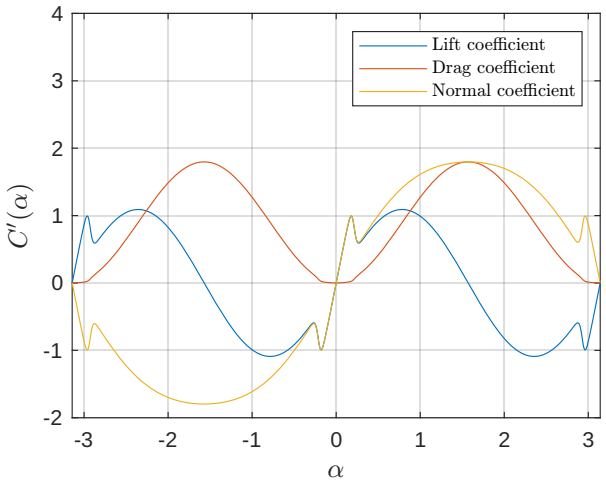


**Figure 4.12:** Approximation for lift, drag and normal coefficients identified for the foil section on NTNU AutoNaut.

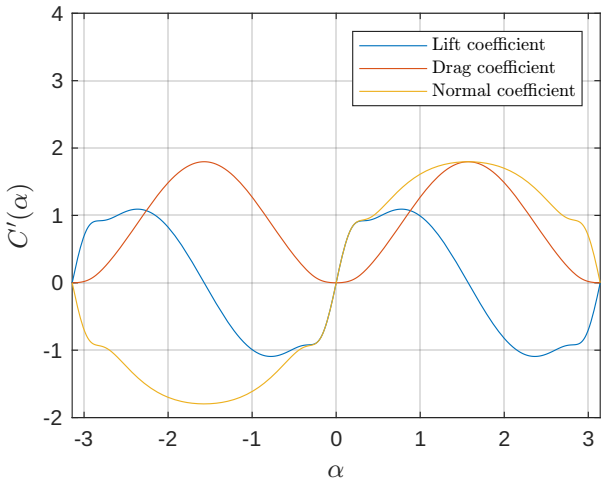


**Figure 4.13:** Lift, drag and normal coefficients used in the simulation model for NTNU AutoNaut to avoid fluttering phenomena.

potential and the current velocity $\mathbf{v}_{\mathrm{c}}^b = \mathbf{v}_c^b = \mathbf{R}_n^b(\boldsymbol{\Theta}_{\mathrm{nb}})\boldsymbol{\nu}_c$. Since the body angular velocities is not simulated directly, they were found from the Euler angles $\boldsymbol{\Theta}_{\mathrm{nb}}$ with the assumption of zero roll angle. From Eq. (2.18), the body angular velocities was found with $\boldsymbol{\omega}_{\mathrm{nb}}^b = \mathbf{T}(\boldsymbol{\Theta}_{\mathrm{nb}})^{-1}\dot{\boldsymbol{\Theta}}_{\mathrm{nb}}$. The relative velocities used for calculating the circulatory forces on the vehicle was

$$\mathbf{v}_{\mathrm{rp}}^b = \underbrace{\mathbf{v}_{\mathrm{nb}}^b + \mathbf{S}(\mathbf{r}_{\mathrm{bp}}^b)^\top \mathbf{T}(\boldsymbol{\Theta}_{\mathrm{nb}})^{-1}\dot{\boldsymbol{\Theta}}_{\mathrm{nb}}}_{\text{motion of pivot point}} \underbrace{-\mathbf{v}_{\mathrm{c}}^b - \mathbf{R}_n^b(\boldsymbol{\Theta}_{\mathrm{nb}})[\boldsymbol{\nabla}\Phi^n]\Big|_{\mathbf{r}=\mathbf{r}_{\mathrm{p}}}}_{\text{- fluid motion}}, \tag{4.15}$$

where $\mathbf{r}_{\mathrm{bp}}^b$ is the position of the pivot points for the foil in consideration and the wave velocity is evaluated at the pivot point $\mathbf{r}_{\mathrm{p}}$.

For evaluations of non-circulatory forces, a time-differentiation of Eq. (4.15) can be employed. However, this acceleration should be evaluated at the midpoint of the foil for the linear added mass force. For practical implementation of the simulation model, it was necessary to find an analytical expression for the kinematic for twice homogeneous transformations to be evaluated for the foils. A derivation for the use in the simulation model can be found in Appendix B.4.

## 4.2 Complete model

A complete model of NTNU AutoNaut based on the method in this work is presented in this section to showcase the

### 4.2.1 Equations of motion for unified model architecture

The USV model is split into a maneuvering part $\Sigma_1$, with position denoted $\boldsymbol{\eta}_m$ in this context, and a seakeeping part $\Sigma_2$ with the perturbation coordinates $\boldsymbol{\xi}$. Fluid memory effects are incorporated in the seakeeping model $\Sigma_2$ by an approximate state-space and non-stationary circulatory effects are incorporated in the foil dynamics $\Sigma_3$ with a velocity-dependent state-space model. The foil dynamics is driven by the joint motion of the maneuvering motion and the seakeeping motion, corrected by inertia forces and simulated as a hybrid model according to Sect. 3.4.2.

$$
\begin{aligned}
\dot{\boldsymbol{\eta}}_{\mathrm{m}} &= \mathbf{J}_{\Theta}(\boldsymbol{\eta}_{\mathrm{m}})[\boldsymbol{\nu}_{\mathrm{c}} + \boldsymbol{\nu}_{\mathrm{r}}], \\
\mathbf{M}\dot{\boldsymbol{\nu}}_{\mathrm{r}} + \mathbf{C}(\boldsymbol{\nu}_{\mathrm{r}})\boldsymbol{\nu}_{\mathrm{r}} + \mathbf{B}(\boldsymbol{\nu}_{\mathrm{r}})\boldsymbol{\nu}_{\mathrm{r}} &= \boldsymbol{\tau}_{\mathrm{wind}} + \boldsymbol{\tau}_{\mathrm{foil}} + \boldsymbol{\tau}_{\mathrm{wave2}} + \boldsymbol{\tau}_{\mathrm{rudd}}(\delta), && \text{(maneuvering } \Sigma_1\text{)} \\
\mathbf{M}_{\mathrm{rao}}(\infty)\ddot{\boldsymbol{\xi}} + \mathbf{B}_{\mathrm{rao}}(\infty)\dot{\boldsymbol{\xi}} + \boldsymbol{\mu}_{\mathrm{r}} + \mathbf{C}_{\mathrm{rao}}\boldsymbol{\xi} &= \boldsymbol{\tau}_{\mathrm{wave1}}, && \text{(seakeeping } \Sigma_2\text{)} \\
\dot{\mathbf{x}} &= \mathbf{A}_{\mathrm{r}}\mathbf{x}_{\mathrm{r}} + \mathbf{B}_{\mathrm{r}}\delta\boldsymbol{\nu}_{\mathrm{r}}, && \text{(fluid memory)} \\
\boldsymbol{\mu}_{\mathrm{r}} &= \mathbf{C}_{\mathrm{r}}\mathbf{x}_{\mathrm{r}}, \\
\\
\boldsymbol{\eta} &= \boldsymbol{\eta}_{\mathrm{m}} + \boldsymbol{\xi}, && \text{(position)} \\
\boldsymbol{\nu} &= \boldsymbol{\nu}_{\mathrm{c}} + \boldsymbol{\nu}_{\mathrm{r}} + \dot{\boldsymbol{\xi}} && \text{(velocity)} \\
\\
\mathbf{M}_{\vartheta}\ddot{\boldsymbol{\vartheta}}_{\mathrm{n}} + \mathbf{B}_{\vartheta}\dot{\boldsymbol{\vartheta}}_{\mathrm{n}} + \mathbf{C}_{\vartheta}(\boldsymbol{\vartheta})\boldsymbol{\vartheta}_{\mathrm{n}} &= \mathbf{C}_{\vartheta}(\boldsymbol{\vartheta})\mathbf{L}_{\vartheta}\boldsymbol{\xi} + \mathbf{Q}_{\text{non circ}} + \tilde{\mathbf{Q}}_{\mathrm{circ}} + \mathbf{Q}_{\mathrm{inertia}}(\ddot{\boldsymbol{\eta}}) && \text{(foil model } \Sigma_3\text{)}, \\
\dot{\mathbf{x}}_{\mathrm{circ}} &= \mathbf{A}(\boldsymbol{\nu}_{\mathrm{r}})\mathbf{x}_{\mathrm{circ}} + \mathbf{B}\mathbf{Q}_{\mathrm{circ}}, && \text{(fluid memory foils)} \\
\tilde{\mathbf{Q}}_{\mathrm{circ}} &= \mathbf{C}(\boldsymbol{\nu}_{\mathrm{r}})\mathbf{x}_{\mathrm{circ}} + \mathbf{D}\mathbf{Q}_{\mathrm{circ}},
\end{aligned}
$$

### 4.2.2 Matrix-vector representation

If the 6-DOF vehicle states and the 3-DOF foil states are collected in a single state vector by

$$
\mathbf{x}_{\mathrm{AutoNaut}} \triangleq [x^n, y^n, z^n, \phi, \theta, \psi, \vartheta_{n1}, \vartheta_{n2}, \vartheta_{n3}]^{\mathsf{T}}, \tag{4.16}
$$

a matrix-vector representation of the USV dynamics is

$$
\mathbf{M}(\mathbf{x}) + \mathbf{B}(\dot{\mathbf{x}})\dot{\mathbf{x}} + \mathbf{C}(\mathbf{x}, \dot{\mathbf{x}})\dot{\mathbf{x}} + \mathbf{G}(\mathbf{x})\mathbf{x} = \boldsymbol{\tau}. \tag{4.17}
$$

The equivalent inertia matrix including added inertia for the complete model is

$$
\mathbf{M}_{\mathrm{AutoNaut}} = \begin{bmatrix}
M_{11} & & & & & & & & \\
& M_{22} & & & & M_{26} & & & \\
& & M_{33} & & M_{35}^{[2]} & & & & \\
& & & M_{44} & & & & & \\
& & M_{53}^{[2]} & & M_{55} & & & & \\
& M_{62} & & & & M_{66} & & & \\
M_{71}^{[1]} & & M_{73}^{[1]} & & & & M_{77} & & \\
M_{81}^{[1]} & & M_{83}^{[1]} & & & & & M_{88} & \\
M_{91}^{[1]} & & M_{93}^{[1]} & & & & & & M_{99}
\end{bmatrix},
$$

the damping matrix is

$$\mathbf{B}_{\text{AutoNaut}} = \begin{bmatrix} B_{11}^{0} & & & & & & & & \\ & B_{22}^{0} & & & & B_{26}^{0} & & & \\ & & B_{33}^{\infty} & & B_{35}^{[2]} & & & & \\ & & & B_{44} & & & & & \\ & & B_{53}^{[2]} & & B_{55}^{\infty} & & & & \\ & B_{62}^{0} & & & & B_{66}^{0} & & & \\ & & & & & & B_{77} & (\cdot)^{[3]} & (\cdot)^{[3]} \\ & & & & & & (\cdot)^{[3]} & B_{88} & (\cdot)^{[3]} \\ & & & & & & (\cdot)^{[3]} & (\cdot)^{[3]} & B_{99} \end{bmatrix},$$

the Coriolis and centripetal matrix is

$$\mathbf{C}_{\text{AutoNaut}} = \begin{bmatrix} 0 & C_{12} & & & & C_{16} & & \\ C_{21} & 0 & & & & C_{26} & & \\ & & 0 & & & & & \\ & & & 0 & & & & \\ & & & & 0 & & & \\ C_{61} & C_{62} & & & & 0 & & \\ & & & & & & 0 & \\ & & & & & & & 0 \\ & & & & & & & \\ & & & & & & & \end{bmatrix},$$

and the restoring matrix with generalized forces are

$$\mathbf{G}_{\text{AutoNaut}} = \begin{bmatrix} 0 & & & & & & & & \\ & 0 & & & & & & & \\ & & G_{33} & & G_{35}^{[2]} & & & & \\ & & & G_{44} & & & & & \\ & & G_{53}^{[2]} & & G_{55} & & & & \\ & & & & & 0 & & & \\ & & & & G_{75} & & G_{77} & & \\ & & & & G_{85} & & & G_{88} & \\ & & & & G_{95} & & & & G_{99} \end{bmatrix}, \qquad \boldsymbol{\tau}_{\text{AutoN.}} = \begin{bmatrix} X^{(2)} \\ Y^{(2)} \\ Z^{(1)} \\ K^{(1)} \\ M^{(1)} \\ N^{(2)} \\ Q_1^{(1)} \\ Q_2^{(1)} \\ Q_3^{(1)} \end{bmatrix}.$$

**Remark 109.** *The matrices above is included to showcase that the overall model is a sparse system.*

## 4.3 Implementation environment

The commercially available software Matrix Laboratory (MATLAB®) and the simulation and model-based design software Simulink® from MathWorks [62] was used for implementation and numerical integration of the equations of motion of the wave-propelled USV.

Parameters and functions in the simulation model are defined in a MATLAB-script. Here, the symbolic library is used for defining symbolic representations of the matrices and functions before they are transferred to numerical functions. A Simulink block diagram implementation with the numerical functions, integrates the vehicle dynamics with a fixed step size of $\Delta t = 0.01$ [s], representing about 10–100 times higher order of magnitude than the fastest dynamics in the simulation model. The developed files for a complete implementation for the case study for NTNU AutoNaut can be found at the platform GitHub [76]. The code base was approximately 1000 lines, and the block-diagram for the simulation in Simulink was contained about 100 elements.

# Chapter 5

# Simulation results and discussion

This chapter presents an analysis of the main results obtained from implementation of the case study from Chapter 4. Simulation results are given in Sect. 5.1 followed by a discussion from the findings of the wave-propelled USV and on the model architecture in general in Sect. 5.2. The main contributions in this work are briefly summarized in Sect. 5.4.

## 5.1 Simulation results

The proposed model architecture with the parameters determined by Chapter 4 was simulated in Simulink. An open-loop simulation illustrates the feasibility of the model, shown in Fig. 5.1.

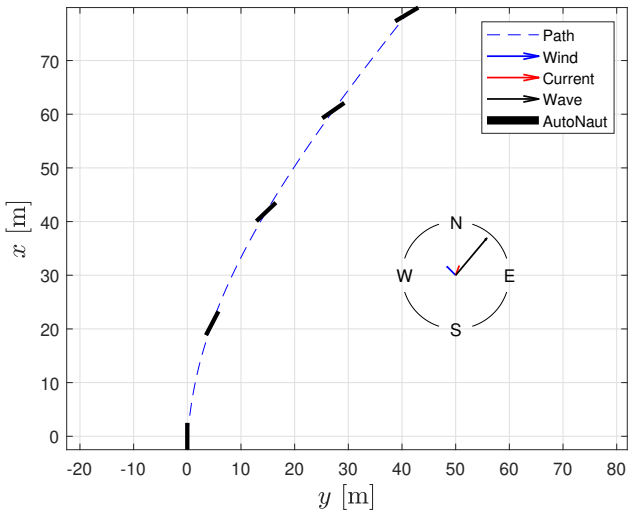


**Figure 5.1:** Simulation for NTNU AutoNaut over $t = 200$ [s]. The wave height was $\zeta_a = 0.6$ [m] with wave frequency $\omega = 2.5$ [s$^{-1}$] and direction $\beta_k = 40°$. Sea currents $V_c = 0.2$ [m/s] was directed to $\beta_{V_c} = 20°$. $V_w = 2.5$ [m/s], $\beta_{V_w} = -45°$.

### 5.1.1 Speed prediction

A distribution of forward speed prediction for NTNU AutoNaut is given in Fig. 5.2.

### 5.1.2 Course control

A classical or advanced line of sight (LOS) control algorithm can be used to compute the desired course angle $\chi_\mathrm{d}$ during path following for instance by choosing between the methods described by Fossen [77]. The desired course angle is fed into a controller to formulate the rudder command. For simulation purposes, a PI derivative controller (PID) was chosen as

$$\delta_\mathrm{d} = \mathrm{sat}_\chi \left( -K_{p_\chi} \, \mathrm{ssa}(\chi - \chi_\mathrm{d}) - K_{i_\chi} \int_{\substack{0 \\ \text{if } |\delta_\mathrm{d}| < \delta^\mathrm{max}}}^{t} \mathrm{ssa}(\chi - \chi_\mathrm{d}) \, \mathrm{d}\tau - K_{d_\chi} r \right), \tag{5.1}$$

where $\chi$ is the course angle and $r$ is the yaw rate. The controller gains was chosen with trial and failure – giving a satisfactory result with

$$K_{p_\chi} = 1.0, \quad K_{i_\chi} = 0.05, \quad K_{d_\chi} = 10. \tag{5.2}$$

Integrator wind-up was prevented by activating the integration only when $|\delta_\mathrm{d}| < \delta_\mathrm{max} = 45°$. The function $\mathrm{sat}_\chi : \mathbb{R} \to [-\pi/4, \pi/4]$ prevents the commanded rudder angle to succeed the limits of $\delta_\mathrm{max}$. The unconstrained course angle error $\tilde{\chi} = \chi - \chi_\mathrm{d}$ is mapped to the interval $[-\pi, \pi)$ using the operator $\mathrm{ssa} : \mathbb{R} \to [-\pi, \pi)$ representing the smallest signed difference between the angles $\chi_\mathrm{d}$ and $\chi$. The steering machine was introduced for

### 5.1.3 Spring stiffness

A comparison of spring stiffness is illustrated in Fig. 5.5.

### 5.1.4 Summary of results from the case study

A direct result of the case study analysis is showcasing the feasibility of a practical simulation of the model architecture by the interconnected sub-models $\Sigma_1$–$\Sigma_3$. Possibly one of the most influential benefit from the case study is the identification of the foil geometry listed in Tab. 4.12 as well the empiric equations for lift and drag curves.

#### Feasible motion predictions

The simulation model is feasible for prediction of 6-DOF motions of the vehicle in sea currents, waves and wind. Open and closed-loop motion predictions for course control was simulated and plotted in Figs. 5.1 and 5.3.

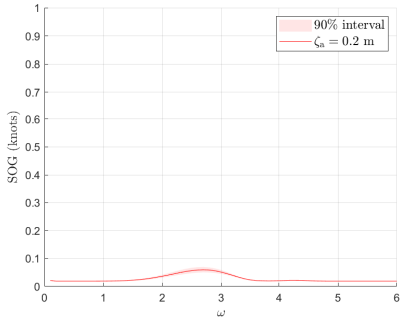


**(a)** Wave amplitude $\zeta_a = 0.2$ [m].

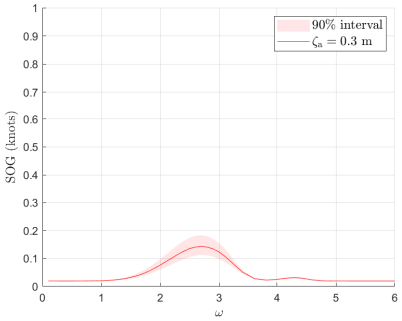


**(b)** Wave amplitude $\zeta_a = 0.3$ [m].

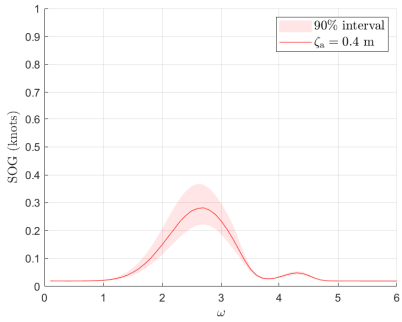


**(c)** Wave amplitude $\zeta_a = 0.4$ [m].

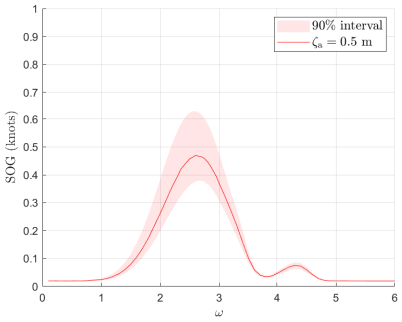


**(d)** Wave amplitude $\zeta_a = 0.5$ [m].

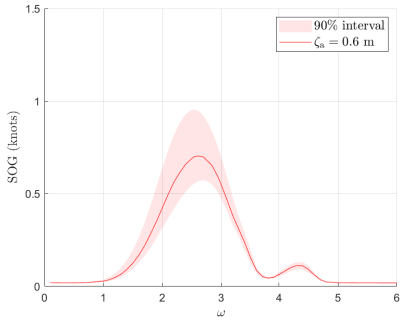


**(e)** Wave amplitude $\zeta_a = 0.6$ [m].

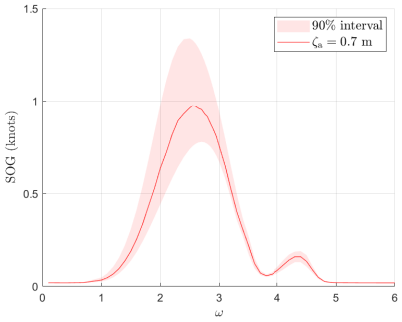


**(f)** Wave amplitude $\zeta_a = 0.7$ [m].

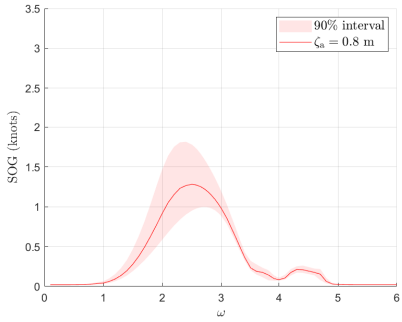


**(g)** Wave amplitude $\zeta_a = 0.8$ [m].

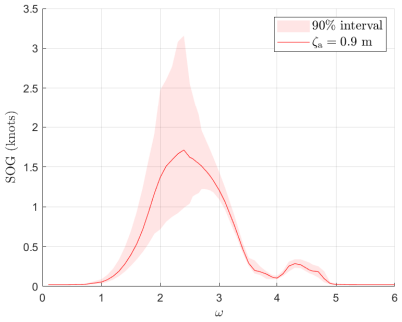


**(h)** Wave amplitude $\zeta_a = 0.9$ [m].

**Figure 5.2:** Speed over ground in beam regular waves with medium spring stiffness for a constant wave height. The shaded regions correspond to a 90 % interval. The environmental configuration is the same as in Fig. 5.1.

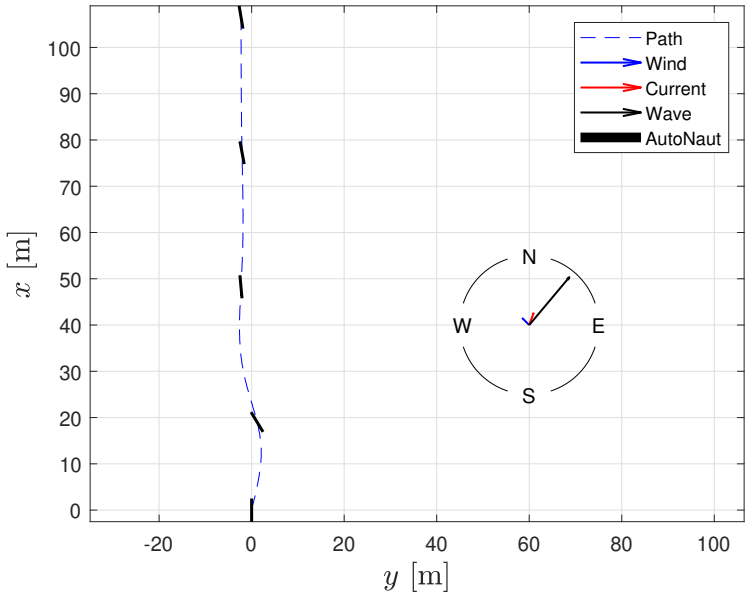


**Figure 5.3:** Closed loop course control simulation for NTNU AutoNaut over $t = 200$ [s] with desired course $\chi_d = 0°$ (North heading).

### Spring setting

The three spring settings was tested in a test-bed analysis given in Fig. 5.5. The soft, medium and stiff spring settings are optimal for different wave-frequency characteristics in the area the AutoNaut is to be operated. According to the simulation model, the soft spring is optimal for $\omega < 1.4$ [s$^{-1}$], the medium spring is best suited around $\omega \simeq 1.8$ [s$^{-1}$] and the stiff springs are best for $\omega > 2.2$ [s$^{-1}$].

**Table 5.1:** Optimal spring stiffness in sea states given by wave frequencies based on wave-propelled thrust. For long-crested waves, the soft springs are best option. For short-crested waves, the stiffest spring is the best.

| Wave frequency | Optimal spring stiffness |
|---|---|
| $\omega \lesssim 1.4$ [s$^{-1}$] | Soft spring |
| $\omega \simeq 1.8$ [s$^{-1}$] | Medium stiff spring |
| $\omega \gtrsim 2.2$ [s$^{-1}$] | Stiff spring |

### Strut lengths

Various lengths of the struts may be tested in the simulation to optimize the strut lengths of the USV. However, the wave-induced motion model is designed for a specific strut length, thus changing this parameter might lead to erroneous results as the validity of the model is not

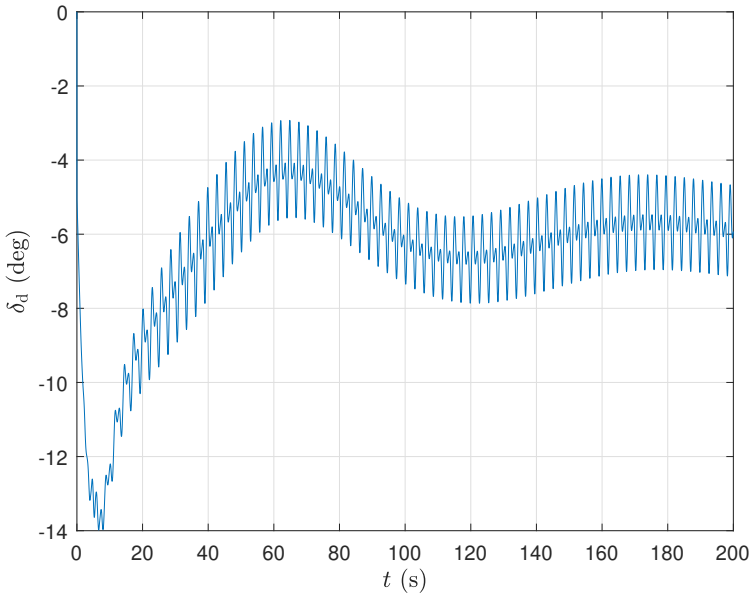


**Figure 5.4:** Commanded rudder control for the simulation plotted in Fig. 5.3. Notice, that first-order wave oscillations are present in the desired rudder control. To prevent this, a wave filter should be added to the control algorithm.

guaranteed. A study of optimal foil placement along a marine craft can is referred to the results of Bøckmann [2].

## 5.2 Discussion

A small discussion on the simulation results follows.

### Impinging waves on hull

Any propulsive thrust from impinging waves on the hull is ignored in this model.

### Validity of linear wave theory

Linear wave theory is only valid for small wave amplitudes, or more precisely, to small wave steepness. According to Krogstad and Arntsen [35] and Pettersen [36], this is limited to the

$$\frac{H}{\lambda} = \frac{1}{7}. \tag{5.3}$$

### Division by zero for Prime normalization system

A disadvantage for the Prime normalization method is that it is unsuited for low-speed applications such as dynamic positioning and wave-propelled USVs. Normalization of the velocities $u$

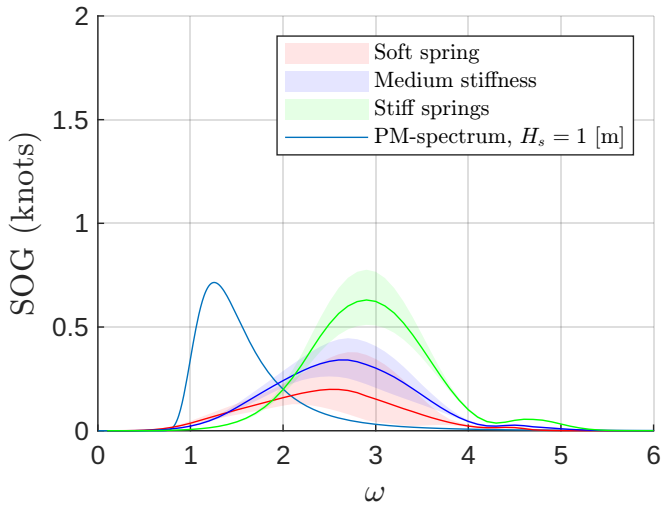


**Figure 5.5:** Simulation of forward speed prediction with 90 % variance interval on NTNU AutoNaut for soft, medium and stiff spring setting. The Pierson-Moskowitz spectrum, scaled by $10 \cdot S(\omega)$, is plotted with significant wave height of $H_s = 1$ [m]. The spring setting for the wave-propelled USV should be evaluated with respect to the wave frequency distribution in the operational area of deployment. The simulation suggest that the soft spring setting is most efficient with regards to wave-propulsion for wave frequencies below $\omega = 1.4$ [$s^{-1}$], the medium setting is efficient for $\omega = 1.4$–$2.2$ [$s^{-1}$] and the stiff spring is most efficient for short-crested sea, typical found in fjords for $\omega > 2.2$ [$s^{-1}$].

and $v$ implies dividing by the speed $U$, which can be zero.

The better approach for comparison of motion derivatives across different wave-propelled USVs would be to use the Bis system [4]. That system is valid for zero speed as well as high-speed applications since division by speed $U$ is avoided.

### Spring setting influence on RAOs

The optimization for the wave-induced motion model from Mounet et al. [67] was based on a data set for NTNU AutoNaut with the medium spring setting. As a result, the model is only validated for a single spring setting. For simulation purposes, the wave-induced motions are thus less accurate when other spring settings are selected. A more accurate model would be to incorporate the spring setting into the parameter vector $\boldsymbol{\alpha}_2$. The following remark discuss the use of different data sets and spring settings, where the two common operational areas for NTNU AutoNaut is shown in Fig. 5.6 from Frohavet and Trondheim Fjord.

**Remark 110.** *The data set used in Mounet et al. [67] from March/April 2022 used the medium stiff springs, while an available data set from December 2022 used the stiffest settings. In both cases the strut length was constant and the torsion spring stiffness at the stern was also constant. Information about the data sets was retrieved from conversation with Øveraas [72].*

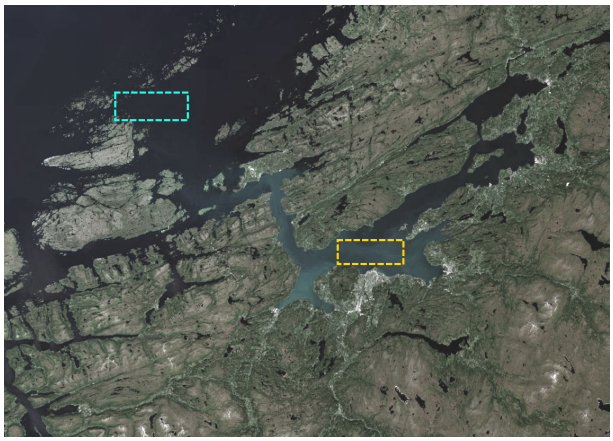

**Figure 5.6:** Field test sites Frohavet (in cyan) and Trondheim Fjord (in yellow) for data sets available for NTNU AutoNaut.

### Redundancy of roll motion

By the assumption for the wave-propulsion model $\Sigma_3$ given in Sect. 3.3, the roll motion $\phi$ of the USV is not considered to affect the foil motions. Since roll is uncoupled from heave $z^n$ and pitch $\theta$ in the wave-induced motion model $\Sigma_2$, the roll motion is redundant in the proposed dynamics.

This insight leads to the proposition that wave-propelled USVs may sufficiently be described by a 5-DOF model for the vehicle motion by surge, sway, heave, pitch and yaw motions only.

### Validation of foil motions

The parameters in the wave-propulsion model $\Sigma_3$ may be validated by measurement of the foil angles $\boldsymbol{\vartheta}$. An objective function for the optimization in Sect. 3.4 could be an absolute or quadratic error measure of the foil angles when the motion of the USV is given. Currently, on NTNU AutoNaut however, no measurement of the foil angles are present. An alternative validation procedure for model $\Sigma_3$ could be an implicit validation. The average speed and variance of the speed of the USV may be a measure for the accuracy of model $\Sigma_3$ because the wave-propelled forces are fed from the foil motions to the maneuvering model $\Sigma_1$. A benefit for this method is that the overall speed model of the USV might is corrected at the expense of correcting the sub-model $\Sigma_3$. Any unwanted error in the maneuvering model $\Sigma_1$ might thus be left uncorrected if implicit methods are employed.

The better alternative for NTNU AutoNaut would probably be to install physical measuring devices, for instance one or more of the following:

- Submerged camera: *Indirect* angle measurement by camera vision techniques
- Installation of angle encoders: *Direct* angle measurement with an encoder mounted on the pivot points
- Pressure sensors: Positioning of pressure sensors on the foils to estimate the relative velocity field and in turn *indirect* angle measurement from sensor fusion

### Centrifugal forces on foils

If the assumption of slow turning by Assumption 19 no longer holds, the foils experience centrifugal forces which cause a small coupling term from the heading rate $p$ correcting the foil angles towards $\boldsymbol{\vartheta} \to \mathbf{0}$. This coupling is straightforward to derive in the case of the heading rate being analyzed separately. However, this effect is believed to be negligible in comparison to the other hydrodynamic forces and model assumptions.

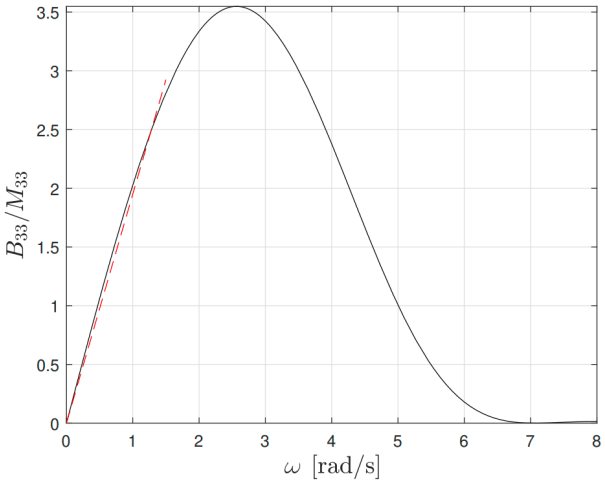


**Figure 5.7:** Linear approximation for damping for slow motion, $\omega < 1.5$ [s$^{-1}$].

### Stability considerations

The model architecture is a highly nonlinear system and stability is a consideration that should be considered when running the simulation model.

The model experiences a weird behavior under certain conditions in which case the surge speed is propelled forward with a finite escape time.

This might be due to the foil forces scaling as $\tau_{\text{foil}} \sim v^2$. In a one-dimensional case for linear damping, $F = m\dot{v} = -bv + cv^2$, whenever quadratic term dominates, then $\dot{x} = kx^2$. Assuming

that the system reaches a dynamical equation $k(t) \geq k_0$ at time $t_0$

$$\begin{aligned}
\dot{x}(t) &= k_0 x(t)^2, \\
\int \frac{\mathrm{d}x}{x(t)^2} &= \int k_0 \, \mathrm{d}t, \\
\left[ -\frac{1}{x(t)} \right]_{t_0}^{t} &= k_0 [t - t_0], \\
\frac{1}{x_0} - \frac{1}{x(t)} &= k_0 \Delta t, \\
x(t) \left[ \frac{1}{x_0} - k_0 \Delta t \right] &= 1, \\
x(t) &= \frac{1}{\frac{1}{x_0} - k_0 \Delta t},
\end{aligned}$$

which diverges $x(t) \to \infty$ as $\Delta t \to \frac{1}{k_0 x_0}$.

This might happen when the phase of the normal force approaches about 15°. According to Fig. 2.26, this happens around $k_\mathrm{f} = 0.3$.

$$k_\mathrm{f} = \frac{c}{2} \frac{\omega}{U}, \qquad \omega = 2 k_\mathrm{f} U / c \tag{5.4}$$

for velocity about 1 [m/s] this corresponds to a frequency of $\omega = 3.125$ [$\mathrm{s}^{-1}$].

**Remark 111.** *A direct stability consideration for the model architecture is thus the necessity of viscous damping, at least in surge in order to mitigate the risk of exciting a finite-escape time.*

## 5.3 Model corrections

This section describes discuss partly some corrections of interest for the model. Unsteady effects on foils

### 5.3.1 Correction for unsteady circulation forces

The basic idea is to evaluate the foil into two segments with chord width $c_\mathrm{max}$ and $c_\mathrm{tip}$. Thus any motion will not operate at the reduced frequency and accidental excite a non-trivial behavior discussed in under "Finite escape time considerations" in Sect. 5.2.

Denote the *maximum chord length* $c_\mathrm{max}$ and the *tip chord length* $c_\mathrm{tip}$. Partition the half span into these two widths according to Fig. 5.8 where $\mu$ is a geometric constant determining the ratio where the max chord length and tip chord length acts.

The foil area is

$$A = S c_m = S[c_\mathrm{max} \mu + c_\mathrm{tip}(1 - \mu)], \tag{5.5}$$

where the tip chord length is

$$c_\mathrm{tip} = \frac{A - S c_\mathrm{max} \mu}{S(1 - \mu)} = \frac{c_m - c_\mathrm{max} \mu}{1 - \mu}. \tag{5.6}$$

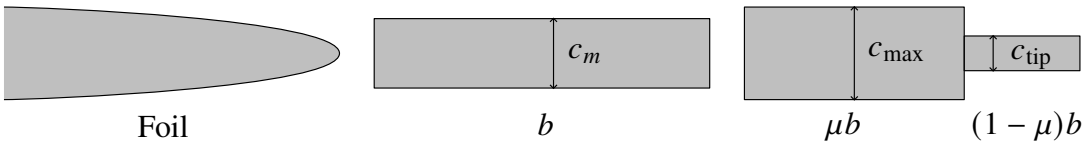


**Figure 5.8:** Simplified foil model approximation for use of evaluation of the Theodorsen function.

### 5.3.2 Shallow water effects

The motion of wave-propelled USVs in shallow water mainly affects the maneuverability derivatives and a the dispersion relation of surface waves. The hydrodynamic forces on the foils can be considered unchanged.

#### Maneuvering model

In shallow water, the hydrodynamic forces for maneuvering become more pronounced because of mirroring effects from the sea bed. Corrections in the maneuvering derivatives are given in Appendix C.3 based on Sheng [78] and Clarke et al. [44].

#### Linear wave theory

When the wave-propelled USV enters shallow water, the assumptions of deep water given in linear wave theory in Sect. 2.3.3 is no longer suitable, thus the dispersion relation given by $\omega^2 = gk$ no longer holds. Still, linear wave theory is developed for any sea depth, and a discussion for shallow waves can for instance be found in Krogstad and Arntsen [35].

#### Forces on hydrofoils

According to Wu [18], the effects of solid boundaries – and also free surface effects – can be neglected when the foils are further than two chord lengths away. For the case study on NTNU AutoNaut, this means that the forces on the foils do not need any correction if a clearance of about 0.5 [m] from the sea bed to the foils are held. This probably do not impose any practical challenges. For very shallow waters with small clearance, this correction is probably not needed anyway if the USV is propelled by an optional auxiliary propeller or towed, thus mitigating the need for a working wave-propulsion model in those scenarios.

#### Effects of operating conditions on foils

Operating conditions is important when considering the forces on foils. This consideration is left as a future work.

## 5.4 Summary of main contributions

This work combines knowledge from multiple fields of study, from engineering cybernetics, modeling and simulation and hydrodynamics. A summary of the finding in this work is:

- Semi-empiric forces on foils beyond stall angle
- An empiric equation for reduction coefficient for added mass was found
- Categorizing the governing equations of motion for wave-propelled USVs
- A semi-empirical equation for lift characteristics
- An empiric calculation of added mass for rectangular foils based on Meyerhoff 1970
- A semi-empirical equation for drag on foils valid through all angles of attack
- An approximation for the center of pressure through all angles of attack
- Proposed unified maneuvering and seakeeping model
- Description of the dynamics for attack angles including d'Alembert's (inertia) forces
- Approximation of unsteady lift and drag forces on foils through a transfer function with speed-dependent terms
- Identification of the terms in the simplest fluid memory effects for a monohull box-shaped vessel
- Case study on AutoNaut vehicle which demonstrates feasibility of the model proposed and a numerical demonstration that it can be used to optimize spring settings for operations
- Viscous drag and added mass from foils are incorporated in a monohull geometry representing the overall hydrodynamic behaviour of the wave-propelled USV
- Determining a source of instability in the model occuring from unsteady forces on the foils
- Determined main dimensions for the AutoNaut foil geometry; where the span is 1.3 m, the mean chord is 19.2 cm, maximum thickness 15% and maximum thickness appear at 30% from leading edge
- Proposed model for identifying the sectional shape of foils consisting of an ellipse and a slope
- Show that simple controller laws can be tested on the simulation model
- Proposed a method for determining the position of an effective rectangular section for foils

- A correction proposed for 3D-effects for the Theodorsen function
- Explains the main limitations of the model and directions forward for further work
- Proposed methods to measure the foil angles to be able to validate more accurately the foil angles from simulation and measurement
- The model can further be incorporated in model-based estimator for wave-propelled vehicles based on noisy measurements from IMU
- The model can be extended to other wave-propelled USVs applying the proposed methodology
- Show that quadratic damping in surge is necessary.

# Chapter 6

# Conclusions and future work

## 6.1 Conclusion

A closed-form simulation model for wave-propelled uncrewed surface vehicles (USVs) which are propelled by corrective passive springs proves feasible with the proposed model architecture. The method proposed to use a unified maneuvering model in surge, sway and yaw motions and a wave-induced motion model in heave, roll and pitch. A quick estimate for the maneuvering model was found through motion derivatives by a small set of design parameters for the main particulars. The model for wave-induced motions incorporated successfully the complex hydrodynamic effects from the correcting hydrofoils on the overall wave-induced motions of the vehicle. This analysis proved possible by an analysis of an efficient monohull geometry.

A case study on a specific wave-propelled USV AutoNaut suggests slightly smaller dimensions for the maneuvering model, and slightly larger dimension in breadth and length for the wave-induced motion model compared to the physical ones.

Stability of the system was enforced by adding viscous drag to the maneuvering model, low-pass filtering of the relative velocity used for unsteady forces on the foils and unnecessary fluttering phenomena on the foils are reduced by enforcing a long blend between attached and detached flow regimes.

The simulation model gives a feasible prediction of the USV motion in 6-DOF for the case study on AutoNaut with an average forward speed matching operational data. A quantitative results from the simulation is that the soft spring setting for the case study is optimal for wave frequencies $\omega \leq 1.4$ [$s^{-1}$], the medium spring stiffness is optimal around $\omega \simeq 1.8$ [$s^{-1}$] and the stiff spring settings is optimal for $\omega > 2.2$ [$s^{-1}$] with regard to forward thrust.

A continuation of this work would be to write a code environment for simulation of the model architecture for a wide range of wave-propelled USVs and perform a validation of the specific wave-propelled USV analyzed in this work. Many new exciting areas for advanced control and safety in marine autonomy for wave-propelled USVs is possible to pursue further with the development of a physical speed model for such vehicles.

## 6.2 Future work

The work in this report has established a physical speed model with emphasize on closed-form expressions on the equations of motion. Suggested continuation of this work is listed below:

1. Peer-review of the assumptions and methods developed and proposed in this work
2. Successful software implementation for general wave-propelled USVs
3. Perform a proper qualitative validation on the case study based on operational data
4. Develop and formulate motion derivatives through Bis system
5. Perform short-term speed predictions on NTNU AutoNaut based on metocean forecast, and compare the results to the regression methods by Øveraas [27]
6. Look into the nonlinear stability properties of the whole system architecture
7. Use the simulation model to test steering control algorithms
8. Look into other use-cases for the model, for instance in Kalman filter or development for a digital twin

A list of other noteworthy future work suggestions are:

**Successful implementation of a general software**

**Validation of the case study**

**Reduce the computational complexity**

**Test steering control algorithms on the simulation model**

**Look into how the model may be employed in Kalman filters**

**Perform model correction of the sytem architecture through machine learning**

**Develop transfer functions from heave and pitch motion to foil angles**

**A priori distribution for environmental states**

**Data assimilation with sensors from AutoNaut**

# Chapter 7

# Bibliography


[1] General conference on weights and measures.

[2] E. Bøckmann, "Wave propulsion of ships," Ph.D. dissertation, Norwegian University of Science and Technology, 2015.

[3] A. Dallolio, H. Øveraas, J. A. Alfredsen, T. I. Fossen, and T. A. Johansen, "Design and validation of a course control system for a wave-propelled unmanned surface vehicle," *Field Robotics*, vol. 2, pp. 774–806, 2022.

[4] T. I. Fossen, *Handbook of marine craft hydrodynamics and motion control*, 2nd ed. Wiley, Trondheim, 2021.

[5] P. Ploé, "Surrogate-based optimization of hydrofoil shapes using RANS simulations," Ph.D. dissertation, Loire Bretagne University, Rennes, France, 2018.

[6] S. F. Hoerner, *Fluid-Dynamic Lift*, 2nd ed., H. V. Borst, Ed. Hoerner Fluid Dynamics, Bakerfields, 1985.

[7] R. F. Burnett, "Wave energy for propelling craft – nothing new," *The Naval Architect*, 1979.

[8] A. Dallolio, H. Øveraas, and T. A. Johansen, "Gain-scheduled steering control for a wave-propelled unmanned surface vehicle," *Ocean Engineering*, vol. 257:111618, 2022.

[9] International Maritime Organization, "Recommendation on a severe wind and rolling criterion (weather criterion) for the intact stability of passenger and cargo ships of 24 metres in length and over," Tech. Rep., 1986, resolution A.562(14).

[10] ——, "Weather criterion for fishing vessels of 24 metres in length and over," Tech. Rep., 1991, resolution A.685(17).

[11] G. Taimuri, J. Matusiak, T. Mikkola, P. Kujala, and S. Hirdaris, "A 6-DoF maneuvering model for the rapid estimation of hydrodynamic actions in deep and shallow waters," *Ocean Engineering*, vol. 218(65):108103, December 2020.

[12] T. Pérez and M. Blanke, "Mathematical ship modeling for control applications," University of Newcastle, Tech. Rep., 2002.

[13] E. N. Jacobs, K. E. Ward, and R. M. Pinkerton, "The characteristics of 78 related airfoil sections from tests in the variable-density wind tunnel," National Advisory Committee for Aeronautics, Tech. Rep., 1933.

[14] T. Theodorsen, "General theory of aerodynamic instability and the mechanism of flutter," National Advisory Committee for Aeronautics. Langley Aeronautical Lab. Langley Field, VA, United States, Tech. Rep., 1934.

[15] S. F. Hoerner, *Fluid-Dynamic Drag*, 2nd ed. Hoerner Fluid Dynamics, Bakerfields, 1965.

[16] J. Anderson, *Fundamentals of Aerodynamics*, 6th ed. McGraw-Hill Education, New York, 2001.

[17] A. G. Tufte, "Hydrodynamics of spring-loaded hydrofoils excited from a wave-propelled uncrewed surface vessel," 2023, not intended for publication.

[18] T. Y.-T. Wu, "Extraction of flow energy by a wing oscillating in waves," *Journal of Ship Research*, vol. 16(01), pp. 66–78, 1972.

[19] E. S. Filippas and K. A. Belibassakis, "Hydrodynamic analysis of flapping-foil thrusters operating beneath the free surface and in waves," *Engineering Analysis with Boundary Elements*, vol. 41, pp. 47–59, April 2014.

[20] D. B. Lopes, J. A. F. D. Campos, and A. J. Sarmento, "An analytical model study of a flapping hydrofoil for wave propulsion," vol. 11A. American Society of Mechanical Engineers (ASME), 2018.

[21] F. C. Eitzen, "Mathematical modelling of a foil propulsion system," 2012, Norwegian University of Science and Technology, master's thesis.

[22] R. Zghyer, "The role of ship simulators and maneuvering models in maritime operations," Ph.D. dissertation, Norwegian University of Science and Technology, 2023.

[23] J. J. Jensen, "Wave loads on ships," in *Load and Global Response of Ships*, vol. 4. Elsevier, 2001, book chapter, from Elsevier Ocean Engineering Book Series.

[24] J. N. Newman, *Marine Hydrodynamics*, J. Grue, Ed. The MIT Press, London, 2017, 40th Anniversary Edition.

[25] J. J. Jensen, A. E. Mansour, and A. S. Olsen, "Estimation of ship motions using closed-form expressions," *Ocean Engineering*, vol. 31, pp. 61–85, 2004.

[26] A. Dallolio, J. A. Alfredsen, T. I. Fossen, and T. A. Johansen, "Experimental validation of a nonlinear wave encounter frequency estimator onboard a wave-propelled USV," in *IFAC-PapersOnLine*, vol. 54. Elsevier B.V., 2021, pp. 188–194.

[27] H. Øveraas, A. Heggernes, A. Dallolio, T. H. Bryne, and T. A. Johansen, "Predicting the speed of a wave-propelled autonomous surface vehicle using metocean forecasts," in *OCEANS 2022 - Chennai*, 2022, pp. 1–6.

[28] A. Dallolio (NTNU). (2022) AutoNaut documentation wiki. [Online]. Available: http://autonaut.itk.ntnu.no/doku.php

[29] SNAME, "Nomenclature for treating the motion of a submerged body through a fluid," The Society of Naval Architects and Marine Engineers, Tech. Rep., 1950, Bulletin 1–5, New York, USA.

[30] O. Egeland and J. T. Gravdahl, *Modeling and Simulation for Automatic Control*. Marine Cybernetics, Trondheim, 2002.

[31] H. Goldstein, C. P. Poole, and J. L. Safko, *Classical mechanics*, 3rd ed. Addison Wesly, 2002.

[32] F. M. White, *Fluid Mechanics*, 7th ed. McGraw-Hill, New York, 2011.

[33] H. Lamb, *Hydrodynamics*, 4th ed. Cambridge University Press, Cambridge, 1916.

[34] K. Churchman. (2015) Photograph "Landscape Photograph of Body of Water". Pexels, Creative Common license. [Online]. Available: https://pexels.com/photo/landscape-photograph-of-body-of-water-1001682/

[35] H. E. Krogstad and A. Arntsen, "Linear wave theory part A: Regular waves," 2000.

[36] B. Pettersen, O. M. Faltinsen, and D. Myrhaug, *Marine Technology Hydrodynamics*. Akademika, NTNU, Trondheim, 2021, in Norwegian.

[37] O. Pinti, "Hydrodynamics modeling and simulation," 2018, Politecnico di Torino and NASA Jet Propulsion Laboratory, California Institute of Technology, master's thesis.

[38] W. E. Cummins, "The impulse response function and ship motion," Department of the Navy David Taylor Model Basin, Tech. Rep., January 1962.

[39] T. I. Fossen, "A nonlinear unified state-space model for ship maneuvering and control in a seaway," *International Journal of Bifurcation and Chaos*, vol. 15(9), pp. 2717–2746, 2005.

[40] P. A. Bailey, W. G. Price, and P. Temarel, "A unified mathematical model describing the maneuvering of a ship travelling in a seaway," *Trans. RINA 140*, pp. 131–149, 1998.

[41] J. M. J. Journée, "Quick strip theory calculations in ship design," *PRADS'92 Conf. Pract. Des. Ships*, vol. I, pp. 5–12, 1992.

[42] O. M. Faltinsen, *Sea Loads on Ships and Offshore Structures*. Cambridge University Press, Cambridge, 1990.

[43] N. Salvesen, E. O. Tuck, and O. Faltinsen, "Ship motions and sea loads," The Society of Naval Architects and Marine Engineers, Tech. Rep., November 1970.

[44] D. Clarke, P. Gedling, and G. Hine, "The application of manoeuvring criteria in hull design using linear theory," London, 1982, The Royal Institution of Naval Architects, spring meetings, paper no. 7.

[45] T. F. Ogilvie, "Recent progress toward the understanding and prediction of ship motions," in *Proceedings of the 5th Symposium on Naval Hydrodynamics*, Bergen, Norway, September 1964, pp. 3–80.

[46] T. Perez and T. I. Fossen, "Joint identification of infinite-frequency added mass and fluid-memory models of marine structures," *Modeling, Identification and Control*, vol. 29, pp. 93–102, 2008.

[47] E. Kristiansen and O. Egeland, "Frequency-dependent added mass in models for controller design for wave motion damping," *IFAC Proceedings*, vol. 36(21), pp. 67–72, September 2003.

[48] E. Kristiansen, Åsmund Hjulstad, and O. Egeland, "State-space representation of radiation forces in time-domain vessel models," *Ocean Engineering*, vol. 32, pp. 2195–2216, December 2005.

[49] T. I. Fossen and T. Perez. (2004–2023) Marine Systems Simulator (MSS). [Online]. Available: https://github.com/cybergalactic/MSS

[50] S. Steen, *Marine Technology Hydrodynamics: Resistance and propulsion, propeller and foil theory*. Akademika, NTNU, Trondheim, 2014, in Norwegian.

[51] C. O. Johnston, "Review, extension, and application of unsteady thin airfoil theory," Center for Intelligent Material Systems and Structures (CIMSS), Virginia Polytechnic Institute and State University, Tech. Rep., 2004.

[52] G. Migeotte, "Design and optimisation of hydrofoil assisted catamarans," Ph.D. dissertation, University of Stellenbosch, Stellenbosch, South Africa, 2002.

[53] C. Sarraf, H. Djeridi, S. Prothin, and J. Y. Billard, "Thickness effect of NACA foils on hydrodynamic global parameters, boundary layer states and stall establishment," *Journal of Fluids and Structures*, vol. 26, pp. 559–578, May 2010.

[54] R. E. Sheldahl and P. C. Klimas, "Aerodynamic characteristics of seven symmetrical airfoil sections through 180-degree angle of attack for use in aerodynamic analysis of vertical axis wind turbines," Tech. Rep., 1981, prepared by Sandia National Laboratories for United States Department of Energy.

[55] M. Drela and H. Youngren. (1986–2013) Xfoil. Software developed by Massachusetts Institute of Technology. [Online]. Available: https://web.mit.edu/drela/Public/web/xfoil/

[56] S. Mirzaeisefat, "Fluttering and autorotation of hinged vertical flat plate induced by uniform current," Ph.D. dissertation, University of Michigan, 2011.

[57] H. Fujii and T. Tuda, "Experimental researches on rudder performance," *Journal of Zosen Kiokai*, pp. 105–111, 1962, in Japanese.

[58] P. Du Cane, *High Speed Small Craft*. David Charles, Newton Abbot, 1972.

[59] W. K. Meyerhoff, "Added masses of thin rectangular plates calculated from potential theory," *Journal of Ship Research*, vol. 14(02), pp. 100–111, June 1970.

[60] M. Abramowitz and I. A. Stegun, *Handbook of Mathematical Functions With Formulas, Graphs, and Mathematical Tables*. United States Department of Commerce, National Bureau of Standards, 1972.

[61] J. G. Balchen, T. Andresen, and B. A. Foss, *Control Theory*. Department of Engineering Cybernetics, NTNU, Trondheim, 2016, in Norwegian.

[62] MathWorks. (2023) Software developer of mathematical computing software for engineers and scientists, among MATLAB® and Simulink®. [Online]. Available: https://www.mathworks.com/

[63] K. Kijima, T. Katsuno, Y. Nakiri, and Y. Furukawa, "On the manoeuvring performance of a ship with the parameter of loading condition," *Society of Naval Architects of Japan*, November 1990.

[64] J. Liu, F. Quadvlieg, and R. Hekkenberg, "Impacts of the rudder profile on manoeuvring performance of ships," *Ocean Engineering*, vol. 124, pp. 226–240, September 2016.

[65] K. Matsumoto and K. Suemitsu, "The prediction of manoeuvring performances by captive model tests," *The Kansai Society of Naval Architects*, vol. 176, March 1980.

[66] J. Brix, "Manoeuvring technical manual," Seehafen Verlag, Tech. Rep., 1993.

[67] R. E. G. Mounet, U. D. Nielsen, A. H. Brodtkorb, H. Øveraas, A. Dallolio, and T. A. Johansen, "Data-driven method for hydrodynamic model estimation applied to an unmanned surface vehicle," 2023.

[68] Y. Yamamoto, H. Ohtsubo, Y. Sumi, and M. Fujino, *Ship Structural Mechanics*. Nariyamatou Book, 1986, in Japanese.

[69] S. Matsui, K. Sugimoto, and K. Shinomoto, "Simplified estimation formula for frequency response function of roll motion of ship in waves," *Ocean Engineering*, vol. 276:114187, May 2023.

[70] Y. Ikeda, Y. Himeno, and N. Tanaka, "On roll damping force of ship: Effects of friction of hull and normal force of bilge keels," *Kansai Society of Naval Architects, Japan*, vol. 161, pp. 41–49, 1976, in Japanese.

[71] AutoNaut Ltd. (2024) AutoNaut is an Uncrewed Surface Vessel (USV) propelled by the motion of the waves. [Online]. Available: https://www.autonautusv.com/

[72] H. Øveraas, 2023, private communication and discussion about the data sets for NTNU AutoNaut, Trondheim.

[73] J. Van Amerongen, "Adaptive steering of ships – a model reference approach to improved maneuvering and economical course keeping," Ph.D. dissertation, Delft University of Technology, 1982.

[74] T. A. Johansen, 2023–2024, private communication and discussion about NTNU AutoNaut dimensions, Trondheim.

[75] S. Timoshenko, *History of strength of materials: with a brief account of the history of theory of elasticity and theory of structures*. Dover Publications, New York, 1983.

[76] A. G. Tufte. (2024) Software files in MATLAB/Simulink for the specific wave-propelled USV AutoNaut. [Online]. Available: https://github.com/teksle/master

[77] T. I. Fossen, "An adaptive line-of-sight (ALOS) guidance law for path following of aircraft and marine craft," *IEEE Transactions on Control Systems Technology*, vol. 31, pp. 2887–2894, November 2023.

[78] Z. Y. Sheng, "Contribution to the discussion of the manoeuvrability committee report," *Proceedings of 16th ITTC, Leningrad*, 1981.

[79] I. H. Abbott and A. E. V. Doenhoff, *Theory of Wing Sections Including a Summary of Airfoil Data*. Dover Publications, New York, 1959.

[80] J. M. Anderson, K. Streitlien, D. S. Barrett, and M. S. Triantafyllou, "Oscillating foils of high propulsive efficiency," *Journal of Fluid Mechanics*, vol. 360, pp. 41–72, April 1998.

[81] H. Babinsky, P. R. R. J. Stevens, A. R. Jones, L. P. Bernal, and M. V. Ol, "Low order modelling of lift forces for unsteady pitching and surging wings," *54th AIAA Aerospace Sciences Meeting*, 2016.

[82] C. T. Borgen, "Application of an active foil propeller," 2010, Norwegian University of Science and Technology, master's thesis.

[83] J. A. Bowker, M. Tan, and N. C. Townsend, "Forward speed prediction of a free-running wave-propelled boat," *IEEE Journal of Oceanic Engineering*, vol. 46, pp. 402–413, 4 2021.

[84] A. Dallolio, "Design and experimental validation of a control architecture for a wave-propelled USV from system design to ocean studies," Ph.D. dissertation, Norwegian University of Science and Technology, 2022.

[85] A. Dallolio, T. K. Bergh, P. R. De, L. Torre, H. Øveraas, and T. A. Johansen, "ENC-based anti-grounding and anti-collision system for a wave-propelled USV," *IEEE Conference: OCEANS 2022 – Chennai*, 2022.

[86] A. Dallolio, H. B. Bjerck, H. A. Urke, and J. A. Alfredsen, "A persistent sea-going platform for robotic fish telemetry using a wave-propelled USV: Technical solution and proof-of-concept," *Frontiers in Marine Science*, vol. 9, July 2022.

[87] A. Gungor, M. S. U. Khalid, and A. Hemmati, "Classification of vortex patterns of oscillating foils in side-by-side configurations," *Journal of Fluid Mechanics*, vol. 951, December 2022.

[88] K. A. Harper, M. D. Berkemeier, and S. Grace, "Modeling the dynamics of spring-driven oscillating-foil propulsion," *IEEE Journal of Oceanic Engineering*, vol. 23, pp. 285–296, July 1998.

[89] J. Hauge, "Oscillating foil propulsion," 2013, Norwegian University of Science and Technology, master's thesis.

[90] B. Åshaug Holm, "Path planning for wave-powered unmanned surface vehicle based on electronic navigational charts and weather data," 2022, Norwegian University of Science and Technology, master's thesis.

[91] M. L. Mantia and P. Dabnichki, "Unsteady panel method for flapping foil," *Engineering Analysis with Boundary Elements*, vol. 33, pp. 572–580, April 2009.

[92] A. Mivehchi, J. Dahl, and S. Licht, "Heaving and pitching oscillating foil propulsion in ground effect," *Journal of Fluids and Structures*, vol. 63, pp. 174–187, May 2016.

[93] H. Øveraas, "Dynamic positioning using model predictive control with short term wave motion prediction," 2020, Norwegian University of Science and Technology, master's thesis.

[94] H. Øveraas, H. S. Halvorsen, O. Landstad, V. Smines, and T. A. Johansen, "Dynamic positioning using model predictive control with short-term wave prediction," *IEEE Journal of Oceanic Engineering*, October 2023.

[95] M. Park, Y. Choi, N. Lee, and D. Kim, "SpReME: Sparse regression for multi-environment dynamic systems," February 2023, preprint.

[96] D. Read, F. S. Hover, and M. S. Triantafyllou, "Forces on oscillating foils for propulsion and maneuvering," *Journal of Fluids and Structures*, vol. 17, pp. 163–183, 2003.

[97] N. Säfström, "Modeling and simulation of rigid body and rod dynamics via geometric methods," Ph.D. dissertation, Norwegian University of Science and Technology, 2009.

[98] A. Sánchez-Caja, J. Martio, and V. M. Viitanen, "A new propulsion concept for high propulsive hydrodynamic efficiency," *Ocean Engineering*, vol. 243, January 2022.

[99] B. Simeon, *Computational Flexible Multibody Dynamics; A Differential-Algebraic Approach*. Springer, 2013.

[100] S. Verma and A. Hemmati, "Evolution of wake structures behind oscillating hydrofoils with combined heaving and pitching motion," *Journal of Fluid Mechanics*, vol. 927, 2021.

[101] H. A. Waiaerhaug, "A method of calculating the lift on submerged hydrofoils," Tech. Rep., November 1963, Norwegian ship model experiment tank publication, no. 71.

[102] C.-T. Chen, *Linear System Theory and Design*, 3rd ed. Oxford University Press, 2009, international edition.

[103] H. H. Khalil, *Nonlinear systems*, 3rd ed. Prentice Hall, Upper Saddle River, 2002.

# Appendix A

# System theory

## A.1 Realization of proper transfer functions

The material in this section is based on linear theory found in the chapter "State-space solutions and realizations" in the linear system theory book from Chen [102].

The following theorem states which transfer function can be realized:

**Theorem 3.** ***(Realizable transfer functions)***
*A transfer function is realizable if and only if it is a proper rational matrix.*

A proper transfer function $g(s)$ can be split into a strictly proper part $g_{\text{sp}}(s)$ and the infinite-frequency part $g(\infty)$

$$g(s) = g_{\text{sp}}(s) + g(\infty), \tag{A.1}$$

such that the strictly proper part is written on the form

$$g_{\text{sp}}(s) = \frac{n_1 s^{r-1} + n_2 s^{r-2} + \cdots + n_{r-1} s + n_r}{s^r + \alpha_1 s^{r-1} + \cdots + \alpha_{r-1} s + \alpha_r}. \tag{A.2}$$

Then the state-space realization $g(s) = \mathbf{C}[\mathbf{s}\mathbb{I}_{r\times r} - \mathbf{A}]^{-1}\mathbf{B} + D$ on the form

$$\begin{aligned} \dot{\mathbf{x}} &= \mathbf{A}\mathbf{x} + \mathbf{B}u, \\ y &= \mathbf{C}\mathbf{x} + Du, \end{aligned} \tag{A.3}$$

can be realized by choosing

$$\mathbf{A} = \begin{pmatrix} -\alpha_1 & -\alpha_2 & \cdots & -\alpha_{r-1} & -\alpha_r \\ 1 & 0 & \cdots & 0 & 0 \\ 0 & 1 & \cdots & 0 & 0 \\ \vdots & \vdots & \ddots & \vdots & \vdots \\ 0 & 0 & \cdots & 1 & 0 \end{pmatrix}, \quad \mathbf{B} = \begin{pmatrix} 1 \\ 0 \\ 0 \\ \vdots \\ 0 \end{pmatrix}, \quad \mathbf{C} = \begin{pmatrix} n_1 & n_2 & \cdots & n_r \end{pmatrix}, \quad D = g(\infty). \tag{A.4}$$

The result can readily be generalized to a matrix transfer functions $\mathbf{G}(s)$ by using the least common denominator of all entries of $\mathbf{G}_{\text{sp}}(s)$.

## A.2 Stability, observability and controllability

A general state equation with states $\mathbf{x}$, measurement $\mathbf{y}$ and input $\mathbf{u}$ is

$$\dot{\mathbf{x}} = \mathbf{f}(\mathbf{x}, \mathbf{u}), \tag{A.5a}$$
$$\mathbf{y} = \mathbf{g}(\mathbf{x}, \mathbf{u}). \tag{A.5b}$$

The definitions below are based on the ones given by Chen [102]. Observability is defined according to the following definition:

**Definition 29.** ***(Observability)***
*The state equation in Eq. (A.5) is observable if for any initial state $\mathbf{x}(t_0)$, there exist a finite $t_1 > t_0$ such that the knowledge of the input $\mathbf{u}$ and the output $\mathbf{y}$ over $[t_0, t_1]$ suffices to determine uniquely the initial state $\mathbf{x}(t_0)$. Otherwise, the equation is said to be unobservable.*

Controllability is defined according to the following definition:

**Definition 30.** ***(Controllability)***
*The state equation in Eq. (A.5a) is said to be controllable if for any initial state $\mathbf{x}(t_0)$ and any final state $\mathbf{x}_1$, there exist an input that transfers $\mathbf{x}_0$ to $\mathbf{x}_1$ in a finite time. Otherwise the equation is said to be uncontrollable.*

Stability is defined according to the following definition:

**Definition 31.** ***(Lyapunov stability)***
*The state equation in Eq. (A.5a) with zero-input $\mathbf{u} = \mathbf{0}$ is marginally stable in the sense of Lyapunov if every finite initial state $\mathbf{x}(t_0)$ excites a bounded response. It is asymptotically stable at the point $\mathbf{x}_e$ if every finite initial state excites a bounded response, which, in addition, approaches the equilibrium point $\mathbf{x}_e$ as $t \to \infty$. If the system is not marginally stable or asymptotically stable, the equation is unstable.*

### Feedback - and networked systems

For stability properties in feedback - and networked systems, the reader is referred to for instance linear system theory by Chen [102], nonlinear system theory presented by Khalil [103] or model properties given in the comprehensive control-oriented modelling and simulation handbook of Egeland and Gravdahl [30].

# Appendix B

# Analytical derivations

## B.1 Inertia forces in equations of motion of hydrofoils

Inertia forces in the foil dynamics may be found through Euler-Lagrange method. The notation here follows that given in Sect. 2.1.4 and the dynamics is found by Eq. (2.15).

### Generalized coordinates

The generalized coordinates for the foil-system can be taken as the position $(x_p, z_p)$ of the pivot point and the foil pitch angle relative to NED $\vartheta_n$, see fig. B.1. The coordinates are a vector $\mathbf{q} \in \mathbb{R}^2 \times \mathbb{S}$

$$\mathbf{q} \triangleq \begin{pmatrix} x_p \\ z_p \\ \vartheta_n \end{pmatrix} = \begin{pmatrix} q_1 \\ q_2 \\ q_3 \end{pmatrix}. \tag{B.1}$$

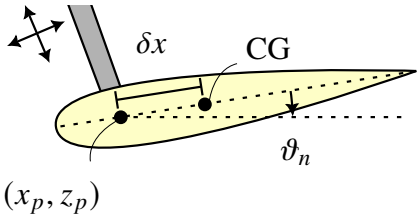


**Figure B.1:** Foil coordinates $(x_p, z_p)$ with angle $\vartheta_n$. The coordinates is such that $x$-axis point to left and $z$-axis point downwards.

From Euler-Lagrange method, the dynamics of the foils including dissipative forces are

$$\left(\frac{\partial L}{\partial \mathbf{q}}\right)^\intercal - \frac{\mathrm{d}}{\mathrm{d}t}\left(\frac{\partial L}{\partial \dot{\mathbf{q}}}\right)^\intercal = \mathbf{Q} - \left(\frac{\partial \mathcal{F}}{\partial \dot{\mathbf{q}}}\right)^\intercal. \tag{B.2}$$

In this study, all hydrodynamic forces excluding circulatory forces and non-circulatory linear forces are included. It is also assumed that buoyancy and gravity forces cancels according to Assumption 18.

### Energies

Potential damping is included with Rayleigh dissipation function

$$\mathcal{F} = \frac{1}{2} M_{\dot{\vartheta}} \dot{\vartheta}_n^2. \tag{B.3}$$

The rotational energy including added kinetic energy of the surrounding fluid is

$$T_{\text{rot}} = \frac{1}{2}(J + M_{\ddot{\vartheta}})\ddot{\vartheta}_n^2. \tag{B.4}$$

The potential energy stored in the spring depends on the contraction $\vartheta_n - \theta$ and stiffness $\kappa$

$$V_{\text{spring}} = \frac{1}{2}\kappa(\vartheta_n - \theta)^2, \tag{B.5}$$

where $\theta$ is treated as an input to the force. Lastly, the linear kinetic energy of the foil is found by the center of mass at foil coordinate $[-\delta x, 0]^\top$ at position

$$\mathbf{r}_{\text{g}} = \begin{pmatrix} x_p \\ z_p \end{pmatrix} + \mathbf{R}_{2\text{D}}(\vartheta_n)^\top \begin{pmatrix} -\delta x \\ 0 \end{pmatrix} = \begin{pmatrix} x_p - \cos(\vartheta_n)\delta x \\ z_p + \sin(\vartheta_n)\delta x \end{pmatrix}, \tag{B.6}$$

where the velocity is

$$\dot{\mathbf{r}}_{\text{g}} = \begin{pmatrix} \dot{x}_p + \delta x \dot{\vartheta}_n \sin(\vartheta_n) \\ \dot{z}_p + \delta x \vartheta_n \cos(\vartheta_n) \end{pmatrix} \equiv \begin{pmatrix} v_1 \\ v_2 \end{pmatrix}, \tag{B.7}$$

such that the linear kinetic energy with mass $m$ is

$$T_{\text{lin}} = \frac{1}{2} m [v_1^2 + v_2^2]. \tag{B.8}$$

Combining Eqs. (B.4), (B.5) and (B.8) yields the Lagrangian

$$\begin{aligned} L &= T_{\text{rot}} + T_{\text{lin}} - V_{\text{spring}}, \\ &= \frac{1}{2} J \dot{\vartheta}_n^2 + \frac{1}{2} M_{\ddot{\vartheta}} \dot{\vartheta}_n^2 + \frac{1}{2} m \left[ \left( \dot{z}_p + \delta x \dot{\vartheta}_n \cos(\vartheta_n) \right)^2 + \left( \dot{x}_p + \delta x \dot{\vartheta}_n \sin(\vartheta_n) \right)^2 \right] - \frac{1}{2} \kappa (\vartheta_n - \theta)^2. \end{aligned} \tag{B.9}$$

### Dynamics

Inserting the Lagrangian from Eq. (B.9) into Eq. (B.2), the dynamics of the foils was found

$$\kappa \vartheta_n - \kappa \theta + J \ddot{\vartheta}_n + M_{\dot{\vartheta}_n} \dot{\vartheta}_n + M_{\ddot{\vartheta}_n} \ddot{\vartheta}_n + \delta x^2 m \ddot{\vartheta}_n + \delta x m \ddot{z}_p \cos(\vartheta_n) + \delta x m \ddot{x}_p \sin(\vartheta_n) = 0, \tag{B.10}$$

which can be reorganised into the same form as Eq. (3.99)

$$\underbrace{(J + \delta x^2 m + M_{\ddot{\vartheta}_n})}_{M_\vartheta} \ddot{\vartheta}_n + \underbrace{M_{\dot{\vartheta}_n}}_{B_\vartheta} \dot{\vartheta}_n + \underbrace{\kappa}_{C_\vartheta} \vartheta_n = \underbrace{\kappa}_{C_\vartheta} \theta \underbrace{-\delta x m \ddot{z}_p \cos(\vartheta_n) - \delta x m \ddot{x}_p \sin(\vartheta_n)}_{\text{inertia moment}}. \tag{B.11}$$

Comparing the dynamics without circulatory moments and non-circulatory moments to Eq. (3.99), the equivalent inertia moments are thus

$$Q_{\text{inertia}} = -\delta x m \ddot{z}_p \cos(\vartheta_n) - \delta x m \ddot{x}_p \sin(\vartheta_n). \tag{B.12}$$

It is seen that the correction introduced by Euler-Lagrange method is a fictitious moment, an inertia moment. This is a d'Alembert or inertia force which originates from d'Alembert's principle of reducing a dynamics problem to a statics problem. For Newton's second law, this means that $F = ma$ is equivalent to study $F - ma = 0$ where the term $-ma$ is a fictitious force.

**Remark 112.** *When the foil angle $\vartheta = \vartheta_n - \theta$ is small, the inertia forces in Eq. (B.12) can be approximated by the vertical contribution by $M_{\text{inertia}} \simeq -\delta x m \ddot{z}_p \cos(\vartheta_n)$.*

**Remark 113.** *We see that when the pivot point is accelerating upwards, $-\ddot{z}$, then a positive moment appears on the right hand side (for small $\vartheta_n$) making an inertial correction. In practice this means that the foils experience a positive acceleration.*

## B.2 Roll force response amplitude operator

The response amplitude operator for the roll moment excited from linear waves to roll motion for the simplified monohull geometry given in Sect. 3.3 is shown here. This derivation follows closely the one given in Jensen et al. [25]. The parameters in this derivation is defined in Sect. 3.3.

Firstly define the *radiation potential* $\varphi_4$ as the complex potential for forced roll motions, meaning waves generated by the roll motion of the vehicle. For a symmetrical body along $x$-axis, this potential is asymptotically equal [24]

$$\varphi_4 = \pm P_4 \mathrm{e}^{kz - j|yk\sin(\beta)|}, \quad y \to \pm\infty, \tag{B.13}$$

where $P_4$ depends on body shape and wave number. $P_4$ is related to the hydrodynamic damping by the relation

$$b_{44} = \rho\omega|P_4|^2. \tag{B.14}$$

The exciting moment for a section in the $yz$-plane is from the Haskind relation

$$k_0(x) = j\omega\rho\, \mathrm{e}^{j\omega t} \int_{-\infty}^{0} \left[\varphi \frac{\partial \varphi_4}{\partial y} - \varphi_4 \frac{\partial \varphi}{\partial y}\right]_{y=-\infty}^{y=\infty} \mathrm{d}y \tag{B.15}$$

where $\varphi$ is the complex wave potential given in section 2.3.3.

Integrating (B.15) with the relation from Newman in (B.14) equates to

$$k_0(x) = \sin(\beta)\sqrt{\frac{\rho g^2}{\omega} b_{44}}\, \mathrm{e}^{-jxk\cos(\beta)} \mathrm{e}^{j\omega t}. \tag{B.16}$$

Integration alogn the vehicle's length $L$ gives the total excitation moment

$$K_0 = \sin(\beta)\sqrt{\frac{\rho g^2}{\omega}}\, \mathrm{e}^{j\omega t} \left\{ \int_0^{\delta L} \sqrt{b_{44,\mathrm{a}}}\, \mathrm{e}^{-jxk\cos(\beta)} \mathrm{d}x + \int_{\delta L}^{L} \sqrt{b_{44,\mathrm{f}}}\, \mathrm{e}^{-jxk\cos(\beta)} \mathrm{d}x \right\}, \tag{B.17}$$

where the forcing function $K_0$ is the real part

$$K_0 = |\sin(\beta)| \sqrt{\frac{\rho g^2}{\omega}} \frac{2}{k_\mathrm{e}} \sqrt{b_{44,\mathrm{a}}} \left[ \sin\left(\delta \frac{k_\mathrm{e} L}{2}\right)^2 + \frac{b_{44,\mathrm{f}}}{b_{44,\mathrm{a}}} \sin\left((1-\delta)\frac{k_\mathrm{e} L}{2}\right)^2 + 2\sqrt{\frac{b_{44,\mathrm{f}}}{b_{44,\mathrm{a}}}} \sin\left(\delta \frac{k_\mathrm{e} L}{2}\right) \sin\left((1-\delta)\frac{k_\mathrm{e} L}{2}\right) \cos\left(\frac{k_\mathrm{e} L}{2}\right) \right]^{1/2}, \tag{B.18}$$

## B.3 Time-domain solution of simple retardation function

In this section the time domain solution of the frequency-domain function

$$\hat{k}'(s') = \frac{q'_0 s'}{s'^2 + p'_1 s' + p'_0}, \tag{B.19}$$

is derived. First the square is completed

$$\hat{k}'(s') = \frac{q'_0 s'}{\left(s' + \frac{p'_1}{2}\right)^2 + p'_0 - \left(\frac{p'_1}{2}\right)^2}, \tag{B.20}$$

and denote $a' \triangleq p'_1/2$ and $\omega_d^2 \triangleq p'_0 - (\frac{p'_1}{2})^2 > 0$ such that one can identify

$$\hat{k}'(s') = q'_0 \cdot \frac{(s'+a')}{(s'+a')^2 + \omega_d^2} - \frac{q'_0 a'}{\omega_d} \cdot \frac{\omega_d}{(s'+a')^2 + \omega_d^2}. \tag{B.21}$$

Equation (B.21) can be solved for the time domain solution $\hat{k}'(t')$ by using look-up tables for common Laplace transform pairs. On the present form, it is recognized as the sum of a damped sin()- and cos()-term with the exponential decay $e^{-a't'}$ with solution

$$\hat{k}'(t') = q'_0 e^{-a't'} \cos(\omega_d t') - \frac{q'_0 a'}{\omega_d} e^{-a't'} \sin(\omega_d t'). \tag{B.22}$$

By substituting for $a'$ and $\omega_d$ into Eq. (B.22) the analytical time-domain solution is identified as

$$\hat{k}'(t') = q'_0 e^{-\frac{p'_1}{2}t'} \cos\left(\left[p'_0 - \left(\frac{p'_1}{2}\right)^2\right]^{\frac{1}{2}} t'\right) - \frac{q'_0 p'_1}{2\left[p'_0 - \left(\frac{p'_1}{2}\right)^2\right]^{\frac{1}{2}}} e^{-\frac{p'_1}{2}t'} \sin\left(\left[p'_0 - \left(\frac{p'_1}{2}\right)^2\right]^{\frac{1}{2}} t'\right). \tag{B.23}$$

## B.4 Kinematics of two consecutive homogeneous transformations

The acceleration kinematics for two consecutive homogeneous transformation is derived. In order to ease the derivation, denote a coordinate-free vector fixed to a specific frame by the notation $[(\vec{\cdot})]^b$, where $\{b\}$ is the frame in which the vector $(\vec{\cdot})$ is fixed in.

Consider the point $x$ defined by frames $\{n\}$, $\{b\}$ and $\{p\}$ illustrated in Fig. B.2. The location of the point is given by the vector $\vec{r}_{\text{px}}$ in frame $\{p\}$ while the frame $\{p\}$ itself is located at point $\vec{r}_{\text{bp}}$ in frame $\{b\}$. With the notation introduced above, the total position of the point is

$$\vec{r}_{\text{nx}} = \vec{r}_{\text{nb}} + [\vec{r}_{\text{bp}} + [\vec{r}_{\text{px}}]^p]^b. \tag{B.24}$$

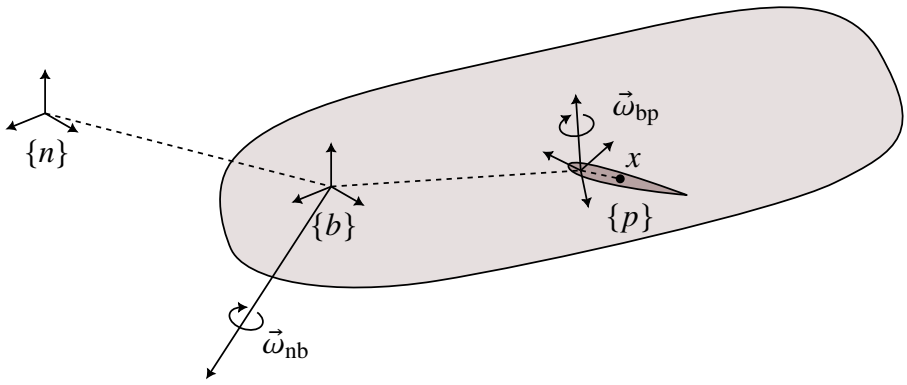


**Figure B.2:** The point $x$ is attached in frame $\{p\}$. Frame $\{p\}$ rotates with an angular velocity $\vec{\omega}_{\text{bp}}$ relative to frame $\{b\}$. Frame $\{b\}$ rotates with an angular velocity $\vec{\omega}_{\text{nb}}$ relative to frame $\{n\}$.

### Derivations

The velocity of point $x$ relative to $\{n\}$ is found through the kinematics of Eq. (2.6) such that

$${}^n\frac{\mathrm{d}}{\mathrm{d}t}\vec{r}_{\text{nx}} = {}^n\frac{\mathrm{d}}{\mathrm{d}t}\vec{r}_{\text{nb}} + {}^n\frac{\mathrm{d}}{\mathrm{d}t}[\vec{r}_{\text{bp}} + [\vec{r}_{\text{px}}]^p]^b, \tag{B.25}$$

and furthermore using that $\vec{v} \equiv \frac{\mathrm{d}}{\mathrm{d}t}\vec{r}$

$$\begin{aligned}
\vec{v}_{\text{nx}} &= \vec{v}_{\text{nb}} + \vec{\omega}_{\text{nb}} \times [\vec{r}_{\text{bp}} + [\vec{r}_{\text{px}}]^p]^b + \left[ {}^b\frac{\mathrm{d}}{\mathrm{d}t}\vec{r}_{\text{bp}} + {}^b\frac{\mathrm{d}}{\mathrm{d}t}[\vec{r}_{\text{px}}]^p \right]^b, \\
&= \vec{v}_{\text{nb}} + \vec{\omega}_{\text{nb}} \times [\vec{r}_{\text{bp}} + [\vec{r}_{\text{px}}]^p]^b + \left[ \vec{v}_{\text{bp}} + \vec{\omega}_{\text{bp}} \times [\vec{r}_{\text{px}}]^p + \left[ {}^p\frac{\mathrm{d}}{\mathrm{d}t}\vec{r}_{\text{px}} \right]^p \right]^b, \\
\vec{v}_{\text{nx}} &= \vec{v}_{\text{nb}} + \vec{\omega}_{\text{nb}} \times [\vec{r}_{\text{bp}} + [\vec{r}_{\text{px}}]^p]^b + \left[ \vec{v}_{\text{bp}} + \vec{\omega}_{\text{bp}} \times [\vec{r}_{\text{px}}]^p + \left[ \vec{v}_{\text{px}} \right]^p \right]^b.
\end{aligned} \tag{B.26}$$

The acceleration is found by once more applying Eq. (2.6), this time on Eq. (B.26) such that

$$
\begin{aligned}
{}^n\frac{\mathrm{d}}{\mathrm{d}t}\vec{v}_{\mathrm{nx}} &= {}^n\frac{\mathrm{d}}{\mathrm{d}t}\vec{v}_{\mathrm{nb}} + \underbrace{{}^n\frac{\mathrm{d}}{\mathrm{d}t}\left(\vec{\omega}_{\mathrm{nb}} \times [\vec{r}_{\mathrm{bp}} + [\vec{r}_{\mathrm{px}}]^p]^b\right)}_{\text{part 1}} + \underbrace{{}^n\frac{\mathrm{d}}{\mathrm{d}t}\left[\vec{v}_{\mathrm{bp}} + \vec{\omega}_{\mathrm{bp}} \times [\vec{r}_{\mathrm{px}}]^p + \left[\vec{v}_{\mathrm{px}}\right]^p\right]^b}_{\text{part 2}}, \\
&= \dot{\vec{v}}_{\mathrm{nb}} + \underbrace{\dot{\vec{\omega}}_{\mathrm{nb}} \times [\vec{r}_{\mathrm{bp}} + [\vec{r}_{\mathrm{px}}]^p]^b + \vec{\omega}_{\mathrm{nb}} \times \vec{\omega}_{\mathrm{nb}} \times [\vec{r}_{\mathrm{bp}} + [\vec{r}_{\mathrm{px}}]^p]^b + \vec{\omega}_{\mathrm{nb}} \times \left[{}^b\frac{\mathrm{d}}{\mathrm{d}t}\vec{r}_{\mathrm{bp}} + {}^b\frac{\mathrm{d}}{\mathrm{d}t}\left[\vec{r}_{\mathrm{px}}\right]^p\right]^b}_{\text{part 1}} \cdots \\
&\quad + \underbrace{\vec{\omega}_{\mathrm{nb}} \times \left[\vec{v}_{\mathrm{bp}} + \vec{\omega}_{\mathrm{bp}} \times [\vec{r}_{\mathrm{px}}]^p + \left[\vec{v}_{\mathrm{px}}\right]^p\right]^b + \left[{}^b\frac{\mathrm{d}}{\mathrm{d}t}\vec{v}_{\mathrm{bp}} + {}^b\frac{\mathrm{d}}{\mathrm{d}t}\left(\vec{\omega}_{\mathrm{bp}} \times [\vec{r}_{\mathrm{px}}]^p\right) + {}^b\frac{\mathrm{d}}{\mathrm{d}t}\left[\vec{v}_{\mathrm{px}}\right]^p\right]^b}_{\text{part 2}}, \\
&= \dot{\vec{v}}_{\mathrm{nb}} + \underbrace{\dot{\vec{\omega}}_{\mathrm{nb}} \times [\vec{r}_{\mathrm{bp}} + [\vec{r}_{\mathrm{px}}]^p]^b + \vec{\omega}_{\mathrm{nb}} \times \vec{\omega}_{\mathrm{nb}} \times [\vec{r}_{\mathrm{bp}} + [\vec{r}_{\mathrm{px}}]^p]^b + \vec{\omega}_{\mathrm{nb}} \times \left[\vec{v}_{\mathrm{bp}} + \vec{\omega}_{\mathrm{bp}} \times \left[\vec{r}_{\mathrm{px}}\right]^p + \left[\vec{v}_{\mathrm{px}}\right]^p\right]^b}_{\text{part 1}} \cdots \\
&\quad + \underbrace{\vec{\omega}_{\mathrm{nb}} \times \left[\vec{v}_{\mathrm{bp}} + \vec{\omega}_{\mathrm{bp}} \times [\vec{r}_{\mathrm{px}}]^p + \left[\vec{v}_{\mathrm{px}}\right]^p\right]^b}_{\text{part 2a}} \cdots \\
&\quad + \underbrace{\left[\dot{\vec{v}}_{\mathrm{bp}} + \dot{\vec{\omega}}_{\mathrm{bp}} \times [\vec{r}_{\mathrm{px}}]^p + \vec{\omega}_{\mathrm{bp}} \times \vec{\omega}_{\mathrm{bp}} \times [\vec{r}_{\mathrm{px}}]^p + \vec{\omega}_{\mathrm{bp}} \times [\vec{v}_{\mathrm{px}}]^p + \vec{\omega}_{\mathrm{bp}} \times \left[\vec{v}_{\mathrm{px}}\right]^p + \left[\dot{\vec{v}}_{\mathrm{px}}\right]^p\right]^b}_{\text{part 2b}}.
\end{aligned}
\tag{B.27}
$$

Simplifying Eq. (B.27), the acceleration of point $x$ in Fig. B.2 is readily found as

$$
\begin{aligned}
\dot{\vec{v}}_{\mathrm{nx}} &= \dot{\vec{v}}_{\mathrm{nb}} + \dot{\vec{\omega}}_{\mathrm{nb}} \times [\vec{r}_{\mathrm{bp}} + [\vec{r}_{\mathrm{px}}]^p]^b + \vec{\omega}_{\mathrm{nb}} \times \vec{\omega}_{\mathrm{nb}} \times [\vec{r}_{\mathrm{bp}} + [\vec{r}_{\mathrm{px}}]^p]^b \cdots \\
&\quad + 2\vec{\omega}_{\mathrm{nb}} \times \left[\vec{v}_{\mathrm{bp}} + \vec{\omega}_{\mathrm{bp}} \times [\vec{r}_{\mathrm{px}}]^p + \left[\vec{v}_{\mathrm{px}}\right]^p\right]^b \cdots \\
&\quad + \left[\dot{\vec{v}}_{\mathrm{bp}} + \dot{\vec{\omega}}_{\mathrm{bp}} \times [\vec{r}_{\mathrm{px}}]^p + \vec{\omega}_{\mathrm{bp}} \times \vec{\omega}_{\mathrm{bp}} \times [\vec{r}_{\mathrm{px}}]^p + 2\vec{\omega}_{\mathrm{bp}} \times \left[\vec{v}_{\mathrm{px}}\right]^p + \left[\dot{\vec{v}}_{\mathrm{px}}\right]^p\right]^b.
\end{aligned}
\tag{B.28}
$$

**Remark 114.** *When $\vec{r}_{bp}$ and $\vec{r}_{px}$ is constant in their respective frames, the acceleration is*

$$
\begin{aligned}
\dot{\vec{v}}_{nx} &= \dot{\vec{v}}_{nb} + \dot{\vec{\omega}}_{nb} \times [\vec{r}_{bp} + [\vec{r}_{px}]^p]^b + \vec{\omega}_{nb} \times \vec{\omega}_{nb} \times [\vec{r}_{bp} + [\vec{r}_{px}]^p]^b \cdots \\
&\quad + 2\vec{\omega}_{nb} \times \left[\vec{\omega}_{bp} \times [\vec{r}_{px}]^p\right]^b + \left[\dot{\vec{\omega}}_{bp} \times [\vec{r}_{px}]^p + \vec{\omega}_{bp} \times \vec{\omega}_{bp} \times [\vec{r}_{px}]^p\right]^b.
\end{aligned}
\tag{B.29}
$$

*Or, written as*

$$
\dot{\mathbf{v}}_{nx} = \dot{\mathbf{v}}_{nb} + \mathbf{S}(\dot{\omega}_{nb})[\mathbf{r}_{bp} + \mathbf{r}_{px}] + \mathbf{S}(\omega_{nb})^2[\mathbf{r}_{bp} + \mathbf{r}_{px}] + 2\mathbf{S}(\omega_{nb})\mathbf{S}(\omega_{bp})\mathbf{r}_{px} + \mathbf{S}(\dot{\omega}_{bp})\mathbf{r}_{px} + \mathbf{S}(\omega_{bp})^2\mathbf{r}_{px}
\tag{B.30}
$$

## B.5 Torsion spring stiffness

A closed-wound spring is illustrated in Fig. B.3 with $N_a$ numbers of active turns, wire diameter $d$, spring diameter $D$ and deflection angle $\theta$.

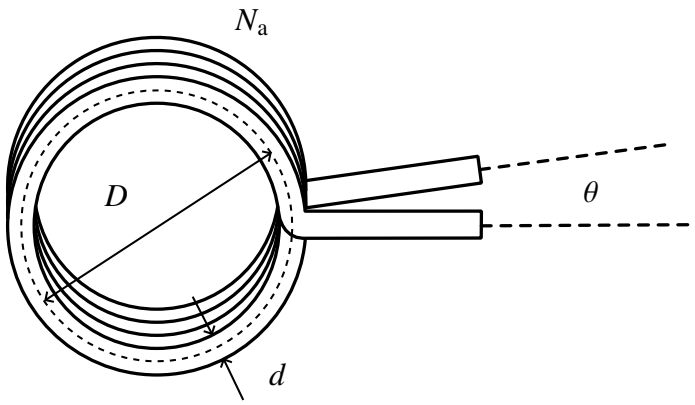


**Figure B.3:** Closed-wound spring.

Castigliano's method was employed to find the deflection in radians in the body of a torsion spring. From Timoshenko, pp. 288–290, [75] the potential energy in equilibrium is

$$V = \frac{1}{2}\int_{\text{coil}} \frac{M^2}{EI}\mathrm{d}\theta, \tag{B.31}$$

with external moment $M$, Young's modulus $E$ and $I$ is the second moment of area of the coil section along the coil length. Let the external moment be $M = Fr$ and integrate over the length of the body-coil wire. The force $F$ will deflect through a distance $r\theta$ and the change in potential energy in Eq. (B.31) equals a change in the force $F$ over the distance $r\theta$ as $\delta V = \delta F \cdot r\theta$. The angle $\theta$ is found

$$\theta = \frac{\partial V}{r\partial F} = \frac{1}{2r}\int_0^{\pi D N_a} \frac{\partial}{\partial F}\left(\frac{F^2 r^2}{EI}\right)\mathrm{d}x = \int_0^{\pi D N_a} \frac{Fr}{EI}\mathrm{d}x = \underbrace{\frac{64 D N_a}{E d^4}}_{1/\kappa} M. \tag{B.32}$$

For an ideal spring, the torsion spring stiffness was found according to Eq. (B.32) on the form

$$\kappa = \frac{E d^4}{64 D N_a}. \tag{B.33}$$

# Appendix C

# Alternative formulations for vehicle derivatives

## C.1 Maneuvering derivatives

**Table C.1:** Alternative empiric relations for maneuvering parameters. Semi-empirical methods for acceleration and velocity derivatives as function of maneuvering design parameters $\{L_\mathrm{d}, B_\mathrm{d}, T_\mathrm{d}, C_\mathrm{B}\}$. From Clarke et al. [44].

| Derivative | Strip | Norrbin | Inoue et al. | Clarke et al. |
|---|---|---|---|---|
| $-Y'_{\dot{v}}/\pi \left(\frac{T_\mathrm{d}}{L_\mathrm{d}}\right)^2$ | 1 | - | - | $1 + 0.16 C_\mathrm{B} \frac{B_\mathrm{d}}{T_\mathrm{d}} - 5.1 \left(\frac{B_\mathrm{d}}{L_\mathrm{d}}\right)^2$ |
| $-Y'_{\dot{r}}/\pi \left(\frac{T_\mathrm{d}}{L_\mathrm{d}}\right)^2$ | 0 | - | - | $0.67 \frac{B_\mathrm{d}}{L_\mathrm{d}} - 0.0033 \left(\frac{B_\mathrm{d}}{T_\mathrm{d}}\right)^2$ |
| $-N'_{\dot{v}}/\pi \left(\frac{T_\mathrm{d}}{L_\mathrm{d}}\right)^2$ | 0 | - | - | $1.1 \frac{B_\mathrm{d}}{L_\mathrm{d}} - 0.41 \frac{B_\mathrm{d}}{T_\mathrm{d}}$ |
| $-N'_{\dot{r}}/\pi \left(\frac{T_\mathrm{d}}{L_\mathrm{d}}\right)^2$ | $\frac{1}{12}$ | - | - | $\frac{1}{12} + 0.017 C_\mathrm{B} \frac{B_\mathrm{d}}{T_\mathrm{d}} - 0.33 \frac{B_\mathrm{d}}{L_\mathrm{d}}$ |
| $-Y'_{v}/\pi \left(\frac{T_\mathrm{d}}{L_\mathrm{d}}\right)^2$ | 1 | $1.69 + 0.08 \frac{C_\mathrm{B}}{\pi} \frac{B_\mathrm{d}}{T_\mathrm{d}}$ | $1.0 + 1.4 \frac{C_\mathrm{B}}{\pi} \frac{B_\mathrm{d}}{T_\mathrm{d}}$ | $1 + 0.40 C_\mathrm{B} \frac{B_\mathrm{d}}{T_\mathrm{d}}$ |
| $-Y'_{r}/\pi \left(\frac{T_\mathrm{d}}{L_\mathrm{d}}\right)^2$ | $-\frac{1}{2}$ | $-0.645 + 0.38 \frac{C_\mathrm{B}}{\pi} \frac{B_\mathrm{d}}{T_\mathrm{d}}$ | $-0.5$ | $-0.5 + 2.2 \frac{B_\mathrm{d}}{L_\mathrm{d}} - 0.080 \frac{B_\mathrm{d}}{T_\mathrm{d}}$ |
| $-N'_{v}/\pi \left(\frac{T_\mathrm{d}}{L_\mathrm{d}}\right)^2$ | $\frac{1}{2}$ | $0.64 - 0.04 \frac{C_\mathrm{B}}{\pi} \frac{B_\mathrm{d}}{T_\mathrm{d}}$ | $\frac{2.0}{\pi} \frac{C_\mathrm{B}}{\pi} \frac{B_\mathrm{d}}{T_\mathrm{d}}$ | $0.5 + 2.4 \frac{T_\mathrm{d}}{L_\mathrm{d}}$ |
| $-N'_{r}/\pi \left(\frac{T_\mathrm{d}}{L_\mathrm{d}}\right)^2$ | $\frac{1}{4}$ | $0.47 - 0.18 \frac{C_\mathrm{B}}{\pi} \frac{B_\mathrm{d}}{T_\mathrm{d}}$ | $\frac{1.04}{\pi} - \frac{4.0}{\pi} \frac{T_\mathrm{d}}{L_\mathrm{d}} \frac{C_\mathrm{B}}{\pi} \frac{B_\mathrm{d}}{T_\mathrm{d}}$ | $0.25 + 0.039 \frac{B_\mathrm{d}}{T_\mathrm{d}} - 0.56 \frac{B_\mathrm{d}}{L_\mathrm{d}}$ |

## C.2 Seakeeping oscillatory derivatives

**Table C.2:** Wave-induced motion derivatives as function of parameters $\boldsymbol{\alpha}_2^*$ and main particulars. Only the damping in heave and pitch is frequency-dependent.

| Derivative | Proposed model approximation |
|---|---|
| $-\tilde{Z}_{\dot{w}}(\omega)$ | $2\rho C_{\mathrm{wp}} BLT^* - m$ |
| $-\tilde{Z}_{w}(\omega)$ | $\left(C_{\mathrm{wp}} \frac{B}{B^*}\right) Lb(\omega)$ |
| $-\tilde{Z}_{z}(\omega)$ | $\rho g C_{\mathrm{wp}} BL$ |
| $-\tilde{K}_{\dot{p}}(\omega)$ | $\left(\frac{T_4^*}{2\pi}\right)^2 \rho g \nabla \mathrm{GM_T} - J_x$ |
| $-\tilde{K}_{p}(\omega)$ | $2\zeta_4^* \left(\frac{T_4^*}{2\pi}\right) \rho g \nabla \mathrm{GM_T}$ |
| $-\tilde{K}_{\phi}(\omega)$ | $\rho g \nabla \mathrm{GM_T}$ |
| $-\tilde{M}_{\dot{q}}(\omega)$ | $2\rho \nabla \mathrm{GM_L} T^* - J_y$ |
| $-\tilde{M}_{q}(\omega)$ | $\left(\frac{B}{B^*} C_{\mathrm{B}}\right) \cdot T \mathrm{GM_L} Lb(\omega)$ |
| $-\tilde{M}_{\theta}(\omega)$ | $\rho g \nabla \mathrm{GM_L}$ |

**Table C.3:** Tabular values for parameters in the non-dimensional transfer function of smallest order for simulation of fluid memory effects for homogeneously loaded box-shaped vessels following the damping from Newman [24] for use in heave and pitch motions. The values are found through a least squares optimization by the impulse response of the retardation function for various ratios $\Lambda_T$.

| Ratio $\Lambda_T$ $= (B/T)$ | $q'_0$ | $p'_0$ | $p'_1$ |
|---|---|---|---|
| 1.0 | 0.2729 | 0.2801 | 0.6209 |
| 1.2 | 0.3007 | 0.3121 | 0.6380 |
| 1.4 | 0.3236 | 0.3387 | 0.6502 |
| 1.6 | 0.3428 | 0.3610 | 0.6593 |
| 1.8 | 0.3591 | 0.3799 | 0.6663 |
| 2.0 | 0.3731 | 0.3961 | 0.6718 |
| 2.2 | 0.3854 | 0.4101 | 0.6763 |
| 2.4 | 0.3961 | 0.4223 | 0.6801 |
| 2.6 | 0.4056 | 0.4330 | 0.6833 |
| 2.8 | 0.4141 | 0.4425 | 0.6860 |
| 3.0 | 0.4217 | 0.4509 | 0.6884 |
| 3.2 | 0.4285 | 0.4585 | 0.6906 |
| 3.4 | 0.4348 | 0.4653 | 0.6925 |
| 3.6 | 0.4404 | 0.4715 | 0.6942 |
| 3.8 | 0.4456 | 0.4771 | 0.6957 |
| 4.0 | 0.4504 | 0.4823 | 0.6971 |
| 4.2 | 0.4548 | 0.4870 | 0.6984 |
| 4.4 | 0.4589 | 0.4913 | 0.6996 |
| 4.6 | 0.4627 | 0.4953 | 0.7007 |
| 4.8 | 0.4662 | 0.4990 | 0.7017 |
| 5.0 | 0.4695 | 0.5024 | 0.7027 |
| 6.0 | 0.4832 | 0.5164 | 0.7066 |
| 7.0 | 0.4934 | 0.5266 | 0.7097 |
| 8.0 | 0.5015 | 0.5344 | 0.7121 |
| 9.0 | 0.5079 | 0.5406 | 0.7141 |
| 10 | 0.5132 | 0.5456 | 0.7158 |
| $\infty$ | 0.5696 | 0.5917 | 0.7376 |

## C.3 Correction of maneuvering derivatives in shallow water

The material in this section is based on Sheng [78] and from Clark et al. [44].

The effects of shallow water on the maneuvering derivatives have been studied experimentally, and it has been found that in general the numerical values increase as the water depth reduces. However, the manner in which each derivative changes with water depth is different. Correction factors have been suggested by Sheng based on slender body theory. The ship was assumed to have a parabolic form for the breadth distribution and elliptical cross section. According to Clarke et al. [44], the formulae given by Sheng are in good agreement with the experimental results. The correction factors are as follows

$$Y'_{\dot{v}}/Y'_{\dot{v}\infty} = K_0 + \frac{2}{3}K_1\frac{B}{T} + \frac{8}{15}K_2\left(\frac{B}{T}\right)^2, \tag{C.1a}$$

$$N'_{\dot{r}}/N'_{\dot{r}\infty} = K_0 + \frac{2}{5}K_1\frac{B}{T} + \frac{24}{105}K_2\left(\frac{B}{T}\right)^2, \tag{C.1b}$$

$$Y'_{v}/Y'_{v\infty} = K_0 + K_1\frac{B}{T} + K_2\left(\frac{B}{T}\right)^2, \tag{C.1c}$$

$$Y'_{r}/Y'_{r\infty} = K_0 + \frac{2}{3}K_1\frac{B}{T} + \frac{8}{15}K_2\left(\frac{B}{T}\right)^2, \tag{C.1d}$$

$$N'_{v}/N'_{v\infty} = K_0 + \frac{2}{3}K_1\frac{B}{T} + \frac{8}{15}K_2\left(\frac{B}{T}\right)^2, \tag{C.1e}$$

$$N'_{r}/N'_{r\infty} = K_0 + \frac{1}{2}K_1\frac{B}{T} + \frac{1}{3}K_2\left(\frac{B}{T}\right)^2, \tag{C.1f}$$

where the correction constant $K_0$, $K_1$ and $K_2$ are

$$K_0 \equiv 1 + \frac{0.0775}{F^2} - \frac{0.0110}{F^3}, \tag{C.2a}$$

$$K_1 \equiv -\frac{0.0643}{F} + \frac{0.0724}{F^2} - \frac{0.043}{F^3}, \tag{C.2b}$$

$$K_2 \equiv \frac{0.0342}{F}, \tag{C.2c}$$

and the parameter $F$ is related to the water depth by

$$F \triangleq \left(\frac{H}{T} - 1\right). \tag{C.3}$$

In the above formulae the subscript $\infty$ refers to the deep water value of the derivative. Unfortunately, no corrections were given for the derivatives $Y'_{\dot{r}}$ and $N'_{\dot{v}}$.

# Appendix D

# Foil contour for NTNU AutoNaut

Projected foil contours for NTNU AutoNaut are illustrated in Fig. D.1 and tabular values are listed in Tab. D.1, were it was assumed that the foil at the stern and bow had the same curvature.

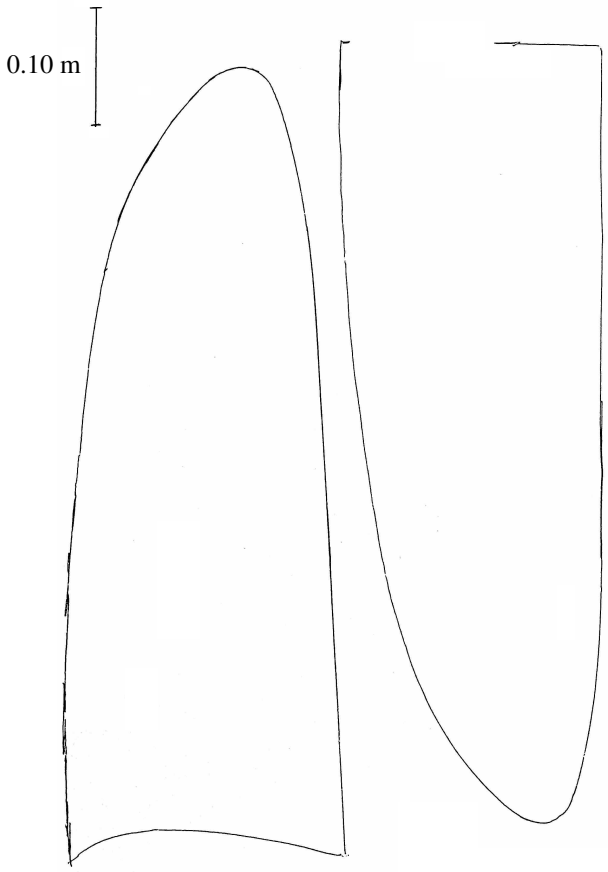


**(a)** Foil at the stern (starboard side). **(b)** Foil at the bow (port side).

**Figure D.1:** Projected foil contours present at NTNU AutoNaut. The shapes were found by hand drawing on a sheet of paper and scanned. Adapted from Tufte [17].

**Table D.1:** Chord length per half span on NTNU AutoNaut. The distances were measured from the projected contour illustrated in Fig. D.1.

| 0–50% $y/2S$ | TE (±0.01) | LE (±0.01) | Chord length $c/2S$ (±0.015) | 50–100% $y/2S$ | TE (±0.01) | LE (±0.01) | Chord length $c/2S$ (±0.015) |
|---|---|---|---|---|---|---|---|
| 0.000 | 0.000 | 0.348 | 0.348 | 0.500 | 0.000 | 0.314 | 0.314 |
| 0.015 | 0.000 | 0.348 | 0.348 | 0.515 | 0.000 | 0.311 | 0.311 |
| 0.030 | 0.000 | 0.348 | 0.348 | 0.530 | 0.000 | 0.309 | 0.309 |
| 0.045 | 0.000 | 0.348 | 0.348 | 0.545 | 0.000 | 0.308 | 0.308 |
| 0.061 | 0.000 | 0.348 | 0.348 | 0.561 | 0.000 | 0.305 | 0.305 |
| 0.076 | 0.000 | 0.348 | 0.348 | 0.576 | 0.000 | 0.302 | 0.302 |
| 0.091 | 0.000 | 0.348 | 0.348 | 0.591 | 0.000 | 0.300 | 0.300 |
| 0.106 | 0.000 | 0.348 | 0.348 | 0.606 | 0.000 | 0.298 | 0.298 |
| 0.121 | 0.000 | 0.348 | 0.348 | 0.621 | 0.002 | 0.295 | 0.294 |
| 0.136 | 0.000 | 0.348 | 0.348 | 0.636 | 0.002 | 0.292 | 0.291 |
| 0.152 | 0.000 | 0.347 | 0.347 | 0.652 | 0.002 | 0.289 | 0.288 |
| 0.167 | 0.000 | 0.347 | 0.347 | 0.667 | 0.002 | 0.285 | 0.283 |
| 0.182 | 0.000 | 0.347 | 0.347 | 0.682 | 0.003 | 0.282 | 0.279 |
| 0.197 | 0.000 | 0.345 | 0.345 | 0.697 | 0.003 | 0.279 | 0.276 |
| 0.212 | 0.000 | 0.345 | 0.345 | 0.712 | 0.003 | 0.276 | 0.273 |
| 0.227 | 0.000 | 0.344 | 0.344 | 0.727 | 0.005 | 0.271 | 0.267 |
| 0.242 | 0.000 | 0.344 | 0.344 | 0.742 | 0.005 | 0.268 | 0.264 |
| 0.258 | 0.000 | 0.342 | 0.342 | 0.758 | 0.006 | 0.264 | 0.258 |
| 0.273 | 0.000 | 0.341 | 0.341 | 0.773 | 0.006 | 0.259 | 0.253 |
| 0.288 | 0.000 | 0.339 | 0.339 | 0.788 | 0.008 | 0.255 | 0.247 |
| 0.303 | 0.000 | 0.338 | 0.338 | 0.803 | 0.009 | 0.248 | 0.239 |
| 0.318 | 0.000 | 0.336 | 0.336 | 0.818 | 0.011 | 0.242 | 0.232 |
| 0.333 | 0.000 | 0.335 | 0.335 | 0.833 | 0.012 | 0.235 | 0.223 |
| 0.348 | 0.000 | 0.333 | 0.333 | 0.848 | 0.014 | 0.227 | 0.214 |
| 0.364 | 0.000 | 0.332 | 0.332 | 0.864 | 0.017 | 0.220 | 0.203 |
| 0.379 | 0.000 | 0.330 | 0.330 | 0.879 | 0.020 | 0.209 | 0.189 |
| 0.394 | 0.000 | 0.329 | 0.329 | 0.894 | 0.023 | 0.200 | 0.177 |
| 0.409 | 0.000 | 0.327 | 0.327 | 0.909 | 0.026 | 0.188 | 0.162 |
| 0.424 | 0.000 | 0.326 | 0.326 | 0.924 | 0.029 | 0.177 | 0.148 |
| 0.439 | 0.000 | 0.323 | 0.323 | 0.939 | 0.032 | 0.164 | 0.132 |
| 0.455 | 0.000 | 0.321 | 0.321 | 0.955 | 0.036 | 0.150 | 0.114 |
| 0.470 | 0.000 | 0.318 | 0.318 | 0.970 | 0.042 | 0.136 | 0.094 |
| 0.485 | 0.000 | 0.317 | 0.317 | 0.985 | 0.053 | 0.118 | 0.065 |
| 0.500 | 0.000 | 0.314 | 0.314 | 1.000 | 0.073 | 0.092 | 0.020 |